

新 制
工
1035
京大附図

Step-Controlled Epitaxial Growth of α -SiC and Device Applications

October 1995

Tsunenobu KIMOTO

Abstract

In this thesis, chemical vapor deposition (CVD) of silicon carbide (SiC) on SiC{0001} substrates and device applications have been studied. Through recent progress in SiC growth techniques, SiC has been recognized as a vital wide bandgap material for high-power, high-frequency, high-temperature, and radiation-resistant devices, owing to its tremendous properties. SiC appears in a number of crystal structures with one-dimensional variation, so-called “polytypes”, which means that the polytype control during growth is crucial for device applications. For this purpose, polytype-controlled epitaxial growth of SiC, which utilizes step-flow growth on off-oriented SiC{0001} substrates (*step-controlled epitaxy*), is presented in this thesis. After detailed analyses on growth mechanism including surface kinetics, characterization of epilayers, impurity doping, and device applications are described.

In Chapter 2, the outline of step-controlled epitaxy is described from a viewpoint of growth mode. Step-flow growth on off-oriented α -SiC{0001} substrates leads to homoepitaxy of α -SiC (step-controlled epitaxy), whereas two-dimensional nucleation results in the growth of 3C-SiC with double positioning twin. Low-temperature growth was attempted, and homoepitaxial growth of 6H-SiC could be achieved at temperatures as low as 1200°C.

In Chapter 3, growth mechanism in step-controlled epitaxy is discussed. The effects of growth temperature, off-angle, substrate polarity are described. Very little polarity dependence and small activation energy of growth rate (2.8kcal/mole) in step-controlled epitaxy can be explained by the fact that SiC growth is controlled by the diffusion of reactants in a stagnant layer. The step-bunching on the surfaces of 6H- and 4H-SiC epilayers is also investigated. Polarity and polytype dependences are discussed based on surface energy consideration.

In Chapter 4, a model describing SiC growth on vicinal {0001} substrates is proposed based on a classical surface diffusion theory. Using the model and several experimental results, critical growth conditions where the growth mode changes from step-flow to two-dimensional nucleation are predicted as a function of growth temperature, growth rate and substrate's off-angle. The obtained chart of growth condition will give a guideline for step-controlled

epitaxy.

In Chapter 5, microscopic surface kinetics in SiC growth is analyzed. Through short-time growth experiments, nucleation on {0001} terraces and step-dynamics are discussed. The polarity dependence of nucleation and the anisotropy in lateral growth rate are presented. A surface diffusion model is proposed to estimate the surface diffusion length of migrating species. The diffusion length was about $13\mu\text{m}$ on 6H-SiC{0001} faces under a typical growth condition at 1500°C . The influences of growth conditions on the surface diffusion lengths are discussed.

In Chapter 6, characterization of epilayers and impurity doping are described. High quality of SiC epilayers was elucidated by a cross-sectional TEM analysis, low-temperature photoluminescence, Hall effect, and deep level analysis. For a low-doped 6H-SiC epilayer ($n=2\times 10^{14}\text{cm}^{-3}$), a high electron mobility of $431\text{cm}^2/\text{Vs}$ could be obtained. The concentration of deep electron traps in epilayers was very small ($< 10^{13}\text{cm}^{-3}$). *In-situ* doping of N, Al, and B was investigated in the wide range of $10^{16}\sim 10^{19}\text{cm}^{-3}$ with excellent controllability, using N_2 , trimethylaluminum (TMA), and B_2H_6 as dopant sources. N^+ , Al^+ , and B^+ implantations into 6H-SiC{0001} epilayers were also investigated. The lowest sheet resistances of 1500°C -annealed samples were $770\Omega/\square$ (n-type) for N^+ implantation, and $22\text{k}\Omega/\square$ (p-type) for Al^+ implantation. B^+ implantation resulted in the formation of resistive layers ($\rho=15\sim 120\Omega\text{cm}$).

In Chapter 7, numerical analyses on the performance of 6H- and 4H-SiC power Schottky rectifiers and MOSFETs and preliminary fabrication of Schottky and pn junction diodes are described. Theoretical simulation showed that the extremely low drift-region resistances (about $1/50\sim 1/500$ of those of Si devices) can be expected in SiC power devices, owing to its high breakdown field. Au/6H-SiC Schottky rectifiers were successfully fabricated with a record breakdown voltage of 1100V and a specific on-resistance of $8.5\text{m}\Omega\text{cm}^2$, which is only $1/20$ of the theoretical limit of a Si rectifier with the same blocking voltage. A very high breakdown voltage of 1720V was obtained for epitaxial pn junction diodes. The pn junction diodes formed by N^+ implantation showed a high breakdown voltage of 450V , and high-temperature operation at 350°C .

In Chapter 8, the summary of the present work is given, together with the remaining problems and suggestions for future studies.

Acknowledgments

The author would like to express his deep gratitude to Prof. Hiroyuki Matsunami for his providing the opportunity to accomplish this work and for his continuous guidance, supervision, and encouragement throughout this study. The author also would like to thank Prof. Akio Sasaki and Prof. Shigeo Fujita for their valuable advice and critical comments on the manuscript.

He wishes to express gratitude to Prof. Wolfgang Jim Choyke at University of Pittsburgh, USA, and Prof. Gerhard Pensl at Universität Erlangen-Nürnberg, Germany, for their instructive advice on characterization.

He is indebted to Associate Prof. Shigehiro Nishino at Kyoto Institute of Technology for his guidance on experimental details and kind encouragement. He is also grateful to Associate Prof. Takashi Fuyuki and Lecturer Masahiro Yoshimoto for their helpful suggestions.

He is also very much obliged to Dr. Kentaro Shibahara, Mr. Naotaka Kuroda, Mr. Tetsuzo Ueda, and Mr. Hironori Nishino for their pioneering works, from which this study has originated. He wishes to thank Dr. Woo Sik Yoo and Dr. Tatsuo Yoshinobu for their constructive advice and encouragement as good friends.

Special thanks are due to Mr. Seiji Yaguchi, from Mitsubishi Heavy Industry, LTD, who made great contribution to the study on ion-implantation. Special thanks also go to Dr. Seongjoo Jang, from Donshing University, Korea, who performed a deep level analysis. The author would like to thank Mr. Tatsuo Urushidani, from Fuji Electric Research and Development Ltd., for his work on fabrication of Schottky rectifiers. He expresses great appreciation to Mr. Atsushi Yamashita, Mr. Akira Itoh, Mr. Sota Kobayashi, and Mr. Hironobu Akita for their contribution to this work. He also thanks Mr. Katsushi Nishino, Mr. Tomoaki Hatayama, Mr. Tadashi Fujii, and all other members of Matsunami Laboratory.

The author is grateful to Prof. Itsuo Kimura and Dr. Ikuo Kanno at Department of Nuclear Engineering for their giving a chance to use a deep level measurement system. He is obliged to Prof. Nobutsugu Imanishi and Dr. Kouji Yoshida at Department of Nuclear Engineering for the use of RBS equipment. The experiments were also supported by staffs and facilities at Sasaki

Laboratory, Fujita Laboratory, Ishikawa Laboratory, Yamada Laboratory, and Matsushige Laboratory.

He is grateful to Prof. Shinichi Nakashima and Associate Prof. Hiroshi Harima at Osaka University for their valuable discussion on Raman scattering data. He wishes to thank Prof. Tadashi Ohachi at Doshisha University for the use of RHEED equipment. Special thanks are due to Dr. Masanori Watanabe and Mr. Toshitake Nakata at Ion Engineering Research Institute for their providing an opportunity to use ion-implantation, Raman scattering, TEM and SIMS measurement systems. He is grateful to Mr. Tetsuyuki Okano at Mastushita Technoreseach, Inc. for his excellent TEM analysis. He also thanks Mr. Hideaki Tanaka at Yakushima Denko K.K. for supply of Acheson crystals.

The author wishes to express gratitude to the Ministry of Education, Science, Sports and Culture, Japan, the Murata Science Foundation and the Kawakami Memorial Foundation for their partial support to this work.

Finally, the author really thanks his parents and wife for their understanding, support, and heartfelt encouragement.

Contents

Abstract	i
Acknowledgments	iii
Contents	v
Chapter 1. Introduction	1
1.1 Background	1
1.2 Silicon Carbide	2
1.2.1 Properties of silicon carbide	2
1.2.2 History and the present situation	7
1.3 Outline of Thesis	13
References	15
Chapter 2. Step-Controlled Epitaxy of α-SiC	19
2.1 Introduction	19
2.2 Chemical Vapor Deposition (CVD) System	20
2.2.1 Wafer preparation	20
2.2.2 CVD apparatus and growth procedures	22
2.3 Step-Controlled Epitaxy	25
2.3.1 Growth on well-oriented 6H-SiC{0001} faces	25
2.3.2 Growth on off-oriented 6H-SiC{0001} faces	28
2.3.3 Growth mode	32
2.4 Low-Temperature Growth	38
2.5 Summary	43
References	43

Chapter 3. Growth Mechanism of Step-Controlled Epitaxy	45
3.1 Introduction	45
3.2 Rate-Determining Step	46
3.2.1 C/Si ratio dependence	46
3.2.2 Off-angle dependence	52
3.2.3 Growth temperature dependence	55
3.2.4 Discussion	57
3.3 Step Bunching	64
3.3.1 Atomic force microscope analysis	64
3.3.2 Transmission electron microscope observation	68
3.3.3 Discussion	75
3.4 Summary	86
References	86
Chapter 4. Critical Growth Conditions for Step-Controlled Epitaxy	89
4.1 Introduction	89
4.2 Growth Model on Vicinal Substrates	90
4.3 Application to SiC Growth	93
4.3.1 Desorption flux n_{s0}/τ	93
4.3.2 Critical supersaturation ratio	99
4.4 Prediction of Step-Flow Growth Condition	102
4.4.1 Surface diffusion length	102
4.4.2 Critical growth condition	107
4.5 Summary	109
References	110
List of Nomenclature	111
Chapter 5. Surface Kinetics in Step-Controlled Epitaxy	113
5.1 Introduction	113
5.2 Nucleation and Step Dynamics	114
5.2.1 Experimental procedures	114
5.2.2 Nucleation on 6H-SiC{0001} terraces	115

5.2.3 Lateral growth of steps	121
5.2.4 Effects of off-orientation	126
5.3 Surface Diffusion Length	130
5.3.1 Estimation of surface diffusion length	130
5.3.2 Influence of growth conditions on diffusion length	133
5.3.3 Discussion	144
5.4 Summary	145
References	146

Chapter 6. Characterization of Epilayers and Impurity Doping

.....	149
6.1 Introduction	149
6.2 Structural Characterization	150
6.3 Physical Properties of Undoped Epilayers	157
6.3.1 Photoluminescence	157
6.3.2 Hall effect measurement	160
6.3.3 Deep level analysis	164
6.4 <i>In situ</i> Doping of Impurities	172
6.4.1 Nitrogen doping	172
6.4.2 Aluminum and Boron doping	175
6.5 Ion Implantation into Epilayers	178
6.5.1 Nitrogen ion implantation	178
6.5.2 Aluminum and boron ion implantations	194
6.6 Summary	200
References	201

Chapter 7. Application to High-Power, High-Temperature Devices

.....	205
7.1 Introduction	205
7.2 Prediction of SiC Power Devices	206
7.2.1 Specific on-resistance	206
7.2.2 Effects of channel mobility	209
7.3 High-Voltage Schottky Rectifiers	214
7.4 High-Voltage, High-Temperature pn Diodes	224

7.5 Summary	234
References	235
Chapter 8. Conclusions	239
8.1 Conclusions	239
8.2 For the Future Work	241
References	245
Appendix	247
List of Publications	249

Chapter 1

Introduction

1.1 Background

Performance of tools and devices is basically limited by the intrinsic properties of materials and their designs or structures. This is, of course, true in semiconductor devices, which support the modern civilization as hardware. Most of the present-day semiconductor devices utilize silicon (Si), owing to the availability of a very high-pure and high-quality crystal and an excellent oxide. Once the material has been fixed, the device performance cannot be improved without the further development of fabrication techniques or the invention of a novel structure. This strategy is reflected in the rapid development of device processing technology for integrating numerous transistors of Si [1]. However, Si technology is now so mature that there remains a little prospect for revolutionary improvement. Although III-V semiconductors such as gallium arsenide (GaAs) play an important role in light-emitting devices and high-frequency applications [2], the technology is also well-developed and some limitations have been already pointed out.

Now that the performance of conventional semiconductor devices is approaching a certain ultimate due to the limitation of the material properties and the processing technology, bringing up a new material may be the most effective way to satisfy the strong and increasing needs for high-power, high-temperature and/or radiation-resistant electronics. Silicon carbide (SiC) with

many outstanding properties, treated in this thesis, is a promising candidate to realize such advanced devices and extend the frontiers of electronics.

On the other hand, crystal growth mechanism has attracted a number of theoretical and experimental scientists. For example, the surface diffusion length of adsorbed species, nucleation, and step growth have been of great interest in material and surface science. Recent progress in crystal growth and *in-situ* observation techniques has made these surface kinetics renewed and exciting subjects for research. However, in spite of the publication of excellent books on crystal growth theory [3], it is difficult to apply the theory to a real growth system, because of too many physical parameters which cannot be easily estimated in real crystals. This is the main reason why there still exists a large gap between theoretical and experimental works in this field. Comprehensive studies should be done to combine the theory and experiments, hopefully yielding a complete understanding.

1.2 Silicon Carbide

1.2.1 Properties of silicon carbide

SiC is a IV-IV compound semiconductor material with a wide bandgap. SiC does not melt and sublimates at high temperatures of 2200°C under atmospheric pressure. From a crystallographic point of view, SiC is the most famous material for showing polytypism [4]. Polytypism is the phenomenon of taking different crystal structures in one-dimensional variation with the same chemical composition. Consider the occupation sites of Si-C pairs in a close-packing system shown in Fig.1.1. Si-C pairs in each plane can occupy one of three sites, denoted by A, B, and C. The variation of occupation sites along one axis brings about different crystal structures named polytypes. The two simplest stacking sequences are ABAB... and ABCABC..., which provide so-called “wurtzite” and “zincblende” structures, respectively. Several materials such as ZnS and GaN can appear in both wurtzite and zincblende structures. SiC, however, crystallizes in surprisingly many (more than 200) polytypes.

Table 1.1 shows the stacking sequences in the c-axis ($\langle 0001 \rangle$ direction)

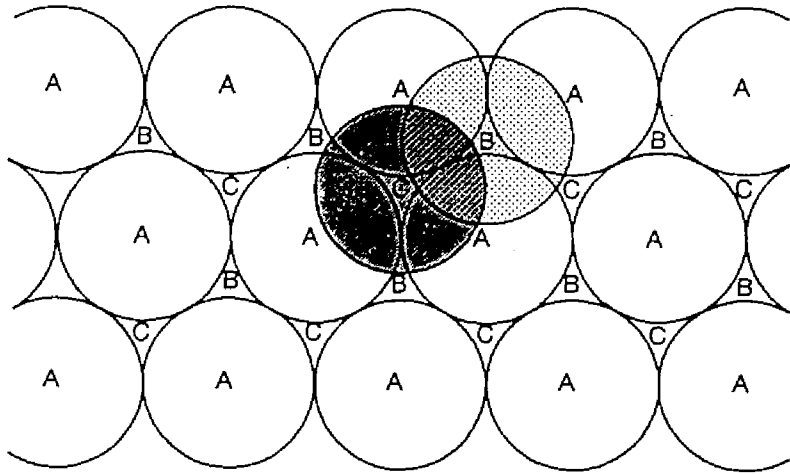


Fig.1.1 Close packing system of spheres.

Table 1.1 Stacking sequence and exciton bandgap at 4.2K of several SiC polytypes [5].

polytype	stacking sequence	E_{gx} at 4.2K (eV)
2H	AB	3.330
3C	ABC	2.390
4H	ABCB	3.265
6H	ABCACB	3.023
15R	ABCACBCABACBCB	2.986

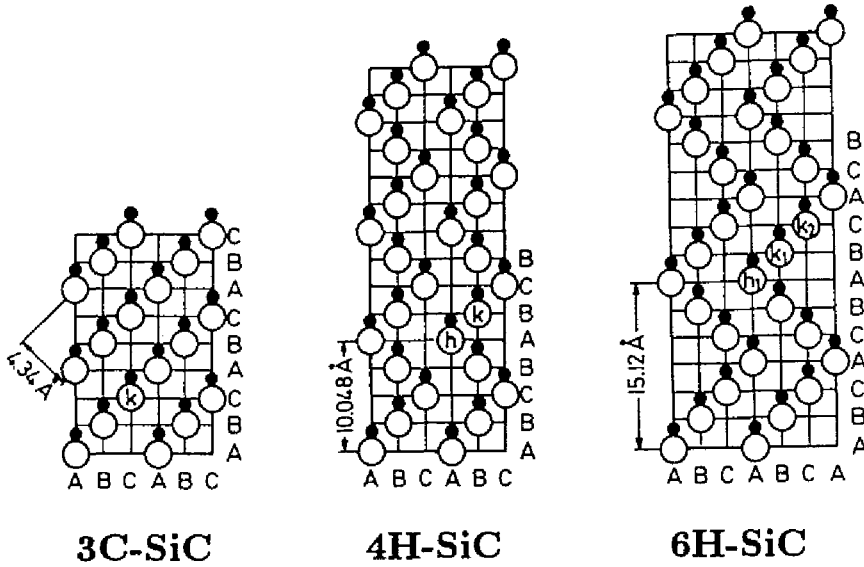


Fig.1.2 Arrangements of Si and C atoms in the SiC(11 $\bar{2}$ 0) plane for 3C-SiC, 4H-SiC, and 6H-SiC polytypes. The marks h and k denote hexagonal and cubic sites, respectively.

Table 1.2 Physical properties of popular SiC polytypes, Si, and GaAs.

	lattice constant(Å)	E_g (eV)	μ (cm^2/Vs)	E_B (V/cm)	v_{sat} (cm/s)
3C-SiC	4.36	2.23	1000	-	2.7×10^7 *
4H-SiC	a=3.09 c=10.08	3.26	900	3×10^6	-
6H-SiC	a=3.09 c=15.12	3.02	450	3×10^6	2×10^7
Si	5.43	1.11	1350	2×10^5	1×10^7
GaAs	5.65	1.43	8000	3×10^5	2×10^7

E_g :bandgap(300K), μ :electron mobility(300K)

E_B :breakdown field, v_{sat} :saturated electron drift velocity

*:theoretical calculation, -:not measured

and the exciton bandgaps at 4.2K of several popular SiC polytypes [5]. In Ramsdell's notation, polytypes are represented by the number of layers in the unit cell and the crystal system (C for cubic, H for hexagonal, and R for rhombohedral). 3C-SiC is often called β -SiC, and others called α -SiC. The structures of 3C-SiC, 4H-SiC, and 6H-SiC are shown in Fig.1.2 where open and closed circles denote Si and C atoms, respectively. The origin of polytype formation has remained an interesting and open question, in spite of the efforts by many investigators [6]. Anyway, it becomes crucial to control polytype during crystal growth of SiC for device applications. In general, 3C-SiC is known as a low-temperature polytype due to its higher probability of appearance at low temperatures ($\sim 1000^\circ\text{C}$). 6H- and 4H-SiC are high-temperature polytypes, which means relatively high temperatures are required to grow these polytypes.

Physical properties of 3C-, 6H-, and 4H-SiC are listed in Table 1.2, together with those of Si and GaAs for comparison. High bonding energy of Si-C atoms (4.53eV) with short bond length (1.89Å) [7] leads to a large energy difference between "bonding" and "anti-bonding" states, resulting in wide bandgaps [8]. For example, bandgaps of 3C- and 6H-SiC at room temperature are 2.23eV and 3.02eV, respectively [9]. These wide bandgaps give SiC very high breakdown field, about ten times higher than that of Si or GaAs [10]. Tight Si-C bonding also yields high-frequency lattice vibration, namely high-energy phonons. The energies of optical phonons in SiC are as high as 100~120meV [11], in contrast to 35~63meV in Si or GaAs [12]. This high phonon energy brings about high saturated electron drift velocity ($2 \times 10^7 \text{cm/s}$ in 6H-SiC) [13] and high thermal conductivity (4.9W/Kcm) [14].

It should be noted that both n- and p-type conductivity can be easily controlled by impurity doping in SiC. This is a rather rare case in wide bandgap materials: ZnS, ZnSe, and GaN have difficulty in p-type doping (though rapid progress has been made), and diamond does in n-type doping.

These outstanding properties with controllable doping make SiC a very attractive semiconductor material. In particular, SiC is a promising candidate for high-power, high-frequency, high-temperature and radiation-resistant devices with excellent performance, which cannot be realized with Si or GaAs based devices.

Table 1.3 Figures of merit for Si, GaAs, and several SiC polytypes.
Each value is normalized by that of Si.

material	JFOM	KFOM	BFOM	BHFFOM
Si	1	1	1	1
GaAs	9	0.41	22	13
3C-SiC	-	5.9	-	-
6H-SiC	900	5.0	920	75
4H-SiC	-	-	1840	150

- :cannot be calculated due to unknown physical properties

As for the limits of device performance, several figures of merit have been proposed. In the early stage, Johnson considered the high-frequency and high-power capability of devices, and proposed Johnson's figure of merit (JFOM) defined by the following equation [15].

$$\text{JFOM} = \frac{E_B^2 v_{\text{sat}}^2}{4\pi^2}, \quad (1.1)$$

where E_B and v_{sat} are the breakdown field and the saturated drift velocity. From the thermal limitation due to generated heat in high-speed switching, Keyes's figure of merit (KFOM) was proposed as follows [16]:

$$\text{KFOM} = \kappa \sqrt{\frac{c v_{\text{sat}}}{4\pi \epsilon}}. \quad (1.2)$$

Here κ , ϵ , and c are the thermal conductivity, the permittivity, and the speed of light in vacuum. Recently, Baliga introduced more realistic figures of merit for unipolar power devices in low-frequency (BFOM) and high-frequency applications (BHFFOM), given by [17,18]

$$\text{BFOM} = \epsilon \mu E_B^3, \quad (1.3)$$

$$\text{BHFFOM} = \mu E_B^2, \quad (1.4)$$

where μ is the mobility. Table 1.3 shows these figures of merit for 3C-, 6H-, 4H-SiC, Si, and GaAs. Here each figure of merit is normalized by the value for Si. SiC demonstrates figures of merit higher than Si and GaAs by orders of magnitude, indicating the great potential for advanced devices. In particular, theoretical simulation has predicted that SiC power devices can replace the present-day Si power devices on account of much lower power dissipation and the reduced chip sizes [19].

1.2.2 History and the present situation of silicon carbide

In general, SiC has taken a position as a material for grinding abrasive, heater, package, varistor, and so on. However, SiC is one of the oldest semicon-

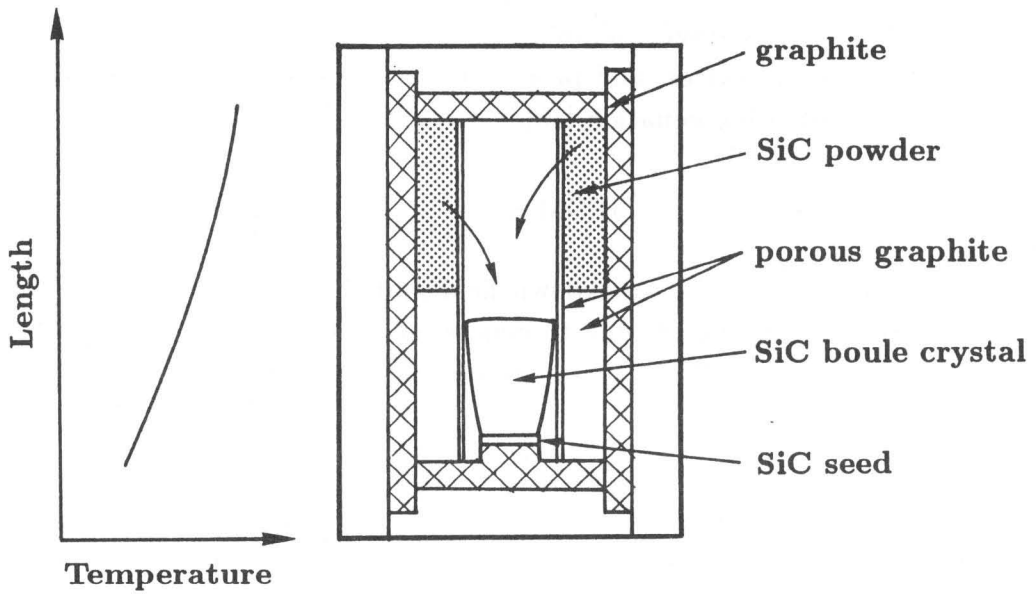


Fig.1.3 Schematic diagram of SiC boule crystal growth system by a modified Lely method [25].

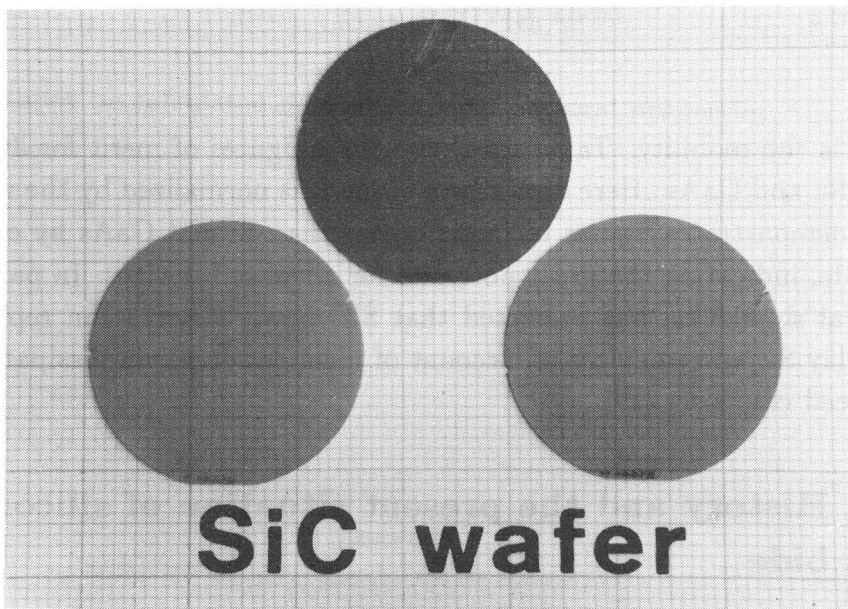


Fig.1.4 Commercial SiC wafers with a 30mm diameter.

ductor materials, as the first electroluminescence has been observed from this material in 1907 [20]. At the initial stage, SiC has been synthesized using silica and coke at very high temperatures of about 2500°C (the Acheson method) [21]. SiC crystals grown by this method cannot be applied for electronic devices due to serious impurity contamination and small sizes with irregular shapes. In 1955, the growth of relatively pure 6H-SiC could be achieved by utilizing a sublimation technique (Lely method) [22]. Based on this development, the concentrated investigation for electronic applications had been performed in 1960s-1970s [23], but this activity fell down due to the difficulty of steady wafer supply and the polytype mixing problem.

One innovation has been achieved in bulk crystal growth utilizing a seeded sublimation method (a modified Lely method) by which large α -SiC boule crystals can be grown with controlling polytypes [24]. A typical growth system is shown in Fig.1.3 [25]. This technique has opened the way for manufacturing α -SiC wafers, and 6H- and 4H-SiC wafers with a 30mm diameter are commercially available today (Fig.1.4) [26]. Since this commercial release of SiC wafers in 1991, the activity of SiC research, especially development of SiC devices, has rapidly grown. Very low-resistivity ($\rho=0.0028 \Omega\text{cm}$) [27] and semi-insulating ($\rho\sim 10^{15} \Omega\text{cm}$) [28] wafers have been also developed, which will lead to the improvement of device performance.

As for epitaxial growth of SiC, there have been two main streams, heteroepitaxial growth of 3C-SiC and homoepitaxial growth of α -SiC. In case of 3C-SiC growth, heteroepitaxy is required, since boule crystals of 3C-SiC, which is a low-temperature polytype, is difficult to grow by a modified Lely method. Through the success in chemical vapor deposition (CVD) of 3C-SiC on Si using a "carbonized buffer layer" technique [29], many investigators have tried the fabrication of SiC devices such as metal-semiconductor field effect transistors (MESFETs) [30,31] and metal-oxide-semiconductor FETs (MOSFETs) [32,33]. However, the quality of 3C-SiC epilayers is poor due to the large mismatch in lattice constants (20%) and thermal expansion coefficients (8%) between 3C-SiC and Si. Now, fundamental research on carbonization of Si [34] and atomic level control in 3C-SiC growth by molecular beam epitaxy (MBE) [35] have been continued to overcome this problem.

Homoepitaxial growth of α -SiC has been performed by liquid phase epi-

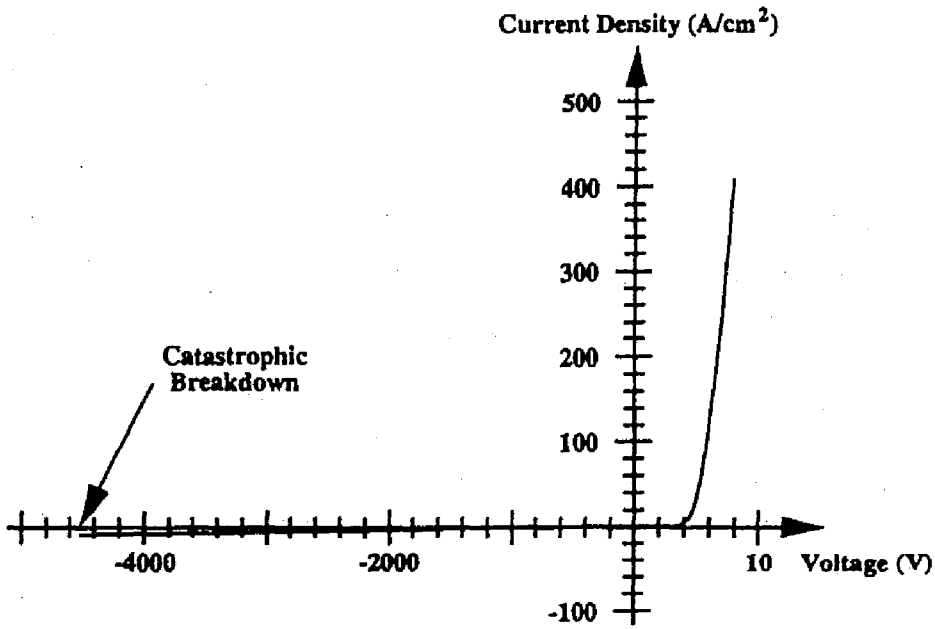


Fig.1.5 Current density - voltage characteristic of a 6H-SiC pn junction diode [46].

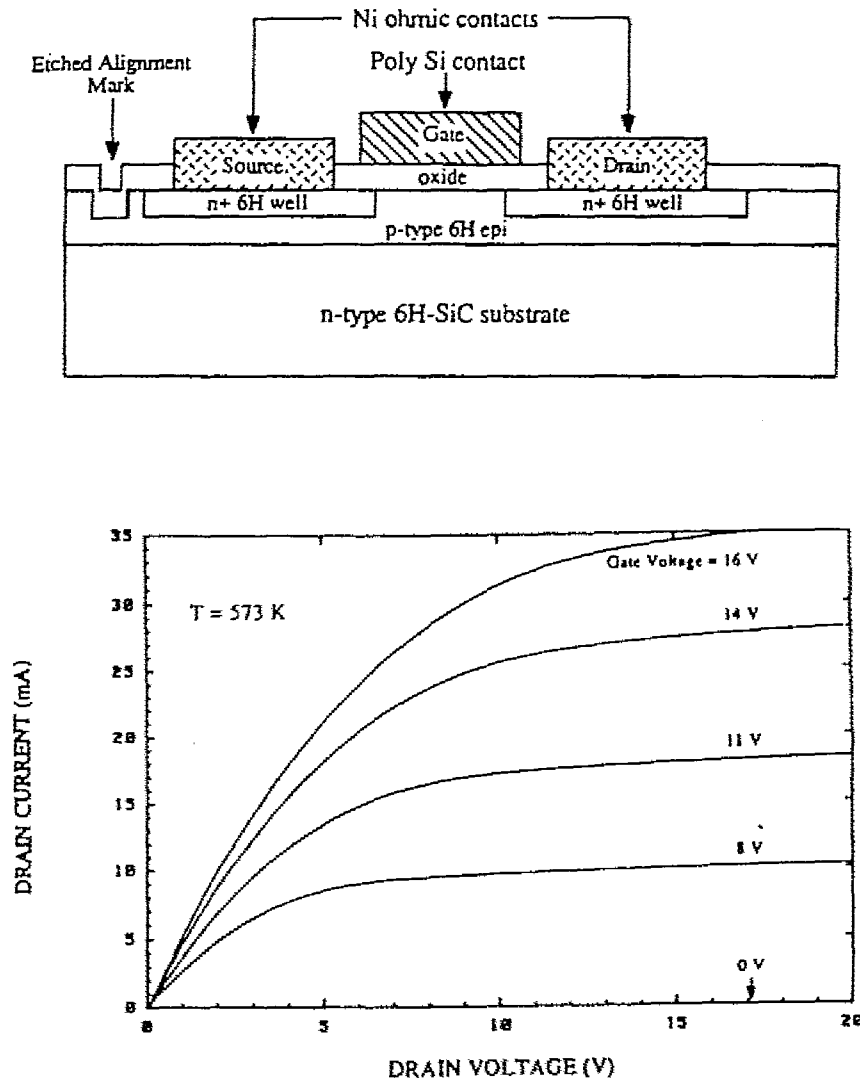


Fig.1.6 Structure and drain current – voltage characteristics of a 6H-SiC enhancement-mode MOSFET at 573K [47].

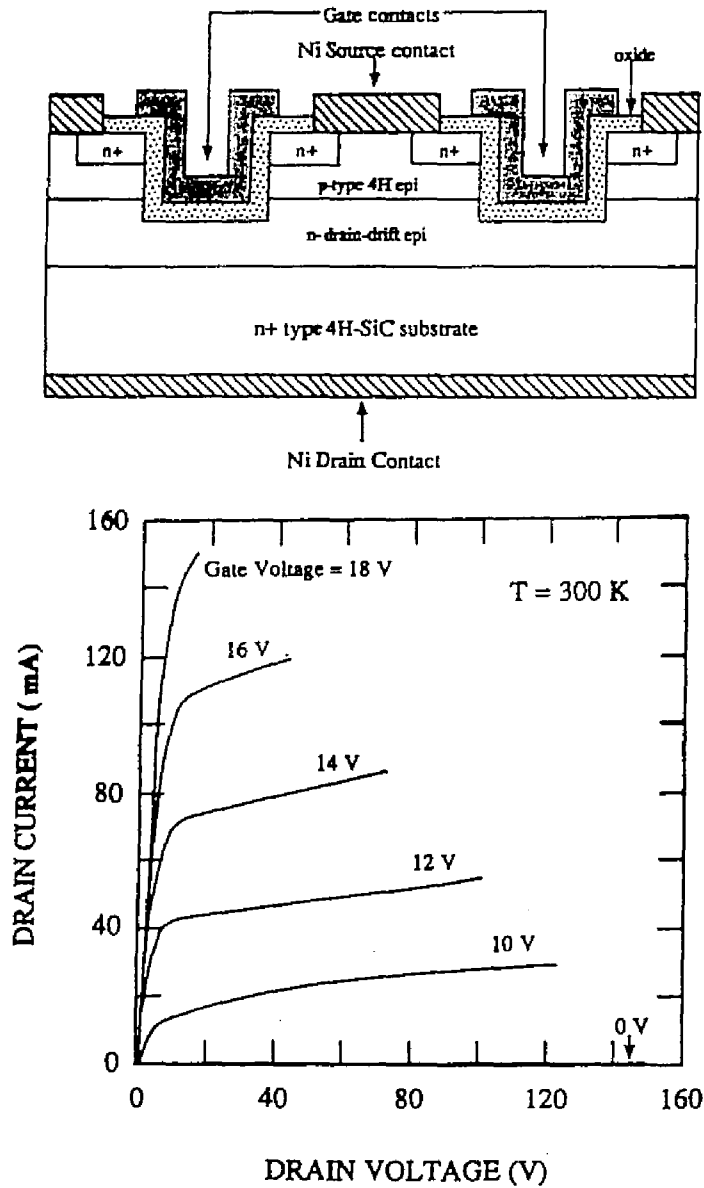


Fig.1.7 Structure and drain current - voltage characteristics of a 4H-SiC vertical power MOSFET at 300K [49].

taxy (LPE) and CVD methods, and blue light-emitting diodes are produced for full-color display devices [36]. Although CVD has advantages in the precise control and uniformity of epilayer thickness and impurity doping, there has been a serious problem of very high growth temperature, which prevented the device fabrication. In case of SiC growth on 6H-SiC{0001} basal planes (conventional condition), growth temperature as high as 1800°C is required for homoepitaxy of 6H-SiC, and twinned crystalline 3C-SiC is grown at lower temperatures [37-40]. In 1986, Kuroda *et al.* found that single crystalline 6H-SiC can be homoepitaxially grown on off-oriented 6H-SiC{0001} at low temperatures of 1400~1500°C [41,42]. This technique was named “*step-controlled epitaxy*”, since *the polytype of epilayers can be controlled by surface steps* existing on the off-oriented substrates. This technique was an epoch-making breakthrough in two senses that (i) *growth temperature can be reduced more than 300°C* and (ii) *epilayers have very high quality enough for device application*.

This innovation motivated the concentrated efforts on development of advanced SiC devices, such as high-voltage diodes [43-46] (for example, see Fig.1.5 [46]), high-temperature FETs operating at 650°C [47] (Fig.1.6), microwave FETs with f_{\max} of 26GHz[48], vertical power devices (Fig.1.7) [49], ultraviolet (UV) detectors [50], and non-volatile memories [51]. Recent progress in device processing technology has made it possible to realize SiC integrated circuits (ICs) operating above 300°C [52,53]. Since high-quality materials have become available, optical and electrical properties such as impurity states [54] and effective masses [55] have become attractive and meaningful subjects for fundamental researchers.

1.3 Outline of Thesis

Owing to recent progress in crystal growth of SiC, the distinctive potential of the material has been demonstrated by real devices. The fabrication of all these devices utilizes “step-controlled epitaxy”, key technology for the development of SiC devices. In spite of the growing activity of SiC, very little is known about growth mechanism of SiC. Although there have been a few reports on mechanism of SiC growth, only qualitative explanation on exper-

imental results has been given [42,56-59]. Quantitative studies and detailed analyses on surface kinetics have never been reported. This may partly result from the device-oriented researches through the world in order to develop advanced SiC devices as soon as possible. It is practically and academically important to know the kinetics of growing surface, and to give the feedback to the growth conditions for further improvement of epilayer quality. Besides, no systematic studies on characterization of SiC epilayers have been reported, while device performance has been strongly emphasized.

The present work has been performed (i) to give an insight into the growth mechanism of SiC and (ii) to characterize the properties of epilayers for device applications. The former study is aimed to provide a guideline in material science, and the latter to exploit novel electronics.

Chapter 2 describes the experimental apparatus, the growth procedures and the introduction of step-controlled epitaxy, where the effects of off-orientation on growth modes are discussed. An attempt for low-temperature growth and basic ideas for polytype control are also described.

Chapter 3 deals with the growth mechanism in step-controlled epitaxy. The effects of growth conditions such as temperature, off-angle, substrate polarity are discussed in detail. The relationship between growth mode and rate-determining step is presented. The step bunching on the growing surface, which verifies step-flow growth, is also described.

Chapter 4 introduces a model for SiC growth on vicinal $\{0001\}$ substrates based on a classical surface diffusion theory. After analyzing nucleation and the surface diffusion of adsorbed species, the critical growth conditions where the growth mode changes from step-flow to two-dimensional nucleation are predicted.

Chapter 5 is assigned for the analysis of surface kinetics. Based on short-time growth experiments, nucleation on terraces and step dynamics are discussed. Polytypes of growth nuclei and lateral motion of steps are described. A diffusion model is proposed to estimate the surface diffusion length of migrating species. The influences of growth conditions on surface kinetics are described in detail.

Chapter 6 first presents the characterization of structure (defects), optical and electrical properties of undoped epilayers, which demonstrates high

purity and high quality of epilayers. Doping of donor (N) and acceptor (B, Al) impurities by *in-situ* process and ion implantation are also investigated.

Chapter 7 is prepared for demonstrating the potential of SiC devices. Theoretical prediction of SiC power device performance is presented. Preliminary experimental results on high-voltage, high-temperature Schottky rectifiers and pn junction diodes are described.

The summary of the present work is given in Chapter 8, including remaining problems and prospects for future studies.

References

- [1] S.M.Sze, *VLSI Technology* (McGraw-Hill International, Tokyo, 1983).
- [2] *Gallium Arsenide and Related Compounds 1993* (Institute of Physics, Bristol, 1994).
- [3] *for example*, B.R.Pamplin, *Crystal Growth* (Pergamon Press, Oxford, 1975); W.A.Tiller, *The Science of Crystallization: Microscopic Interfacial Phenomena* (Cambridge University Press, Cambridge, 1991).
- [4] A.R.Verma and P.Krishna Eds., *Polymorphism and Polytypism in Crystals* (John Wiley & Sons, Inc. New York, 1966).
- [5] W.J.Choyke, *Mat. Res. Bull.*, **4**, S141(1969).
- [6] *for example*, V.Heine, C.Cheng, and R.J.Needs, *J. Am. Ceram. Soc.*, **74**, 2630(1991); W.S.Yoo and H.Matsunami, *Amorphous and Crystalline Silicon Carbide IV*, C.Y.Yang, M.M.Rahman, and G.L.Harris Eds, (Springer-Verlag, Berlin, 1992), p.66.
- [7] *CRC Handbook of Chemistry and Physics*, D.R.Lide Ed.,(CRC Press, Boca Raton, 1993).
- [8] W.A.Harrison, *Electronic Structure and the Properties of Solids - The Physics of the Chemical Bond* (W.H.Freeman and Company, San Francisco, 1980).
- [9] W.J.Choyke and L.Patrick, *Silicon Carbide - A High Temperature Semiconductor* -, J.R.O'Conner and J.Smiltens, Eds., (Pergamon Press, Oxford, 1960), p.306.
- [10] W. von Muench and I.Pfaffeneder, *J. Appl. Phys.*, **48**, 4831(1977).
- [11] D.W.Feldman, J.H.Parker Jr., W.J.Choyke, L.Patrick, *Phys. Rev.*, **173**, 787(1968).
- [12] S.M.Sze, *Physics of Semiconductor Devices* (John Wiley & Sons, New York, 1981).

- [13] W. von Muench and E.Pettenpaul, *J. Appl. Phys.*, **48**, 4823(1977).
- [14] G.A.Slack, *J. Appl. Phys.*, **35**, 3460(1964).
- [15] E.O.Johnson, *RCA Rev.*, **26**, 163(1965).
- [16] R.W.Keyes, *Proc. IEEE*, **60**, 225(1972).
- [17] B.J.Baliga, *J. Appl. Phys.*, **53**, 1759(1982).
- [18] B.J.Baliga, *IEEE Trans. Electron Device Letters*, **10**, 455(1989).
- [19] M.Bhatnagar and B.J.Baliga, *IEEE Trans. Electron Devices*, **ED-40**, 645(1993).
- [20] H.J.Round, *Electric World*, **19**, 309(1907).
- [21] A.G.Acheson, *Eng. Pat. No.17911*(1892).
- [22] J.A.Lely, *Ber. Deut. Keram. Ges.*, **32** 229(1955).
- [23] *for example*, R.B.Campbell and H.C.Chang, *Semiconductors and Semimetals*, R.K.Willardson and A.C.Beer, Eds. **Vol. 7** (Applications and Devices Part B) (Academic Press, New York, 1971), Chapt.7: *Silicon Carbide 1973*, R.C.Marshall, J.W.Faust, Jr., and C.E.Ryan Eds., (Univ. of South Carolina Press, Columbia, 1974).
- [24] Yu.M.Tairov and V.F.Tsvetkov, *J. Crystal Growth*, **52**, 146(1981).
- [25] G.Ziegler, P.Lanig, D.Theis and C.Weyrich, *IEEE Trans. Electron Devices*, **ED-30**, 277(1983).
- [26] Cree Research Inc., NC, USA.
- [27] J.W.Palmour, V.F.Tsvetkov, L.A.Lipkin, and C.H.Carter Jr., *Compound Semiconductors 1994*, H.Goronkin and U.Mishra, Eds. (Institute of Physics, Bristol, 1995), p.377.
- [28] H.M.Hobgood, R.C.Glass, G.Augustine, R.H.Hopkins, J.Jenny, M.Skowronski, W.C.Mitchel, and M.Roth, *Appl. Phys. Lett.*, **66**, 1364(1995).
- [29] S.Nishino, H.Suhara and H.Matsunami, *Ext. Abstr. 15th Conf. on Solid State Devices and Materials* (Tokyo, 1983), p.317.
- [30] S.Yoshida, H.Daimon, M.Yamanaka, E.Sakuma, S.Misawa and K.Endo, *J. Appl. Phys.*, **60**, 2989(1986).
- [31] G.Kelner, S.Binari, K.Sleger and H.Kong, *IEEE Trans. Electron Device Lett.*, **8**, 428(1987).
- [32] K.Shibahara, T.Saito, S.Nishino and H.Matsunami, *IEEE Trans. Electron Device Lett.*, **7**, 692(1986).
- [33] J.W.Palmour, H.S.Kong and R.F.Davis, *J. Appl. Phys.*, **64**, 2168(1988).
- [34] T.Hatayama, Y.Tarui, T.Yoshinobu, T.Fuyuki, and H.Matsunami, *J. Crystal Growth*, **136**, 333(1994).
- [35] T.Yoshinobu, M.Nakayama, H.Shioimi, T.Fuyuki, and H.Matsunami, *J. Crystal Growth*, **99**, 520(1990).
- [36] K.Koga and T.Yamaguchi, *Prog. Crystal Growth and Charact.*, **23**, 127(1991).
- [37] V.J.Jennings, A.Sommer, and H.Chang, *J. Electrochem. Soc.*, **113**, 728(1966).
- [38] W. von Muench and I. Phaffeneder, *Thin Solid Films*, **31**, 39(1976).

- [39] S.Nishino, H.Matsunami, and T.Tanaka, *J. Crystal Growth*, **45**, 144(1978).
- [40] S.Yoshida, E.Sakuma, H.Okumura, S.Misawa, and K.Endo, *J. Appl. Phys.*, **62**, 303(1987).
- [41] N.Kuroda, K.Shibahara, W.S.Yoo, S.Nishino, H.Matsunami, *Ext. Abstr. the 34th Spring Meeting of the Japan Society of Applied Physics and Related Societies* (Tokyo, 1987), p.135 (in Japanese).
- [42] N.Kuroda, K.Shibahara, W.S.Yoo, S.Nishino, and H.Matsunami, *Ext. Abstr. the 19th Conf. on Solid State Devices and Materials* (Tokyo, 1987), p.227.
- [43] P.G.Neudeck, D.J.Larkin, J.A.Powell, L.G.Matus, and C.S.Salupo, *Appl. Phys. Lett.*, **64**, 1386(1994).
- [44] M.Bhatnagar, P.K.McLarty, and B.J.Baliga, *IEEE Electron Device Lett.*, **13**, 501(1992).
- [45] T.Kimoto, T.Urushidani, S.Kobayashi, and H.Matsunami, 1993, *IEEE Electron Device Lett.*, **14**, 548(1993).
- [46] O.Kordina, J.P.Bergman, A.Henry, E.Janzén, S.Savage, J.André, L.P.Ramberg, U.Lindefelt, W.Hermansson, and K.Bergman, *Appl. Phys. Lett.*, **67**, 1561(1995)
- [47] J.W.Palmour, J.A.Edmond, H.S.Kong, and C.H.Carter Jr., *Physica B*, **185**; 461(1993).
- [48] S.Sriram, R.C.Clarke, A.A.Burk Jr., H.M.Hobgood, P.G.McMullin, P.A.Orphanos, R.R.Siergiej, T.J.Smith, C.D.Brandt, M.C.Driver, and R.H.Hopkins, *IEEE Electron Device Lett.*, **15**, 458(1994).
- [49] J.W.Palmour, J.A.Edmond, H.S.Kong, and C.H.Carter, Jr., *Silicon Carbide and Related Materials*, M.G.Spencer, R.P.Devaty, J.A.Edmond, M.A.Khan, R.Kaplan, M.M.Rahman, Eds., (Inst. of Physics, London, 1994), p.499.
- [50] D.M.Brown, E.T.Downey, M.Ghezzi, J.W.Kretchmer, R.J.Šaia, Y.S.Liu, J.A.Edmond, G.Gati, J.M.Pimbley, and W.E.Schneider, *IEEE Trans. Electron Devices*, **ED-40**, 325(1993).
- [51] W.Xie, J.A.Cooper, Jr., M.R.Melloch, J.W.Palmour, and C.H.Carter, Jr., *IEEE Electron Device Lett.*, **15**, 212(1994).
- [52] D.M.Brown, M.Ghezzi, J.W.Kretchmer, V.Krishnamarthy, G.Michon, and G.Gati, *Trans. 2nd High Temperature Electronics Conf.* (Charlotte, 1994), XI-17.
- [53] W.Xie, J.A.Cooper, Jr., and M.R.Melloch, *IEEE Electron Device Lett.*, **15**, 455(1994).
- [54] G.Pensl and W.J.Choyke, *Physica B*, **185**, 264(1993).
- [55] N.T.Son, O.Kordina, A.O.Konstantinov, W.M.Chen, E.Sörman, B.Monemar, and E.Janzén, *Appl. Phys. Lett.*, **65**, 3209(1994).
- [56] H.S.Kong, J.T.Glass, and R.F.Davis, *J. Appl. Phys.*, **64**, 2672(1988).
- [57] T.Ueda, H.Nishino, H.Matsunami, *J. Crystal Growth*, **104**, 695(1990).
- [58] H.Matsunami, T.Ueda, and H.Nishino, *Mat. Res. Soc. Sympo. Proc.*, **162**,

397(1990).

- [59] J.A.Powell, D.J.Larkin, L.G.Matus, W.J.Choyke, J.L.Bradshaw, L.Henderson, M.Yoganathan, J.Yang, and P.Pirouz, *Appl. Phys. Lett.*, **56**, 1442(1990).

Chapter 2

Step-Controlled Epitaxy of α -SiC

2.1 Introduction

The best way to obtain high-quality epilayers is “homoepitaxy”, which is free from lattice-mismatch between epilayers and substrates. In the epitaxial growth of α -SiC (mainly 6H-SiC), homoepitaxy has been investigated by sublimation, LPE, and CVD for a long time [1-6]. Although rather high-quality 6H-SiC layers can be grown and have been applied to several devices, there has been a serious problem of its high growth temperature. For the reproducible homoepitaxial growth of 6H-SiC by these methods on well-oriented {0001} faces, which was a usual case, high temperatures over 1700~1800°C were required [6-8].

Recently Kuroda et al. have developed “step-controlled epitaxy”, by which single crystalline 6H-SiC with very smooth surfaces can be grown on off-oriented 6H-SiC{0001} substrates at 1500°C by CVD [9]. Epitaxial growth at such a low temperature can be attributed to lateral growth from atomic steps, which forces grown layers to inherit the stacking order of substrates.

Although the growth temperature for homoepitaxy of 6H-SiC has been drastically reduced by step-controlled epitaxy, it is still high compared with the growth of Si or other semiconductor materials. For device fabrication, in

particular, a low-temperature process is preferred to suppress impurity contamination from a growth system, impurity redistribution, and thermally induced damage.

In this chapter, the concept and experimental results of step-controlled epitaxy are explained after describing the growth system and procedures. An attempt for low-temperature growth of 6H-SiC by step-controlled epitaxy is also presented together with discussion on growth mode.

2.2 Chemical Vapor Deposition System

2.2.1 Wafer preparation

Two kinds of α -SiC crystals were used as substrates, crystals grown by the Acheson method or a modified Lely (sublimation) method. Since the basal plane of the Acheson crystals is $\{0001\}$ face, the off-oriented substrates were prepared by angle-lapping of the basal plane. As for crystals grown by a modified Lely method, both commercially available and home-made wafers were used. In the growth of 6H-SiC boule crystals in our sublimation system, typical source temperature, seed temperature, and pressure were 2200°C, 2100°C, and 80Torr, respectively. Under this condition, a growth rate of about 0.5mm/h is obtained. After the crystal orientation of grown boules was determined using the back-reflection Laue method, the crystals were sliced into wafers by a diamond cutter. Off-orientation was 0~10° (typically 5~6°) toward $\langle 11\bar{2}0 \rangle$, if not specified. Most wafers were N-doped n-type with a resistivity of 0.1~1 Ω cm.

All the wafers, except for ones used as well-oriented $\{0001\}$ substrates, were carefully polished, and reactive ion etching (RIE) and thermal oxidation were performed to remove the surface damage introduced through the polishing process. The wafers prepared by this process showed an almost ideal χ_{\min} as low as 2.0% in the channeling measurement of Rutherford backscattering using a 2.0MeV He²⁺ beam [10].

SiC $\{0001\}$ is a polar face, and is either (0001)Si or (000 $\bar{1}$)C. Both Si and C faces were used to investigate the substrate polarity effect. The polarity was identified by oxidation (dry O₂ at 1000°C for 5h) utilizing the difference in

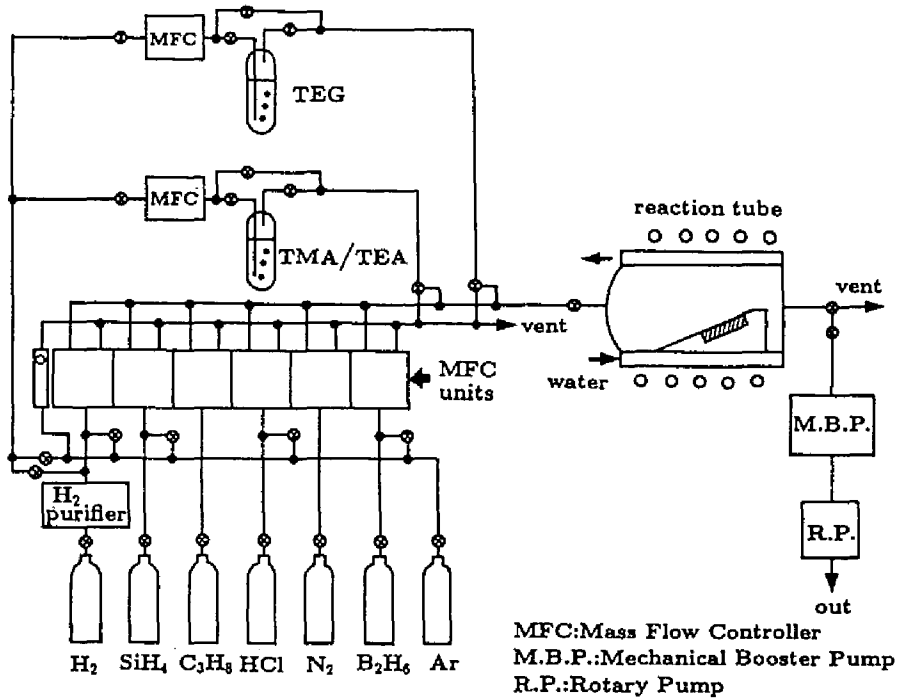


Fig.2.1 Schematic diagram of the CVD system.

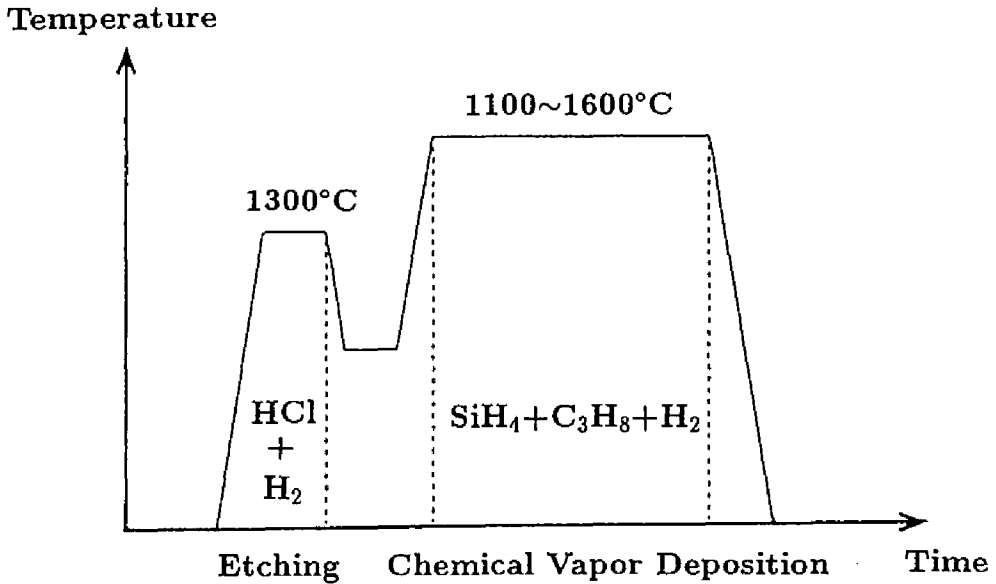


Fig.2.2 Temperature and gas flow program for CVD growth.

oxidation rates between both faces (the oxidation is faster on (000 $\bar{1}$)C faces) [11,12].

The polytypes of substrates were identified with the absorption edges in ultraviolet~visible-light transmission spectra and fluoroluminescence excited by a high-pressure mercury lamp, and confirmed by X-ray diffraction and photoluminescence.

2.2.2 CVD apparatus and growth procedures

Figure 2.1 shows a schematic diagram of the CVD growth system used in this work. Crystal growth was carried out by atmospheric-pressure CVD in a horizontal reaction tube made of fused quartz. SiH_4 (1% in H_2) and C_3H_8 (1% in H_2) were used as source gases. Carrier gas was H_2 purified with a Ag-Pd purifier. The flow rates of SiH_4 and C_3H_8 were 0.05~0.60sccm (typically 0.30sccm) and 0.03~0.50sccm (typically 0.20sccm), respectively. The H_2 flow rate was fixed at 3.0slm, which provides a linear gas velocity of 6~10cm/s above the substrates. N_2 was used for n-type doping, and trimethyl-aluminum(TMA)/triethyl-aluminum(TEA) and B_2H_6 for p-type doping. Since TMA and TEA are liquid at room temperature, they were introduced by bubbling with hydrogen. Hydrogen chloride (HCl) gas was used for etching of a substrate surface before CVD growth.

Substrates were set on a SiC-coated graphite susceptor, and heated by radio frequency (RF) induction using a 400kHz, 15kW RF generator. The substrate temperature was monitored by a pyrometer. Since the susceptor temperature was measured in this study, the real substrate temperature may be slightly lower than the monitored value. The susceptor was inclined at an angle of 10° toward the upper stream of gas flow to improve the uniformity in epilayer thickness [13].

Figure 2.2 shows the temperature and gas flow program of the CVD growth. The growth procedure consists of two steps. The first step is the etching of substrates with HCl gas (typical condition: 1300°C, 10min). The second step is epitaxial growth. The growth temperature was varied in the range of 1100~1600°C.

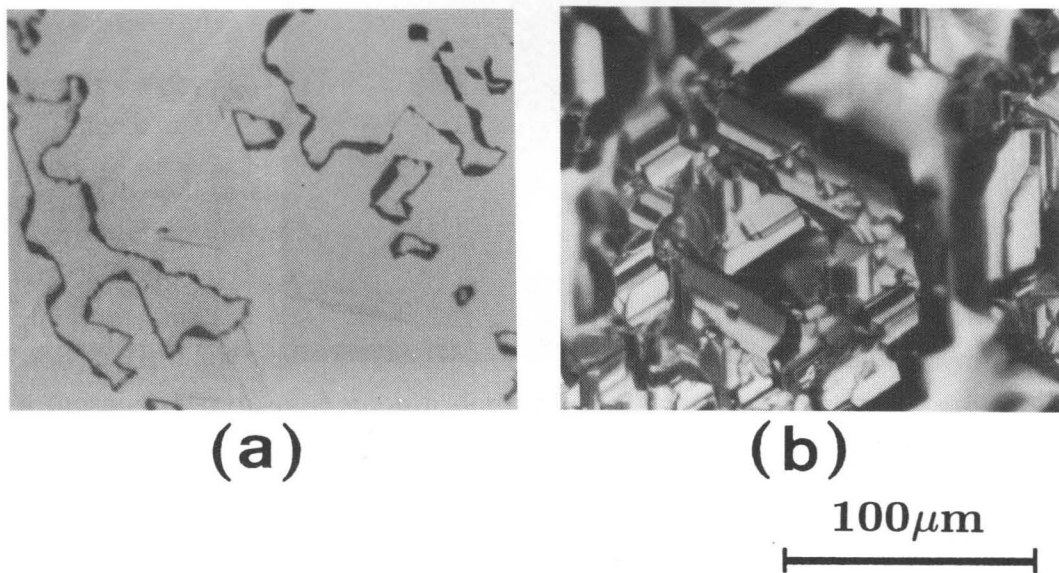


Fig.2.3 Surface morphology of layers grown on well-oriented (a) 6H-SiC(0001)Si face and (b) (0001)C face. Growth temperature and growth rate are 1500°C and 2 μm/h.

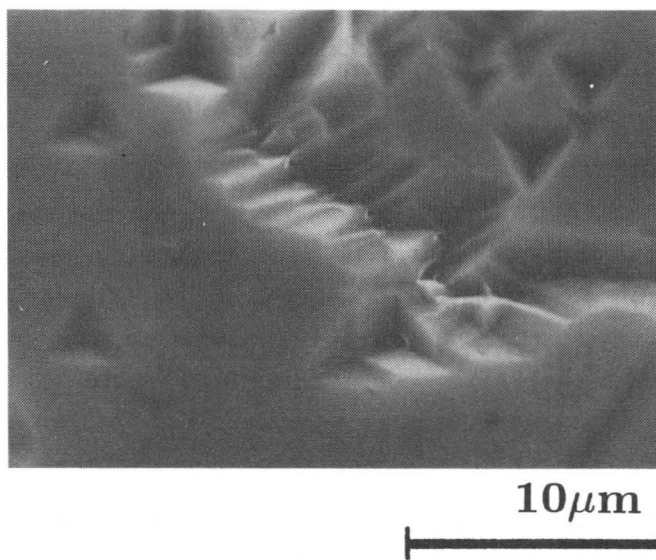
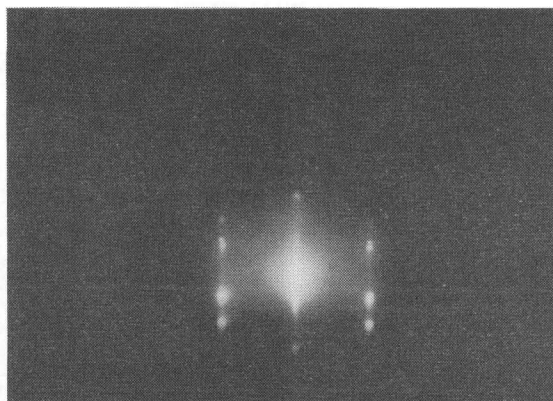
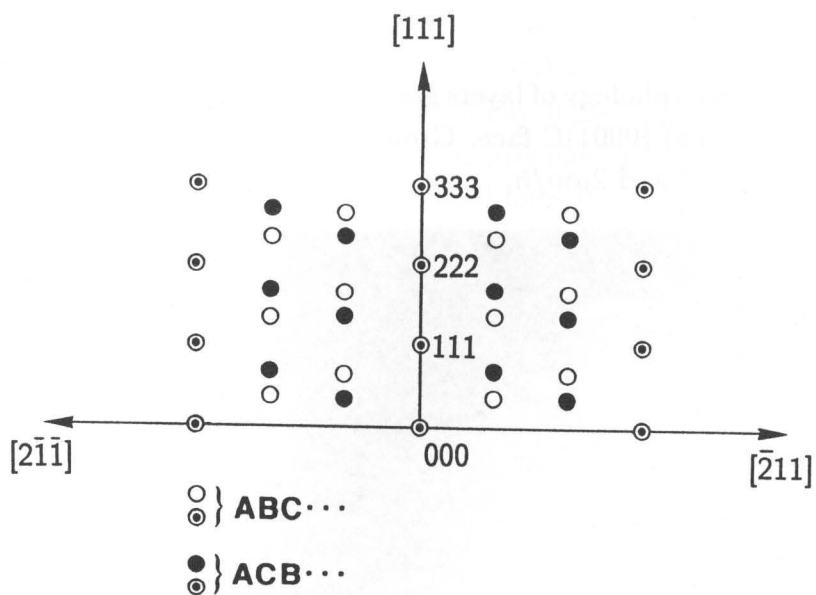


Fig.2.4 Etched surface of a layer grown on well-oriented 6H-SiC(0001)Si face.



(a)



(b)

Fig.2.5 (a) $\langle 1\bar{1}0 \rangle$ -azimuth RHEED pattern obtained for an epilayer on well-oriented 6H-SiC(0001)Si face.
 (b) theoretical RHEED pattern of 3C-SiC(111) with double positioning twin.

2.3 Step-Controlled Epitaxy

2.3.1 Growth on well-oriented 6H-SiC{0001} faces

On well-oriented 6H-SiC{0001} faces, 6H-SiC epilayers cannot be grown reproducibly unless the growth temperature is raised up to 1800°C [6-8]. Figure 2.3 shows the surface morphology of layers grown on well-oriented (a) (0001)Si and (b) (000 $\bar{1}$)C faces at 1500°C under the typical gas flow condition (SiH₄:0.30sccm, C₃H₈:0.20sccm). On a (0001)Si face, the epilayer shows a mosaic pattern, and smooth domains are separated by step- or groove-like boundaries. On a (000 $\bar{1}$)C face, the grown surface is rough, and island-like growth is observed.

Figure 2.4 shows a scanning electron microscope (SEM) photograph for an etched surface of a layer grown on a well-oriented (0001)Si face. The etching was performed by molten KOH at 450°C for 1min. Triangular etch pits indicating 3-fold symmetry are observed, which suggests the growth of cubic phase. Note that the etch pits are 180°-rotated relative to each other across the groove boundaries. This result means the neighboring domains separated by the boundaries have twin relationship so called "double positioning twin" [14].

Polytypes of grown layers were identified by a reflection high-energy electron diffraction (RHEED) analysis. Prior to the RHEED analysis, the samples were etched by molten KOH at 600°C for 30sec to get spot patterns. Figure 2.5(a) shows a $\langle 1\bar{1}0 \rangle$ -azimuth RHEED pattern from an epilayer on a (0001)Si face. The theoretical $\langle 1\bar{1}0 \rangle$ -azimuth RHEED pattern calculated for 3C-SiC(111) containing twinning around the (111) direction (double positioning twin) is shown in Fig.2.5(b). In this figure, open and closed circles represent diffraction spots from single crystalline 3C-SiC(111) with ABC... stacking and ACB... stacking domains, respectively. White circles with dots are common diffraction spots for these two domains. Thus, the grown layer can be identified as twinned crystalline 3C-SiC(111) with double positioning domains. The polytype was confirmed by photoluminescence and Raman scattering. Similar results were obtained for layers grown on (000 $\bar{1}$)C faces.

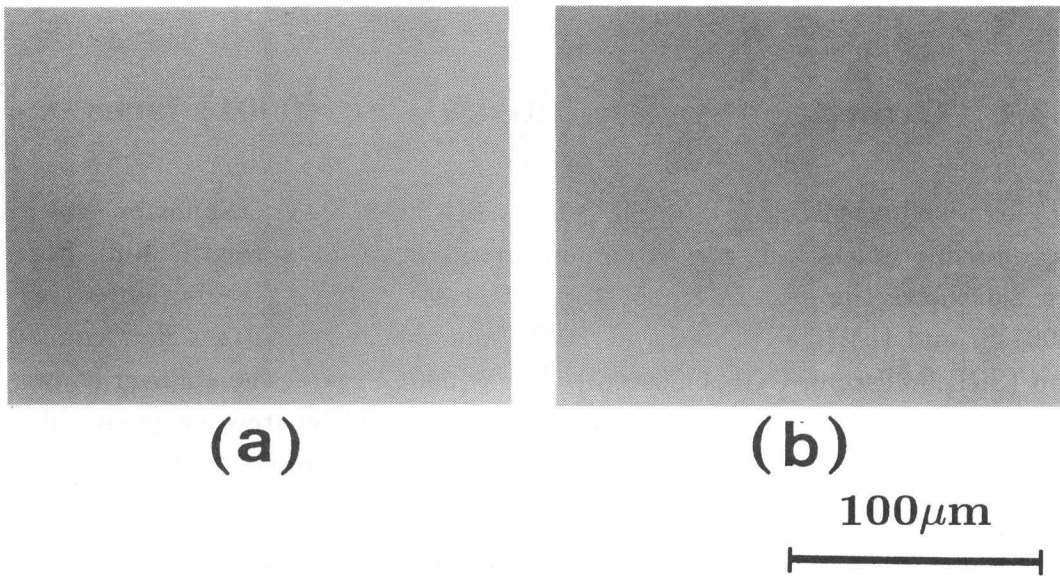


Fig.2.6 Surface morphology of layers grown on off-oriented (a) 6H-SiC(0001)Si face and (b) (000 $\bar{1}$)C face. Growth temperature and growth rate are 1500°C and 2 μm/h. Off-orientation is 6° toward $\langle 11\bar{2}0 \rangle$.

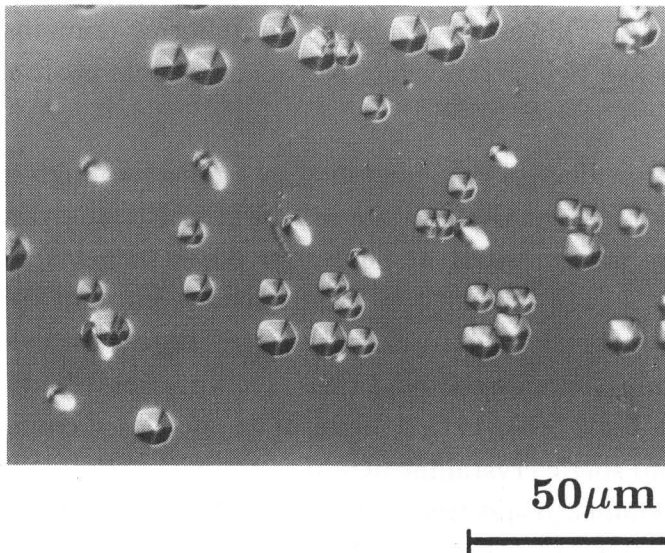
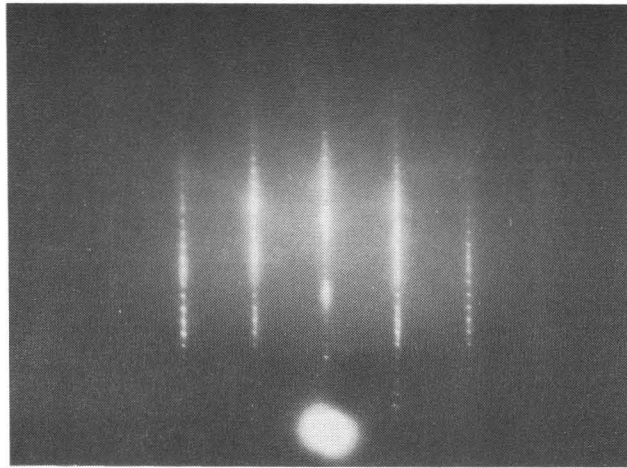
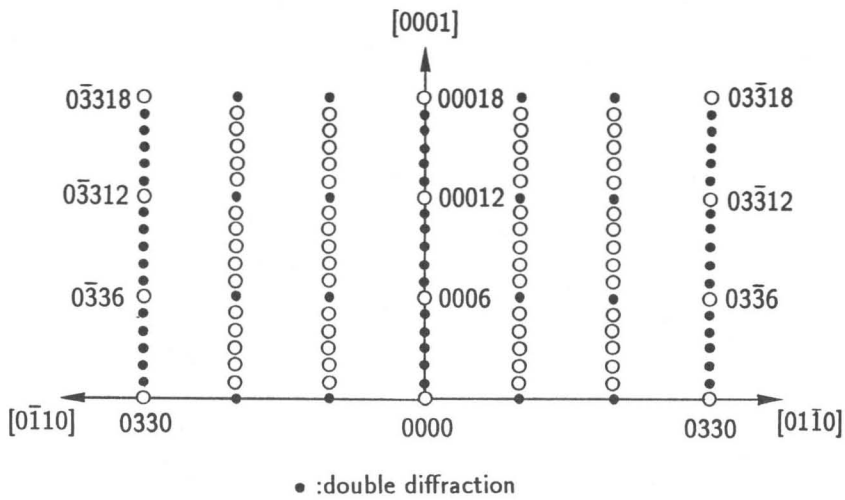


Fig.2.7 Etched surface of a layer grown on 6° off-oriented 6H-SiC(0001)Si face.



(a)



(b)

Fig.2.8 (a) $\langle 11\bar{2}0 \rangle$ -azimuth RHEED pattern obtained for an epilayer on 6° off-oriented 6H-SiC(0001)Si face.
 (b) theoretical RHEED pattern of single crystalline 6H-SiC(0001).

2.3.2 Growth on off-oriented 6H-SiC{0001} faces

Figure 2.6 shows the surface morphology of layers grown on off-oriented (a) (0001)Si and (b) (000 $\bar{1}$)C faces at 1500°C under the same gas flow condition as in Fig.2.3. The off-angle is 6° toward (11 $\bar{2}$ 0). A drastic change in surface morphology is observed by the off-angle introduction: Grown layers show specular smooth surfaces, which is independent of the surface polarity of substrates.

Figure 2.7 shows a SEM photograph for an etched surface of a layer grown on an off-oriented (0001)Si face. Etch pits with rounded hexagonal shape are observed, indicating the growth of hexagonal phase. Figure 2.8 shows (a) observed and (b) theoretical (11 $\bar{2}$ 0)-azimuth RHEED patterns of 6H-SiC(0001). Based on these results, the grown layer is identified as single crystalline 6H-SiC(0001). The polytype of grown layers was verified by transmission electron microscope (TEM) observation. Figure 2.9 shows a high-resolution cross-sectional TEM image of a layer grown on an off-oriented substrate, which demonstrates the stacking sequence of 6H-SiC (ABCACB...). Thus, homoepitaxy of 6H-SiC is successfully achieved by utilizing off-oriented substrates at a low temperature of 1500°C.

This growth technique is applicable to homoepitaxy of any other polytypes such as 4H-SiC, 15R-SiC, and 21R-SiC. Figure 2.10 shows the Raman scattering spectra of TO (transverse optical) mode for layers grown on off-oriented (a) 4H-SiC and (b) 15R-SiC(0001) at 1500°C. The thickness of epilayers is about 10 μ m. Only the peaks characteristic to 4H- or 15R-SiC are observed in each spectrum, and no incorporation of other polytypes (3C-SiC or 6H-SiC) is detected.

The dependence of epilayer polytype on the off-angle and off-direction reported by Kuroda *et al.* is shown in Fig.2.11 [9]. The substrate and growth temperature are 6H-SiC(0001) and 1500°C. Off-angles larger than 1.0° are required for homoepitaxy of 6H-SiC. Kong *et al.* and Ueda *et al.* have investigated the off-direction dependence in detail [15-17]. On off-oriented 6H-SiC(0001) inclined toward (1 $\bar{1}$ 00), stripe-like morphology appears and the incorporation of 3C-SiC occurs by long-time growth [16]. Based on these results,

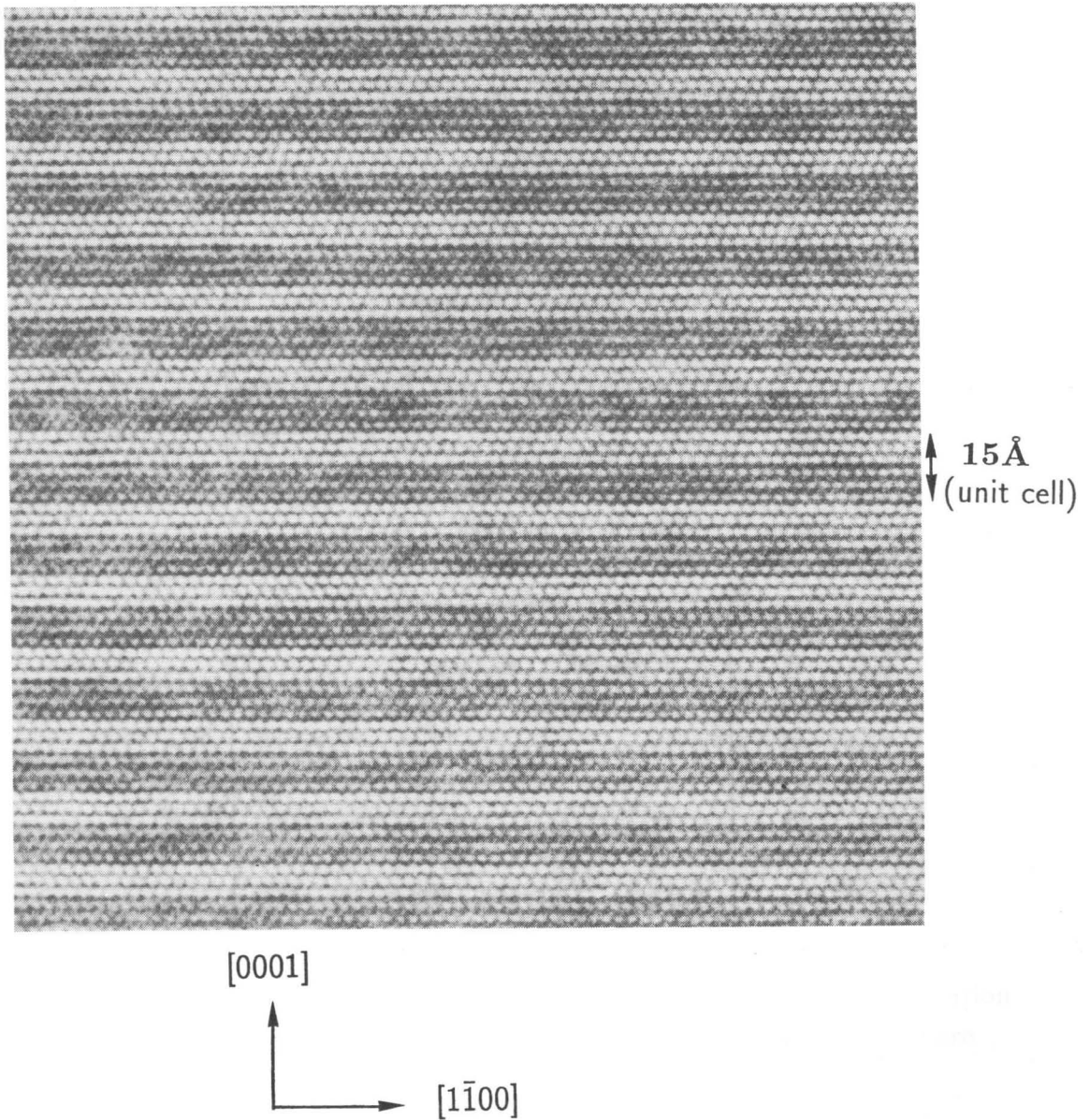


Fig.2.9 High-resolution cross-sectional TEM image of an epilayer on 6° off-oriented 6H-SiC(0001)Si face.

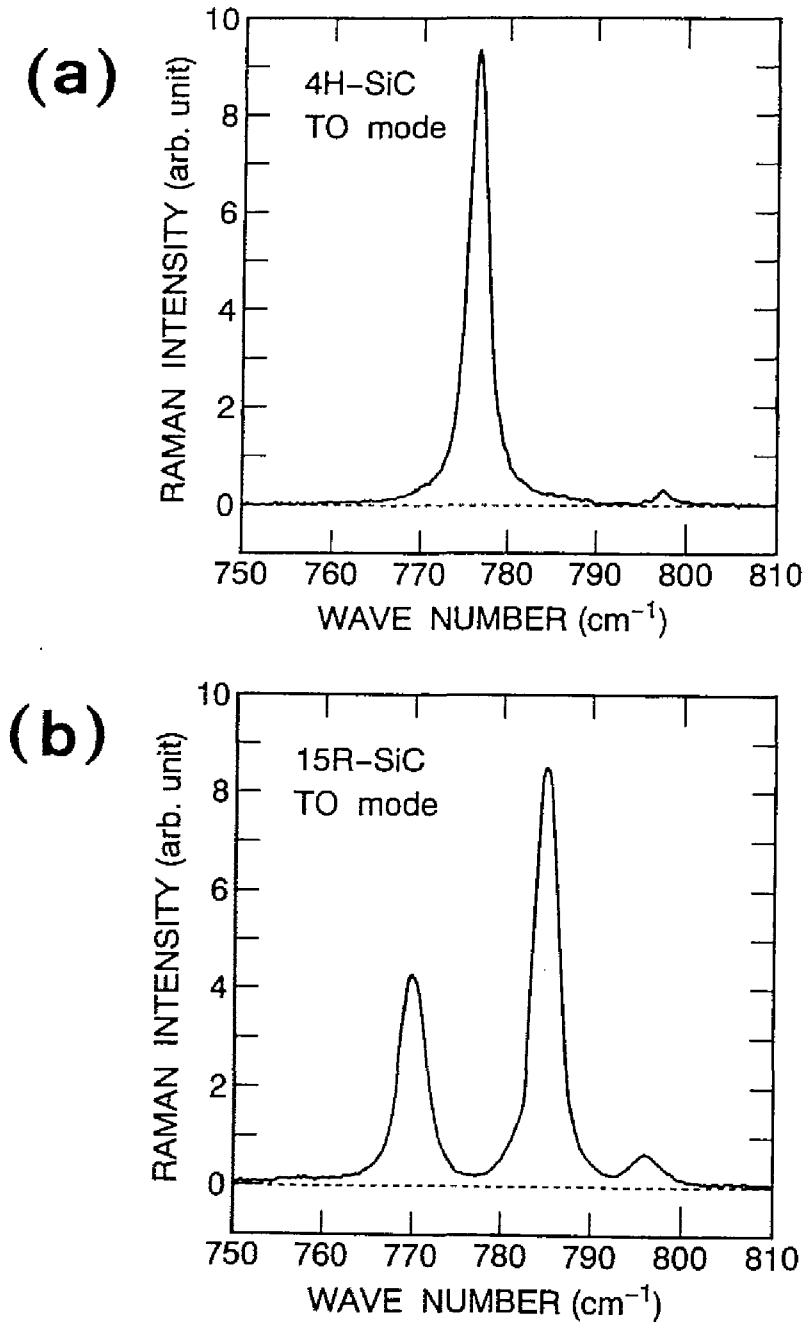


Fig.2.10 TO mode Raman spectra from epilayers grown on off-oriented (a) 4H-SiC and (b) 15R-SiC(0001) substrates.

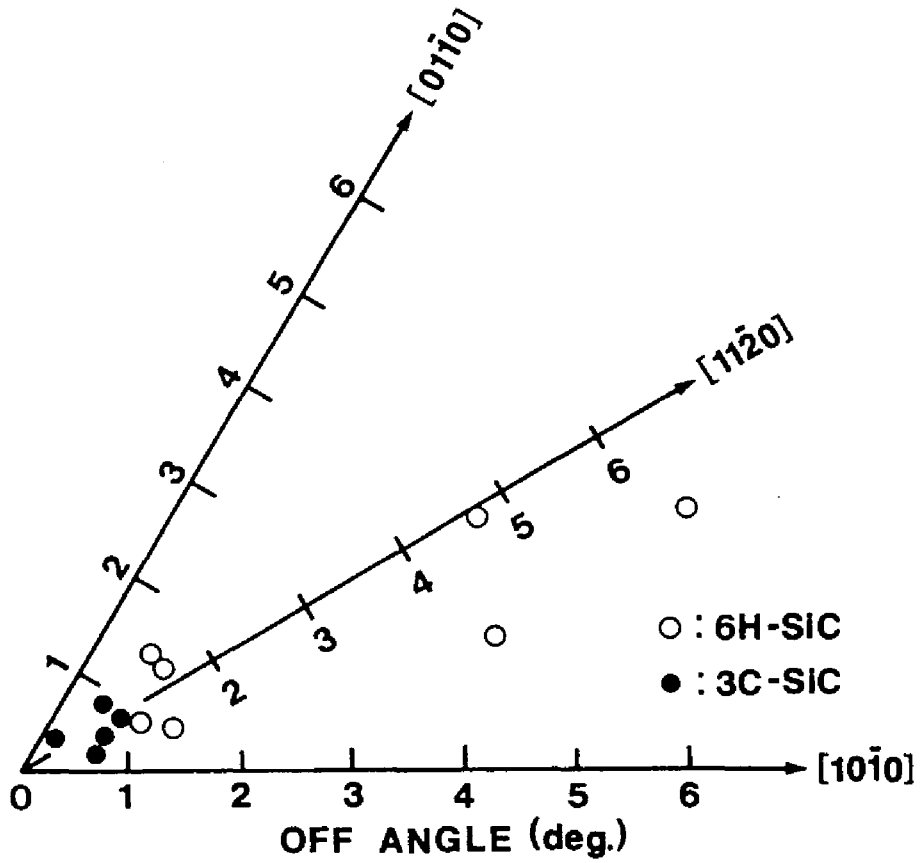


Fig.2.11 Relationship between polytypes of grown layers and off-orientation of 6H-SiC substrates. Growth temperature and growth rate are 1500°C and 2 μ m/h [9].

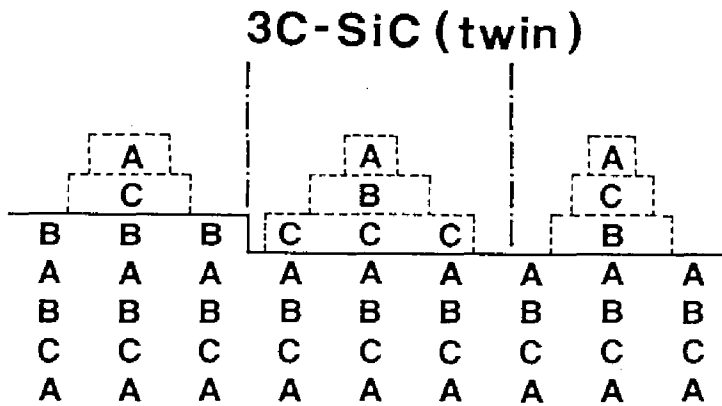
4~6° off-angle toward $\langle 11\bar{2}0 \rangle$ was mainly employed in this study. The effects of off-orientation on growth mechanism will be discussed in great detail in Chapters 3 and 4.

2.3.3 Growth mode

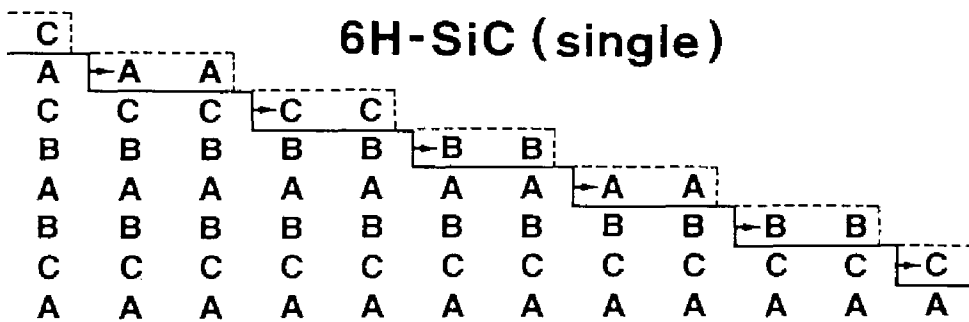
SiC{0001} surfaces consist of {0001} terraces and steps. According to a classical growth theory, adsorbed species migrate on the surface and are incorporated into a crystal at steps and kinks where the potential is low [18]. However, nucleation on terraces takes place when the supersaturation is high enough. The supersaturation is a strong function of growth temperature, surface migration length of adsorbed species, terrace width, and the supply of source gases. Taking account of these factors, the difference of growth mechanism on well- and off-oriented substrates can be qualitatively explained as follows.

On well-oriented {0001} faces, the step density is very low and vast terraces exist. Then, crystal growth may initially occur on terraces through two-dimensional nucleation due to high supersaturation on the surface. The polytype of grown layers is determined by growth conditions, mainly growth temperature. This leads to the growth of 3C-SiC, which is stable at low temperatures. This phenomenon has been predicted by theoretical studies using quantum-mechanical energy calculation [19] and an electrostatic model [20]. As the stacking order of 6H-SiC is ABCACB..., the growing 3C-SiC can take two possible stacking orders of ABCABC... and ACBACB..., as shown in Fig.2.12(a). Thus, two-dimensional nucleation on terraces may result in the growth of twinned crystalline 3C-SiC.

On off-oriented substrates, the step density is high, and the terrace width is narrow enough for adsorbed species to reach steps. At a step, the incorporation site is uniquely determined by bonds from the step, as shown in Fig.2.12(b). Hence, homoepitaxy can be achieved through the lateral growth from steps (step-flow growth), inheriting the stacking order of substrates. A schematic illustration for the incorporation sites on SiC{0001} faces is shown in Fig.2.13, by which the uniqueness of site occupation can be expected at a step.



(a)



(b)

Fig.2.12 Schematic images of the relationship between growth modes and polytypes of grown layers. (a) 3C-SiC is grown through two-dimensional nucleation, and (b) homoepitaxy of 6H-SiC is achieved owing to step-flow growth.

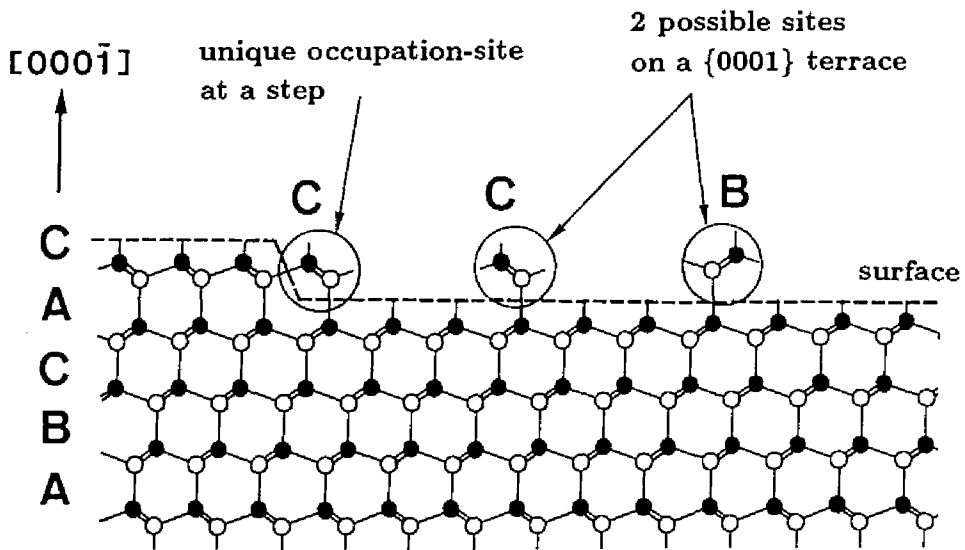


Fig.2.13 Schematic illustration of incorporation sites on 6H-SiC $\{0001\}$ surface. White and black circles denote Si and C atoms, respectively.

In general, epitaxial growth on off-oriented (vicinal) substrates has been extensively studied for many materials [21-24]. Recent investigations on the growth of III-V semiconductors have shown that the quality of epilayers is significantly improved by utilizing off-oriented substrates [25], or suppress the incorporation of ambient oxygen [26]. Although the key method in step-controlled epitaxy of SiC (the use of off-oriented substrates) itself is similar to those studies, this technique possesses a special meaning that the polytypes of SiC epilayers can be controlled by the step density of substrates, i.e. the surface steps serve as a template which forces the replication of the substrate polytype in the epilayer. This is the terminological origin of "step-controlled epitaxy".

From an academic point of view, growth modes are of great interest: step-flow or two-dimensional nucleation. Although the *in-situ* observation of adsorbed species is difficult in CVD, several evidences indicating the growth modes can be obtained by careful observation of grown surfaces.

Figure 2.14(a) shows the surface morphology for a layer grown on a well-oriented 6H-SiC(0001) face at 1500°C. Many trigonal pyramids can be seen on the surface of each 3C-domain. This kind of morphology is enhanced under high supersaturation conditions such as high flow rates of source gases or low growth temperatures, and is never seen in case of 6H-growth on off-oriented substrates. This morphology can be explained by the growth through self-consistent nucleation [27] as shown in Fig.2.14(b). Initially a two-dimensional nucleus is formed on a terrace, and the nucleus grows laterally, capturing the migrating species. With the growth of the nucleus, the supersaturation on the nucleus becomes higher, and the second nucleus is formed on the first nucleus. The repetition of this process leads to the formation of "vicinal hillock" as shown in Fig.2.14(a).

The surface morphologies characteristic to the case of 6H-growth are shown in Figs 2.15(a) "triangle-shaped shadows" and (c) "line-shaped shadows". These surface pits can be observed at some defect sites (pin holes, scratch, *etc.*) especially for low-temperature growth. A supposed mechanism of the pit formation is given in Figs.2.15(b) and (d), where some pinning points impede the step-advance. Note that all the "shadows" are formed toward the off-direction, which means that steps move laterally toward the off-direction,

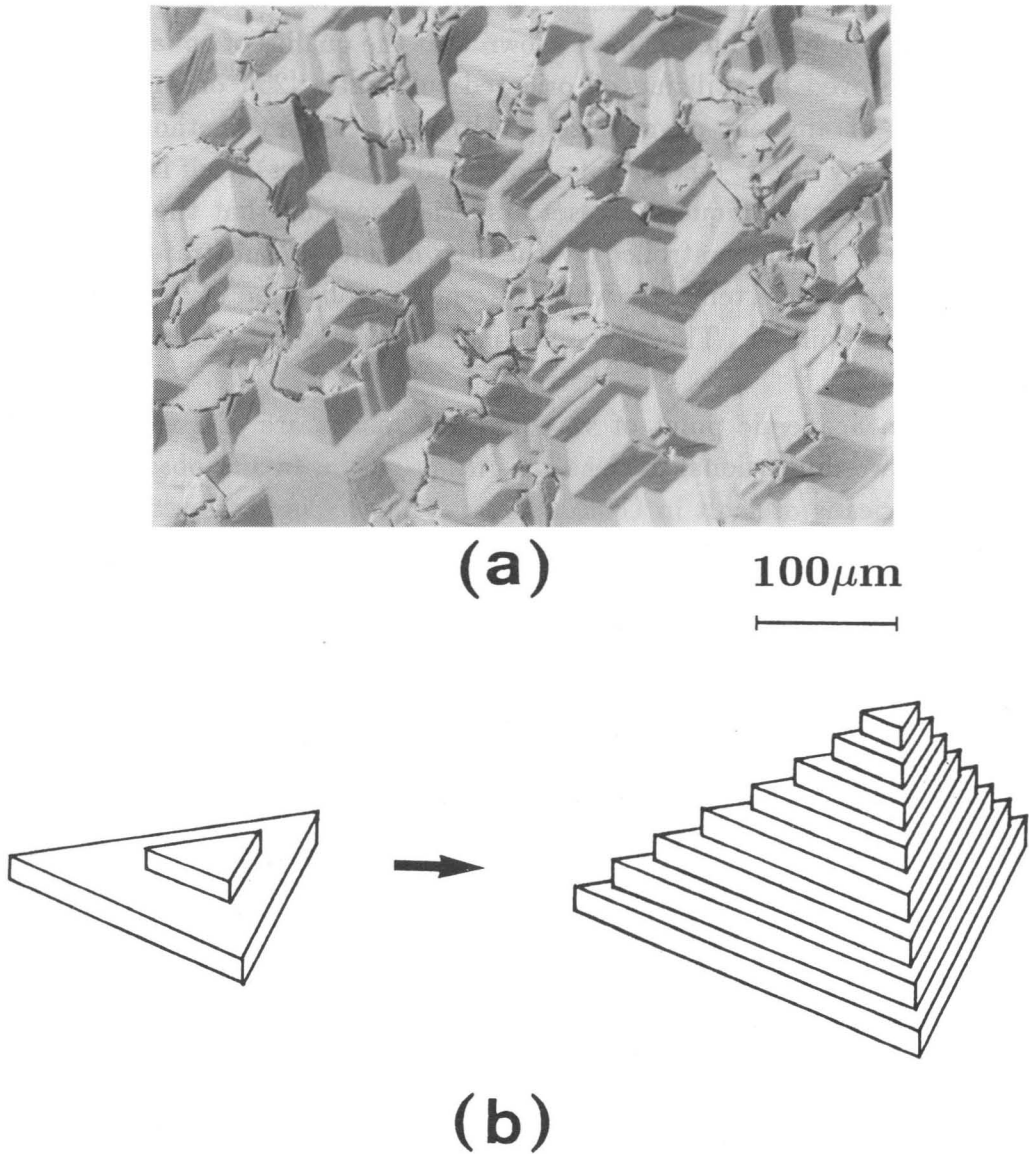


Fig.2.14 (a) Surface morphology of a layer grown on a well-oriented 6H-SiC (0001) substrate. “Vicinal hillocks” formed by self-consistent nucleation can be observed.
(b) Formation mechanism of vicinal hillocks.

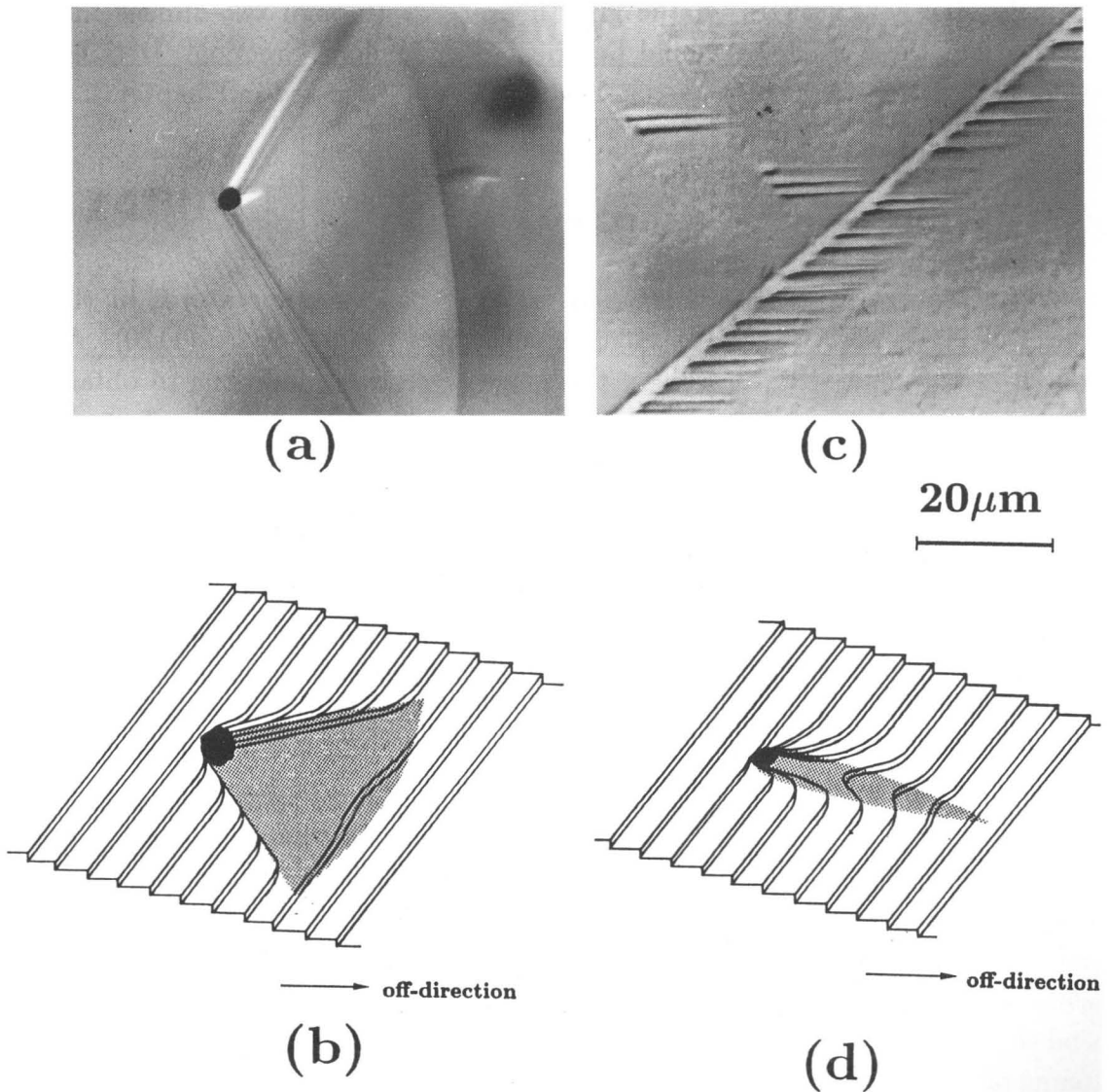


Fig.2.15 Surface pits characteristic to 6H-SiC growth on off-oriented substrates. (a) “triangle-shaped shadow” and (b) its formation mechanism. (c) “line-shaped shadow” and (d) its formation mechanism.

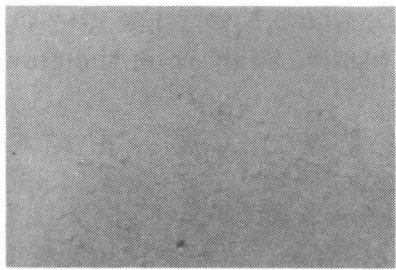
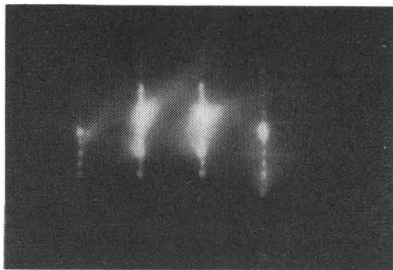
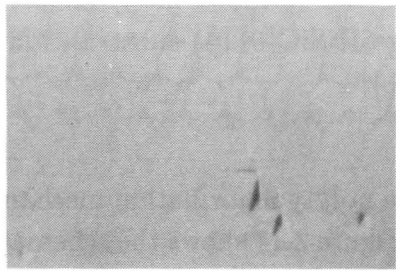
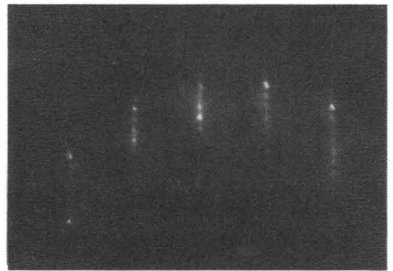
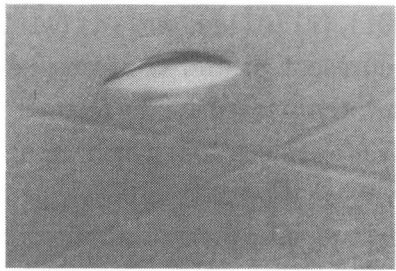

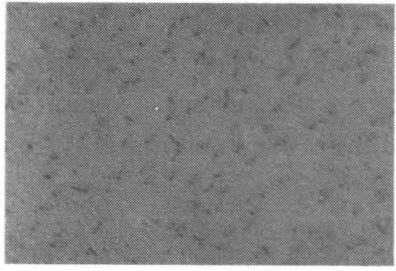
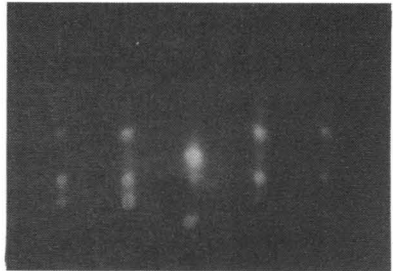
namely step-flow growth. If the growth proceeds through two-dimensional nucleation, these shadows should be oriented in random direction. Detailed surface structures relating the step-flow growth are discussed in Chapter 3.

2.4 Low-Temperature Growth

CVD growth of 6H-SiC was investigated at low temperatures in the range of 1100~1400°C. The off-angle of substrates was 6° toward $\langle 11\bar{2}0 \rangle$. As the growth temperature decreases, the range of growth conditions to obtain a smooth surface becomes narrower. The author investigated the effects of SiH₄ and C₃H₈ flow rates on the crystallinity of grown layers and determined the optimum condition. It was turned out that lower SiH₄ flow rate (corresponds to lower supersaturation) and higher C/Si ratio are preferable for low-temperature epitaxial growth. Here, the former will be effective to suppress two-dimensional nucleation on terraces, and the latter may compensate for lower decomposition ratio of C₃H₈ at lower temperatures.

Figure 2.16 shows the growth temperature dependence of surface morphology and RHEED pattern for the layers grown on off-oriented (000 $\bar{1}$)C faces. The growth time was 60min, by which about 1 μ m epilayers were formed. There was no significant difference between epilayers on Si and C faces. The surface morphology deteriorated by lowering growth temperature; triangle-shaped shadow, pits and hillocks increased for low-temperature growth. However, homoepitaxial growth of 6H-SiC was achieved at a temperature as low as 1200°C. This result indicates that step-flow growth occurs even at 1200°C, and the grown layers inherit the stacking order of substrates. Thus, the growth temperature for 6H-SiC homoepitaxy can be reduced by more than 600°C by using off-oriented substrates.

At 1100°C, however, surface morphology becomes rough and twinned crystalline 3C-SiC was grown. Quite similar results were obtained on (0001)Si faces. This is attributed to the suppressed surface migration of adsorbed species at the low temperature and the occurrence of two-dimensional nucleation on terraces. Since the nucleation rate on terraces can be restrained by lowering supersaturation, further reduction of SiH₄ flow rate might lead

T_{growth}	Surface	RHEED
1400°C		
1300°C		
1200°C		
1100°C		

50 μm 

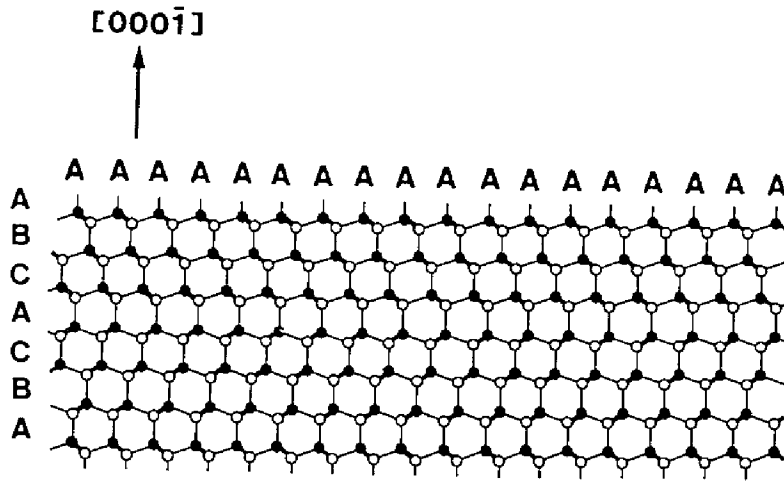
Fig.2.16 Growth temperature dependence of surface morphology and $(11\bar{2}0)$ -azimuth RHEED pattern for the layers grown on 6° off-oriented $6\text{H-SiC}(000\bar{1})\text{C}$ faces.

to 6H-SiC homoepitaxial growth at lower than 1100°C. In fact, Tanaka *et al.* reported homoepitaxial growth of 6H-SiC on off-oriented 6H-SiC(0001) substrates at 1050°C by MBE, where a very low growth rate of 50~100Å/h was employed [28]. The quantitative analysis on the growth mode is given in Chapter 4.

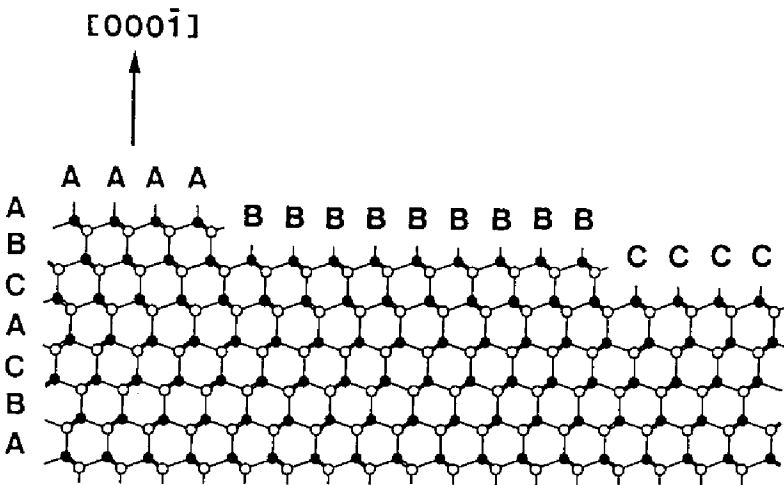
As for low-temperature growth of 6H-SiC by CVD, Powell and Will succeeded homoepitaxial growth of 6H-SiC at 1320~1390°C on “*a* faces (perpendicular to {0001} faces)” [29]. The author’s group succeeded in homoepitaxy of 6H-SiC at 1100°C by using 6H-SiC(0 $\bar{1}$ 1 $\bar{4}$) substrates [30], which has an inclination of 54.74° from {0001}.

These results suggest the polytype formation mechanism in SiC epitaxial growth at low temperatures. Figure 2.17 shows the schematic diagrams of bond configurations for four kinds of 6H-SiC substrates; (a) well-oriented (000 $\bar{1}$), (b) several degree off-oriented (000 $\bar{1}$), (c) (0 $\bar{1}$ 1 $\bar{4}$), and (d) (1 $\bar{1}$ 00) faces. In each figure, white and black circles represent Si and C atoms. As mentioned above, 3C-SiC, which is stable at low temperatures, is formed in low-temperature growth without the substrate’s off-orientation. Even on 6° off-oriented {0001} faces, twinned crystalline 3C-SiC is grown at 1100°C, probably due to nucleation on {0001} terraces where no information about the stacking sequence exists. On (0 $\bar{1}$ 1 $\bar{4}$) and (1 $\bar{1}$ 00) faces, however, there are no more {0001} terraces, and the stacking sequence of 6H-SiC (ABCACB...) appears directly on the surfaces. In this case, the occupation site of adsorbed species is uniquely fixed by the bonds at any site on the surface. Thus, (0 $\bar{1}$ 1 $\bar{4}$) and (1 $\bar{1}$ 00) (or (11 $\bar{2}$ 0)) faces possess much potential for low-temperature growth of 6H-SiC.

Although low-temperature homoepitaxy of 6H-SiC can be achieved, the quality of epilayers becomes poor with lowering temperature. The etch pit density and background doping concentration show serious increase for epilayers grown at lower temperatures [31]. Since these results may be partly attributed to the insufficient decomposition of C₃H₈, a new feed-stock which is active at low temperatures may be effective to improve the quality.



(a)



(b)

Fig.2.17 Schematic diagrams of bond configurations for (a) well-oriented $(000\bar{1})$, (b) several degree off-oriented $(000\bar{1})$. White and black circles denote Si and C atoms, respectively. (continued)

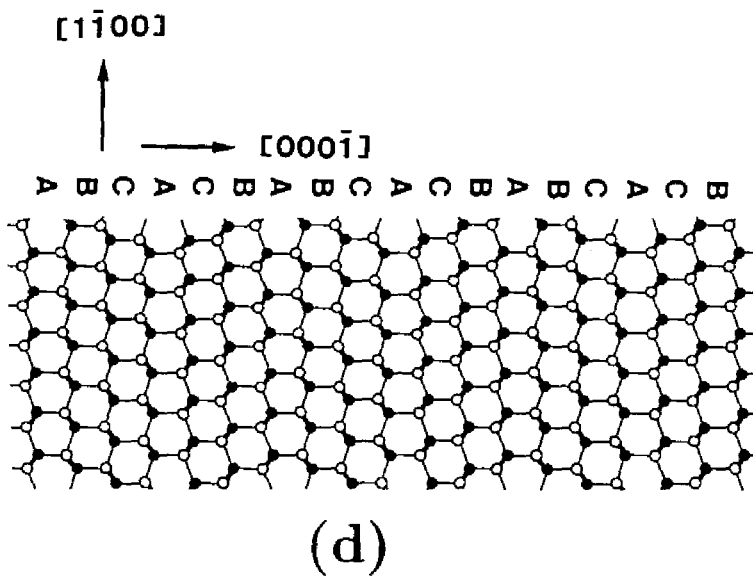
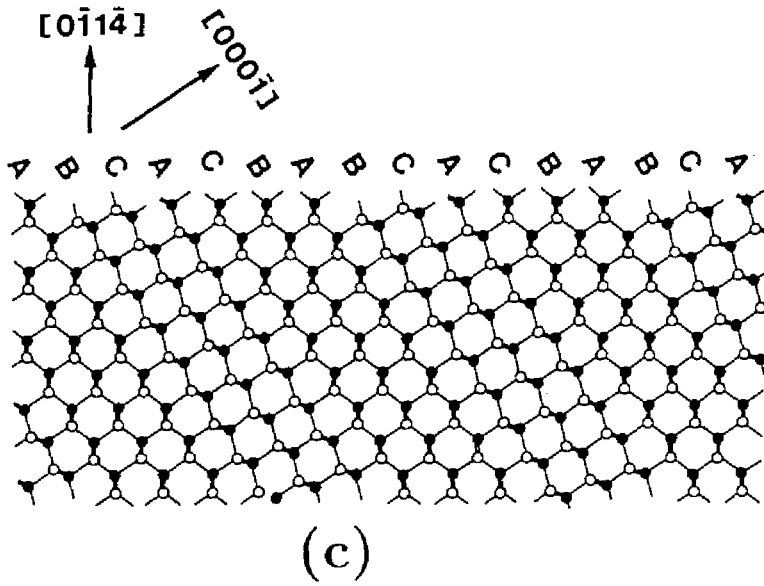


Fig.2.17 Schematic diagrams of bond configurations for (c) $(0\bar{1}1\bar{4})$, and (d) $(1\bar{1}00)$ surfaces.

2.5 Summary

CVD growth of SiC on off-oriented α -SiC{0001} faces was investigated at low temperatures of 1100~1500°C. By the introduction of off-orientation into substrates, homoepitaxy of α -SiC with a very smooth surface could be achieved (step-controlled epitaxy). The mechanism was explained from a view point of growth mode: Step-flow growth realizes homoepitaxy of α -SiC, whereas two-dimensional nucleation leads to the growth of 3C-SiC with double positioning twin. This technique is effective for both (0001)Si and (000 $\bar{1}$)C faces, and applicable to any polytypes.

Single crystalline 6H-SiC could be grown at temperatures as low as 1200°C utilizing step-flow growth. However, twinned crystalline 3C-SiC was grown at 1100°C; this fact can be ascribed to the suppressed surface migration of adsorbed species at the low temperature and to the occurrence of two-dimensional nucleation on terraces. For further reduction of growth temperature, growth on (0 $\bar{1}$ 1 $\bar{4}$) and (1 $\bar{1}$ 00) (or (11 $\bar{2}$ 0)) faces using a new feed-stock may be hopeful.

References

- [1] B.Wessels, H.C.Gatos, and A.F.Witt, *Silicon Carbide 1973*, R.C.Marshall, J.W.Faust, Jr., and C.E.Ryan Eds., (Univ. of South Carolina Press, Columbia, 1974), p.25.
- [2] R.W.Brandner and R.P.Sutton, *Br. J. Appl. Phys.*, **2**, 309(1969).
- [3] W.von Muench, W.Kuerzinger, and I.Pfaffeneder, *Solid-State Electron.*, **19**, 871(1976).
- [4] M.Ikeda, T.Hayakawa, S.Yamagiwa, H.Matsunami, and T.Tanaka, *J. Appl. Phys.*, **50**, 8215(1979).
- [5] S.Yoshida, E.Sakuma, H.Okumura, S.Misawa, and K.Endo, *J. Appl. Phys.*, **62**, 303(1987).
- [6] Y.Matsushita, T.Nakata, T.Uetani, T.Yamaguchi, and T.Niina, *Jpn. J. Appl. Phys.*, **29**, L343(1990).
- [7] V.J.Jennings, A.Sommer, and H.C.Chang, *J. Electrochem. Soc.*, **113**, 728(1966).
- [8] S.Nishino, H.Matsunami, and T.Tanaka, *J. Crystal Growth*, **45**, 144(1978).
- [9] N.Kuroda, K.Shibahara, W.S.Yoo, S.Nishino, and H.Matsunami, *Ext. Abstr. the 19th Conf. on Solid State Devices and Materials* (Tokyo, 1987), p.227.

- [10] A.Itoh, T.Kimoto, and H.Matsunami, unpublished.
- [11] W. von Muench and I.Pfaffeneder, *J. Electrochem. Soc.*, **122**, 642(1975).
- [12] A.Suzuki, H.Ashida, N.Furui, K.Mameno, and H.Matsunami, *Jpn. J. Appl. Phys.*, **21**, 579(1982).
- [13] K.Shibahara, Ph.D. Thesis, Faculty of Engineering, Kyoto University (1987).
- [14] J.W.Matthews, Ed., *Epitaxial Growth, part B* (Academic Press, New York, 1975), Chapt.5.
- [15] H.S.Kong, J.T.Glass, and R.F.Davis, *J. Appl. Phys.*, **64**, 2672(1988).
- [16] T.Ueda, H.Nishino, and H.Matsunami, *J. Crystal Growth*, **104**, 695(1990).
- [17] H.Matsunami, T.Ueda, and H.Nishino, *Mat. Res. Soc. Symp. Proc.*, **162**, 397(1990).
- [18] B.R.Pamplin, *Crystal Growth* (Pergamon Press, Oxford, 1975).
- [19] V.Heine, C.Cheng, and R.J.Needs, *J. Am. Ceram. Soc.*, **74**, 2630(1991).
- [20] W.S.Yoo and H.Matsunami, *Amorphous and Crystalline Silicon Carbide IV*, C.Y.Yang, M.M.Rahman, and G.L.Harris Eds, (Springer-Verlag, Berlin, 1992), p.66.
- [21] J.H.Neave, P.J.Dobson, B.A.Joyce, and J.Zhang, *Appl. Phys. Lett.*, **47**, 100(1985).
- [22] T.Fukui and H.Saito, *Appl. Phys. Lett.*, **50**, 824(1987).
- [23] T.Nishinaga, T.Shitara, K.Mochizuki, and K.I.Cho, *J. Crystal Growth*, **99**, 482(1990).
- [24] K.A.Bertness, C.Kramer, J.M.Olson, and J.Moreland, *J. Electronic Mat.*, **23**, 195(1994).
- [25] *for example*, N.Chand, E.E.Becker, J.P. van der Ziel, S.N.G.Chu, and N.K.Dutta, *Appl. Phys. Lett.*, **58**, 1704(1991).
- [26] N.Chand, S.N.G.Chu, and M.Geva, *Appl. Phys. Lett.*, **59**, 2874(1991).
- [27] A.A.Chernov, *J. Crystal Growth*, **42**, 55(1977).
- [28] S.Tanaka, R.S.Kern, and R.F.Davis, *Appl. Phys. Lett.*, **65**, 2851(1994).
- [29] J.A.Powell and H.A.Will, *J. Appl. Phys.*, **44**, 5177(1973).
- [30] A.Yamashita, W.S.Yoo, T.Kimoto, and H.Matsunami, *Jpn. J. Appl. Phys.*, **31**, 3655(1992).
- [31] T.Kimoto, S.Kobayashi, K.Nishino, W.S.Yoo, and H.Matsunami, *Ext. Abstr. the 39th Spring Meeting of Japan Society of Applied Physics and Related Societies* (Chiba, 1992), p.224 (in Japanese).

Chapter 3

Growth Mechanism of Step-Controlled Epitaxy

3.1 Introduction

Nowadays, high-quality α -SiC epilayers have become available owing to the development of step-controlled epitaxy. Advanced SiC devices which realize the tremendous potential of SiC cannot be fabricated without this technique. Recent improvement of growth systems and growth condition has brought about the reduction of background doping level in the range of 10^{14}cm^{-3} [1-4], which is promising for fabrication of high-power devices with blocking voltages of several kV or more.

There have been several studies on growth mechanism of step-controlled epitaxy, and the polarity and off-direction dependences were investigated [5-10]. However, the phenomena experimentally obtained were discussed only qualitatively in all the previous reports, and the growth mechanism such as the rate-determining process and surface diffusion is still not clear. Besides, there have been few studies relating the effects of growth temperature, C/Si ratio (atomic ratio of C and Si in supplied source gases), and off-angle on the growth.

Although step-flow growth itself is a well-known phenomenon in crystal growth, the comprehensive understanding has not been given. It is of great sci-

entific interest to investigate the relationship between substrate's off-orientation and growth mechanism.

Furthermore, the formation of multiple-height steps (step bunching) has been a long-standing problem in crystal growth and surface science. Recent development of scanning tunneling microscopy (STM) and atomic force microscopy (AFM) has allowed direct observation of real surfaces, and considerable efforts have been done in epitaxial growth of Si [11] and III-V semiconductors [12,13] to reveal the step bunching mechanism. In SiC growth, quite a few studies have been reported about step structure on SiC surfaces [14-18]. Recently, Tanaka *et al.* reported homoepitaxial growth of 6H-SiC on off-oriented 6H-SiC(0001) substrates by MBE [18], and they observed the formation of multiple-height (3~4 bilayers) steps by transmission electron microscopy (TEM). However, step structure of 6H-SiC grown by CVD has never been reported.

In this chapter, the effects of C/Si ratio, growth temperature, and substrate's polarity on the polytype of grown layers and growth rate are investigated in detail. The rate-determining step is discussed based on these results. Next, 6H- and 4H-SiC surfaces grown by step-controlled epitaxy are investigated by AFM and TEM. Clear step bunching is observed for both polytypes. The step bunching mechanism is discussed from a viewpoint of the equilibrium shape of crystal.

3.2 Rate-Determining Step

3.2.1 C/Si ratio dependence

It is well-known that V/III ratio is an important parameter in epitaxial growth of III-V semiconductors [19]. On the analogy of this dependence, C/Si ratio should give significant influence on the growth of SiC. In this study, the effects of C/Si ratio on surface morphology and growth rate are investigated.

The flow rate of C_3H_8 was varied in the range of 0.10~0.40sccm by keeping the flow rate of SiH_4 fixed at 0.15 or 0.30sccm. The growth temperatures were 1200°C and 1500°C. 6H-SiC{0001} grown by the Acheson method were used as substrates. Off-angle was 6° toward (11 $\bar{2}$ 0). The thickness of

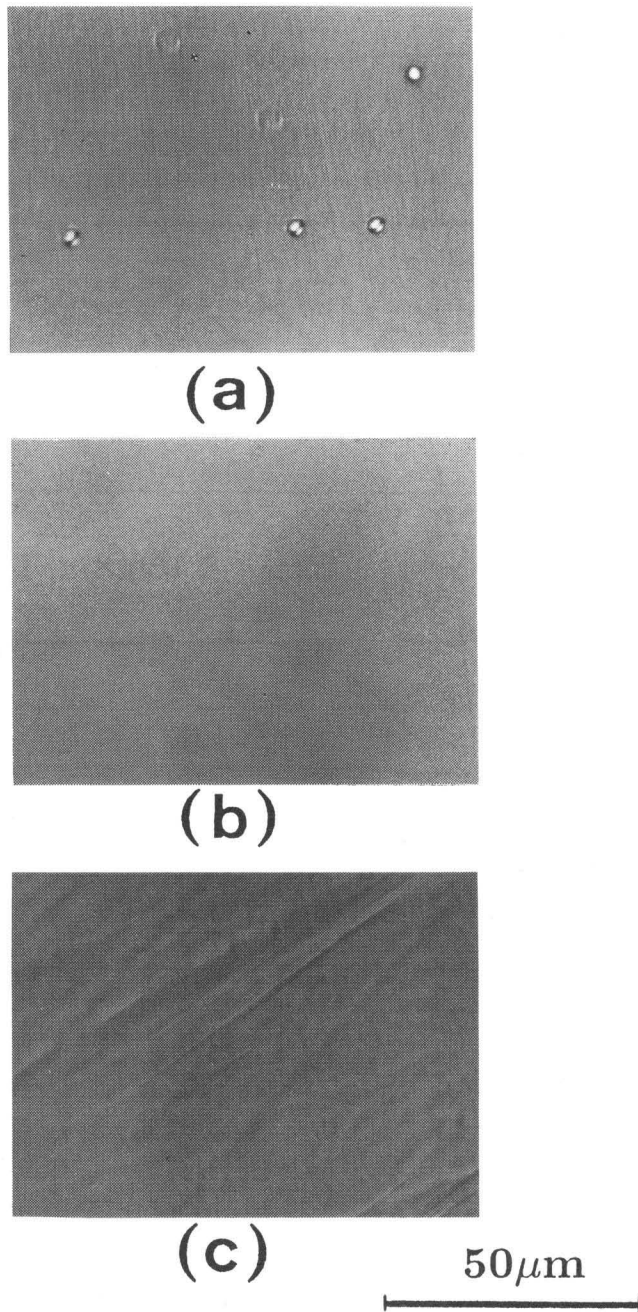


Fig.3.1 C/Si ratio dependence of surface morphology for layers grown at 1500°C on $6\text{H-SiC}(000\bar{1})\text{C}$ faces with 6° -off toward $\langle 11\bar{2}0 \rangle$.
(a) $\text{C/Si} = 1.0$ (Si-rich), (b) $\text{C/Si} = 2.0$ (moderate), (c) $\text{C/Si} = 3.8$ (C-rich).

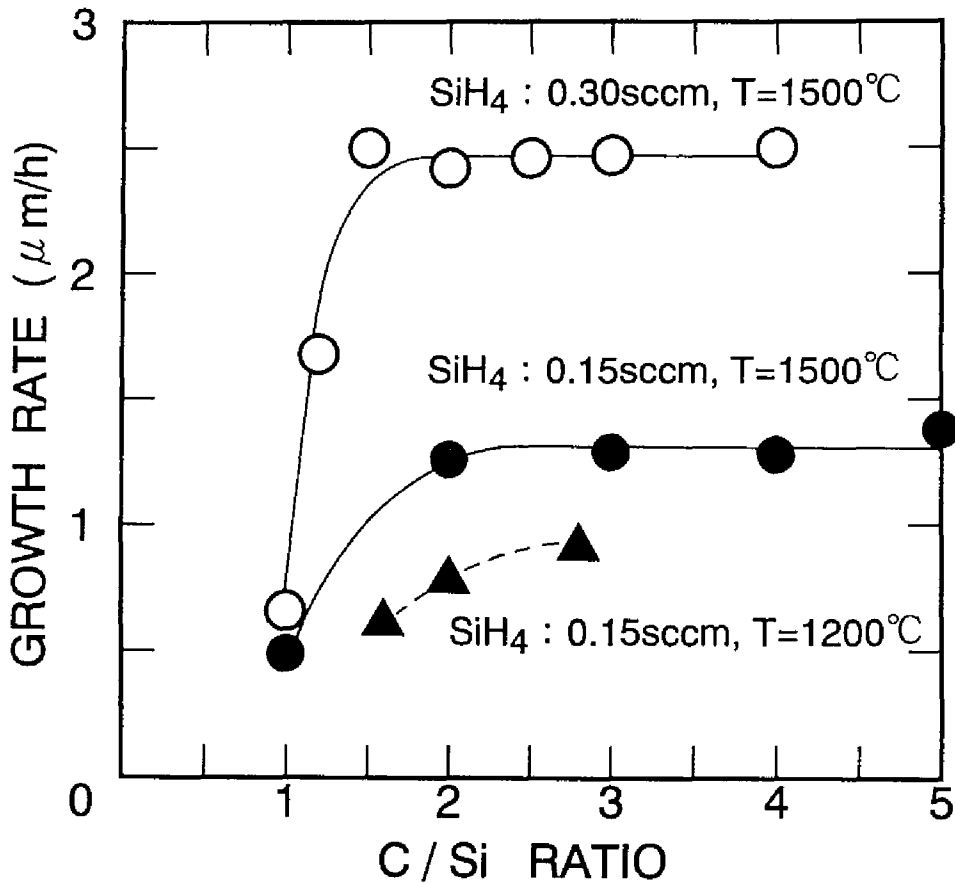


Fig.3.2 Dependence of growth rate on C/Si ratio. Closed and open circles are the results for a SiH₄ flow rate of 0.15 sccm and 0.30 sccm at 1500°C, and closed triangles at 1200°C. Substrates are 6H-SiC (000 $\bar{1}$)C faces.

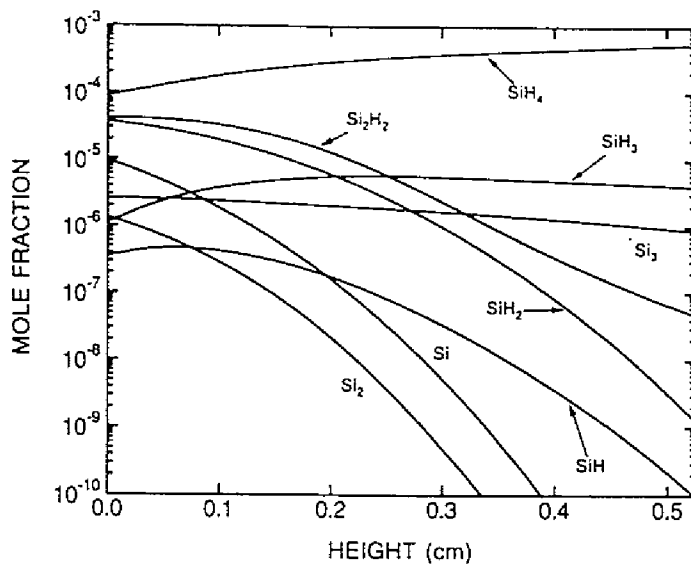
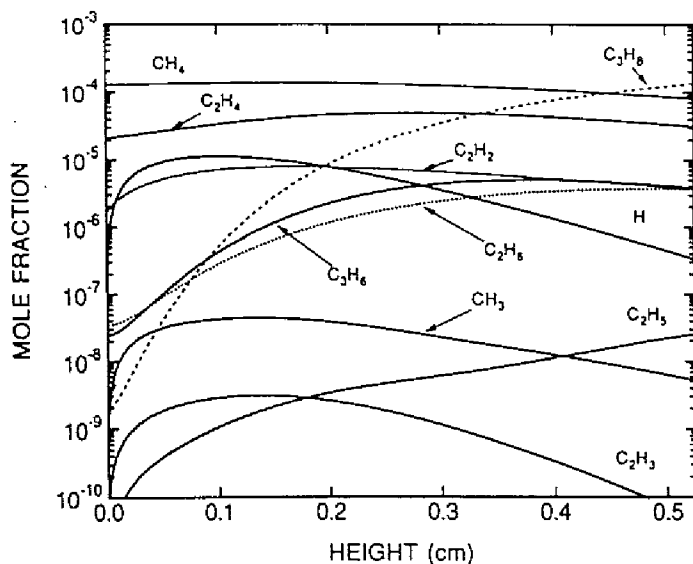
**(a)****(b)**

Fig.3.3 Concentration profiles of dominant species near the substrate surface in a SiH_4 - C_3H_8 - H_2 system [21]. (a) Si related and (b) C related species. The horizontal axis means the height from the sample surface. Substrate temperature is 1352°C .

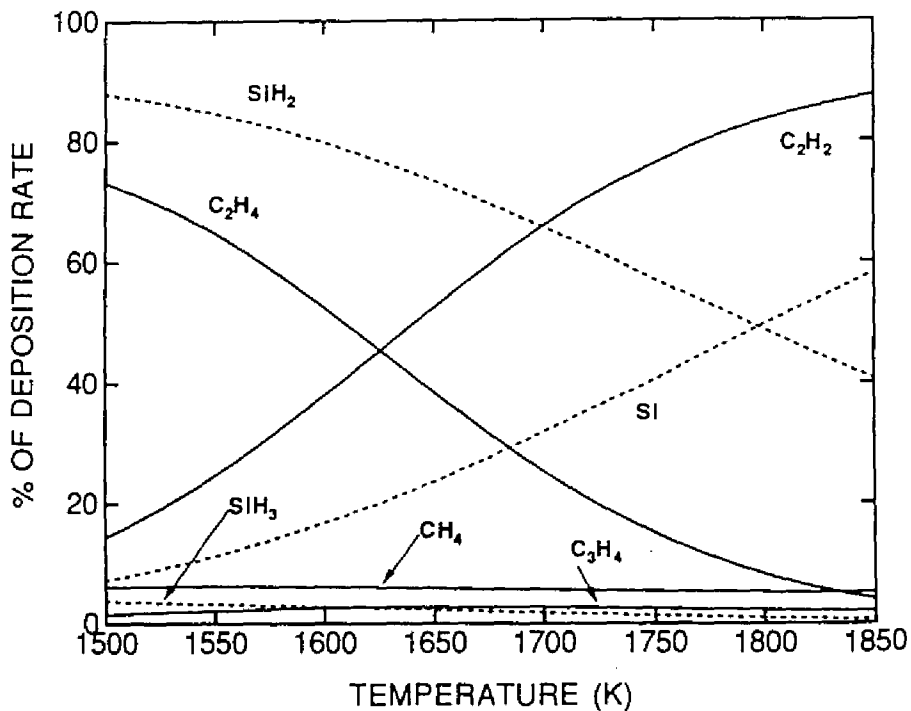


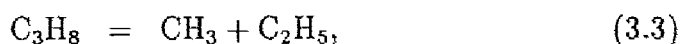
Fig.3.4 Dominant species contributing to SiC growth as a function of growth temperature [21].

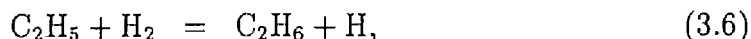
grown layers was determined by a cross-sectional view in scanning electron microscope (SEM) observation utilizing the difference in contrast of images between n- and p-type grown layers.

Figure 3.1 shows Nomarski micrographs for the layers grown on 6H-SiC(000 $\bar{1}$)C faces at 1500°C under various C/Si ratios for a SiH₄ flow rate of 0.30sccm. The thickness of epilayers is about 5μm. The surface morphology is severely affected by the C/Si ratio. The feature of surface morphology can be classified into three types : Si-rich, moderate, and C-rich. Under the moderate C/Si ratio condition (C/Si=1.2~3.0), perfectly featureless surfaces can be obtained. The grown layers show relatively flat surfaces with Si droplets under the Si-rich condition (C/Si < 1.2). Wavy or stripe-like morphology is observed for the C-rich condition (C/Si > 3.0).

The C/Si ratio dependence of growth rate on (000 $\bar{1}$)C face is shown in Fig.3.2. In the figure, closed and open circles are the results for SiH₄ flow rates of 0.15sccm and 0.30sccm at 1500°C. In the region of C/Si > 1.4 (moderate and C-rich conditions), the growth rate has an almost constant value. In this region, the growth rate increases proportionally with the flow rate of SiH₄. This dependence of growth rate indicates that the supply of SiH₄ limits the growth. Wessels *et al.* investigated the growth on well-oriented {0001} faces using SiH₄ and C₃H₈ at 1500~1700°C [20]. They also observed that the supply of SiH₄ controlled the rate of SiC growth. In the region of C/Si < 1.4 (Si-rich), the growth rate decreases remarkably. This may be caused by the lack of C sources. Quite similar results were obtained for the growth on off-oriented Si faces. At 1200°C, the growth rate is inclined to saturate under the higher C/Si ratio condition, as shown by closed triangles in Fig.3.2.

Allendorf and Kee have analyzed gas phase and surface reactions at 1200~1600°C in a SiH₄-C₃H₈-H₂ system [21]. Stinespring and Wohmhoudt also reported a similar analysis on gas phase kinetics [22]. Dominant reactions of SiH₄ and C₃H₈ decomposition are expressed as follows [21,22]:





A typical result simulated for the gas phase kinetics is shown in Fig.3.3, which gives the concentration profile of dominant species near the substrate surface [21]. Figure 3.4 shows the dominant species which contribute to SiC growth as a function of growth temperature [21]. Thus, the dominant species may be Si, SiH₂, Si₂H₂ species from SiH₄, and CH₄, C₂H₂, C₂H₄ molecules from C₃H₈.

The above results suggest that Si (or SiH₂) species are preferentially adsorbed on the surface. The adsorbed Si species may migrate on terraces, and the crystal growth proceeds through the incorporation of Si at atomic steps and its carbonization by hydrocarbon molecules. Of course, Si-C species can also migrate on the terraces. However, Si-C species are supposed to have much shorter migration length than Si adatoms due to the larger mass, and to make minor contribution to SiC growth. These speculations are partially supported by a study on gas source MBE of SiC. Yoshinobu *et al.* achieved the epitaxial growth of SiC by repeating alternate supply of Si₂H₆ and C₂H₂ at 1000°C [23]. However, no crystal growth or only island-like deposits were obtained by simultaneous supply of both gases. Based on the results, they showed that the reaction between adsorbed Si atoms on a surface and C₂H₂ molecules is essential to the growth of SiC. In fact, no deposition occurs in the present CVD system without SiH₄ supply.

3.2.2 Off-angle dependence

In order to study the effects of substrate's off-orientation in detail, the off-angle dependence on both faces was examined. Figure 3.5 shows the surface morphology for layers grown at 1500°C on (0001)Si substrates with (a) 2°, (b) 5°, and (c) 10° off-angles. Epilayers show very smooth surfaces independent of off-angle. Although Wang and Davis reported that surface pits of 6H-SiC epilayers increased with increasing off-angle [10], such dependence was not observed in this study.

Figure 3.6 shows the growth rates for various off-angles at 1500°C. The

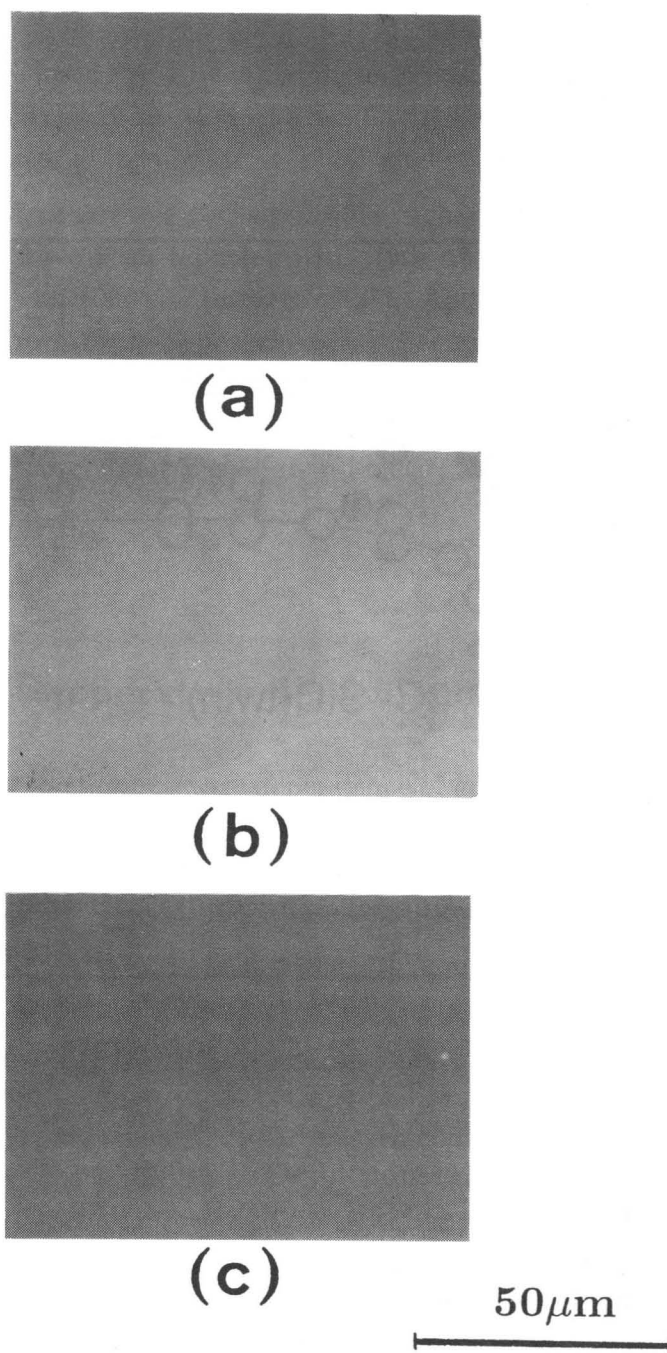


Fig.3.5 Off-angle dependence of surface morphology for layers grown at 1500°C on $6\text{H-SiC}(0001)\text{Si}$ faces. Off-orientation is (a) 2° , (b) 5° , and (c) 10° toward $\langle 11\bar{2}0 \rangle$.

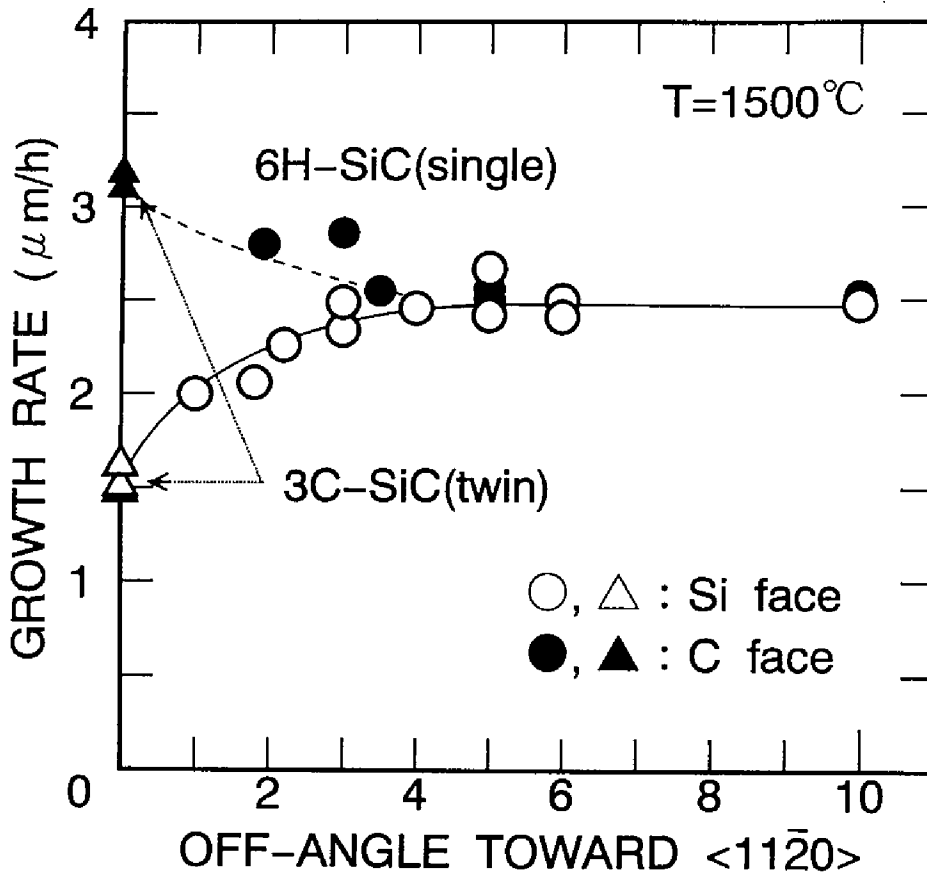


Fig.3.6 Dependence of growth rate at 1500°C on off-angle of substrates. The flow rates of SiH_4 and C_3H_8 are 0.30sccm and 0.20sccm, respectively. Closed circles and triangles show the growth of 3C-SiC and open marks that of 6H-SiC.

flow rates of SiH_4 and C_3H_8 are 0.30 and 0.20sccm, respectively. In this figure, open (on Si face) and closed (on C face) triangles mean the growth of 3C-SiC, and open and closed circles mean that of 6H-SiC. 6H-SiC can be homoepitaxially grown on substrates with more than 1° off-angle.

On well-oriented substrates (off-angle= 0°) higher growth rates are obtained on C faces, as have been reported [24]. This might be ascribed to the higher nucleation rate on $(000\bar{1})\text{C}$ terraces [9,25]. As the off-angle increases, the growth rates on both faces approach each other and become almost the same value of $2.5\mu\text{m/h}$ for the off-angle from 4° to 10° . As the terrace width becomes narrower with the increase of off-angle, step-flow growth becomes dominant. This may bring about a change in kinetics of reactants, which will be discussed in 3.2.4.

3.2.3 Growth temperature dependence

Figure 3.7 shows the temperature dependence of growth rate in the range between 1200°C and 1600°C , in which the epitaxial growth of 6H-SiC does occur. The flow rates of SiH_4 and C_3H_8 are 0.15 and $0.10\sim 0.14$ sccm, respectively, and the off-angle is $5\sim 6^\circ$. Under these conditions, smooth surfaces are obtained, as shown in Fig.2.16.

As the growth temperature decreases, the growth rate decreases with a very small activation energy of 2.8kcal/mole. For CVD growth on well-oriented $\{0001\}$ faces, activation energies of 12 [24], 20 [26] or 22 kcal/mole [20] were reported. Wessels *et al.* explained that the growth could be well described by adsorption-desorption kinetics of Si, and they assigned the activation energy (22 kcal/mole) to that for Si adsorption based on thermodynamic consideration [20]. However, step-controlled epitaxy brings about a much smaller activation energy (2.8kcal/mole) as mentioned above. There is little difference between the growth rates on Si and C faces even at low temperatures. Karmann *et al.* also reported similar insensitivity of growth rate to temperature in CVD on 6H-SiC substrates with 2° off-orientation toward $(1\bar{1}00)$ [27]. This small activation energy and little polarity dependence are analyzed in the next subsection.

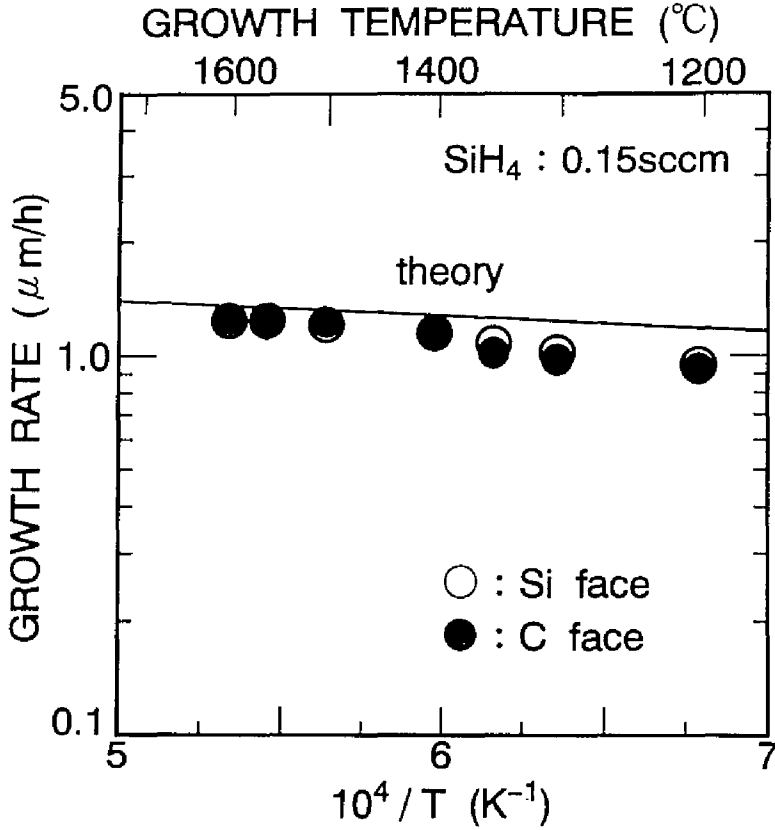


Fig.3.7. Temperature dependence of growth rates on off-oriented 6H-SiC(0001) Si and (000 $\bar{1}$)C faces. The flow rates of SiH₄ and C₃H₈ are 0.15 and 0.10~0.14sccm, respectively. The calculated result based on a stagnant layer model is shown by a solid curve.

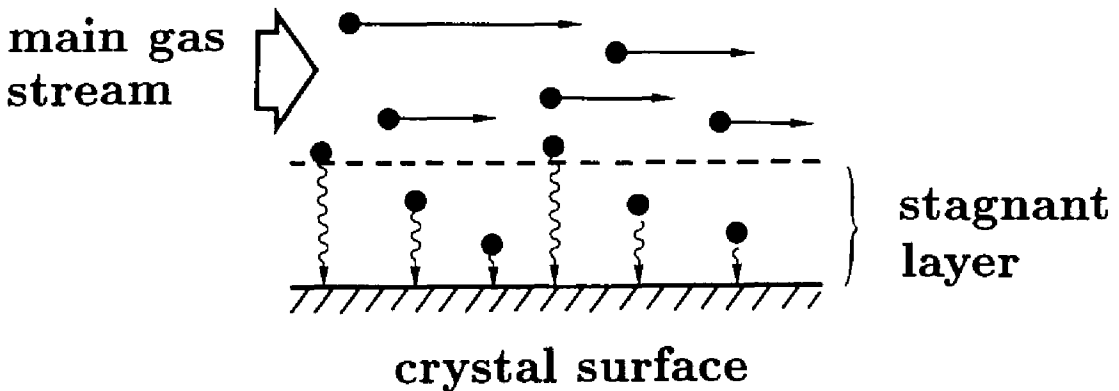


Fig.3.8 Schematic illustration of a stagnant layer model.

3.2.4 Discussion

The author obtained two notable results which suggest a clear difference in the growth mechanism on well-oriented and off-oriented faces ; (i) small activation energy and (ii) no polarity effect on the growth rate in step-controlled epitaxy. In this section, the small activation energy obtained in step-controlled epitaxy and the rate-determining step are discussed.

The activation energy of growth rate is generally regarded as an energy required for proceeding the slowest reaction which limits the growth. Up to now, a lot of studies on the activation energy have been reported for CVD of various materials. In those studies, several assignments for the activation energies, which depend on growth systems, have been done to the adsorption energy of reactants, the energy for decomposition of source gases, etc.

There are two types of controls in crystal growth, (1) surface-reaction control, and (2) mass-transport control (especially diffusion control in CVD [28]). The author assumes both types of controls and analyzes the temperature dependence of growth rate.

First, surface-reaction control is considered. If the growth of 6H-SiC is limited by surface reactions, the growth rate should be directly proportional to the velocity of atomic steps on a surface (v_{step}), because 6H-SiC would be grown through step-flow growth. Therefore, the growth rate can be given by the product of v_{step} and $\tan\theta$, where θ is the off-angle of a substrate. Since v_{step} can be calculated after the BCF (Burton, Cabrera and Frank) theory [29], the growth rate (R) is expressed by the following equation:

$$R = v_{\text{step}} \tan \theta = 2\sigma a \nu \tan \theta \tanh\left(\frac{\lambda_0}{2\lambda_s}\right) \exp\left(-\frac{E_{\text{kink}} + \frac{1}{2}E_{\text{des}} + \frac{1}{2}E_{\text{diff}}}{kT}\right), \quad (3.8)$$

where σ , a , ν , λ_0 and λ_s are the supersaturation, the jump distance of adsorbed species, the frequency of atomic vibration, the distance between atomic steps, and the average surface migration length. E_{kink} , E_{des} and E_{diff} are the energy of evaporation from kinks on to a surface, desorption energy from a surface to vapor, and activation energy for surface diffusion, respectively.

Based on this model, the growth-rate activation energy is the sum of several activation energies (E_{kink} , E_{des} and E_{diff}), or at least one of them which controls the growth most dominantly. These activation energies, however,

cannot explain the small activation energy experimentally obtained, because E_{kink} , E_{des} and E_{diff} are generally known to be more than 10~20kcal/mole [28]. For the growth of Si, E_{diff} , which would be the smallest among them, is estimated to be 40.7kcal/mole on Si(111) [30] and 14~23kcal/mole on Si(001) [31,32]. Although E_{diff} for SiC growth has never been reported, E_{diff} or other activation energies may hardly take the value of about 3kcal/mole. Thus, the growth will not be controlled by surface reactions.

As for the growth governed by diffusion, Eversteyn *et al.* have developed a stagnant layer model based on gas flow pattern experiments, and applied to a real growth system to improve the uniformity of epilayer thickness [33]. They explained the growth rates quantitatively for CVD of Si in a horizontal reactor. In this case, the diffusion of reactants from main gas stream to a crystal surface controls the growth (Fig.3.8). Since the growth rate of SiC is determined by the supply of Si species as described in 3.2.1, the proposed model for Si growth will be applicable to the present system with some modification. The growth rate at the sample position of x_0 (distance from the front edge of a susceptor: 2.0cm) can be described by the following expression [33]:

$$R(x_0) = \frac{h_0 D_0 T_s P_0}{n_0 k T_0^2 \delta(x_0)} \exp\left\{-\frac{D_0 T_s}{T_0 v_0 b} \int_0^{x_0} \frac{dx}{\delta(x)}\right\}, \quad (3.9)$$

where D_0 is the diffusion coefficient of SiH₄ in H₂ at 300K (0.20cm²/s) [33], P_0 the partial pressure of SiH₄ at the inlet of a reactor (4.95x10⁻⁵atm) calculated by the ratio of SiH₄ and the total flow rate, and v_0 the mean gas velocity under a non-heated condition (10cm/s). T_s is the substrate temperature, T_0 300K, b the free height of the reactor (2.0cm), h_0 the spacing of the 6H-SiC{0001} face (0.252nm), and n_0 the density of adsorption sites on the surface (1.21x10¹⁵cm⁻²). Here, the condensation coefficient, which is the ratio of the number of atoms incorporated into a growing layer to that arriving on a surface, was assumed to be unity.

$\delta(x)$ is the stagnant layer thickness at point x , and is given by the following equation in the ideal case (laminar flow with uniform velocity) [34]:

$$\delta(x) = \sqrt{\frac{\mu x}{v_0 \rho}}, \quad (3.10)$$

where ρ and μ are the gas density and gas viscosity. Although it is difficult to know the exact thickness of a stagnant layer in the present case where some temperature gradient and no ideal laminar flow may exist, $\delta(x)$ can be estimated as the first approximation by eq.(3.10). Using the values of v_0 (10cm/sec), ρ (8.13×10^{-5} g/cm³) and μ (8.7×10^{-5} P) [35] in this system, $\delta(x_0)$ is calculated to be 0.51cm.

The temperature dependence of growth rate was calculated using eq.(3.9) neglecting complex flow dynamics caused by heating. The calculated result is shown by a solid curve in Fig.3.7. The absolute value of growth rate shows surprisingly good agreement between experimental and theoretical results calculated from the simple model. For example, the growth rates on off-oriented Si and C faces at 1500°C are 1.21~1.25 μ m/h, and theoretical value is 1.32 μ m/h. The growth rate can be predicted within an error of 15% in this temperature range. The small error in calculated growth rates may be ascribed to the underestimation of $\delta(x_0)$ or other factors due to a complex gas flow. An error in temperature measurement or the contribution of desorption reaction from a growing surface might be also the origin for the difference between theoretical and experimental values.

The predicted growth rate increases gradually with temperature increase. This is owing to, mainly, the enhancement of diffusion in a stagnant layer. Although eq.(3.9) is not an activation-type formula, the calculated curve in the range of 1200~1600°C yields an apparent activation energy of 2.4kcal/mole using the method of least squares. This shows a very good agreement with the experimental result. Therefore, the growth would be limited by mass transport in step-controlled epitaxy. This fact gives good explanation for little difference in the growth rates on Si and C faces, because no polarity dependence should be observed in the growth controlled by mass transport.

Varying susceptor tilt-angle caused a change of growth rate or its distribution on a substrate. This can be attributed to a change in gas velocity and the thickness of the stagnant layer.

Here consider the effect of substrate's off-orientation on the growth mode. Figure 3.9 shows schematic images of growth mechanism on (a) well-oriented and (b) off-oriented 6H-SiC{0001} faces. As described previously, SiC growth on well-oriented substrates proceeds through two-dimensional nucleation on

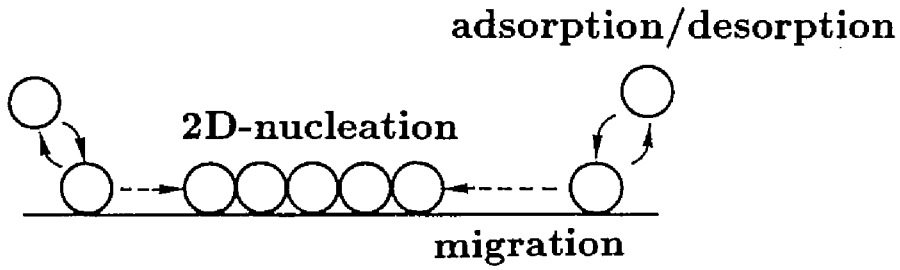
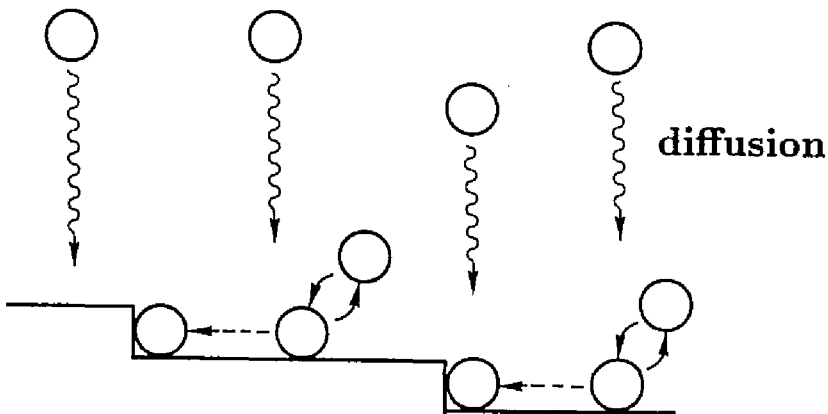
(a)**(b)**

Fig.3.9 Schematic images of growth mechanism; on (a) well-oriented, and (b) off-oriented 6H-SiC{0001} faces.

terraces, which needs a large activation energy. The growth will be controlled by a surface reaction, such as adsorption of Si species [20]. On off-oriented substrates, the lateral growth from atomic steps is promoted, and no more nucleation is needed. As a result, the growth may not be controlled by surface reactions. This will cause the growth rate to be limited by mass transport (diffusion of reactants in a stagnant layer).

Wang and Davis reported the CVD growth of 6H-SiC on off-oriented substrates at 1350~1600°C using a SiH₄-C₂H₄-H₂ system [10]. They obtained the activation energies of 15kcal/mole and 13kcal/mole for the (0001)Si faces and (000 $\bar{1}$)C faces, respectively. These large activation energies may be attributed to a smaller substrate off-angle. In their study, CVD was carried out on {0001} faces 3~4°-off toward $\langle 11\bar{2}0 \rangle$. As is seen in Fig.3.6, the growth on 3~4°-off substrates belongs to the transition region from surface reaction-limited growth to diffusion-limited growth. Since the growth is controlled partially by surface reactions, higher activation energies are expected. This consideration is supported by the fact that the growth on C faces yields higher growth rates in their system.

Figure 3.10 shows growth rate vs. flow rate of SiH₄ at 1500°C under a constant C/Si ratio (2.0) condition. Theoretical growth rates were calculated using eq.(3.9) by varying the partial pressure of SiH₄ (P_0). Experimental and calculated results are shown by open circles and a solid line in the figure. The slope for both the plots is unity.

A condensation coefficient (the ratio of the number of atoms incorporated into a growing layer to that arriving on a surface) is of interest from a viewpoint of efficiency in crystal growth. The growth rate R depends on the flux of source reactants J and on the condensation coefficient η as follows:

$$R = \eta \frac{Jh_0}{n_0}. \quad (3.11)$$

Using this equation and Fig.3.10, the condensation coefficient η can be estimated as 0.9 ± 0.05 , which indicates almost all the reactants are incorporated into the crystal.

In general, the condensation coefficient is a function of the substrate off-angle and growth temperature. There are two types of step-flow growth

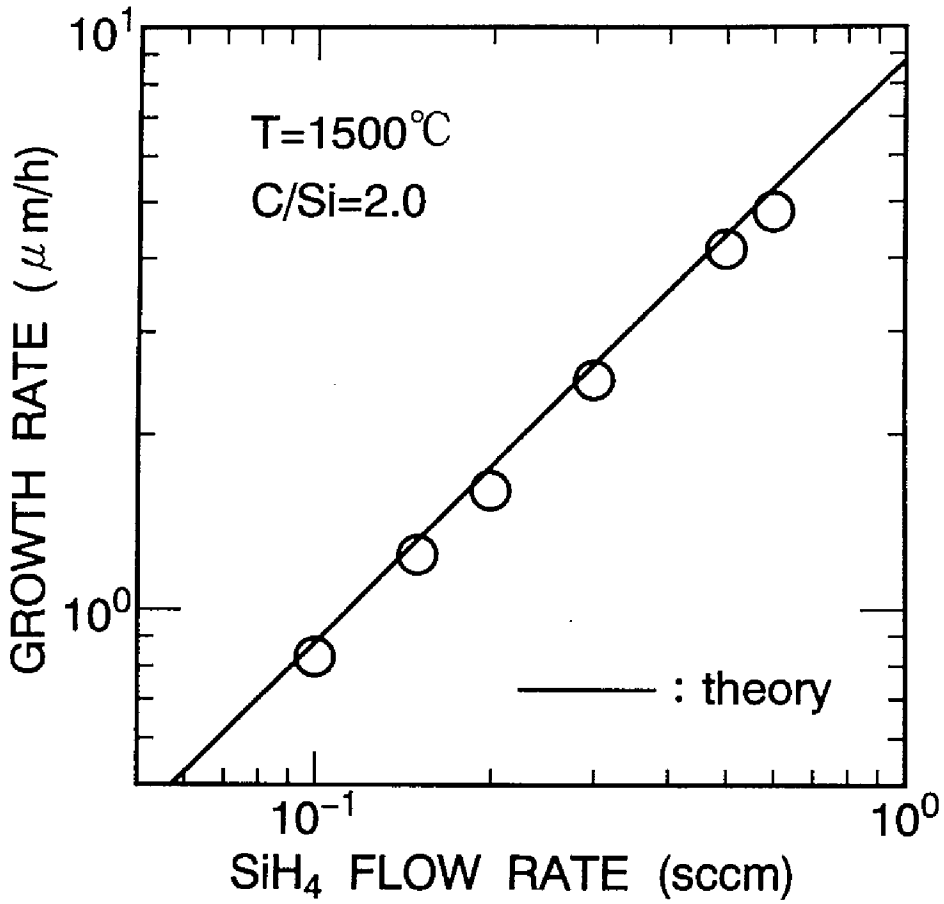


Fig.3.10 SiH_4 flow rate dependence of growth rate at 1500°C . Experimental and calculated results are shown by open circles and a solid line, respectively.

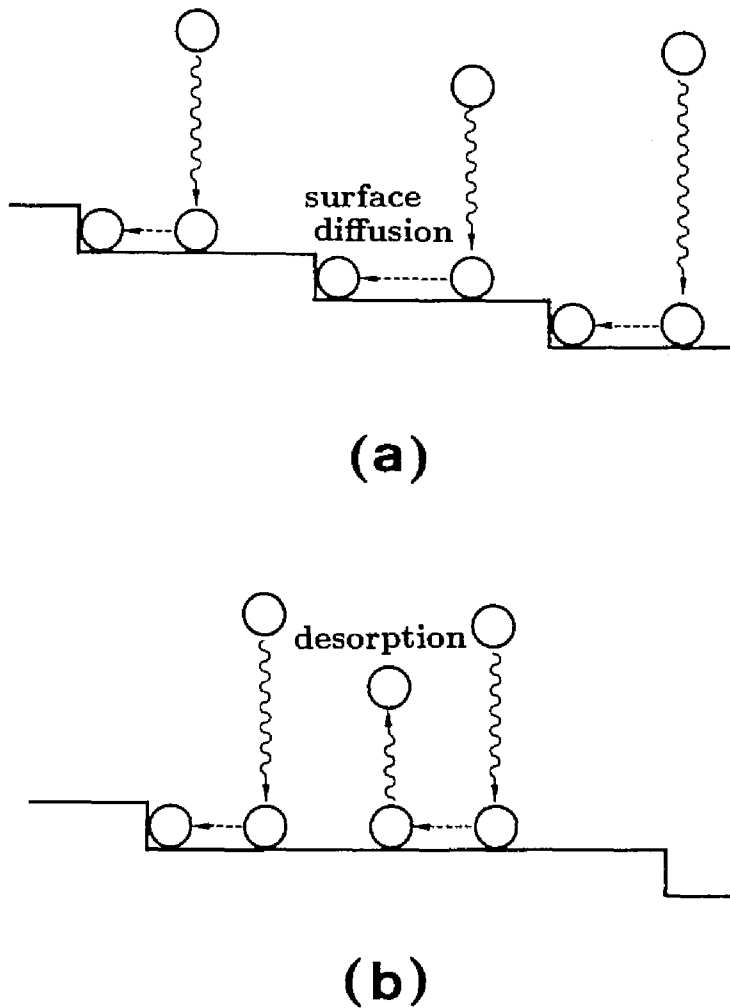


Fig.3.11 Schematic images of two types of step-flow growth. (a) $\lambda_s > \lambda_0$ and (b) $\lambda_s < \lambda_0$ (supersaturation is low).

as shown in Fig.3.11, dependent on the surface kinetics determined by the relationship between surface diffusion length λ_s and terrace width λ_0 . When λ_s is longer than λ_0 (Fig.3.11(a)), all the adsorbed species can reach steps, and they are incorporated into the growing layers ($\eta=1$), if the steps are perfect sink. In the case that λ_s is not longer than λ_0 and supersaturation on the terraces is low enough to suppress nucleation (Fig.3.11(b)), the desorption process cannot be neglected and only a part of the adsorbed species contributes to the growth ($\eta < 1$). As shown in Fig.3.6, the growth rate takes an almost constant value when the substrate's off-angle is larger than 3° . This result indicates that the desorption of adsorbed species is negligible on the substrates with more than 3° .

3.3 Step Bunching

The step structure of 6H- and 4H-SiC epilayers was investigated. The growth temperature and growth rate were 1550°C and $2.5\mu\text{m/h}$. Both commercially available and home-made wafers were used. The SiC{0001} substrate's off-angle is $3\sim 10^\circ$ toward $(11\bar{2}0)$. As-grown surfaces were examined with AFM and TEM observation. The AFM analysis was performed in air, using an SPI3700 system (Seiko Instruments). Samples for cross-sectional TEM observation were prepared using a standard technique, and each sample was examined along the $(1\bar{1}00)$ or $(11\bar{2}0)$ zone axis with JEM-4000EX-II (JEOL) operated at 400keV.

3.3.1 Atomic force microscope analysis

In the AFM analysis, wafers before epitaxial growth show a flat surface, and clear steps could not be discerned. Figure 3.12 shows the $800\text{nm}\times 800\text{nm}$ AFM images of 6H-SiC epilayers grown on (a) $(0001)\text{Si}$ and (b) $(000\bar{1})\text{C}$ faces, respectively. The AFM images of 4H-SiC epilayers are also shown in Fig.3.13. The off-angle of substrates is 5° . The steps go down from the left to the right. Significantly distinctive difference in surface structure between both the faces can be observed. Epitaxial growth on a $(0001)\text{Si}$ face yields "apparent

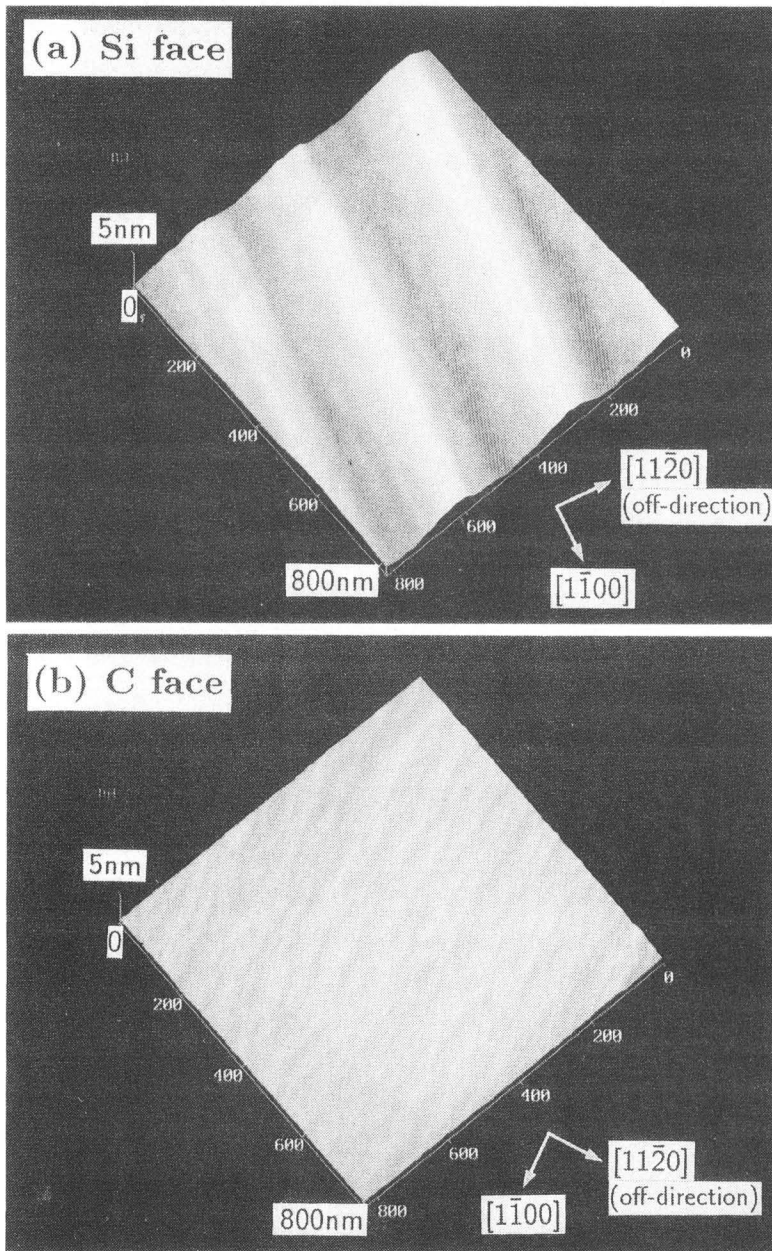


Fig.3.12 AFM images of vicinal 6H-SiC{0001} surfaces (a) (0001)Si and (b) (000 $\bar{1}$)C faces with 5 μ m-thick epilayers. Off-orientation is 5° toward $\langle 11\bar{2}0 \rangle$. The surface steps go down from the left to the right.

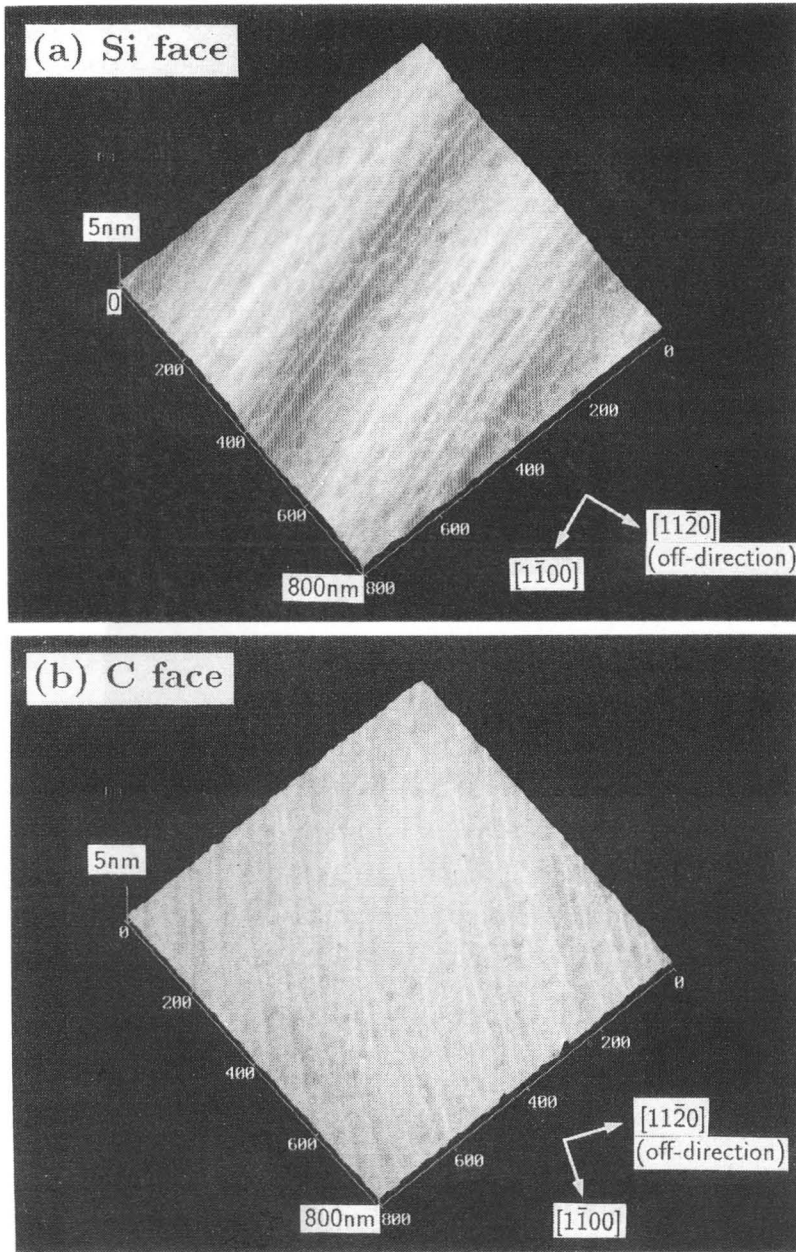


Fig.3.13 AFM images of vicinal 4H-SiC{0001} surfaces (a) (0001)Si and (b) (000 $\bar{1}$)C faces with 5 μ m-thick epilayers. Off-orientation is 5° toward $\langle 11\bar{2}0 \rangle$. The surface steps go down from the left to the right.

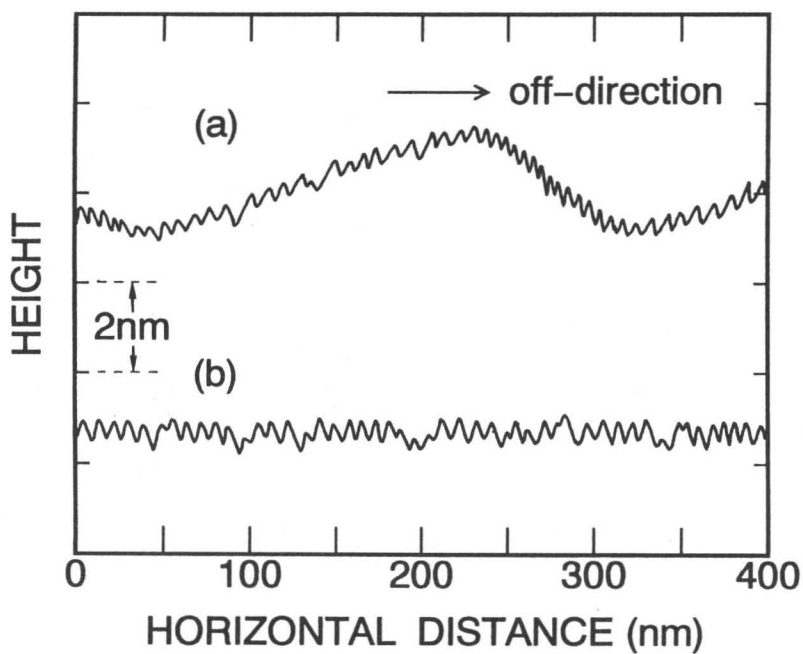


Fig.3.14 Height profiles of 6H-SiC epilayers grown on 5° off-oriented (a) (0001)Si and (b)(000 $\bar{1}$)C faces.

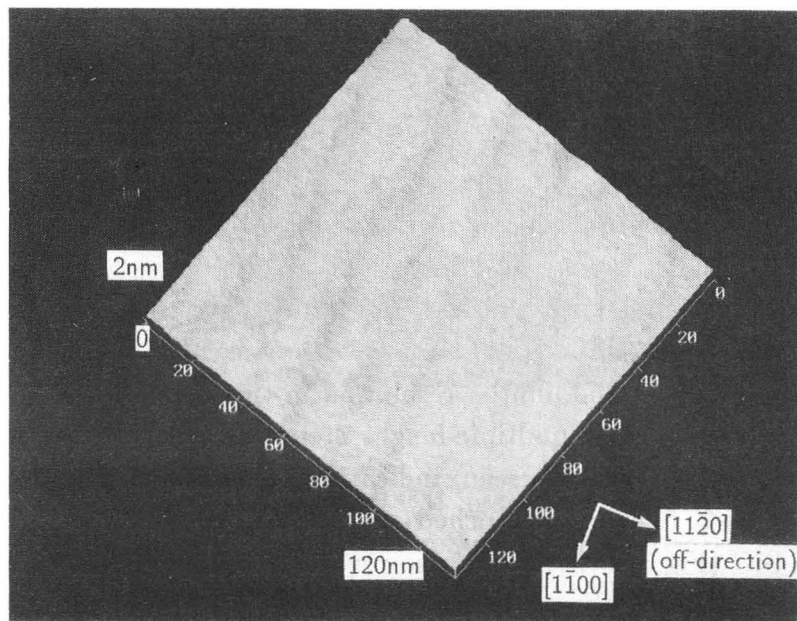


Fig.3.15 High-resolution AFM image of 6H-SiC(0001)Si surface.

macrosteps” with an average terrace width of 280nm and an average step height of 3nm. On a $(000\bar{1})\text{C}$ face, the surface is rather flat and no macrosteps are observed. Although 4H-SiC epilayers had basically similar step structures, the 4H-SiC(0001)Si faces showed real macrosteps with 110~160nm width and 10~15nm height in some regions.

Figure 3.14 shows the height profiles of 6H-SiC epilayers on (a) (0001)Si and (b) $(000\bar{1})\text{C}$ faces, obtained from the AFM data. This observation revealed that each macrostep on the (0001)Si face is not a single multiple-height step but composed of a number of “microsteps”. In other words, the macrostep is the envelope of microsteps with different terrace widths. On the $(000\bar{1})\text{C}$ face, microsteps with several bilayer height are uniformly distributed on the surface.

A typical high-resolution AFM image of 6H-SiC(0001)Si surface is shown in Fig.3.15, where microsteps are observed. Step edges are relatively straight, and the microsteps have several Si-C bilayer height (single Si-C bilayer height = 0.252nm). But the exact number of bilayers at steps could not be determined due to the limited height resolution of the present AFM system. We examined epilayers with various off-angles of 3~10°. The terrace width decreased with increasing the off-angle, but very little difference in step structure was observed.

3.3.2 Transmission electron microscope observation

Figure 3.16 shows typical cross-sectional TEM images for surfaces of (a) 6H-SiC and (b) 4H-SiC epilayers. Substrates are (0001)Si 3.5° off-oriented toward $[11\bar{2}0]$, and the epilayer thickness is 10 μm . Since the observation was done along the $[\bar{1}100]$ zone axis, the separation of each Si-C pair is lacking in the images because of the limited resolution in this configuration. In each figure, {0001} terraces and multiple-height steps are clearly observed. No island growth on the terraces is seen, indicating step-flow growth. Note that the number of Si-C bilayer at bunched steps is 3 for 6H-SiC (Fig.3.16(a)), and 4 for 4H-SiC (Fig.3.16(b)). It is also revealed that the edges of bunched steps are not abrupt but show a gentle slope of 10~30°. This result for step bunching on 6H-SiC is consistent with the previous report on MBE growth of 6H-SiC [18].

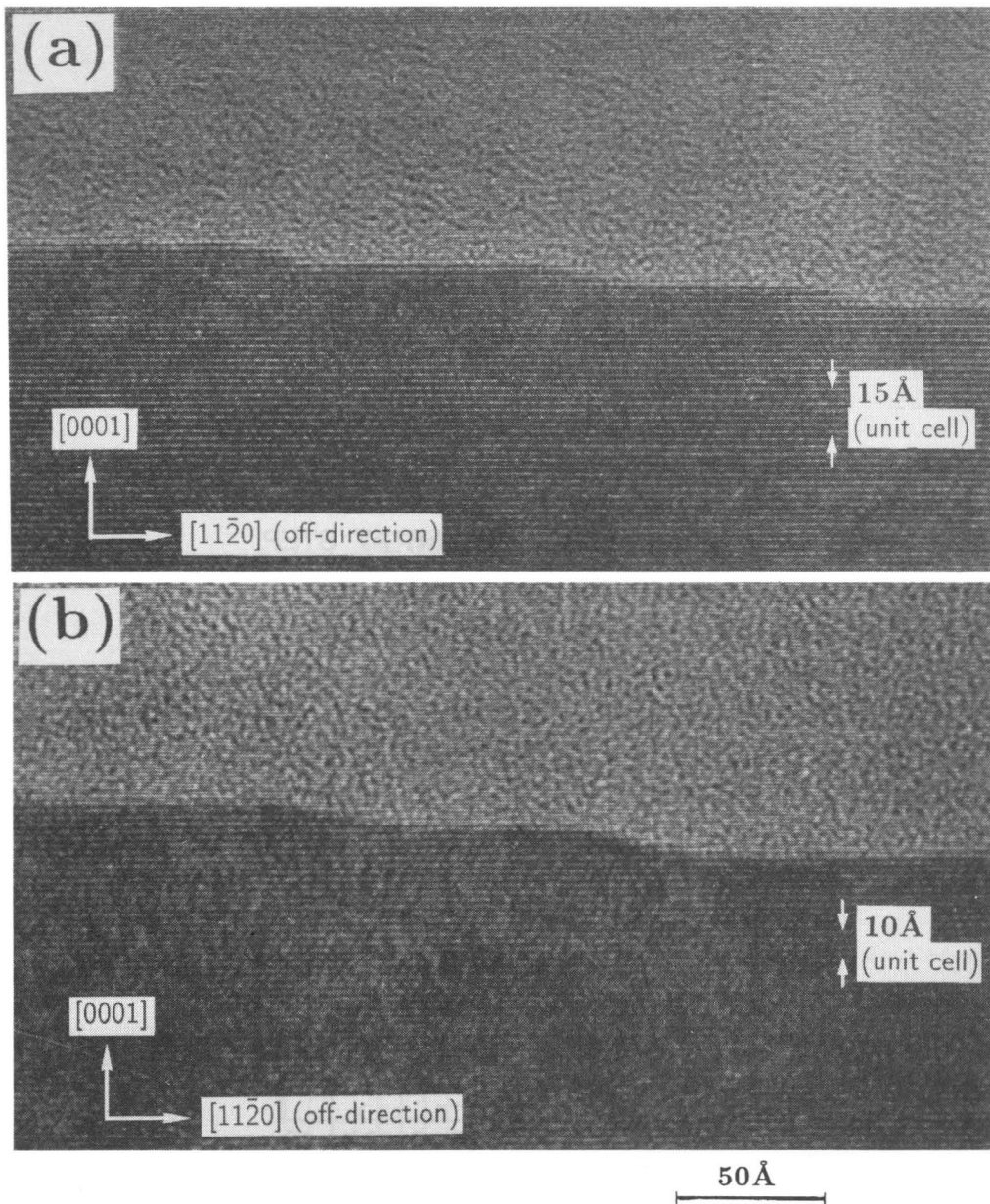
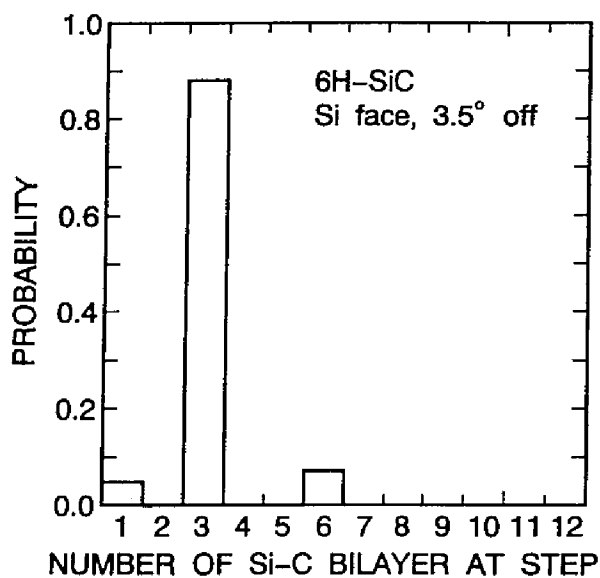
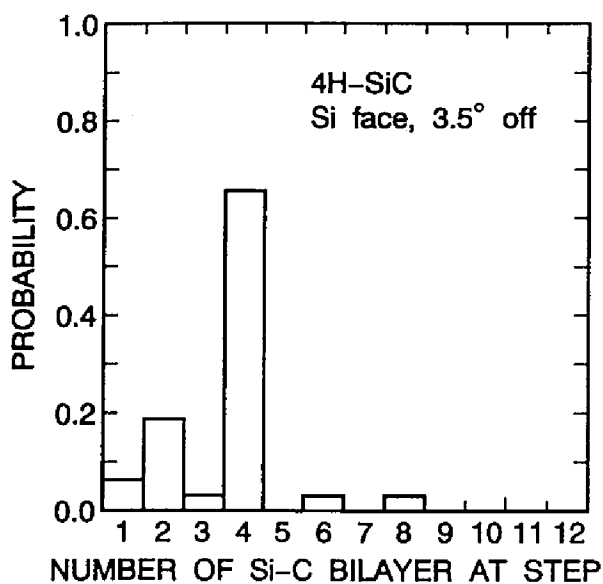


Fig.3.16 Typical cross-sectional TEM images for the surfaces of (a) 6H-SiC and (b) 4H-SiC epilayers. Substrates are (0001)Si 3.5° off-oriented toward [11 $\bar{2}$ 0]. Samples are examined along the [1 $\bar{1}$ 00] zone axis.

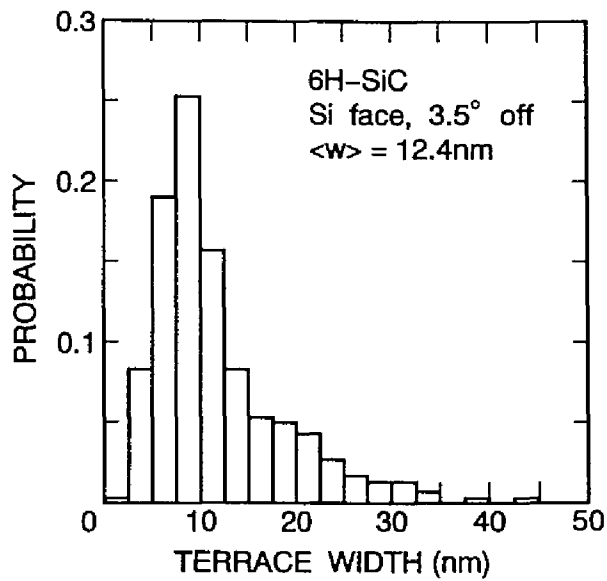


(a)

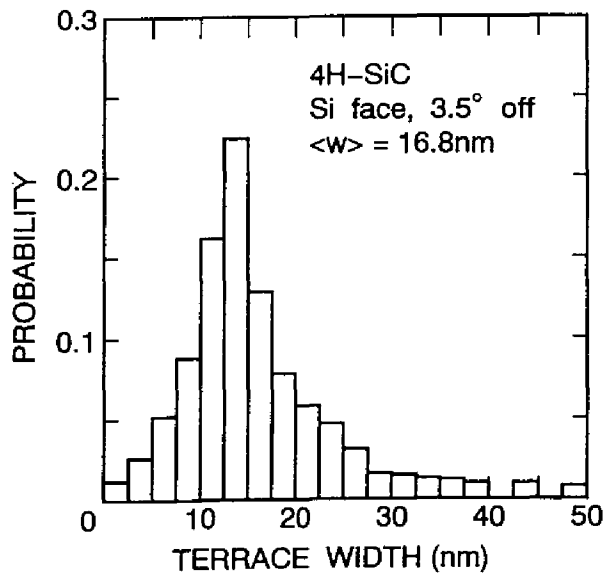


(b)

Fig.3.17 Histograms of step height for the surfaces of (a) 6H-SiC and (b) 4H-SiC epilayers. Substrates are (0001)Si 3.5° off-oriented toward $\langle 11\bar{2}0 \rangle$.



(a)



(b)

Fig.3.18 Histograms of terrace width for the surfaces of (a) 6H-SiC and (b) 4H-SiC epilayers. Substrates are (0001)Si 3.5° off-oriented toward $\langle 11\bar{2}0 \rangle$.

The authors examined more than 200 steps for each sample, and made histograms of step height and terrace width. Figure 3.17 shows the histograms of step height for the surfaces of (a) 6H-SiC and (b) 4H-SiC epilayers grown on a Si face. In 6H-SiC, 88% of steps are composed of 3 Si-C bilayers (half of unit cell), and 7% of steps have 6 Si-C bilayer height (unit cell). On the other hand, 4 bilayer-height (unit cell) steps are the most dominant (66%) and 2 bilayer-height steps also show high probability (19%) on 4H-SiC. Single Si-C bilayer-height steps are relatively few (5% or less) on both 6H- and 4H-SiC.

Figure 3.18 shows the histograms of terrace width for the surfaces of (a) 6H-SiC and (b) 4H-SiC epilayers. Substrates are (0001)Si 3.5° off-oriented toward $\langle 11\bar{2}0 \rangle$. Although the average terrace width of single Si-C bilayer steps is calculated as 4.1nm, the average values ($\langle w \rangle$) experimentally obtained are much larger, 12.4nm for 6H-SiC and 16.8nm for 4H-SiC, due to considerable step bunching. The different average terrace width between 6H-SiC and 4H-SiC, in spite of the same off-angle, originates from the different height of multiple steps as mentioned above. The terrace-width distribution is large, and vast terraces with more than 30nm width do exist in both polytypes. From a view point of epitaxial growth, narrow terraces are preferable to achieve step-flow growth. This is crucial in SiC growth, because the nucleation on terraces leads to the growth of 3C-SiC. In this sense, 4H-SiC, which shows a larger terrace width, may have a disadvantage of relatively higher probability for nucleation on terraces. To overcome this problem, a slightly higher growth temperature would be helpful, since the longer surface diffusion length of adsorbed species and lower supersaturation on terraces are expected at higher temperatures. Larger off-angles of substrates might be also effective in 4H-SiC growth.

Figure 3.19 shows cross-sectional TEM images for surfaces of (a) 6H-SiC and (b) 4H-SiC epilayers grown on $(000\bar{1})$ C faces 3.5° off-oriented toward $[11\bar{2}0]$. In contrast to the bunched steps on Si faces, single Si-C bilayer-height steps are dominant on C faces for both polytypes. The histograms of step height for the surfaces of (a) 6H-SiC and (b) 4H-SiC epilayers on a C face are shown in Fig.3.20. Single bilayer-height steps show the highest probability of 70~80%. The origin of this striking polarity dependence is not known. The migrating species, surface coverage, and exact bond configuration at step edges should be analyzed to reveal the mechanism. However, small amount of

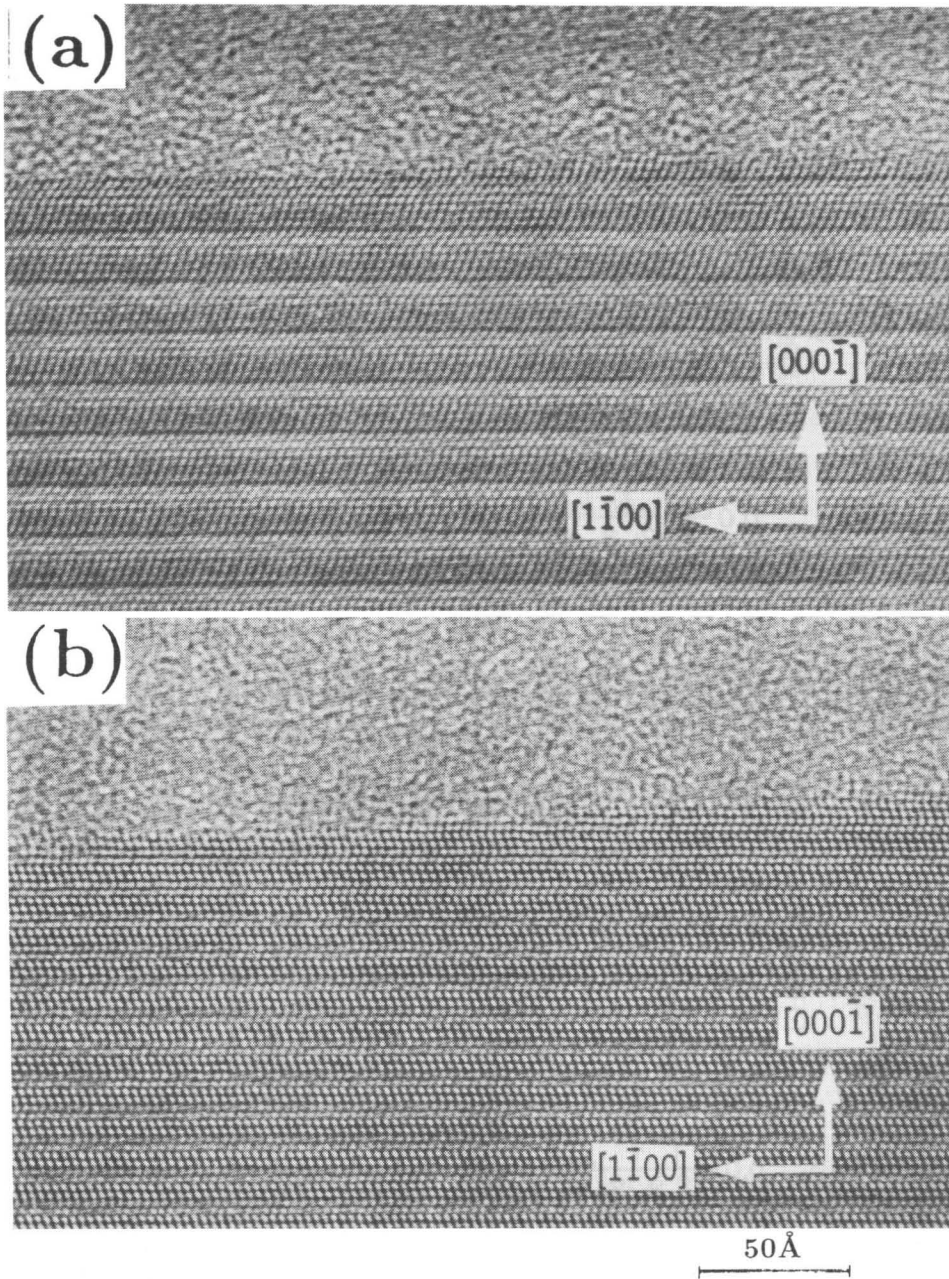
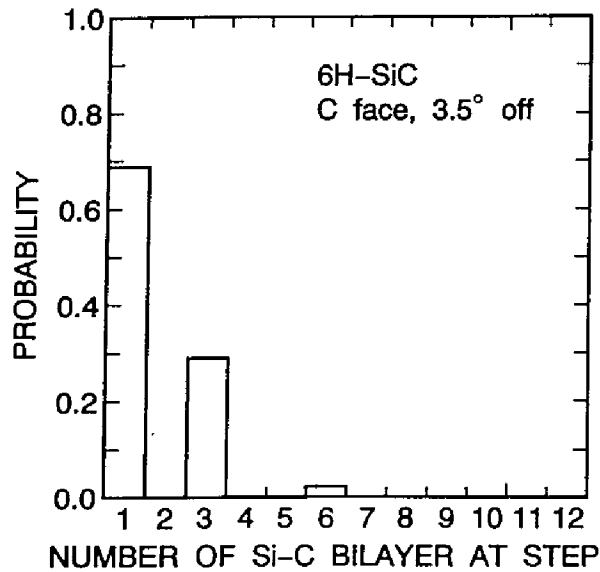
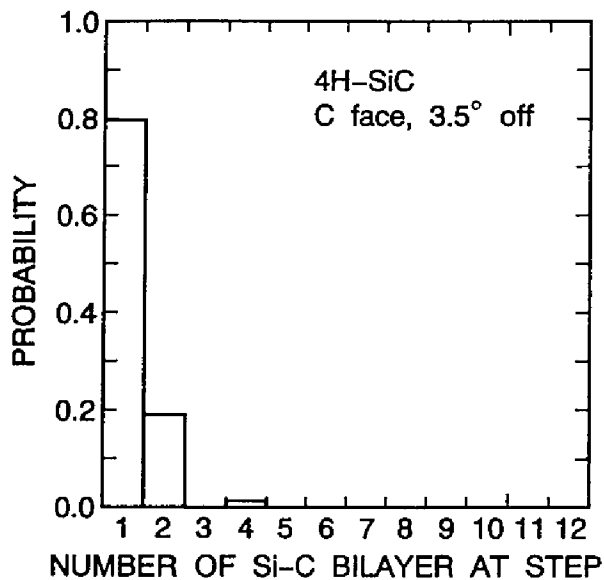


Fig.3.19 Typical cross-sectional TEM images for the surfaces of (a) 6H-SiC and (b) 4H-SiC epilayers. Substrates are $(000\bar{1})\text{C}$ 3.5° off-oriented toward $[11\bar{2}0]$. Samples are examined along the $[2\bar{1}\bar{1}0]$ zone axis.



(a)



(b)

Fig.3.20 Histograms of step height for the surfaces of (a) 6H-SiC and (b) 4H-SiC epilayers. Substrates are $(000\bar{1})\text{C}$ 3.5° off-oriented toward $(11\bar{2}0)$.

bunched steps have, again, 3 or 6 bilayer height in 6H-SiC, and 2 or 4 bilayer height in 4H-SiC.

3.3.3 Discussion

As for the mechanism of step bunching, several models have been proposed. Frank explained that impurity atoms adsorbed on a terrace impede the step advance, initiating the step bunching [36]. Schwoebel and Shipsey proposed an interesting model to explain step motion (Fig.3.21) [37]. According to their model, the step motion is determined by the incorporation probabilities of adsorbed species at the up-step site (γ_-) and down-step site (γ_+). When $\gamma_+ > \gamma_-$, an arbitrary initial distribution of step spacing tends toward a sequence of uniformly spaced steps, while for $\gamma_+ < \gamma_-$, individual steps coalesce into steps of multiple height (Schwoebel effect) [37,38]. On the other hand, another idea has been proposed that step bunching is a kind of the surface equilibrium process in which the free energy is minimized during crystal growth [39-41].

Since SiC epilayers are undoped with a N donor concentration of below 10^{16}cm^{-3} in the present case, the impurity effect can be neglected. Although the Schwoebel effect might be concerned with the present step bunching, real crystal surface seems to satisfy $\gamma_+ > \gamma_-$. Figure 3.21 shows a hypothetical potential associated with surface diffusion [37]. The adsorbed species which approach from the left of a step must surpass a potential barrier to be incorporated at the step, suggesting $\gamma_+ > \gamma_-$. This leads to the formation of uniform step distribution owing to a pseudorepulsive interaction between steps. Besides, this effect has difficulty to explain why 3 Si-C bilayer-height steps are dominant in 6H-SiC and 4 Si-C bilayer-height steps in 4H-SiC. Thus, the step bunching mechanism is discussed from a viewpoint of the surface equilibrium process, in the followings.

The mechanism of "apparent macrostep" formation on 6H- and 4H-SiC (0001)Si faces (Fig.3.12(a) and Fig.3.13(a)) is not clear at present. However, the surface is quite similar to so-called "hill-and-valley (or faceted)" structure, which often appears on grown surfaces with off-orientation from a low-index plane [39-41]. The off-oriented surfaces will spontaneously rearrange to min-

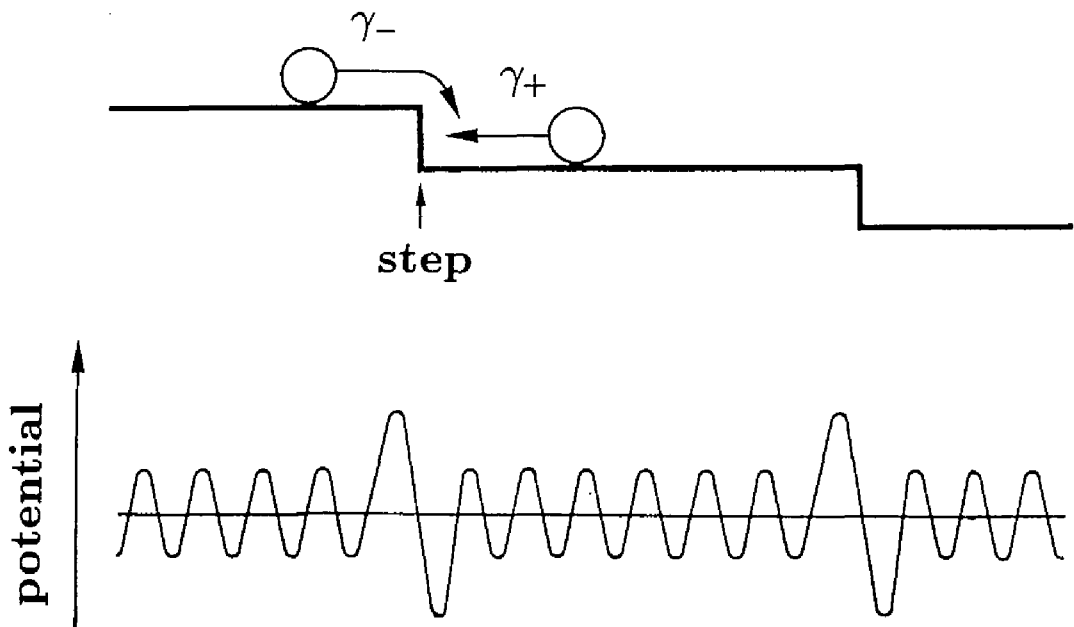


Fig.3.21 Schematic illustration of surface steps explaining the Schwoebel effect [37]. Migrating species are captured at steps with incorporation probabilities of γ_- and γ_+ , depending on the direction from which the species approach. A hypothetical potential for adsorbed species is also shown.

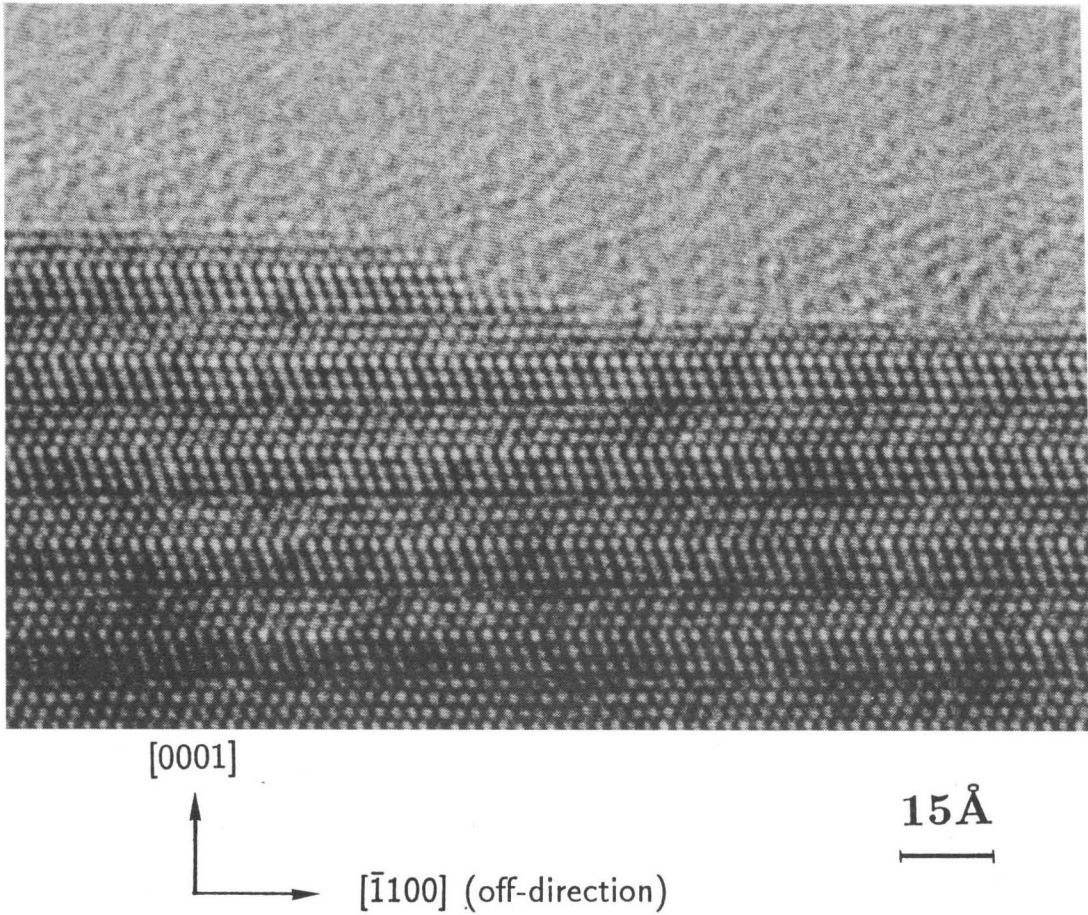


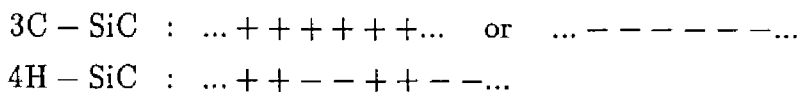
Fig.3.22 Typical cross-sectional TEM image of the surface of a 6H-SiC epilayer. The substrate is $(0001)\text{Si}$ 5° off-oriented toward $[1\bar{1}00]$. The sample is examined along the $[11\bar{2}0]$ zone axis.

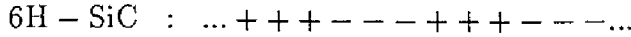
imize their total surface energies, even if this involves an increase in surface area. Pearson *et al.* calculated the surface free energies of SiC as 2220erg/cm² for the (0001)Si face and 300erg/cm² for the (000 $\bar{1}$)C face [42]. Thus, the surface energy may be reduced by the formation of "hill-and-valley" structure on off-oriented (0001)Si, which has much higher surface energy. If the orientation dependence of surface energy is given, quantitative analyses can be made based on the Wulff's construction [39,41,43]. However, the lack of detailed surface energy for SiC prevents further analyses.

As shown in Figs.3.17 and 3.20, the formation of 3 or 6 bilayer-height steps seems to be inherent in 6H-SiC growth, and 2 or 4 bilayer-height steps in 4H-SiC growth. Similar observation has been reported on 6H-SiC surfaces grown by the Lely method [16] and MBE [18]. In order to clarify the origin of step-height difference between two polytypes, cross-sectional TEM observation was done along the [11 $\bar{2}$ 0] zone axis, by which clear lattice images can be obtained. Here, epilayers were grown on substrates off-oriented toward [1 $\bar{1}$ 00] to examine along the direction perpendicular to the off-direction. A TEM image of a 6H-SiC epilayer is shown in Fig.3.22. In this case, 6 bilayer-height steps are composed of ABCACB layer steps, which correspond to exactly the unit cell.

As mentioned above, the origin of step bunching may be correlated with the surface equilibrium process. Heine *et al.* showed that surface energies are different for each SiC bilayer plane owing to the peculiar stacking sequence [44]. Based on this model, Chien *et al.* studied the growth mechanism on α -SiC{0001}, and reported that possible step bunching in 6H-SiC is the formation of 3 bilayer-height steps (ABC or ACB layer steps) [45]. Here, this model is introduced, and is applied to the growth of 6H- and 4H-SiC.

SiC polytypes can be represented by the different stacking sequence along the (0001) direction. Each Si-C layer is stacked in two different orientations on the layer below it, and the orientation for the n th layer can be designated by the symbol $\sigma_n = \pm 1$ [44]. For example, 3C-, 4H-, and 6H-SiC can be expressed by





The total energy per unit Si-C pair can be given by [44]

$$U = E_0 - J_1\sigma_n\sigma_{n+1} - J_2\sigma_n\sigma_{n+2} - J_3\sigma_n\sigma_{n+3} - K\sigma_n\sigma_{n+1}\sigma_{n+2}\sigma_{n+3}, \quad (3.12)$$

where E_0 is the energy of the crystal without interaction between layers, J_n the energy of interaction between n th neighbor planes, and K the coefficient of the four-spin coupling term that can be interpreted as a modification of the third-neighbor interaction. From the fitting of total energies for several SiC polytypes, these parameters were given as follows (in meV per Si-C pair atoms):

$$J_1 = 4.40, \quad J_2 = -2.56, \quad J_3 = -0.05, \quad K = -0.45. \quad (3.13)$$

Using eqs.(3.12) and (3.13), total energies for popular polytypes are calculated:

$$U(2H) = E_0 + J_1 - J_2 + J_3 - K = E_0 + 7.36, \quad (3.14)$$

$$U(3C) = E_0 - J_1 - J_2 - J_3 - K = E_0 - 1.34, \quad (3.15)$$

$$U(4H) = E_0 - J_2 - K = E_0 + 3.01, \quad (3.16)$$

$$U(6H) = E_0 - \frac{1}{3}J_1 + \frac{1}{3}J_2 + J_3 + \frac{1}{3}K = E_0 - 2.52, \quad (3.17)$$

which means

$$U(6H) < U(3C) < U(4H) < U(2H). \quad (3.18)$$

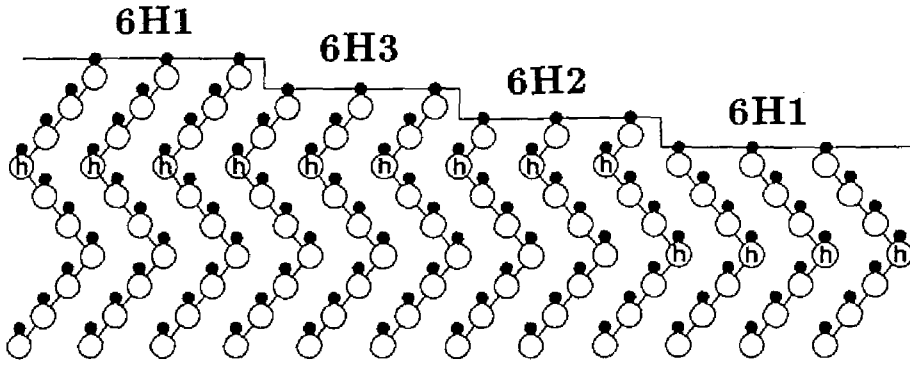
Next, consider adding one new layer (σ_{new}) on a surface layer (σ_s), without allowing the underlying layers (σ_{s-1} , σ_{s-2}) to change. From eq.(3.12), the extra energy ΔU for adding one new layer can be written by

$$\Delta U = E_0 - J^*\sigma_{\text{new}}\sigma_s, \quad (3.19)$$

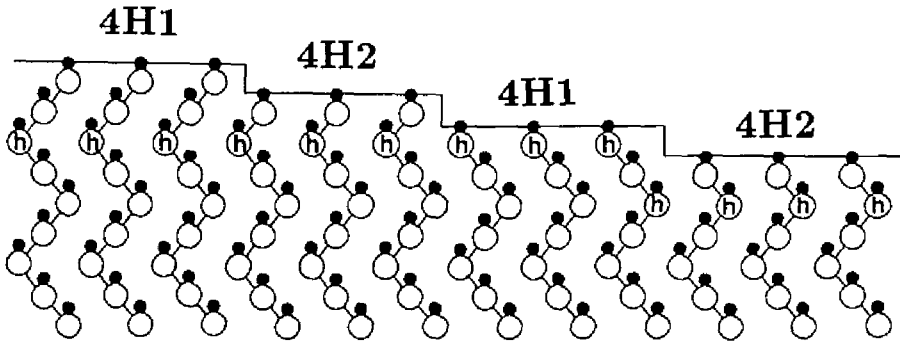
where

$$J^* = J_1 + J_2\sigma_s\sigma_{s-1} + J_3\sigma_s\sigma_{s-2} + K\sigma_{s-1}\sigma_{s-2}. \quad (3.20)$$

Using this equation, the sites favorable in total energy can be predicted in crystal growth on SiC{0001} faces [44,45].



(a)



(b)

Fig.3.23 Possible terraces on (a) 6H-SiC and (b) 4H-SiC{0001} surfaces. h in a white circle denotes a hexagonal site.

There exist several types of terraces on SiC{0001}, as illustrated in Fig.3.23. 6H-SiC has three distinct terraces 6H1, 6H2, and 6H3, and 4H-SiC does two terraces 4H1 and 4H2. The J^* values for these terraces can be calculated as follows.

6H-SiC:

$$J^*(6H1) = 1.33\text{meV} \quad (3.21)$$

$$J^*(6H2) = 6.56\text{meV} \quad (3.22)$$

$$J^*(6H3) = 2.34\text{meV} \quad (3.23)$$

4H-SiC:

$$J^*(4H1) = 2.34\text{meV} \quad (3.24)$$

$$J^*(4H2) = 6.56\text{meV} \quad (3.25)$$

Here, it is assumed that homoepitaxy is realized owing to step-flow growth. Then, the extra energies for depositing one new layer on the terraces are obtained from eq.(3.19).

6H-SiC:

$$6H1 \quad \text{terrace} \quad \Delta U = E_0 + 1.33 \quad (3.26)$$

$$6H2 \quad \text{terrace} \quad \Delta U = E_0 - 6.56 \quad (3.27)$$

$$6H3 \quad \text{terrace} \quad \Delta U = E_0 - 2.34 \quad (3.28)$$

4H-SiC:

$$4H1 \quad \text{terrace} \quad \Delta U = E_0 + 2.34 \quad (3.29)$$

$$4H2 \quad \text{terrace} \quad \Delta U = E_0 - 6.56 \quad (3.30)$$

In 6H-SiC, deposition on 6H2 terraces is the most favorable, and that on 6H1 terraces is the most costly from a viewpoint of total energy. Therefore, the

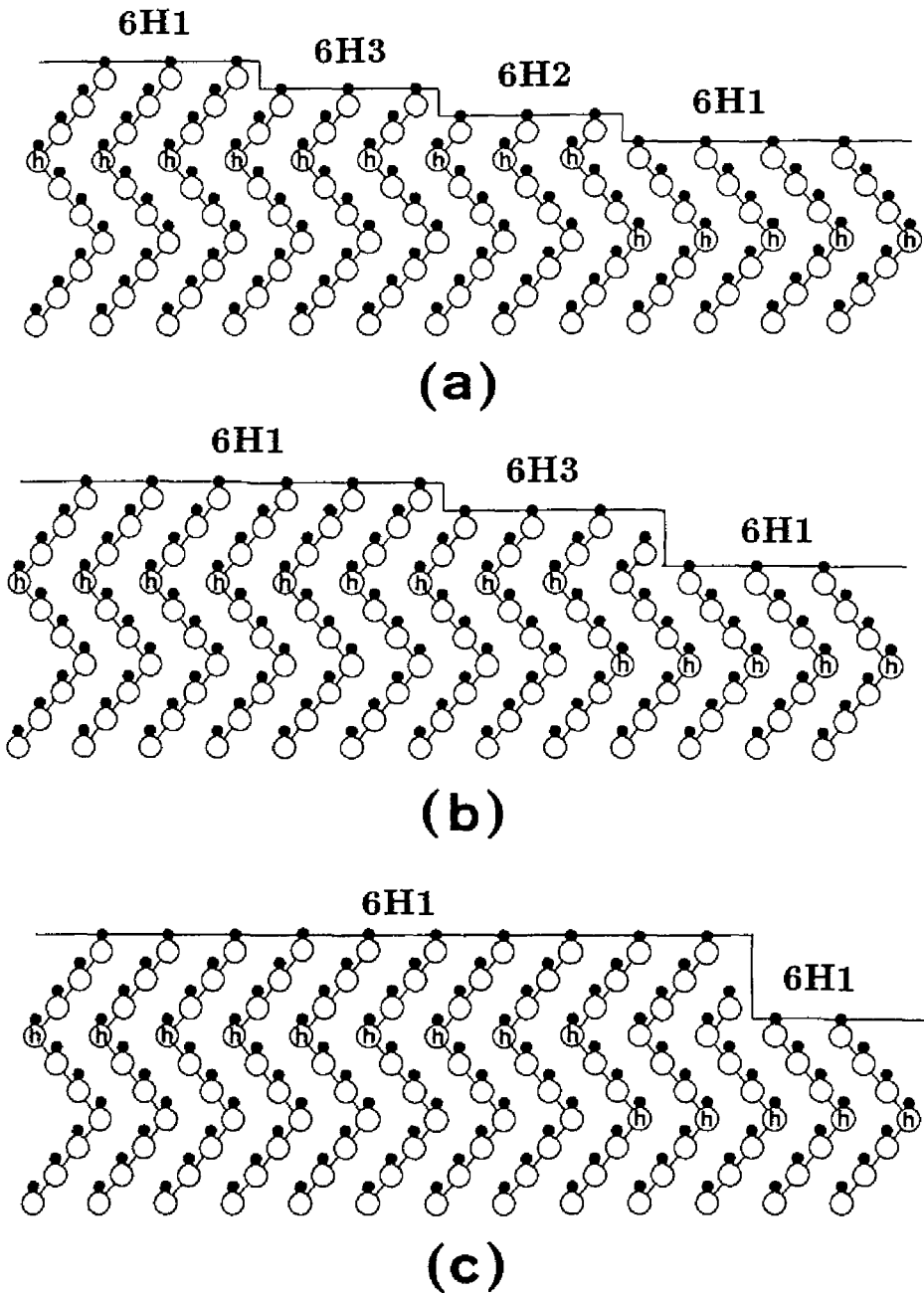


Fig.3.24 Illustration of step bunching in 6H-SiC growth. (a) initial, (b) transient, and (c) formation of 3 bilayer-height steps.

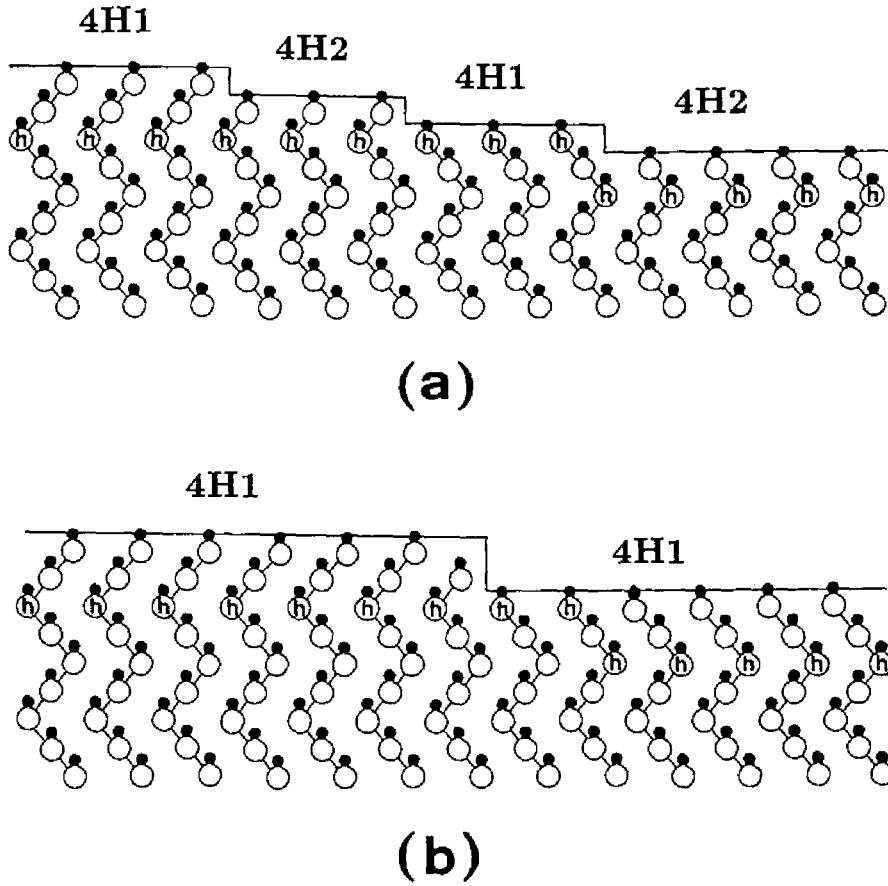


Fig.3.25 Illustration of step bunching in 4H-SiC growth. (a) initial and (b) formation of 2 bilayer-height steps.

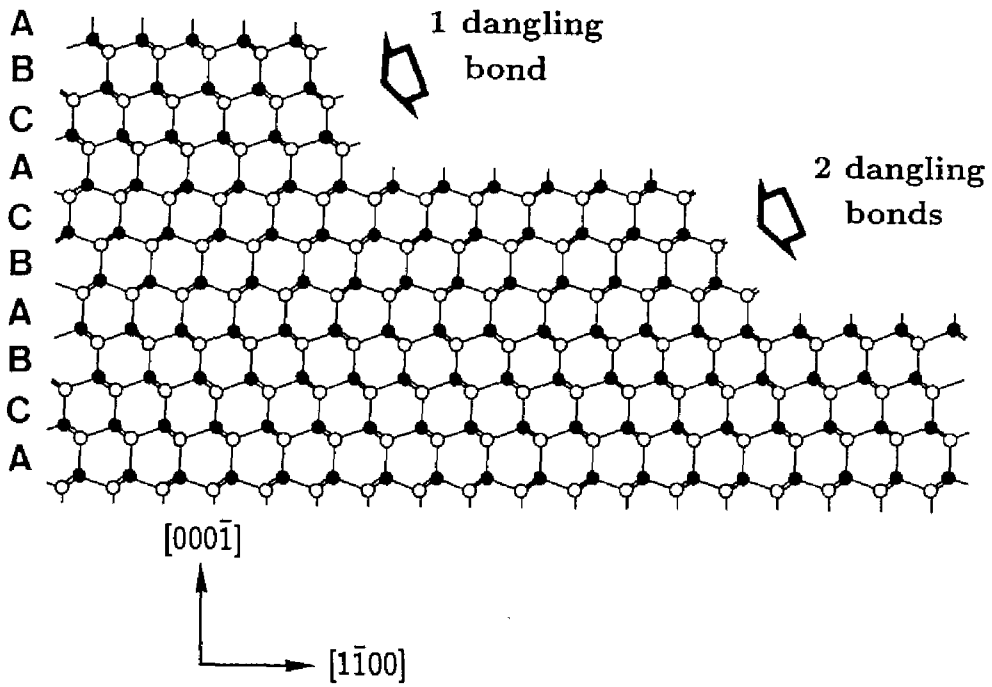


Fig.3.26 Bond configuration of a 6H-SiC{0001} surface with 3 bilayer-height steps.

step velocity may be the fastest on 6H2 terrace due to preferential deposition on the terraces. The steps on 6H2 terraces overtake the steps on 6H1 terraces, forming 2 bilayer steps, as shown in Fig.3.24. Since the step velocity is inversely proportional to the step height, the steps on 6H3 terraces subsequently overtake the 2 bilayer steps, thereby forming 3 bilayer-height steps. Thus, 3 bilayer-height steps with ABC or ACB layers do emerge. Similar mechanism is expected in 4H-SiC growth, as shown in Fig.3.25. The step velocity may be faster on 4H2 terraces than on 4H1 terraces, which creates 2 bilayer-height steps with AB or CB stacking.

Further development of multiple steps into 6 bilayer-height steps in 6H-SiC may result from the different sticking probability at ABC steps and ACB steps due to the different number of dangling bonds at the steps [46]. Figure 3.26 shows the bond configuration of an off-oriented 6H-SiC{0001} surface with 3 bilayer-height steps. Note that a ACB step has only one dangling bond per edge atom, whereas a ABC step does two dangling bonds. In the same manner, it can be derived that 2 bilayer-height steps (AB or CB steps) develop into 4 bilayer-height steps in 4H-SiC (stacking sequence:ABCB).

According to this idea, the bunched steps may have 6 bilayer-height in 6H-SiC and 4 bilayer-height in 4H-SiC in the final stage. In our observation, however, the formation of multi-steps with a unit-cell height takes place frequently in 4H-SiC growth, and not in 6H-SiC growth (6 bilayer-height steps are relatively few). Although this origin is not clear at present, one possible reason is the difference in the average terrace width between 6H- and 4H-SiC. According to the model shown in Figs. 3.24 and 3.25, steps with the half unit-cell height may be formed at first. After this step bunching, the average terrace width is narrower on 4H-SiC than on 6H-SiC due to the different step height. On 3.5°-off {0001} substrates, for example, the average terrace width with 2 bilayer-height steps (4H-SiC) is 8.2nm, whereas the width with 3 bilayer-height steps (6H-SiC) is 12.4nm. The closer step distribution on 4H-SiC surface may lead to the higher probability for a step to meet the nearest neighbor step, resulting in the formation of bunched steps with the unit-cell height. In general, the step bunching probability strongly depends on the undulation of step edges. Further investigations on step structure and theoretical analyses are required.

3.4 Summary

Growth mechanism of epitaxial growth of SiC on off-oriented 6H-SiC (0001)Si and (000 $\bar{1}$)C faces was studied in detail. Significant effects of C/Si ratio on surface morphology of grown layers and growth rate were observed. The growth rate was limited by the supply of Si species. The crystal growth may proceed through the incorporation of Si species at atomic steps and their carbonization by hydrocarbon molecules. A very small activation energy of growth rate (2.8kcal/mole) was obtained. This can be quantitatively interpreted based on a stagnant layer model in which crystal growth is controlled by the diffusion of reactants. Step-flow growth, which does not need two-dimensional nucleation, is controlled by mass transport. This is consistent with little difference in the growth rates on off-oriented Si and C faces. The condensation coefficient was estimated as 0.9 ± 0.05 on substrates with off-angle of more than 3° .

Step bunching on 6H- and 4H-SiC epilayers grown on off-oriented {0001} faces was investigated with AFM and TEM. Macroscopically, hill-and-valley structures were observed on off-oriented (0001)Si faces, whereas surfaces were rather flat on off-oriented (000 $\bar{1}$)C faces. On a Si face, 3 bilayer-height steps were the most dominant on 6H-SiC and 4 bilayer-height steps on 4H-SiC. In contrast, single bilayer-height steps showed the highest probability on a C face. The distribution of step height and terrace width was presented. For the same off-angle, the terrace width is wider on 4H-SiC, due to the larger step height. The mechanism of step bunching was discussed with consideration of surface equilibrium process.

References

- [1] D.J.Larkin, P.G.Neudeck, J.A.Powell, and L.G.Matus, *Silicon Carbide and Related Materials*, M.G.Spencer, R.P.Devaty, J.A.Edmond, M.A.Khan, R.Kaplan, M.M.Rahman, Eds., (Inst. of Physics, Bristol, 1994), p.51.
- [2] A.A.Burk, Jr., D.L.Barrett, H.M.Hobgood, R.R.Siergiej, D.J.Larkin, J.A.Powell, and W.J.Choyke, *Silicon Carbide and Related Materials*, M.G.Spencer, R.P.Devaty, J.A.Edmond, M.A.Khan, R.Kaplan, M.M.Rahman, Eds., (Inst.

- of Physics, Bristol, 1994), p.29.
- [3] O.Kordina, A.Henry, C.Hallin, R.C.Glass, A.O.Konstantinov, C.Hemmingsson, N.T.Son, and E.Janzén, *Mat. Res. Soc. Sympo. Proc.*, **339**, 405(1994).
 - [4] R.Rupp, P.Lanig, J.Völkl, D.Stephani, *J. Crystal Growth*, **146**, 37(1995).
 - [5] N.Kuroda, K.Shibahara, W.S.Yoo, S.Nishino and H.Matsunami, *Extended Abstracts of the 19th Conf. on Solid State Devices and Materials*, Tokyo(1987), p.227.
 - [6] H.S.Kong, J.T.Glass and R.F.Davis, *J. Appl. Phys.*, **64**, 2672(1988).
 - [7] J.A.Powell, D.J.Larkin, L.G.Matus, W.J.Choyke, J.L.Bradshaw, L.Henderson, M.Yoganathan, J.Yang and P.Pirouz, *Appl. Phys. Lett.*, **56**, 1442(1990).
 - [8] T.Ueda, H.Nishino and H.Matsunami, *J. Crystal Growth*, **104**, 695(1990).
 - [9] H.Matsunami, T.Ueda and H.Nishino, *Mat. Res. Soc. Symp. Proc.*, **162**, 397(1990).
 - [10] Y.C.Wang and R.F.Davis, *J. Electron. Mat.*, **20**, 869(1991).
 - [11] X.S.Wang, J.L.Goldberg, N.C.Bartelt, T.L.Einstein, and E.D.Williams, *Phys. Rev. Lett.*, **65**, 2430(1990).
 - [12] M.Kasu and N.Kobayashi, *Appl. Phys. Lett.*, **62**, 1262(1993).
 - [13] S.L.Skala, S.T.Chou, K.Y.Cheng, J.R.Tucker, and J.W.Lyding, *Appl. Phys. Lett.*, **65**, 722(1994).
 - [14] C.S.Chang, I.S.T.Tsong, Y.C.Wang, and R.F.Davis, *Surf. Sci.*, **256**, 354(1991).
 - [15] A.J.Steckl, M.D.Roth, J.A.Powell, and D.J.Larkin, *Appl. Phys. Lett.*, **62**, 2545(1993).
 - [16] S.Tyc, *Silicon Carbide and Related Materials*, M.G.Spencer, R.P.Devaty, J.A.Edmond, M.A.Khan, R.Kaplan, M.M.Rahman, Eds., (Inst. of Physics, Bristol, 1994), p.333.
 - [17] M.A.Kulakov, P.Heuell, V.F.Tsvetkov, and B.Bullemer, *Surf. Sci.*, **315**, 248(1994).
 - [18] S.Tanaka, R.S.Kern, and R.F.Davis, *Appl. Phys. Lett.*, **65**, 2851(1994).
 - [19] G.B.Stringfellow, *Organometallic Vapor Phase Epitaxy: Theory and Practice* (Academic Press, San Diego, 1989).
 - [20] B.Wessels, H.C.Gatos and A.F.Witt, *Silicon Carbide 1973*, R.C.Marshall, J.W.Faust,Jr. and C.E.Ryan, Eds., (University of South Carolina Press, Columbia, 1974), p.25.
 - [21] M.D.Allendorf and R.J.Kee, *J. Electrochem. Soc.*, **138**, 841(1991).
 - [22] C.D.Stinespring and J.C.Wormhoudt, *J. Crystal Growth*, **87**, 481(1988).
 - [23] T.Yoshinobu, M.Nakayama, H.Shiomi, T.Fuyuki and H.Matsunami, *J. Crystal Growth*, **99**, 520(1990).
 - [24] H.S.Kong, J.T.Glass, and R.F.Davis, *J. Mater. Res.*, **4**, 204(1989).
 - [25] T.Kimoto and H.Matsunami, *J. Appl. Phys.*, **76**, 7322(1994).
 - [26] V.J.Jennings, A.Sommer and H.C.Chang, *J. Electrochem. Soc.*, **113**, 728(1966).

- [27] S.Karmann, C.Haberstroh, F.Engelbrecht, W.Suttrop, A.Schöner, M.Schadt, R.Helbig, G.Pensl, R.A.Stein, and S.Leibenzeder, *Physica B*, **185**, 75(1993).
- [28] D.W.Shaw, *Crystal Growth - Theory and Techniques Vol.1*, C.H.L.Goodman Ed., (Plenum Press, London, 1974), Chapt.1.
- [29] W.K.Burton, N.Cabrera and F.C.Frank, *Philos. Trans. Roy. Soc. London*, **A243**, 299(1951).
- [30] B.A.Joyce, R.R.Bradley and G.R.Booker, *Phil. Mag.*, **15**, 1167(1967).
- [31] Y.W.Mo, J.Kleiner, M.B.Webb and M.G.Lagally, *Phys. Rev. Lett.*, **66**, 1998(1991).
- [32] G.Brocks, P.J.Kelly and R.Car, *Phys. Rev. Lett.*, **66**, 1729(1991).
- [33] F.C.Eversteyn, P.J.W.Severin, C.H.J.v.d.Brekel and H.L.PEEK, *J. Electrochem. Soc.*, **117**, 925(1970).
- [34] R.M.Olsen, *Essentials of Engineering Fluid Flow* (International Textbook, Scranton, Pennsylvania, 1966).
- [35] *CRC Handbook of Chemistry and Physics*, R.C.Weast Ed. (CRC Press, Boca Raton, 1975).
- [36] F.C.Frank, *Growth and Perfection of Crystals*, R.H.Doremus, B.W.Roberts, and D.Turnbull, Eds., (Wiley, New York, 1958), p.411.
- [37] R.L.Schwoebel and E.J.Shipsey, *J. Appl. Phys.*, **37**, 3682(1966).
- [38] Y.Tokura, H.Saito, and T.Fukui, *J. Crystal Growth*, **94**, 46(1989).
- [39] C.Herring, *Phys. Rev.*, **82**, 87(1951).
- [40] W.A.Tiller, *The Science of Crystalization: Microscopic Interfacial Phenomena*, (Cambridge Univ. Press, Cambridge, 1991), Chapt.2.
- [41] E.D.Williams, R.J.Phaneuf, J.Weil, N.C.Bartelt, and T.L.Einstein, *Surf. Sci.*, **294**, 219(1993).
- [42] E.Pearson, T.Takai, T.Halicioglu and W.A.Tiller, *J. Crystal Growth*, **70**, 33(1984).
- [43] G.Wulff, *Z. Kristallogr.*, **34**, 449(1901).
- [44] V.Heine, C.Cheng, and R.J.Needs, *J. Am. Ceram. Soc.*, **74**, 2630(1991).
- [45] F.R.Chien, S.R.Nutt, W.S.Yoo, T.Kimoto, and H.Matsunami, *J. Mater. Res.*, **9**, 940(1994).
- [46] P.Heuell, M.A.Kulakov, and B.Bullemer, *Silicon Carbide and Related Materials*, M.G.Spencer, R.P.Devaty, J.A.Edmond, M.A.Khan, R.Kaplan, M.M.Rahman, Eds., (Inst. of Physics, Bristol, 1994), p.353.

Chapter 4

Critical Growth Conditions for Step-Controlled Epitaxy

4.1 Introduction

Step-flow growth has been one of the most attractive subjects from a viewpoint of crystal growth. Since Burton, Cabrera, and Frank (BCF) laid theoretical foundation (BCF theory) on dynamics of atomic steps [1], several modifications of the BCF theory [2-4] and applications to molecular beam epitaxy (MBE) of Si [5,6] and GaAs [7] have been studied. In these reports, condensation coefficients [6] or surface diffusion lengths of adatoms [7] were investigated by applying the theory to experimental results. More recently, there has been growing interest in step kinetics, because the performance of some semiconductor devices has been improved by the introduction of substrate's off-orientation [8,9]. Surface diffusion lengths of adatoms [7,10] and step structures [11,12] have been discussed through in-situ RHEED and STM observation.

Growth mode, rate-determining step and step structure in step-controlled epitaxy of SiC were discussed in the previous chapter. However, very little is known about microscopic mechanism in crystal growth of SiC. Besides, one may have a question: How or under which conditions can we achieve step-flow growth?

In this chapter, vapor phase epitaxial growth of SiC on off-oriented 6H-SiC{0001} substrates is quantitatively analyzed based on the BCF theory with some modifications. The effects of surface polarity on surface diffusion lengths of adsorbed species and nucleation rates are described in detail. Surface reactions and step-flow growth conditions are discussed based on the results.

4.2 Growth Model on Vicinal Substrates

A simple surface diffusion model is considered, where steps with a height h are separated by an equal distance λ_0 as shown in Fig.4.1. In the present system, reactants arriving at a crystal surface are thermally decomposed and adsorbed. The adsorbed species diffuse on terraces toward steps. Some of the adsorbed species can reach steps and are incorporated into the crystal, and the others reevaporate to vapor. Some species will coalesce to form nuclei if supersaturation on terraces is high enough.

When nucleation on terraces does not occur, the effective incoming flux onto the surface should be equal to the diffusion flux toward steps. Then, the continuity equation of adsorbed species is expressed by [1]

$$-D_s \frac{d^2 n_s(y)}{dy^2} = J - \frac{n_s(y)}{\tau_s}, \quad (4.1)$$

where $n_s(y)$ is the number of adsorbed species per unit area on the surface (hereafter, $n_s(y)$ is described as adatom concentration), J the flux of reactants arriving at the surface, τ_s the mean residence time of adsorbed species, and D_s the surface diffusion coefficient. Here, the steps are assumed as uniform and perfect sinks for the incoming species, that is, the capture probability of adsorbed species at steps is unity, independent of the direction from which adsorbed species approach the steps. Reflection of impinging reactants on the surface is neglected (the sticking coefficient is assumed to be unity). This assumption is valid in the present system, because the condensation coefficient is about 0.9 as discussed in 3.2.4. Under the boundary condition that the supersaturation ratio α ($=n_s/n_{s0}$) equals unity at steps; $n_s=n_{s0}$ at $y=\pm\lambda_0/2$,

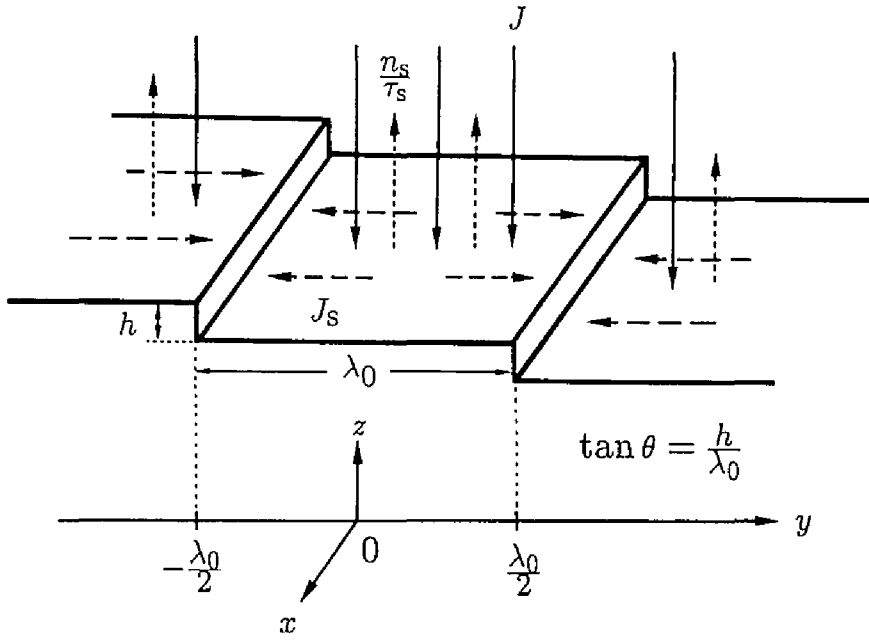


Fig.4.1 Schematic illustration of simple surface diffusion model, where steps with a height h are separated by an equal distance λ_0 .

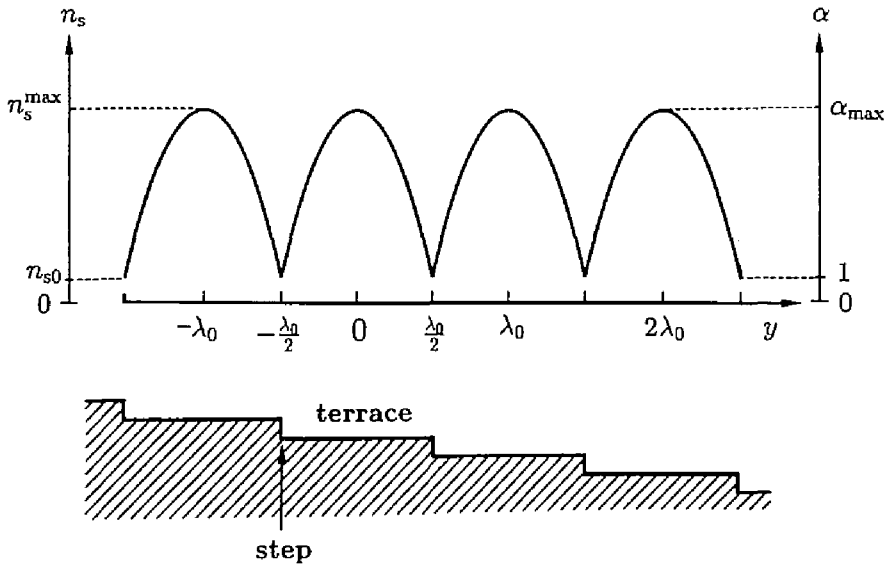


Fig.4.2 The distribution of adatom concentration and supersaturation ratio $\alpha (=n_s/n_{s0})$ on off-oriented surface.

the adatom concentration on the terraces can be given as a solution of eq.(4.1):

$$n_s(y) = J\tau_s + (n_{s0} - J\tau_s) \frac{\cosh(y/\lambda_s)}{\cosh(\lambda_0/2\lambda_s)}, \quad (4.2)$$

where n_{s0} is the adatom concentration at equilibrium, and λ_s is the surface diffusion length of adsorbed species, which is given by the following equation [1]:

$$\lambda_s = \sqrt{D_s\tau_s} = a \exp\left(\frac{E_{\text{des}} - E_{\text{diff}}}{2kT}\right). \quad (4.3)$$

Here, a , k , and T are the jump distance (interatomic distance), Boltzmann constant, and absolute temperature, respectively. E_{des} and E_{diff} are the activation energies for desorption and surface diffusion. This λ_s is an average length for adsorbed species to migrate on a "step-free" surface before desorption.

The flow of adsorbed species in the y direction $J_s(y)$ is given by [1]

$$J_s(y) = -D_s \frac{dn_s(y)}{dy} = \lambda_s \left(J - \frac{n_{s0}}{\tau_s}\right) \frac{\sinh(y/\lambda_s)}{\cosh(\lambda_0/2\lambda_s)}. \quad (4.4)$$

Since the capture probability of migrating species at steps is assumed to be unity, the step velocity v_{step} is given by the following equation using the $J_s(y)$ at steps ($y=\lambda_0/2$);

$$v_{\text{step}} = 2 \frac{J_s(y)}{n_0} \Big|_{y=\lambda_0/2} = \frac{2\lambda_s}{n_0} \left(J - \frac{n_{s0}}{\tau_s}\right) \tanh\left(\frac{\lambda_0}{2\lambda_s}\right). \quad (4.5)$$

Here, n_0 is the density of adatom sites on the surface, and migrating species from both the left and right sides of steps are considered. In step-flow growth, the growth rate (R) is given by the product of the step velocity and $\tan\theta$ ($=h/\lambda_0$), where θ is the off-angle of a substrate. Thus, the following equation is satisfied.

$$R = v_{\text{step}} \tan\theta = \frac{2h\lambda_s}{n_0\lambda_0} \left(J - \frac{n_{s0}}{\tau_s}\right) \tanh\left(\frac{\lambda_0}{2\lambda_s}\right). \quad (4.6)$$

Figure 4.2 shows the distribution of adatom concentration and the supersaturation ratio (α) on a surface. Since α takes a maximum value α_{max} at the center of a terrace, nucleation occurs most easily at this position. Based on eqs.(4.2) and (4.6), α_{max} can be expressed by

$$\alpha_{\text{max}} = 1 + \frac{\lambda_0 n_0 R \tau_s}{2\lambda_s h n_{s0}} \tanh\left(\frac{\lambda_0}{4\lambda_s}\right). \quad (4.7)$$

The α_{\max} depends on experimental conditions such as growth rate, growth temperature, and terrace width. This α_{\max} is an essential parameter which determines whether the growth mode is step-flow or two-dimensional nucleation.

Since a two-dimensional nucleation rate J_{nuc} increases exponentially with the supersaturation ratio on a surface, nucleation becomes significant when α_{\max} exceeds a critical value α_{crit} . Thus, the growth modes are determined according to the relationship between α_{\max} and α_{crit} as follows;

$$\alpha_{\max} > \alpha_{\text{crit}} \quad ; \quad \text{two - dimensional nucleation,} \quad (4.8)$$

$$\alpha_{\max} < \alpha_{\text{crit}} \quad ; \quad \text{step - flow.} \quad (4.9)$$

Under the critical condition, the following equation is satisfied,

$$\alpha_{\max} = \alpha_{\text{crit}}. \quad (4.10)$$

Using eq.(4.7), the above equation can be rearranged as,

$$\frac{\lambda_0}{4\lambda_s} \tanh\left(\frac{\lambda_0}{4\lambda_s}\right) = \frac{(\alpha_{\text{crit}} - 1)h n_{s0}}{2n_0 R \tau_s}. \quad (4.11)$$

This is the basic equation which describes the growth mode. In eq.(4.11), R and λ_0 are determined by growth conditions, and n_0 and h are inherent parameters of a material. If the values of n_{s0}/τ_s and α_{crit} are known, λ_s can be calculated from eq.(4.11). Then, by finding out the critical condition experimentally, the surface diffusion length can be estimated.

4.3 Application to SiC growth

4.3.1 Desorption flux n_{s0}/τ_s

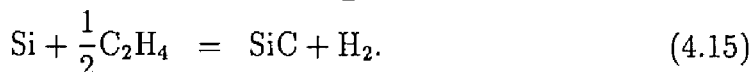
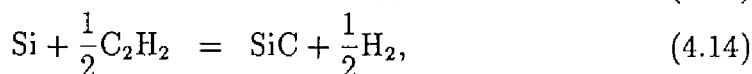
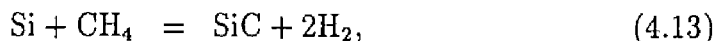
As described in section 4.2, n_{s0}/τ_s has to be known for evaluation of the surface diffusion length by the use of eq.(4.11), but n_{s0}/τ_s in the SiC growth system has never been reported. Although it is difficult to estimate n_{s0} and τ_s independently, n_{s0}/τ_s can be calculated from the equilibrium vapor pressure P_0 using the Knudsen's equation from the kinetic theory of gasses [13];

$$\frac{n_{s0}}{\tau_s} = \frac{P_0}{\sqrt{2\pi mkT}}, \quad (4.12)$$

where m is the mass of concerned species. Here, P_0 can be calculated from the chemical equilibrium constants of the reaction system.

It is complicated to define P_0 in a growth system of compound materials, because the chemical reactions of two elemental species are concerned in the growth. In the case of MBE of GaAs, P_0 has been approximated as an equilibrium vapor pressure of Ga in the reaction of $\text{Ga} + \frac{1}{2}\text{As}_2 = \text{GaAs}$ or $\text{Ga} + \frac{1}{4}\text{As}_4 = \text{GaAs}$, based on the fact that the growth rate is limited by the supply of Ga atoms under the As-rich condition [7,10]. In the present growth system, the supply of Si species controls the growth (see the subsection 3.2.1). A study on gas source MBE of SiC has also shown that the SiC growth is limited by the supply of Si species, and the reaction between adsorbed Si atoms on a surface and hydrocarbon molecules is essential to the growth of SiC [14]. Then, P_0 in SiC growth can be assumed to be an equilibrium vapor pressure of Si species in surface reactions.

As for the reaction species in CVD growth of SiC, thermodynamic analyses on gas phase kinetics at 1200~1600°C in a $\text{SiH}_4\text{-C}_3\text{H}_8\text{-H}_2$ system showed that dominant species impinging on the surface were Si and SiH_2 yielded from SiH_4 , and CH_4 , C_2H_2 , C_2H_4 from C_3H_8 (see Fig.3.3) [15,16]. The analyses revealed that the contribution of active C radicals such as C and CH_x ($x=1,2,3$) to the growth was negligible. The author confirmed this prediction by the fact that the supply of only C_3H_8 and H_2 yielded no deposition of C films. By considering the reactions between Si and three kinds of hydrocarbon molecules on the assumption that chemical equilibrium is established at the vapor-solid interface, the author calculated the equilibrium vapor pressures in the following reactions:



The equilibrium vapor pressure of Si (P_{Si}) can be obtained from the equilibrium equations for these reactions as follows:

$$P_{\text{Si}}^{K_1}(T) = \frac{P_{\text{H}_2}^2}{K_1 P_{\text{CH}_4}}, \quad (4.16)$$

$$P_{\text{Si}}^{K_2}(T) = \frac{\sqrt{P_{\text{H}_2}}}{K_2 \sqrt{P_{\text{C}_2\text{H}_2}}}, \quad (4.17)$$

$$P_{\text{Si}}^{K_3}(T) = \frac{P_{\text{H}_2}}{K_3 \sqrt{P_{\text{C}_2\text{H}_4}}}, \quad (4.18)$$

where P_{CH_4} , $P_{\text{C}_2\text{H}_2}$, and $P_{\text{C}_2\text{H}_4}$ are the partial pressures of CH_4 , C_2H_2 , and C_2H_4 , respectively. K_1 , K_2 , and K_3 are the equilibrium constants for the above reactions, which are obtained by thermochemical calculation using the Gibbs' free energies and specific heats for the concerned species as follows [17]:

$$K = \exp\left(-\frac{\Delta G_{\text{T}}^0}{R_{\text{g}}T}\right) = \exp\left(-\frac{\Delta H_{298}^0 - T\Delta S_{298}^0 - T\Delta C_{\text{p}}M_0}{R_{\text{g}}T}\right), \quad (4.19)$$

where

$$M_0 = \ln T - (1 + \ln 298) + \frac{298}{T}. \quad (4.20)$$

Here, ΔG_{T}^0 , ΔH_{298}^0 , and ΔS_{298}^0 are the change of Gibbs' free energy, the change of standard enthalpy of formation, and the change of standard entropy. R_{g} and ΔC_{p} are the gas constant and the change of specific heat. Thermochemical data used for calculation are listed in Table 4.1 [18].

Using the partial pressures of H_2 and hydrocarbon molecules, the temperature dependence of P_{Si} in each reaction was calculated from eqs.(4.16)~(4.18), and is shown in Fig.4.3(a). P_{Si} for the reaction (4.14) takes minimum values in the temperature range under consideration. This result indicates that the reaction between Si and C_2H_2 is the most active and dominant for SiC growth, because a fast reaction leads to its larger equilibrium constant and lower partial pressure of Si. This is consistent with an analysis by Allendorf and Kee [16] who showed Si and C_2H_2 were the most contributing species to SiC growth (Fig.3.4). Then, P_{Si} for the reaction (4.14) was regarded as the equilibrium vapor pressure of Si (P_{Si}) in this system.

Figure 4.3(b) shows the temperature dependence of $n_{\text{s0}}/\tau_{\text{s}}$ calculated from eq.(4.12). The $n_{\text{s0}}/\tau_{\text{s}}$ for the reaction (4.14) takes minimum values as does P_{Si} . The $n_{\text{s0}}/\tau_{\text{s}}$, which corresponds to desorption flux at equilibrium, increases exponentially with temperature. Then, the supersaturation ratio defined as $n_{\text{s}}/n_{\text{s0}}$ becomes significantly high for low-temperature growth, which can be

Table 4.1 Thermochemical data used in the present calculation [18].

Species	ΔH_{298}^0 (kJ/mole)	S_{298}^0 (J/(mole K))	C_p (J/(mole K))			
			300K	600K	900K	1200K
Si	450.6	167.9	22.23	24.15	25.85	27.18
CH ₄	-74.5	186.1	35.71	52.23	67.60	78.83
C ₂ H ₂	228.0	200.8	44.23	58.29	66.11	72.05
C ₂ H ₄	52.2	219.2	43.06	70.66	89.20	101.63
H ₂	0.0	130.6	28.84	29.33	29.91	30.92
SiC	-111.9	16.51	26.76	41.72	47.05	49.80

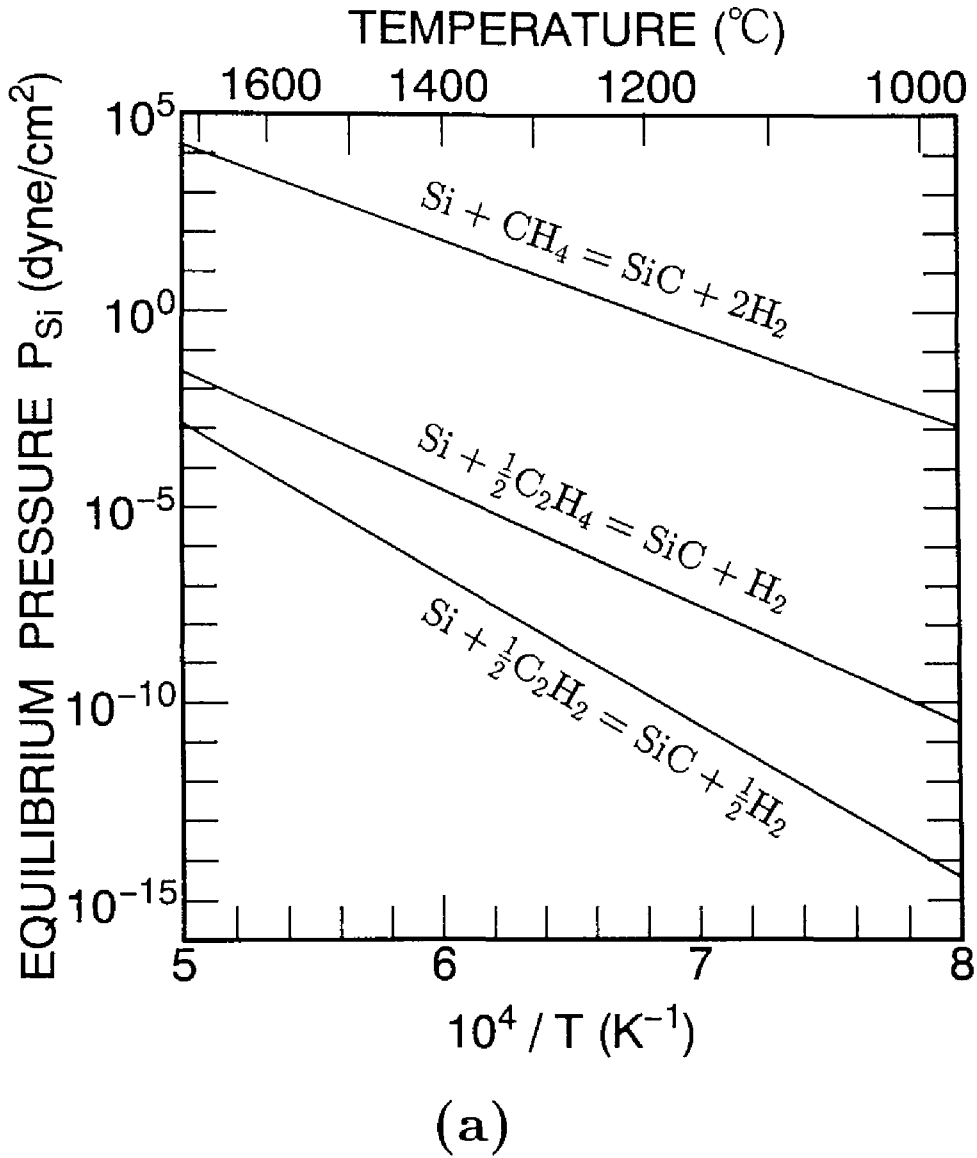


Fig.4.3 (a) Temperature dependence of equilibrium vapor pressure of Si (P_{Si}) in reactions between Si and hydrocarbon molecules calculated from eqs.(4.16)-(4.18).

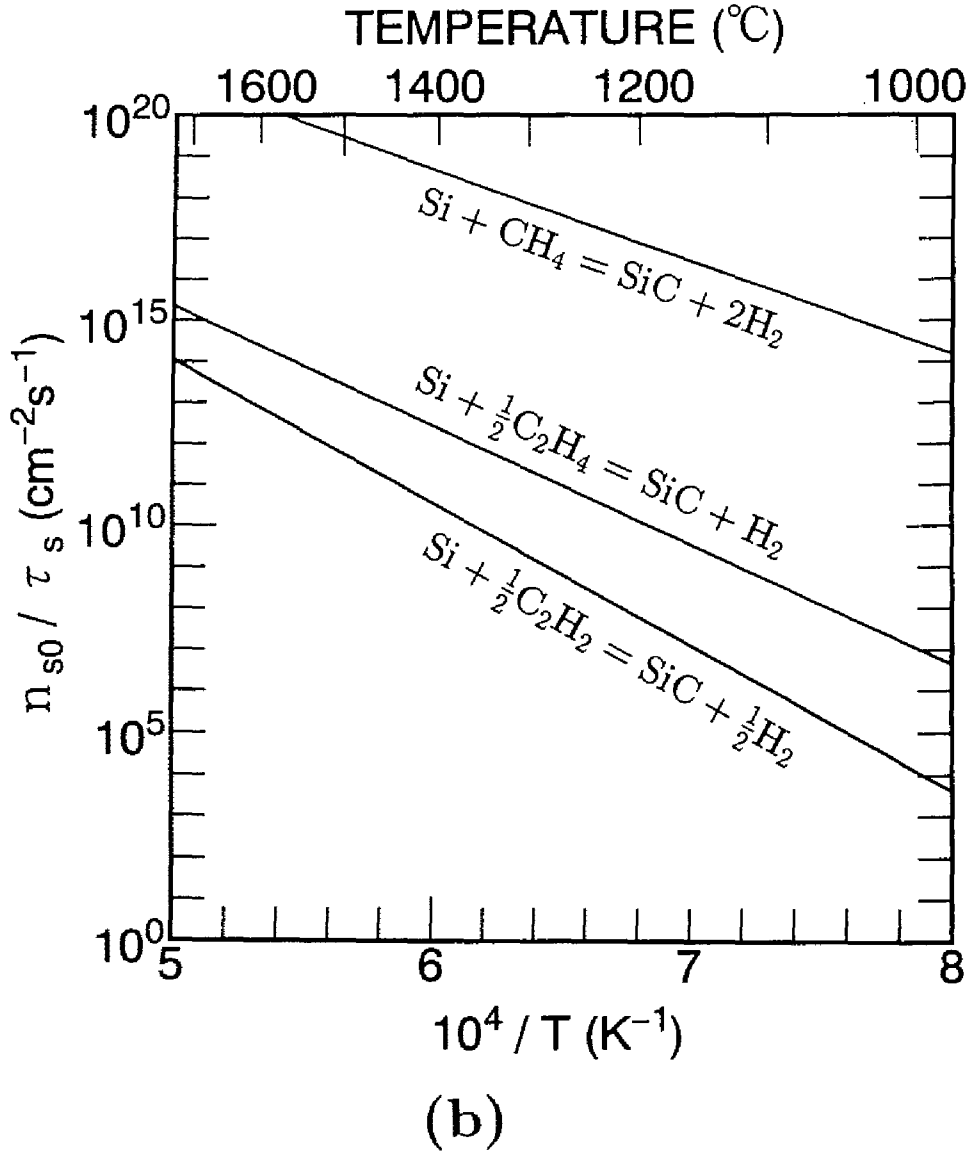


Fig.4.3 (b) Temperature dependence of desorption flux (n_{s0}/τ_s).

easily speculated from eq.(4.7). This is the reason why nucleation is promoted at low temperatures.

4.3.2 Critical supersaturation ratio

Nucleation on terraces becomes dominant when α_{\max} exceeds a critical supersaturation ratio α_{crit} . In principle, α_{crit} is intrinsic to a surface of a material if temperature is fixed. When the critical nucleation rate J_{nuc}^* is assumed to be $10^{12}\text{cm}^{-2}\text{s}^{-1}$, which corresponds to one nucleation per unit time on a $10\text{nm}\times 10\text{nm}$ area (the average terrace widths in this study are $3\sim 30\text{nm}$), the α_{crit} is given by the following equation for a disk-shaped nucleus (see the Appendix A.1) [19]

$$\alpha_{\text{crit}} = \exp\left\{\frac{\pi h_0 \sigma^2 \Omega}{(65 - \ln 10^{12}) k^2 T^2}\right\}, \quad (4.21)$$

where Ω and σ are the volume of a Si-C pair and the surface free energy.

Although there have been no reports on the surface free energy of 6H-SiC{0001}, it has been calculated as 2220 and 300erg/cm² for 3C-SiC(111)Si and ($\bar{1}\bar{1}\bar{1}$)C faces, respectively [20]. Since 6H-SiC(0001)Si and (000 $\bar{1}$)C faces have the same atomic configurations as 3C-SiC(111)Si and ($\bar{1}\bar{1}\bar{1}$)C faces near the surfaces, respectively, σ for 3C-SiC{111} faces was employed for 6H-SiC{0001} in this study. The values of h_0 (0.252nm) and Ω ($2.07\times 10^{-23}\text{cm}^3$) were used for calculation.

The temperature dependence of α_{crit} for (0001)Si and (000 $\bar{1}$)C faces is shown in Fig.4.4. α_{crit} decreases with the increase in temperature, which means that a lower supersaturation ratio is enough to cause nucleation at higher temperatures. However, in real crystal growth, nucleation is promoted at lower temperatures owing to significant decrease in n_{s0}/τ_s as shown in Fig.4.3(b). Much attention should be paid to the polarity dependence of α_{crit} . The α_{crit} for (000 $\bar{1}$)C faces takes quite low values of nearly unity. This result indicates that nucleation occurs much more frequently on (000 $\bar{1}$)C faces under the same supersaturation conditions.

Figures 4.5(a) and (b) show Nomarski micrographs for the layers grown on well-oriented 6H-SiC(0001)Si and (000 $\bar{1}$)C faces at 1500°C. The flow rates of

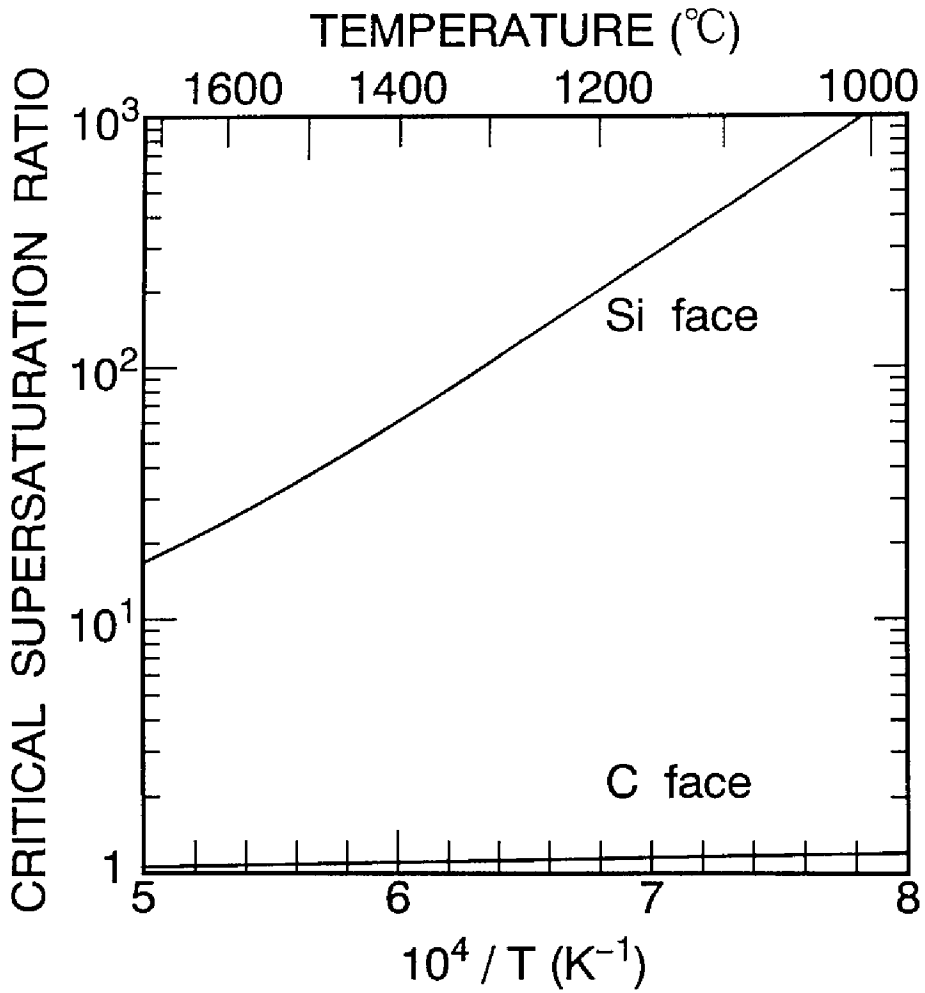


Fig.4.4 Temperature dependence of critical supersaturation ratio (α_{crit}) for (0001)Si and (000 $\bar{1}$)C faces.

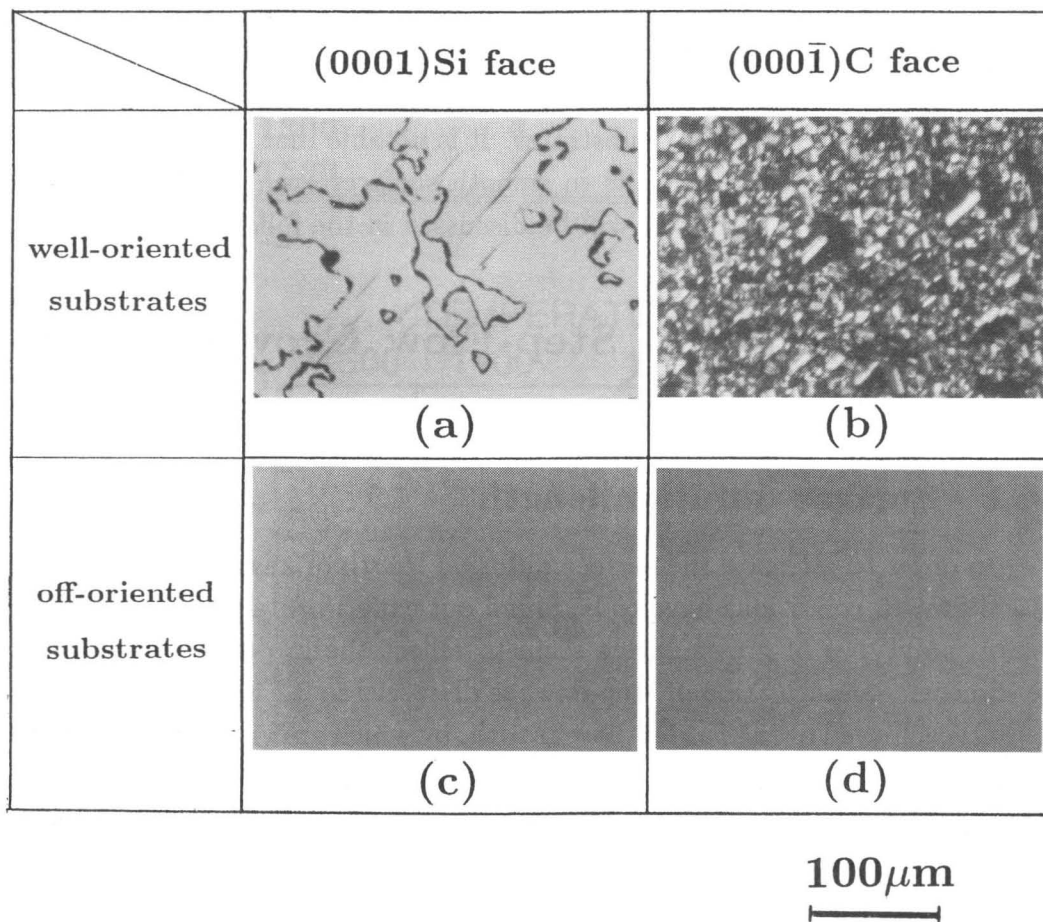


Fig.4.5 Surface morphology of layers grown on well-oriented faces ((a) and (b)) and off-oriented faces ((c) and (d)). The micrographs (a) and (c) show surfaces of epilayers on (0001)Si, (b) and (d) on (000 $\bar{1}$)C faces. The growth temperature is 1500°C. The off-angle is 6° toward $\langle 11\bar{2}0 \rangle$.

SiH_4 and C_3H_8 are 0.30 and 0.20sccm, respectively. The layers grown on both faces were identified to be twinned crystalline 3C-SiC. However, the surface of the layers grown on a C face is considerably rougher due to island-like growth. This difference in surface morphology is believed to result from the different α_{crit} of the individual faces, as is theoretically predicted in Fig.4.4.

Surface morphology for the layers grown on 6° off-oriented 6H-SiC(0001)Si and (000 $\bar{1}$)C faces is shown in Figs.4.5(c) and (d). The growth condition is the same as in Figs.4.5(a) and (b). Specular smooth surfaces were obtained, independent of the polarity of substrates. It is notable that the off-orientation introduced into substrates results in smooth surfaces even on C faces which have very low α_{crit} . The reason will be discussed in the following section.

4.4 Prediction of Step-Flow Growth Conditions

4.4.1 Surface diffusion length

In order to estimate the surface diffusion length of adsorbed species, the critical growth conditions have to be found out experimentally. In the present system, polytypes of grown layers seem to reflect the growth mode whether two-dimensional nucleation or step-flow, as discussed in 2.3.3. Homoepitaxy of 6H-SiC is achieved owing to step-flow growth, by which grown layers inherit the stacking order of substrates. 3C-SiC is heteroepitaxially grown through two-dimensional nucleation, because 3C-SiC is stable at these low temperatures. Then, the growth modes were distinguished by identifying the polytypes of grown layers.

Critical growth conditions were found through CVD growth under various growth conditions. Growth temperature and off-angle were varied in the range of 1100~1500°C and 0~10° (toward (11 $\bar{2}$ 0)), respectively. Both 6H-SiC(0001)Si and (000 $\bar{1}$)C faces were employed to investigate the substrate polarity effect.

Table 4.2 summarizes some of the critical growth conditions at various growth temperatures. Higher growth temperature, larger off-angle and lower

Table 4.2 Typical critical growth conditions experimentally obtained.

Growth temperature (°C)	Off-angle (°)	Terrace width (nm)	Growth rate ($\mu\text{m/h}$)
1100	6	7.2	0.80
1200	3	14.4	0.95
1300	6	7.2	2.50
1500	1	43.3	2.00

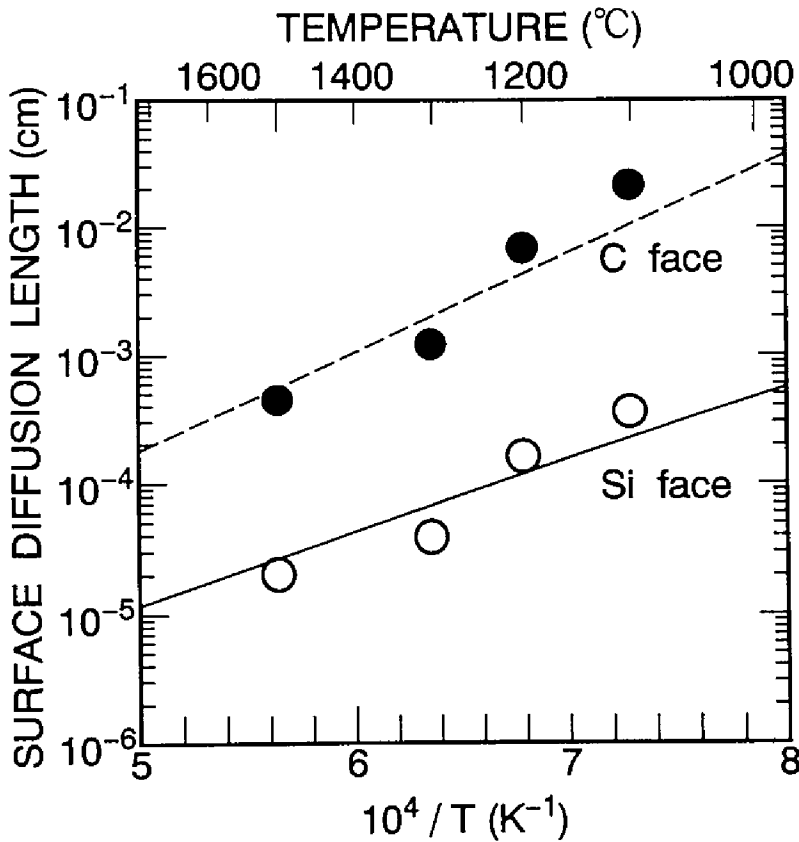


Fig.4.6 Temperature dependence of surface diffusion length (λ_s) of adsorbed species on Si and C faces.

growth rate are preferable to homoepitaxy of 6H-SiC (step-flow growth). Very little dependence of the critical conditions on the substrate polarity was observed.

Figure 4.6 shows the temperature dependence of surface diffusion length on both faces calculated from eq.(4.11) using several data discussed above. In eq.(4.11), the terrace width λ_0 was calculated as $h/\tan \theta$, where h and θ are the step height and off-angle, respectively. Note that h was assumed as 3 Si-C bilayer height ($0.252 \times 3 = 0.756\text{nm}$), based on the result of step bunching presented in 3.3. In the figure, solid and dotted lines denote the fitting results using eq.(4.3). Since the surface diffusion lengths obtained in this study are the average lengths to migrate on a "step-free" surface before desorption, they decrease at high temperatures due to enhanced desorption. The surface diffusion lengths on C faces are longer than those on Si faces by more than one order of magnitude. Although nucleation occurs much more easily on $(000\bar{1})$ C faces, there are no significant differences in surface morphology and critical growth conditions for the growth on off-oriented substrates. The longer surface diffusion lengths on C faces may compensate frequent nucleation on the terraces. The activation energies of λ_s are determined to be -1.0eV and -1.5eV on Si and C faces, respectively. Based on eq.(4.3), these activation energies mean $-(E_{\text{des}} - E_{\text{diff}})/2$. The origin of polarity dependence of activation energy is not clear, probably due to differences in chemical reactivity, step structure, etc. The activation energies of $-0.27 \sim -0.34\text{eV}$ have been reported for Ga adatoms on GaAs(001) faces [7]. The higher activation energies in the present system may be attributed to larger $E_{\text{des}} - E_{\text{diff}}$ caused by stronger bond-strength in SiC.

Although the terrace width was assumed to be completely uniform on the surface in the above model, this is not correct on a real surface. In fact, the author found the significant distribution of terrace width on SiC{0001} epilayers, as described in 3.3. Here, the influences of terrace-width fluctuation on the present calculation are discussed.

Figure 4.7 shows the distribution of supersaturation ratio on a vicinal surface with non-uniform terrace widths. At a fixed growth temperature, which involves a constant surface diffusion length, the maximum supersaturation ratio α_{max} strongly depends on terrace widths: α_{max} is higher on a wider

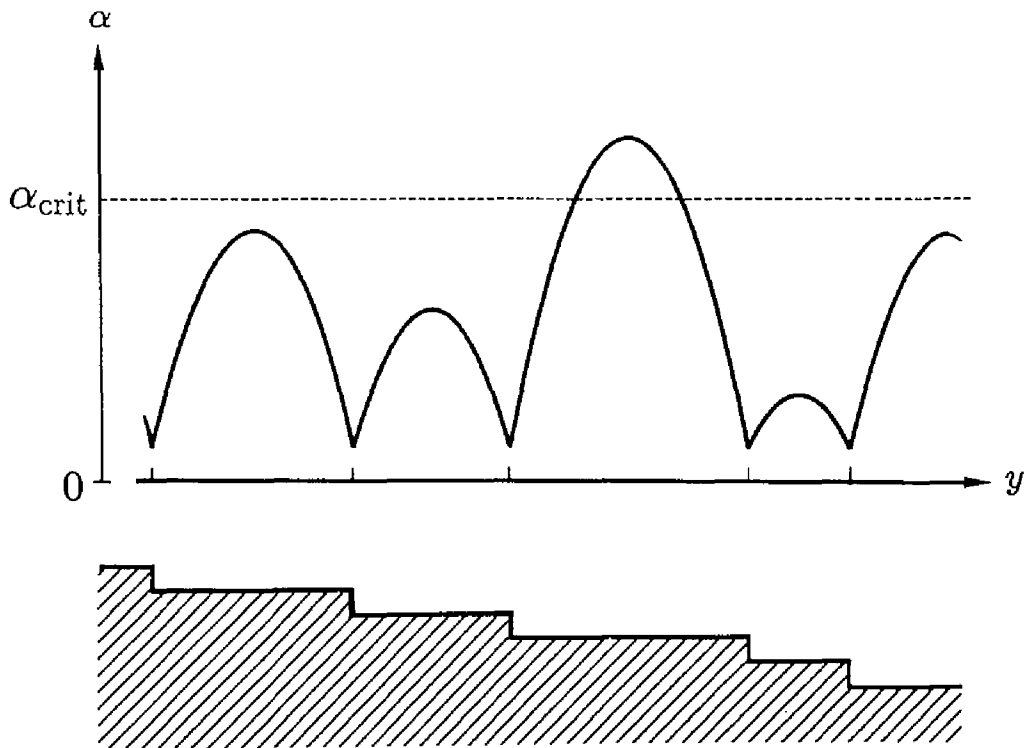
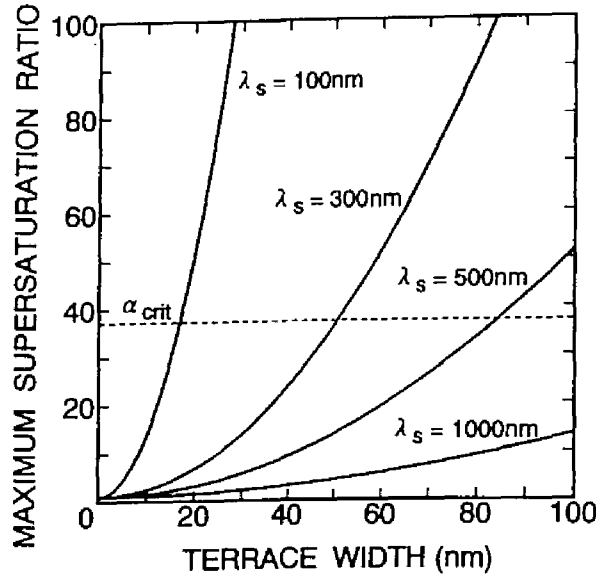
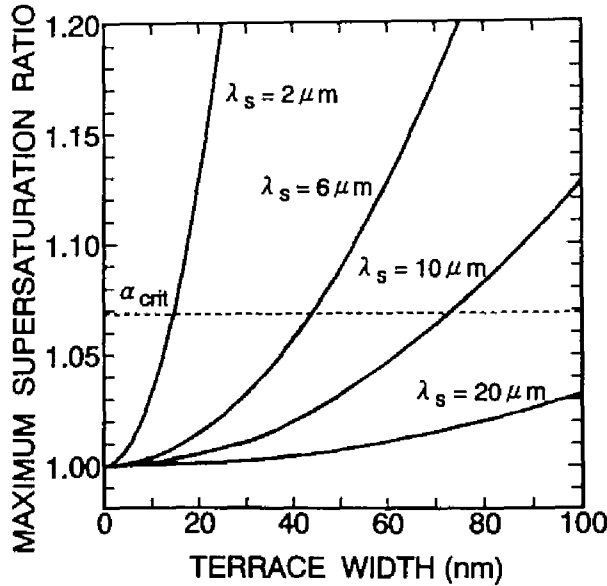


Fig.4.7 Distribution of supersaturation ratio on a vicinal surface with non-uniform terrace widths. α_{max} on a wider terrace may exceed α_{crit} .



(a)



(b)

Fig.4.8 Relationship between the maximum supersaturation ratio α_{max} and the terrace width λ_0 with various surface diffusion lengths λ_s as a parameter. Substrates are vicinal (a) (0001)Si and (b) (000 $\bar{1}$)C faces. Growth temperature and the flux of reactants were assumed as 1500°C and $5 \times 10^{15} \text{cm}^{-2} \text{s}^{-1}$.

terrace. Assuming that steps are perfect sinks, α_{\max} is given by

$$\alpha_{\max} = \frac{J\tau_s}{n_{s0}} + \left(1 - \frac{J\tau_s}{n_{s0}}\right) \frac{1}{\cosh(\lambda_0/2\lambda_s)}, \quad (4.22)$$

which can be easily obtained from eq.(4.2).

Figure 4.8 shows the relationship between the maximum supersaturation ratio α_{\max} and the terrace width λ_0 with various surface diffusion lengths λ_s as a parameter. Growth temperature and the flux of reactants were assumed as 1500°C and $5 \times 10^{15} \text{cm}^{-2}\text{s}^{-1}$. Both Si (Fig.4.8(a)) and C faces (Fig.4.8(b)) were considered. α_{\max} increases almost exponentially with increasing terrace width, indicating the considerable influence of terrace width fluctuation. This tendency is reduced for longer surface diffusion length. For perfect step-flow growth on the whole area of substrates, α_{\max} on the widest terrace must be lower than α_{crit} . If a terrace with $2\langle w \rangle$ width ($\langle w \rangle$: the average terrace width) exists on the surface, twice of the surface diffusion length ($2\lambda_s$) calculated for "uniform" terrace width is required for step-flow growth, as can be seen from eq.(4.22). Since rather vast terraces of which width is 5~10 times wider than the average value can be observed on a real surface, the surface diffusion lengths obtained in this calculation may be underestimated at least by a factor of 5~10. Further discussion on surface diffusion lengths is given in 5.3.3.

4.4.2 Critical growth condition

Since the temperature dependences of n_{s0}/τ_s , α_{crit} , and λ_s have been obtained, critical growth conditions, in turn, can be predicted under various conditions using eq.(4.11). For example, if the growth temperature and off-angle of substrates (terrace width) are fixed, a critical growth rate (maximum growth rate to realize step-flow) can be calculated. Although the underestimation of surface diffusion lengths was suggested in the previous subsection, the following calculation is not seriously affected by the underestimation due to the consistent assumption on the uniform distribution of terraces and on the average surface diffusion lengths estimated in this model.

Critical growth conditions are shown by curves in Fig.4.9 for substrate's off-angles of 0.2, 1, 3, 6, and 10°. In the figure, the top-left and bottom-

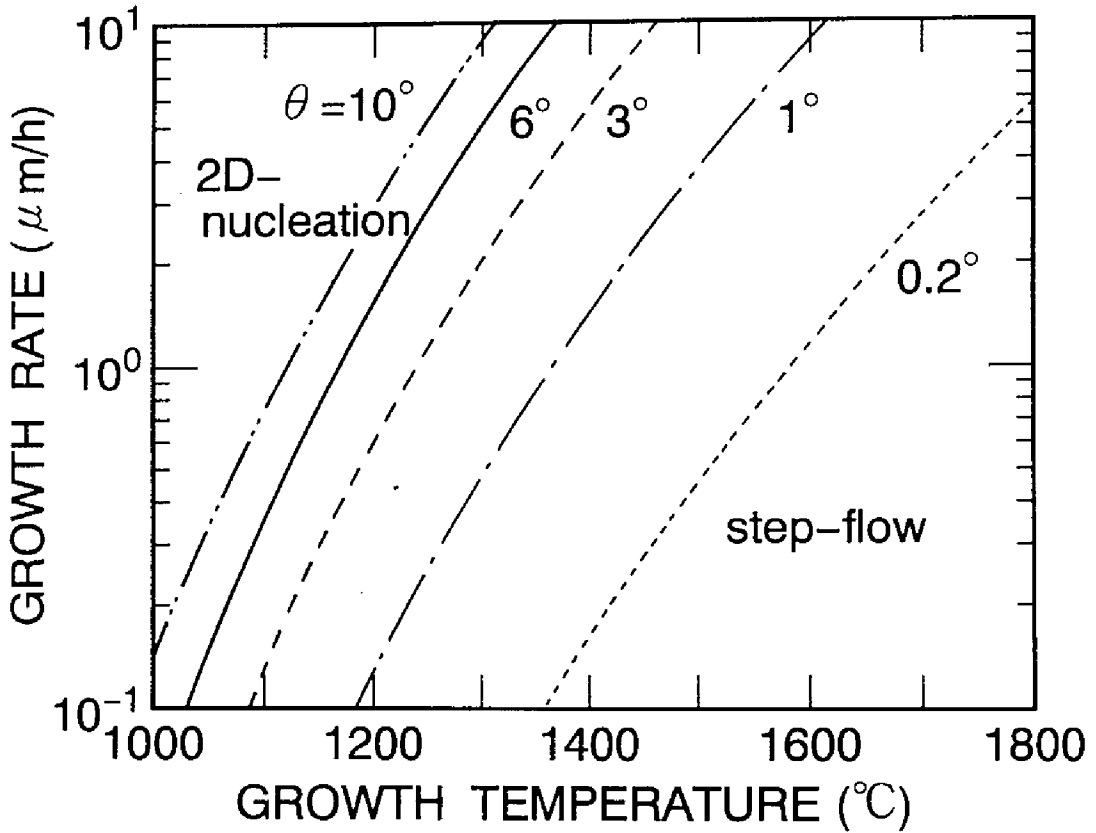


Fig.4.9 Critical growth conditions as a function of growth temperature, growth rate, and substrate's off-angles ($\theta=0.2, 1, 3, 6,$ and 10°). Top-left regions and bottom-right regions from the curves correspond to two-dimensional nucleation and step-flow growth conditions, respectively.

right regions separated by the curves correspond to the two-dimensional nucleation and step-flow growth conditions, respectively. Almost no difference in the critical conditions was obtained on Si and C faces. The higher growth rate and lower off-angle are available for step-flow growth at higher growth temperatures. At 1800°C, a very small off-angle of 0.2°, which yields almost “well-oriented” faces, is enough to achieve step-flow growth with a moderate growth rate of 6 μm/h. This may be one of the reasons why 6H-SiC can be homoepitaxially grown on well-oriented faces if growth temperature is raised up to 1700~1800°C [21-24]. Powell *et al.* reported that the preferable nucleation of 3C-SiC occurs at defect sites on 6H-SiC(0001) vicinal surfaces [25]. The role of defects for the 3C-SiC nucleation may become important on the substrates with small off-angles. On the contrary, large off-angles more than 5° are needed to realize homoepitaxy of 6H-SiC at a low temperature of 1200°C.

4.5 Summary

Chemical vapor deposition of SiC on off-oriented 6H-SiC{0001} substrates was quantitatively analyzed based on the BCF theory. A simple diffusion model describing the growth on vicinal surfaces was proposed, and was applied to SiC growth. Desorption flux n_{s0}/τ_s and critical supersaturation ratio α_{crit} were calculated using a classical crystal growth theory and thermochemical analysis.

By measuring the critical growth conditions where the growth mode changed from step-flow to two-dimensional nucleation, the surface diffusion lengths of adsorbed species on 6H-SiC(0001)Si and (000 $\bar{1}$)C faces were estimated with the model. The growth on well-oriented (000 $\bar{1}$)C faces yields high-density of islands on the surface. This result can be explained by a low critical supersaturation ratio predicted on (000 $\bar{1}$)C faces. However, in step-flow growth conditions, longer surface diffusion lengths of adsorbed species on (000 $\bar{1}$)C faces brought about little difference in growth mode and morphology on both faces. Growth conditions where step-flow growth takes place were predicted as a function of growth parameters such as temperature, growth rate and off-angle of substrates. This result will give a guideline for step-controlled

epitaxy of SiC.

References

- [1] W.K.Burton, N.Cabrera and F.C.Frank, *Philos. Trans. Roy. Soc. London*, **A243**, 299(1951).
- [2] R.L.Schwoebel, *J. Appl. Phys.*, **37**, 3682(1966).
- [3] K.Voigtlaender, H.Risken, and E.Kasper, *Appl. Phys.*, **A39**, 31(1986).
- [4] A.K.Myers-Beaghton and D.D.Vvedensky, *Phys. Rev.*, **B42**, 5544(1990).
- [5] H.C.Abbink, R.M.Broudy, and G.P.McCarthy, *J. Appl. Phys.*, **39**, 4673(1968).
- [6] E.Kasper, *Appl. Phys.* **A28**, 129(1982).
- [7] T.Shitara and T.Nishinaga, *Jpn. J. Appl. Phys.*, **28**, 1212(1989).
- [8] N.Chand, E.E.Becker, J.P.van der Ziel, S.N.G.Chu, and N.K.Dutta, *Appl. Phys. Lett.*, **58**, 1704(1991).
- [9] N.Chand, P.R.Berger, and N.K.Dutta, *Appl. Phys. Lett.*, **59**, 186(1991).
- [10] T.Nishinaga and T.Suzuki, *J. Crystal Growth*, **128**, 37(1993).
- [11] M.D.Pashley, K.W.Haberern, and J.M.Gaines, *Appl. Phys. Lett.*, **58**, 406(1991).
- [12] X.S.Wang, J.L.Goldberg, N.C.Bartelt, T.L.Einstein, and E.D.Williams, *Phys. Rev. Lett.*, **65**, 2430(1990).
- [13] J.O.Hirschfelder, F.Curties and R.B.Bird, *Molecular Theory of Gases and Liquids* (John Wiley & Sons, New York, 1954).
- [14] T.Yoshinobu, M.Nakayama, H.Shiomi, T.Fuyuki and H.Matsunami, *J. Crystal Growth*, **99**, 520(1990).
- [15] C.D.Stinespring and J.C.Wormhoudt, *J. Crystal Growth*, **87**, 481(1988).
- [16] M.D.Allendorf and R.J.Kee, *J. Electrochem. Soc.*, **138**, 841(1991).
- [17] B.H.Mahan, *University Chemistry* (Addison-Wesley Publishing, 1969).
- [18] D.R. Stull and H.Prophet, *JANAF Thermochemical Tables* (U.S. Government Printing Office, 1971).
- [19] J.P.Hirth and G.M.Pound, *Condensation and Evaporation, Nucleation and Growth Kinetics* (Pergamon Press, Oxford, 1963), Chapt.D.
- [20] E.Pearson, T.Takai, T.Halicioglu, and W.A.Tiller, *J. Crystal Growth*, **70**, 33(1984).
- [21] V.J.Jennings, A.Sommer, and H.C.Chang, *J. Electrochem. Soc.*, **113**, 728(1966).
- [22] W.v.Muench and I.Pfaffeneder, *Thin Solid Films*, **31**, 39(1976).
- [23] S.Nishino, H.Matsunami, and T.Tanaka : *J. Crystal Growth*, **45**, 144(1978).
- [24] S.Yoshida, E.Sakuma, H.Okumura, S.Misawa, and K.Endo, *J. Appl. Phys.*, **62**, 303(1987).
- [25] J.A.Powell, J.B.Petit, J.H.Edgar, I.G.Jenkins, L.G.Matus, J.W.Yang, P.Pirouz, W.J.Choyke, L.Clemen, and M.Yoganathan, *Appl. Phys. Lett.*, **59**, 333(1991).

List of Nomenclature

a	jump distance on a surface
ΔC_p	change of the specific heat
D_s	surface diffusion coefficient of adsorbed species
E_{des}	activation energy for desorption
E_{diff}	activation energy for surface diffusion
ΔG_T^0	change of the Gibbs' free energy
h	step height
h_0	spacing of SiC{0001} faces
ΔH_{298}^0	change of the standard enthalpy of formation
J	flux of reactants arriving at a surface
J_{nuc}^*	critical nucleation rate
J_s	flow of adsorbed species on a terrace
k	Boltzmann constant
$K_i(i=1,2,3)$	equilibrium constant
m	mass of a reactant
n_0	density of adatom sites on a surface
n_s	number of adsorbed species per unit area
n_{s0}	number of adsorbed species per unit area at equilibrium
P_0	equilibrium vapor pressure
P_{Si}	equilibrium vapor pressure of Si
R	growth rate
R_g	gas constant
ΔS_{298}^0	change of the standard entropy
T	absolute temperature
v_{step}	step velocity
α	supersaturation ratio
α_{crit}	critical supersaturation ratio
α_{max}	maximum supersaturation ratio on a terrace
λ_0	average terrace width
λ_s	average surface diffusion length
σ	surface free energy
τ_s	mean residence time of adsorbed species
Ω	volume of a Si-C pair

Chapter 5

Surface Kinetics in Step-Controlled Epitaxy

5.1 Introduction

Through studies on the growth mechanism of step-controlled epitaxy, macroscopic kinetics have been revealed. However, real crystal growth consists of complicated microscopic surface processes of nucleation and step-motion. Although considerable attention has been given to step dynamics in crystal growth of Si and III-V semiconductors through *in-situ* RHEED and STM observation, very few approaches have been made on step dynamics in SiC growth. The author tried a theoretical study on the supersaturation and step velocity on 6H-SiC{0001} in Chapter 4. These results should be verified by experiments.

In general, the quality of grown layers is strongly influenced by the surface diffusion length. From a viewpoint of crystal growth, the surface diffusion length is a critical parameter which determines whether crystal growth proceeds through step-flow or two-dimensional nucleation. It is scientifically and practically important to make clear how the surface diffusion of migrating species is affected by growth conditions. Although several studies on the surface diffusion length have been reported in MBE of III-V semiconductors [1-4], there have been no reports in SiC growth.

In order to analyze step-dynamics on a growing surface, *in-situ* observation of surfaces by STM may be a powerful technique. However, it is technically difficult in a CVD system, where relatively high pressure in a growth chamber prevents *in-situ* observation. Then, a method to analyze step-dynamics through *ex-situ* observation has been required.

In this chapter, the formation of nuclei and lateral growth rates of steps in SiC growth are studied through short-time growth experiments. The effects of growth temperature, substrate polarity and off-orientation on the surface processes are investigated in detail. A simple model to estimate the surface diffusion length from the lateral growth rates of steps is proposed, and the surface diffusion length is analyzed in CVD growth of SiC. The effects of growth temperature and flow rates of source gases on surface diffusion lengths are described.

5.2 Nucleation and Step Dynamics

5.2.1 Experimental procedures

The CVD system used here is the same as described in 2.2.2. In CVD growth of SiC, the flow rates of SiH₄, C₃H₈, and H₂ were 0.03~0.30sccm, 0.02~0.30sccm, and 3.0slm, respectively. Growth temperature was varied in the range of 1200~1600°C. Growth time was very short, 10~600sec.

Single crystals of 6H-SiC{0001} grown by the Acheson method were used as substrates. Since nucleation is sensitive to surface conditions such as impurities and defects introduced through a polishing process [5], as-grown natural surfaces giving basal planes (well-oriented {0001} faces) were employed in the present study. In some experiments, epilayers with 2μm thickness grown on off-oriented {0001} faces at 1500°C were used. In this case, the off-angle was 3~5° toward (11 $\bar{2}$ 0).

The observation of nucleus formation can be done by short-time growth [6,7]. In order to investigate step-motion, a method similar to that in ref.7 was employed. Circular "mesa-tables" with 120 nm height and 20~300μm diameter were formed on the SiC substrates, and the lateral growth rates were

measured from the advance of table edges by short-time growth. The mesa-tables were formed by conventional photolithography and reactive ion etching (RIE). After the RIE, samples were oxidized at 1100°C for 5h, and the thermal oxide layers were stripped with HF etching to remove damaged layers formed through the RIE process.

The polytypes of nuclei and grown layers were identified by Raman scattering measurement. An Ar⁺ laser with 515.4nm line and 2μm beam diameter was used as an excitation source. The measurement was carried out using microscopic equipment at room temperature in backscattering geometry.

5.2.2 Nucleation on 6H-SiC {0001} terraces

Figure 5.1(a) shows a Nomarski photograph for a surface with circular mesa-tables before growth. The surfaces after 30sec growth at 1600°C and 300sec growth at 1200°C are shown in Figs. 5.1(b) and (c), respectively. The substrates are well-oriented (0001)Si faces, and the flow rates of SiH₄ and C₃H₈ are 0.15 and 0.10sccm, respectively. Under this condition, a typical growth rate is 1.2μm/h. In Figs.5.1(b) and 5.1(c), the formation of many growth nuclei on the terraces can be observed. Besides, the table edges advance laterally, which will be discussed in 5.2.3.

During high-temperature growth at 1500~1600°C, nuclei with a distorted hexagonal shape are formed on the {0001} faces as shown in Fig.5.1(b). The nuclei appear in various sizes from 20 to 50μm. The facets of all the nucleus edges are arranged parallel to {1 $\bar{1}$ 00} faces. At the initial stage of crystal growth, small "critical" nuclei are formed and they grow laterally by capturing migrating species. Then, the faceting of the nucleus edges may be ascribed to the fact that the hexagonal shape inherits from that of critical nuclei and/or that anisotropy in the lateral growth rate distorts the shape.

Triangular nuclei are formed in low-temperature growth at 1200~1300°C as shown in Fig.5.1(c). In this case, the nuclei have very small sizes of less than 5μm in spite of longer growth time than in the case of Fig.5.1(b). Although the facets of nuclei are also arranged parallel to {1 $\bar{1}$ 00} faces, two different orientations can be observed. The two types of nuclei are 180°-rotated relative to each other. Twin crystals of 3C-SiC containing double positioning

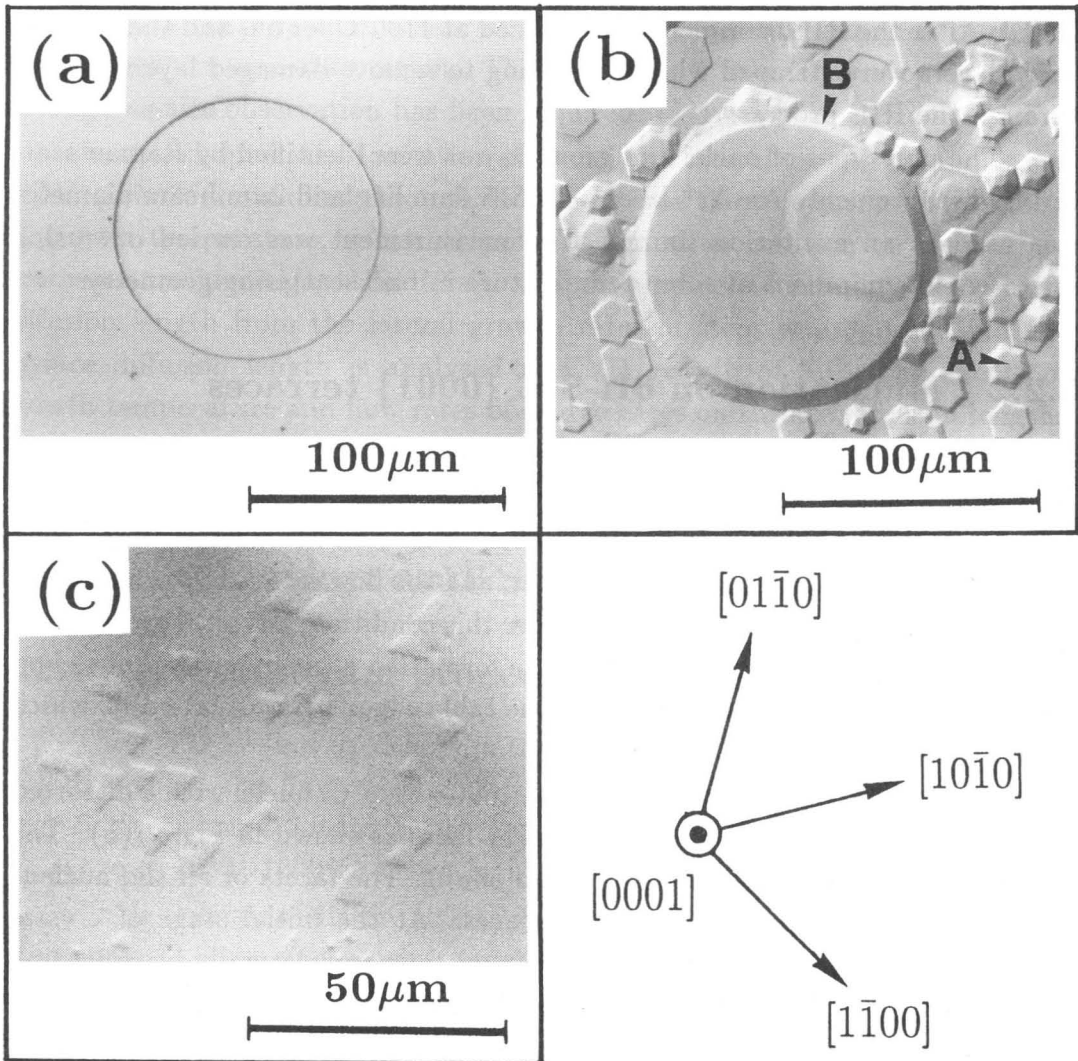


Fig.5.1 Nomarski photographs for SiC{0001} faces with circular mesa-tables; (a) before growth, (b) after 30sec growth at 1600°C, and (c) after 300sec growth at 1200°C.

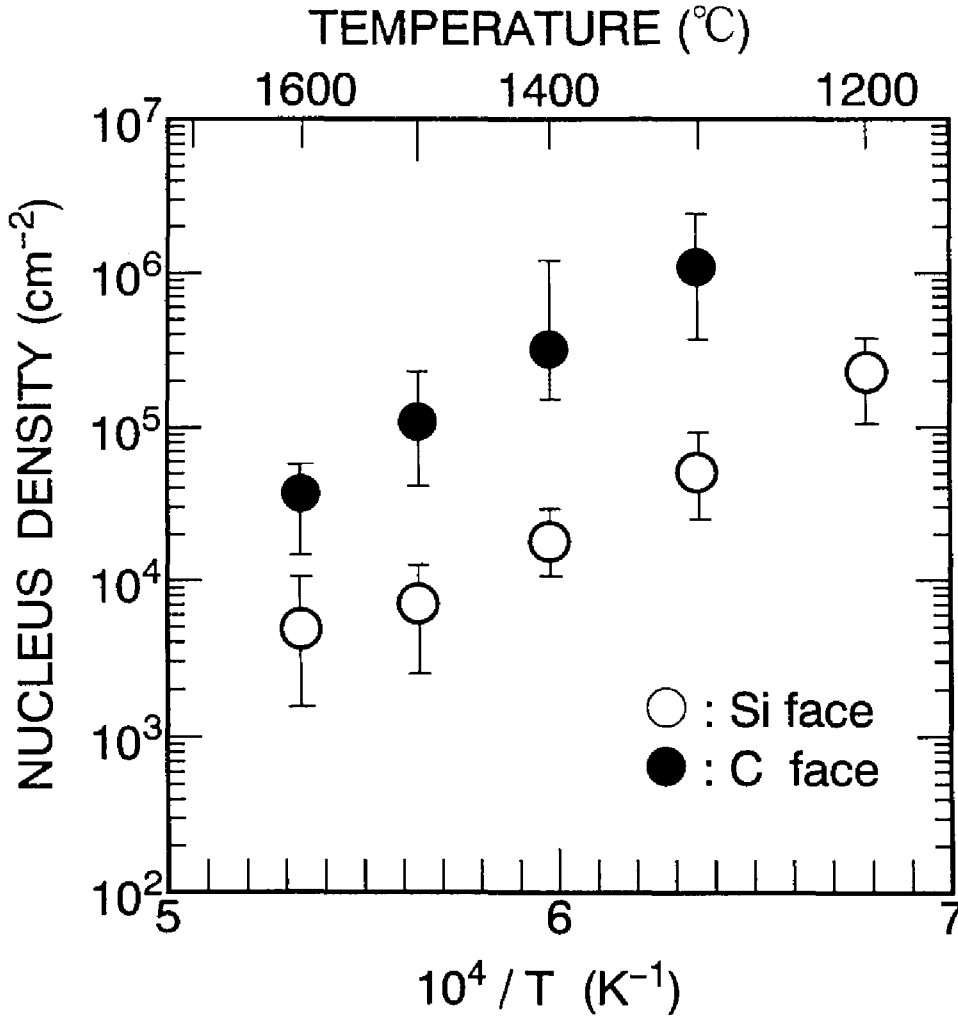


Fig.5.2 Temperature dependence of nucleus density on well-oriented (0001)Si and (000 $\bar{1}$)C faces. The flow rates of SiH₄ and C₃H₈ are 0.15 and 0.10sccm, respectively.

domains are grown on 6H-SiC{0001} basal planes at temperatures lower than 1700~1800°C [8-11]. Since the 180°-rotated triangular nuclei seem to be 3C-SiC with two different orientations, the nuclei may be the origin of double positioning domains.

Figure 5.2 shows the temperature dependence of nucleus density (the number of nuclei per unit area) on well-oriented (0001)Si and (000 $\bar{1}$)C faces. The flow rates of SiH₄ and C₃H₈ are 0.15 and 0.10sccm, respectively. The nucleus density increases significantly at low temperatures, which can be attributed to the higher supersaturation caused by reduced equilibrium vapor pressure and the suppressed surface diffusion of adsorbed species. The activation energies in the nucleus formation on Si and C faces are estimated to be -53kcal/mole and -67kcal/mole, respectively.

The nucleus density is higher on (000 $\bar{1}$)C faces than on (0001)Si faces by more than one order of magnitude. Pearson *et al.* calculated the surface free energies of SiC using many-body potential energy functions, and showed that the C face has much lower surface free energy (300erg/cm²) than the Si face (2220erg/cm²) [12]. Since nucleation takes place preferably on a face with lower free energy [5], higher nucleation rate is expected on (000 $\bar{1}$)C faces (see also Fig.4.4). This may be the reason why the growth on well-oriented (000 $\bar{1}$)C faces yields much higher growth rate and the grown layers have rougher surfaces [9,10]. As for nucleation on SiC{0001} faces, Powell *et al.* reported that preferential nucleation does occur at "defect sites" on the surface [13]. Since the sample surfaces have defect sites which originate from screw dislocations or RIE damage, this effect may become dominant in the case of low nucleation rate.

In crystal growth of SiC, the polytypes of grown layers are of great interest. Figure 5.3 shows TO (transverse optical) mode Raman spectra for (a) a substrate before growth, (b) a "nucleus site" (position A in Fig.5.1(b)), and (c) a "step site" (position B in Fig.5.1(b)) after growth at 1600°C for 600sec. Three peaks at 768, 789 and 796cm⁻¹ were observed for each sample. Note that the peak intensity ratio is different between Figs.5.3(b) and (c). TO-mode Raman spectra obtained from 6H-SiC{0001} consist of a main peak at 789cm⁻¹ and relatively weak peaks at 768 and 796cm⁻¹ (see the spectrum

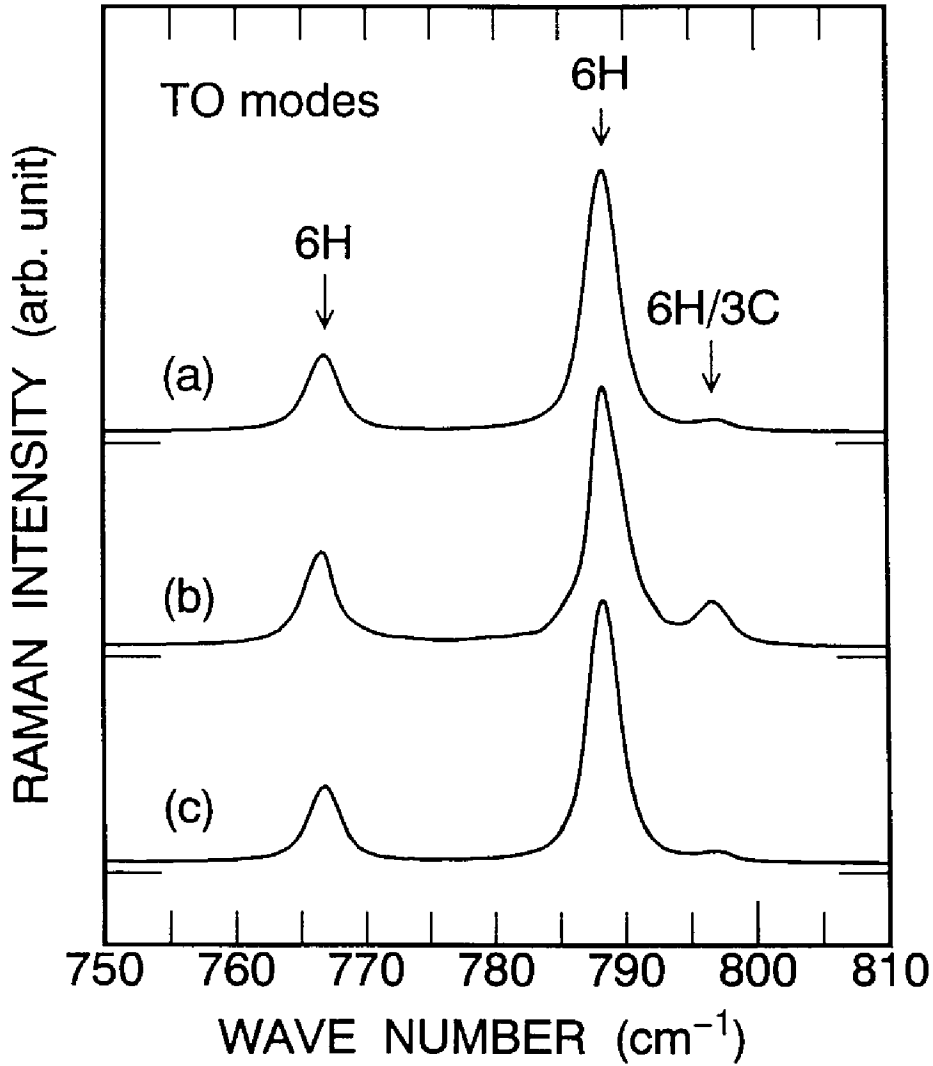


Fig.5.3 TO mode Raman spectra for (a) a substrate before growth, (b) a "nucleus site" (position A in Fig.1(b)), and (c) a "step site" (position B in Fig.1(b)) after growth at 1600°C for 600sec.

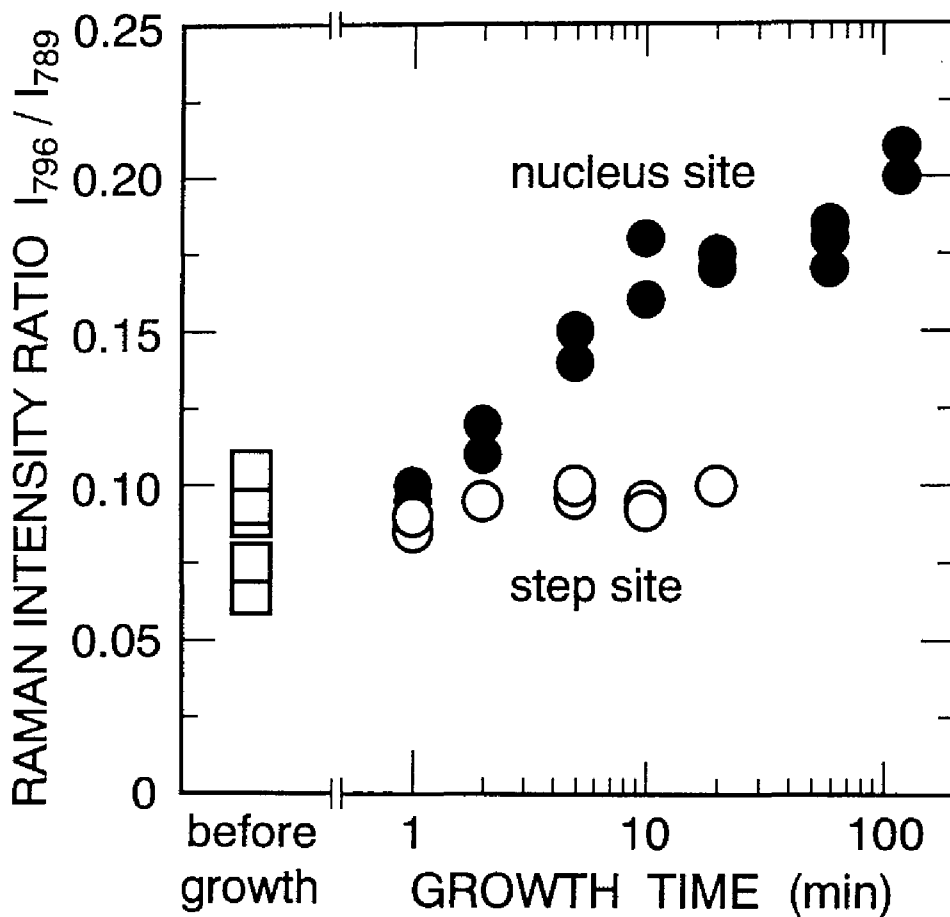


Fig.5.4 Dependence of Raman intensity ratio (I_{796}/I_{789}) on growth time.

from a substrate in Fig.5.1(a)),¹ whereas only one strong peak at 796cm^{-1} is observed from 3C-SiC [14,15]. We investigated the intensity ratio of Raman peaks at 796 and 789cm^{-1} (I_{796}/I_{789}) in order to distinguish the polytypes of grown layers. This I_{796}/I_{789} ratio should become higher when the component of 3C-SiC in the measured volume increases.

Figure 5.4 shows the dependence of the Raman intensity ratio (I_{796}/I_{789}) on growth time. The growth temperature was 1600°C . From substrates before growth, the ratios of $0.07\sim 0.11$ were obtained, which are typical for 6H-SiC {0001} crystals. At nucleus sites, the I_{796}/I_{789} ratio increases monotonously with growth time, and reaches 0.20 after 120min growth, indicating the increase in 3C-SiC component with growth time. The appearance of peaks at 768 and 789cm^{-1} for nucleus sites, as shown in Fig.5.3(b), may originate from the substrate underlying the thin grown layer (thickness= $2.4\mu\text{m}$ after 120min growth), in which the excitation light can penetrate (the penetration depth is estimated to be longer than $100\mu\text{m}$ [16]). Thus, the polytype of growth nuclei formed on {0001} terraces may be 3C-SiC. This result is consistent with the fact that 3C-SiC is grown on well-oriented 6H-SiC{0001} at temperatures lower than $1700\sim 1800^\circ\text{C}$ [8-11]. The I_{796}/I_{789} ratio at step sites takes values of $0.08\sim 0.10$, and shows very little change with growth time. This can be explained by a model that layers grown through lateral growth from steps inherit the stacking order of substrates.

5.2.3 Lateral growth of steps

The lateral advance of table edges had an almost linear dependence on time, and was independent of the table diameters. Figure 5.5 shows the temperature dependence of lateral growth rate on well-oriented (0001)Si faces. The flow rates of SiH_4 and C_3H_8 are 0.15 and 0.10sccm, respectively. The lateral growth rates are very large compared with the vertical growth rate ($1.2\mu\text{m}/\text{h}$ at 1600°C). This relationship results from the fact that adsorbed species are preferably incorporated into the crystal at atomic steps and/or kinks. The

¹In a perfect backscattering alignment, the peak at 796cm^{-1} cannot be observed from 6H-SiC{0001}. The appearance of this peak may be caused by a slight deviation of optical alignment (after Dr.H.Harima and Prof.S.Nakashima in Osaka University).

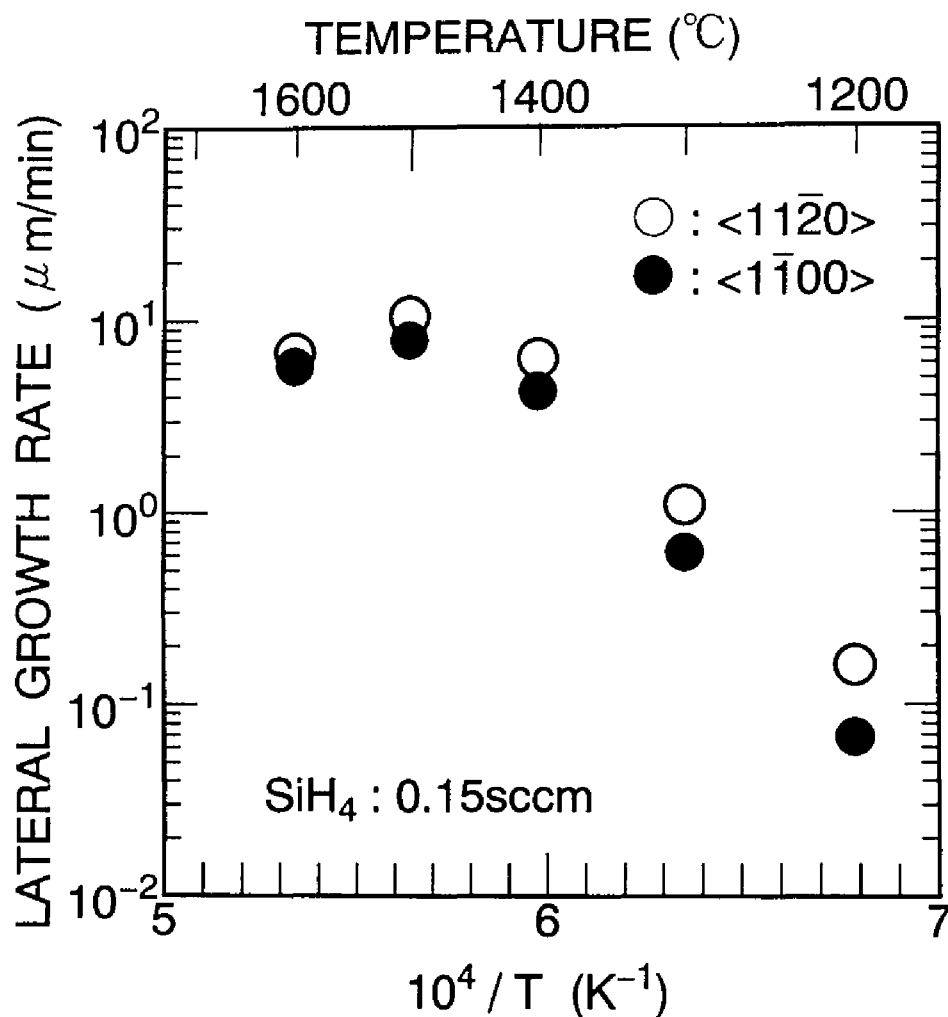
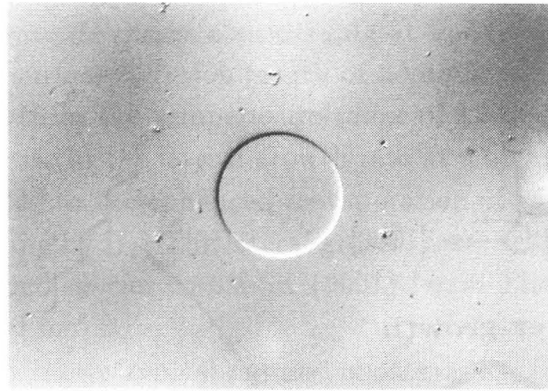
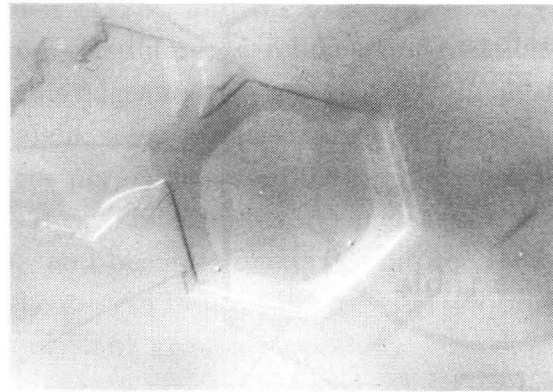


Fig.5.5 Temperature dependence of lateral growth rate on well-oriented (0001)Si faces. The flow rates of SiH_4 and C_3H_8 are 0.15 and 0.10sccm, respectively.



(a)



(b)

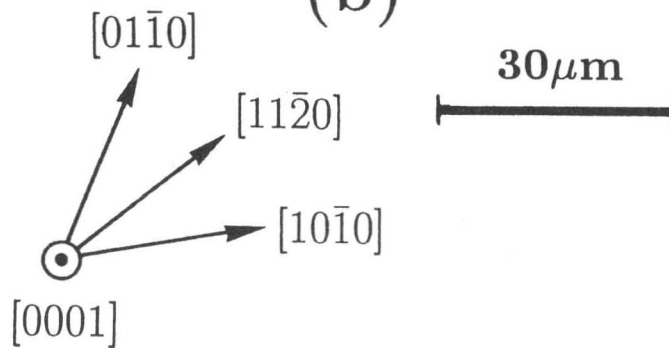


Fig.5.6 Nomarski photographs showing anisotropy in lateral growth rates; (a) before growth and (b) after 60sec growth at 1600°C .

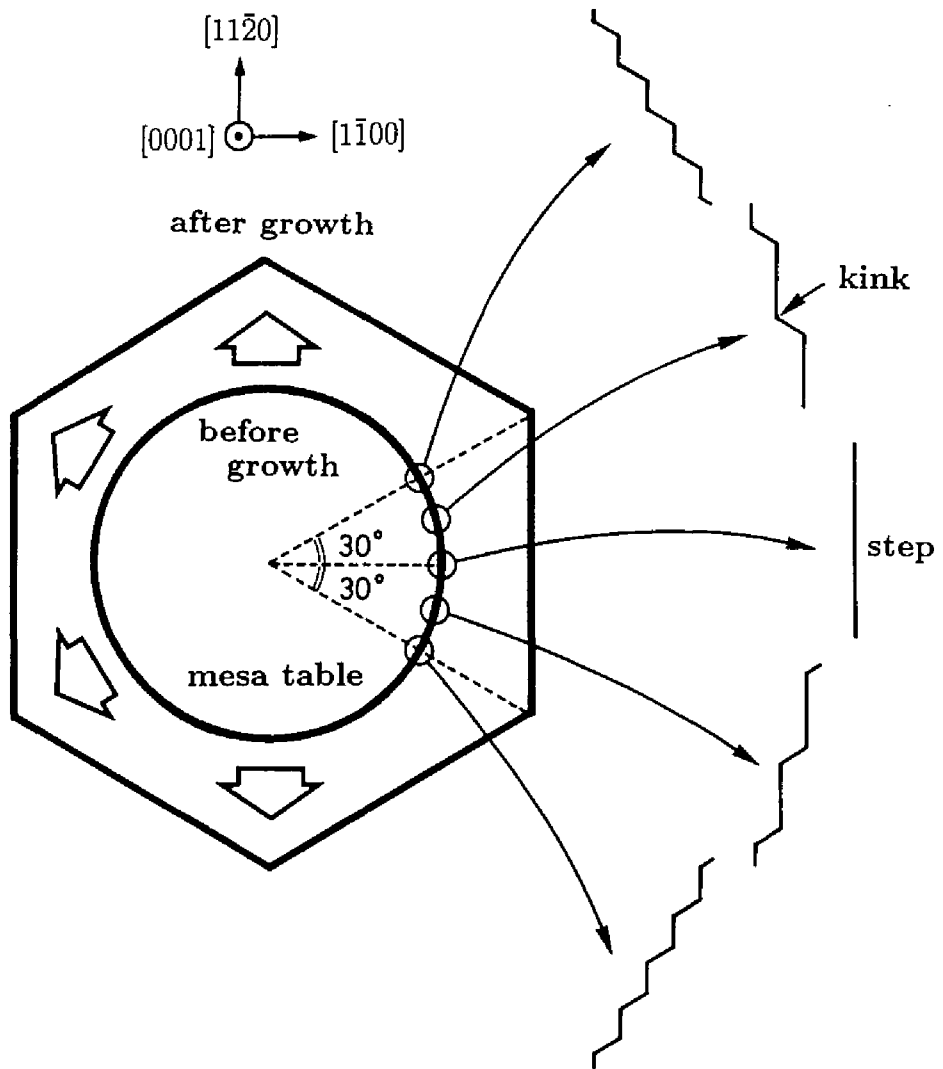


Fig.5.7 Schematic representation of step configurations on 6H-SiC{0001} faces.

lateral growth rate decreases considerably at low temperatures, owing to the decrease in the surface diffusion length of adatoms. The activation energy for the lateral growth in the temperature range of 1200~1500°C is 85kcal/mole. The slight decrease in the lateral growth rate at a high temperature of 1600°C may be attributed to the enhanced reevaporation of adsorbed species to vapor and/or the etching by H₂. The lateral growth rates reflect the surface diffusion length of adsorbed species on 6H-SiC{0001} faces. The details of this analysis will be discussed in 5.3.

Figure 5.6 shows typical surface photographs, (a) before and (b) after growth at 1600°C for 60sec. The original circular mesa-table deforms into a hexagonal shape due to the anisotropy in lateral growth rates. The fastest growth direction is $\langle 11\bar{2}0 \rangle$, and the lowest direction $\langle 1\bar{1}00 \rangle$. The anisotropy may originate from the difference in bond configurations at table edges. Microscopically, the table edges are composed of very small straight steps and kinks. Because the straight steps would align parallel to the crystal facets ($\{1\bar{1}00\}$ faces), table edges perpendicular to the $\langle 1\bar{1}00 \rangle$ direction can be regarded as straight macro-steps. The kink density increases with the deviation of direction from $\langle 1\bar{1}00 \rangle$, and becomes maximum in the $\langle 11\bar{2}0 \rangle$ direction, as shown in Fig.5.7. Then, the growth in the $\langle 1\bar{1}00 \rangle$ and $\langle 11\bar{2}0 \rangle$ directions is referred to be "step growth" and "kink growth" hereafter.

The lateral growth rates are given by

$$v_{\text{step}} = \gamma_{\text{step}} \frac{d_{\text{step}} J_s h_0}{n_{\text{step}} h}, \quad (5.1)$$

$$v_{\text{kink}} = \gamma_{\text{kink}} \frac{d_{\text{kink}} J_s h_0}{n_{\text{kink}} h}. \quad (5.2)$$

Here, v_{step} and v_{kink} are the lateral growth rates for step and kink growth, respectively. d_{step} and d_{kink} are the spacing of faces perpendicular to the $\langle 1\bar{1}00 \rangle$ and $\langle 11\bar{2}0 \rangle$ directions, n_{step} and n_{kink} the adatom site densities along steps and kinks, J_s the incoming adatom flow at table edges, respectively. h and h_0 are the height of table and the spacing of 6H-SiC{0001} faces. γ_{step} and γ_{kink} are the incorporation probabilities of migrating species at steps and kinks. By substituting d_{step} ($\sqrt{3}a/2$: a is lattice constant), d_{kink} ($a/2$), n_{step} ($1/a$), and

n_{kink} ($1/(\sqrt{3}a)$) into eqs.(5.1) and (5.2), the following equation can be derived;

$$\frac{\gamma_{\text{step}}}{\gamma_{\text{kink}}} = \frac{v_{\text{step}}}{v_{\text{kink}}}. \quad (5.3)$$

Thus, the ratio of incorporation probabilities at steps and kinks is directly given by the ratio of lateral growth rates.

Figure 5.8 shows the temperature dependence of $\gamma_{\text{step}}/\gamma_{\text{kink}}$ ratio. The ratio increases monotonously to unity with growth temperature, indicating that the anisotropy can be reduced in high-temperature growth. This may be ascribed to the increase in γ_{step} with temperature, because γ_{kink} is supposed to be less condition-dependent. Nishizawa *et al.* studied the anisotropy in Si growth using a $\text{SiCl}_4\text{-H}_2$ system, and obtained anisotropy ratios of 0.77 and 0.43 at 1200°C and 1100°C , respectively [17]. Thus, the present result shows similar tendency.

5.2.4 Effects of off-orientation

Figure 5.9 shows a surface photograph after growth at 1500°C for 60sec on an off-oriented $6\text{H-SiC}(000\bar{1})\text{C}$ substrate. The off-orientation was 5° toward $(11\bar{2}0)$. Note that no nuclei were observed, which can be attributed to the fact that the growth proceeds through step-flow. The polytype of grown layers was identified as 6H-SiC by Raman scattering measurement. In this case, the formation of $\{0001\}$ facets was observed at the table edges as shown in Fig.5.9. All the facets were located at the upstream sides of step-flow (off-orientation).

The facet formation can be explained with schematic cross-sectional views of a vicinal $\text{SiC}\{0001\}$ surface as shown in Fig.5.10. As the growth proceeds, the atomic steps advance laterally on the $\{0001\}$ faces. After enough time growth, atomic steps at the upstream side are bunched to form vast $\{0001\}$ terraces (facets). According to this model, the width of $\{0001\}$ facets (w) can be expressed by

$$w = \frac{h}{\tan \theta}, \quad (5.4)$$

where θ is the off-angle of substrates. Using the values of h (120nm) and θ (5°), the width is calculated to be $1.4\mu\text{m}$. This value shows good agreement with the experimental result ($1.7\mu\text{m}$).

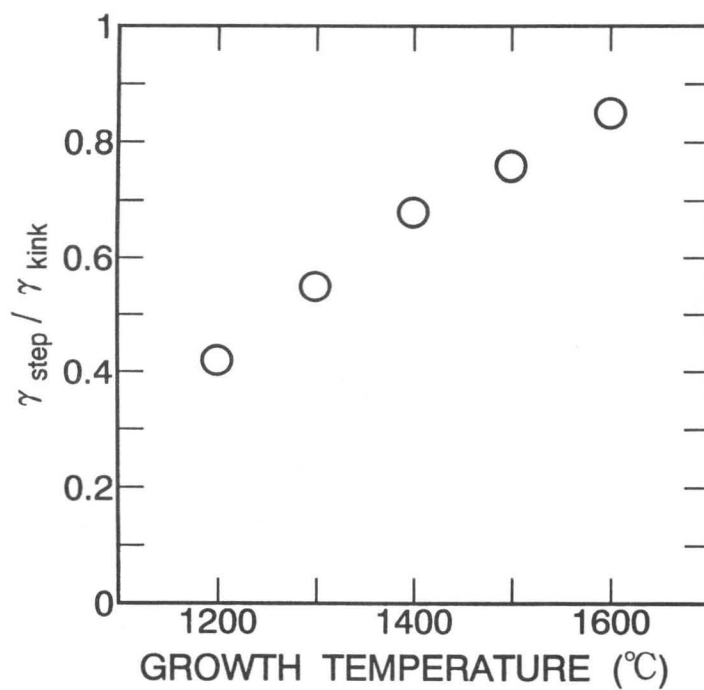


Fig.5.8 Temperature dependence of $\gamma_{\text{step}}/\gamma_{\text{kink}}$ ratio.

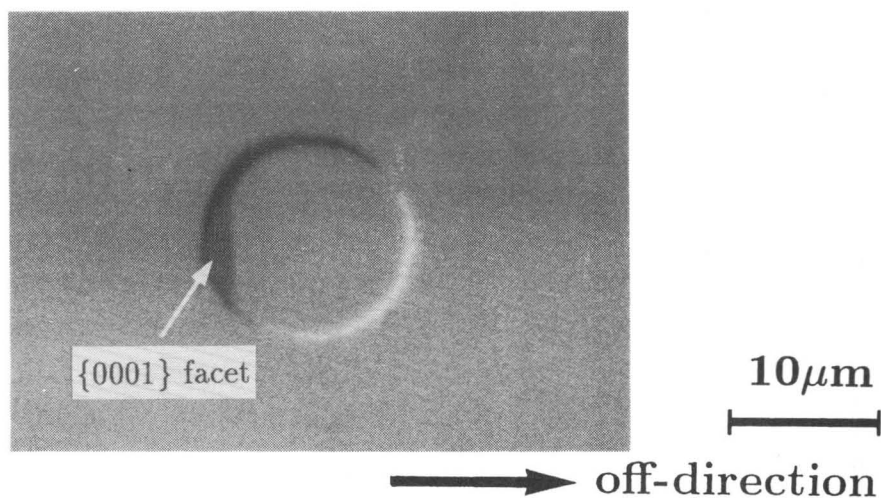
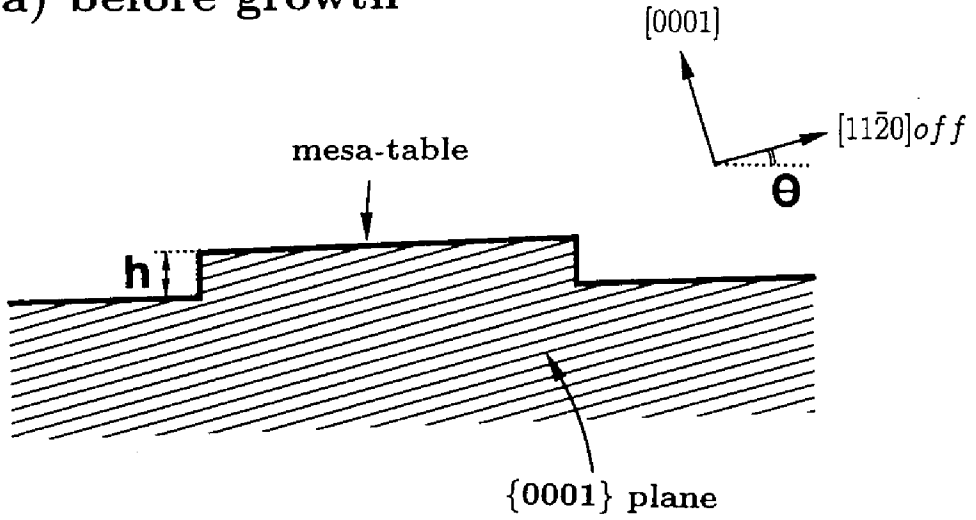


Fig.5.9 Nomarski photograph of a circular mesa-table after 60sec growth at 1500°C on 5° off-oriented 6H-SiC {0001} face.

(a) before growth



(b) after growth

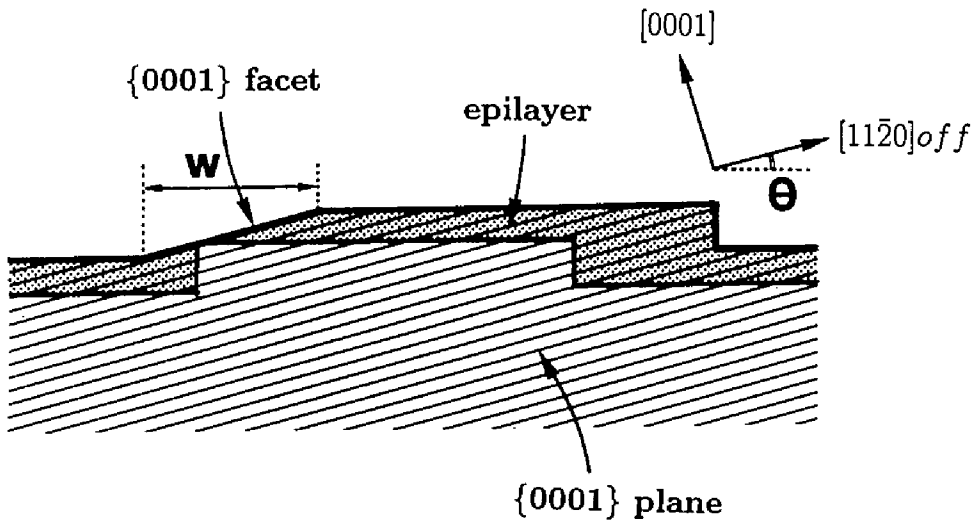


Fig.5.10 Schematic images of the $\{0001\}$ facet formation mechanism on vicinal 6H-SiC $\{0001\}$ faces; (a) before growth and (b) after growth.

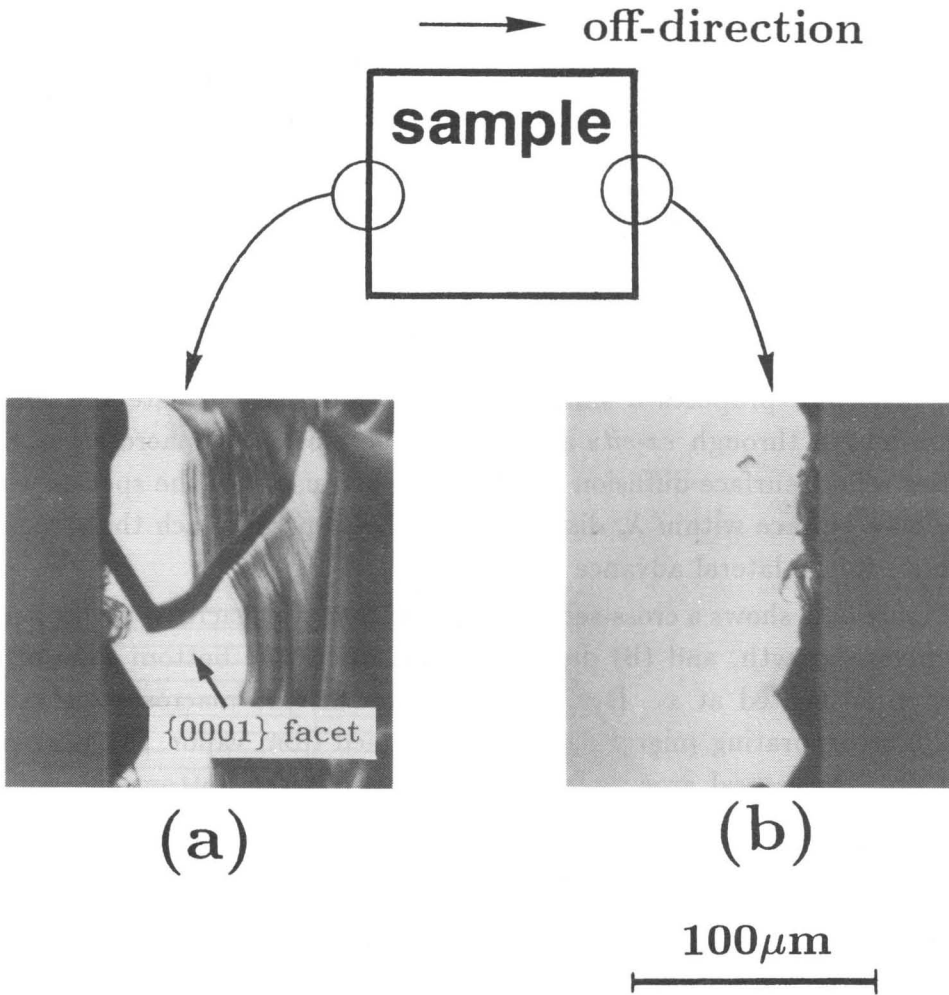


Fig.5.11 Photographs of off-oriented 6H-SiC{0001} with 5 μm thick epilayer. (a) upstream side and (b) downstream side of off-orientation. At the upstream side edge, {0001} facet is formed.

This {0001} facet formation can be observed in usual CVD growth on off-oriented substrates. Figure 5.11 shows typical photographs of sample edges with $5\mu\text{m}$ thick epilayers. Here, Figs.5.11(a) and (b) correspond to the upstream side and downstream side of off-orientation. Every sample with an epilayer has {0001} facets at the upstream side of off-orientation.

5.3 Surface Diffusion Length

5.3.1 Estimation of surface diffusion length

The author proposes a simple diffusion model to estimate the surface diffusion length through *ex-situ* analyses on the motion of macrosteps. Step velocities reflect surface diffusion lengths (λ_s), because only the species which adsorb on a surface within λ_s distance from the step can reach the step, and contribute to the lateral advance of the step.

Figure 5.12 shows a cross-sectional illustration of a macrostep with height h , (a) before growth, and (b) during growth, where the bottom edge of the macrostep is located at x . During crystal growth, the macrostep advances laterally, incorporating migrating species supplied from vapor. As is seen in Fig.5.12(b), the lateral growth rate is the fastest at the bottom layer of the macrostep, which leads to the formation of gradually inclined (stepped) region. Considering the effects of growth on this inclined region, the differential lateral growth rate (dx/dt) at the bottom can be expressed by the sum of the lateral component of a growth rate on this inclined region (v_{incl}) and the lateral growth rate of the step (v_{step}). The v_{incl} at time t can be calculated from the flux of reactants onto a surface and the slope of the inclined region ($\tan \theta = v_{\text{step}} t/h$) as follows;

$$v_{\text{incl}} = \frac{J h_0 v_{\text{step}} t}{n_0 h}, \quad (5.5)$$

where J , n_0 , and h_0 are the flux of reactants, the density of adatom sites ($1.21 \times 10^{15} \text{cm}^{-2}$), and the spacing of 6H-SiC{0001} face (0.252nm), respectively. Here, it was assumed that the condensation coefficient is unity on the inclined region where a high density of steps exist.

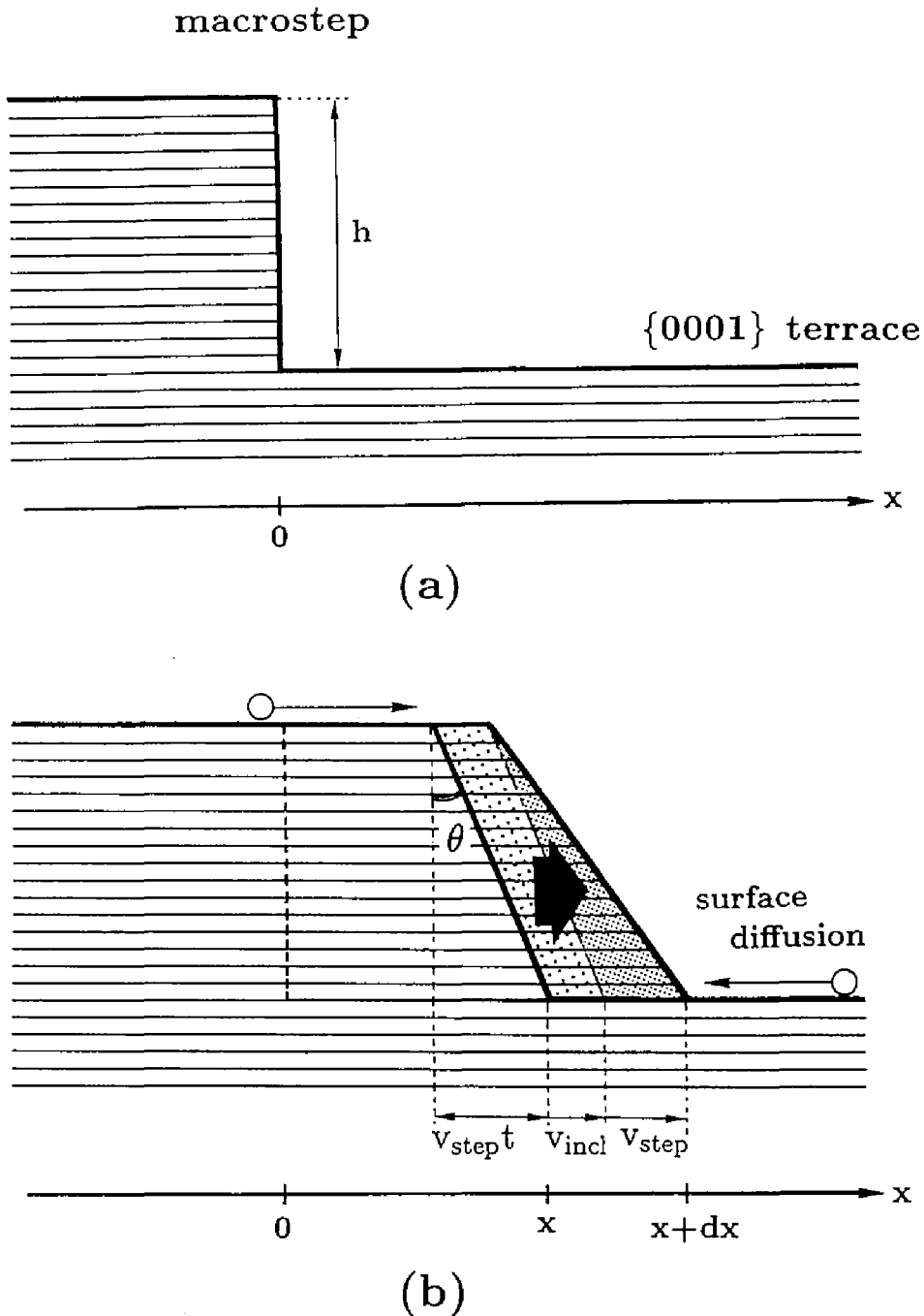


Fig.5.12 A schematic illustration of a surface diffusion model, (a) before growth, and (b) during growth. A macrostep with height h advances laterally by the capture of migrating species.

On the other hand, the v_{step} is proportional to the number of migrating species (Γ) which can reach the step per unit time. Based on the theory proposed by Burton, Cabrera, and Frank (BCF theory), the Γ is given by [18]

$$\Gamma = 2 \int_0^{\infty} J \exp\left(-\frac{x}{\lambda_s}\right) dx = 2J\lambda_s. \quad (5.6)$$

Here, the flows of migrating species from the left and right sides of the step are considered. When the incorporation probability at the macrostep is assumed to be unity, all the species reaching the step per unit time are incorporated into the crystal to form a triangle with a base v_{step} and a height h in the cross-sectional view, as shown in Fig.5.12(b). From this relationship, v_{step} can be expressed by the following equation.

$$v_{\text{step}} = \frac{2\Gamma h_0}{n_0 h} = \frac{4J\lambda_s h_0}{n_0 h}. \quad (5.7)$$

Using eqs.(5.5) and (5.7), the differential lateral growth rate dx/dt is given by

$$\frac{dx}{dt} = v_{\text{incl}} + v_{\text{step}} = \frac{Jh_0 v_{\text{step}}}{n_0 h} t + v_{\text{step}}. \quad (5.8)$$

By integrating eq.(5.8) in the range from $t=0$ to t , the lateral advance of the macrostep $x(t)$ is obtained as follows ;

$$x(t) = \frac{4J\lambda_s h_0}{n_0 h} \left(\frac{Jh_0}{2n_0 h} t^2 + t \right). \quad (5.9)$$

This equation indicates that the lateral advance of the macrostep is proportional to the surface diffusion length. Therefore, the surface diffusion length is expressed by

$$\lambda_s = \frac{n_0 h}{4Jh_0} x / \left(\frac{Jh_0}{2n_0 h} t^2 + t \right). \quad (5.10)$$

Since the flux J can be calculated based on a stagnant layer model [19], the surface diffusion length can be estimated by analyzing the lateral advance of preformed macrosteps after short-time growth. This method may be applied to growth systems of other materials by both CVD and MBE.

Experimental procedures are basically the same as those in 5.2. Circular “mesa-tables”, which can be regarded as “artificial macrosteps”, were formed on the 6H-SiC{0001} substrates. The typical height and diameter of the mesa-tables were 120nm and 20~300 μ m, respectively.

5.3.2 Influence of growth conditions on surface diffusion length

One point we should check is the dependence of lateral growth rate on the macrostep height. In the present model, v_{step} should be inversely proportional to the macrostep height h as is expected from eq.(5.7). The dependence of v_{step} on macrostep height (h) is shown in Fig.5.13. The obtained v_{step} is almost inversely proportional to h , supporting the present assumption. Thus, the height of mesa-tables was fixed at 120nm in most experiments.

Figure 5.14 shows the temperature dependence of surface diffusion length on 6H-SiC{0001} faces calculated from the lateral advance of macrosteps (table-edges) using eq.(5.10). The open and closed circles denote the lengths on (0001)Si and (000 $\bar{1}$)C faces, respectively. The data indicated by triangles will be discussed later. No significant difference in the surface diffusion lengths on both faces was observed. The diffusion length on the (0001)Si face was $13\mu\text{m}$ at 1500°C , and decreased down to $0.15\mu\text{m}$ at 1200°C . The activation energy derived in the range of $1200\sim 1500^\circ\text{C}$ was 82kcal/mole . The small decrease in surface diffusion length at 1600°C may be caused by enhanced desorption and/or etching by H_2 at the high temperature.

In general, the lifetime of migrating species is determined by competitive processes of desorption to vapor and capture at steps or growth nuclei. These processes are schematically shown in Fig.5.15. Since we estimated the surface diffusion length in consideration of both processes mentioned above, the diffusion length is expressed by

$$\lambda_s = \sqrt{D_s \frac{\tau_{\text{sd}}\tau_{\text{sc}}}{\tau_{\text{sd}} + \tau_{\text{sc}}}}. \quad (5.11)$$

Here, D_s , τ_{sd} , and τ_{sc} are the surface diffusion coefficient, the lifetime of migrating species before desorption, and the lifetime before incorporation into steps or growth nuclei. D_s decreases with lowering temperature according to activation-type relationship as follows [18].

$$D_s = D_0 \exp\left(-\frac{E_{\text{diff}}}{kT}\right), \quad (5.12)$$

where E_{diff} is the activation energy for surface diffusion. k and T are the

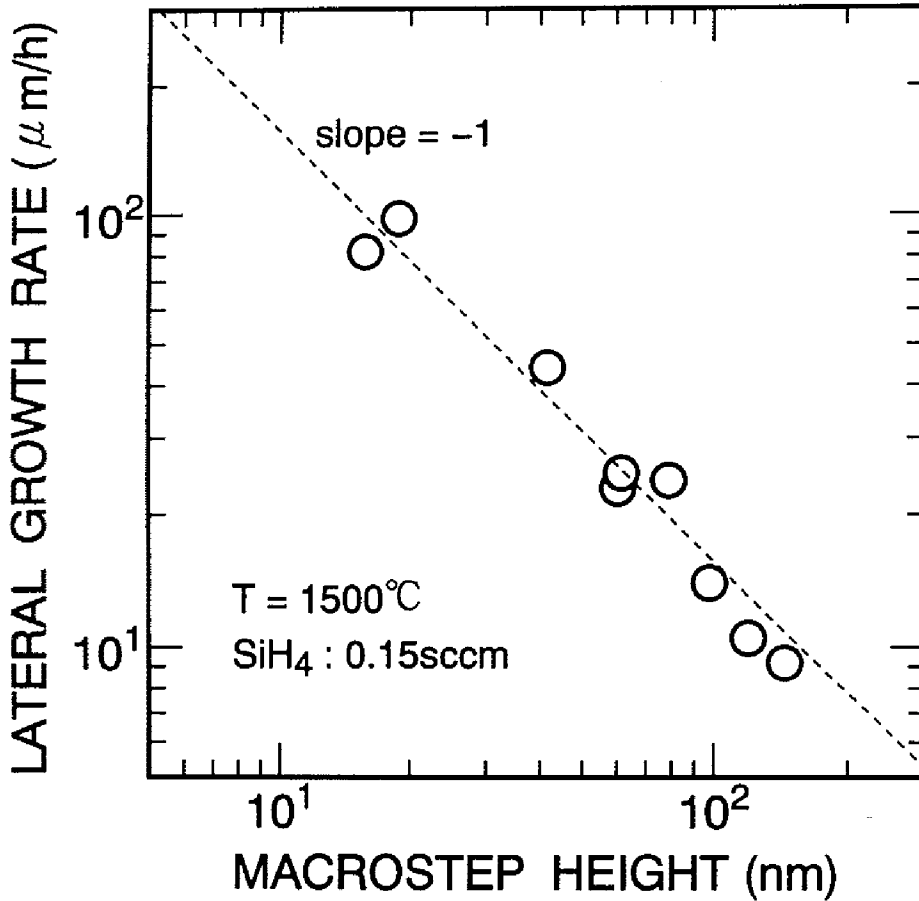


Fig.5.13 Dependence of lateral growth rate on macrostep height.

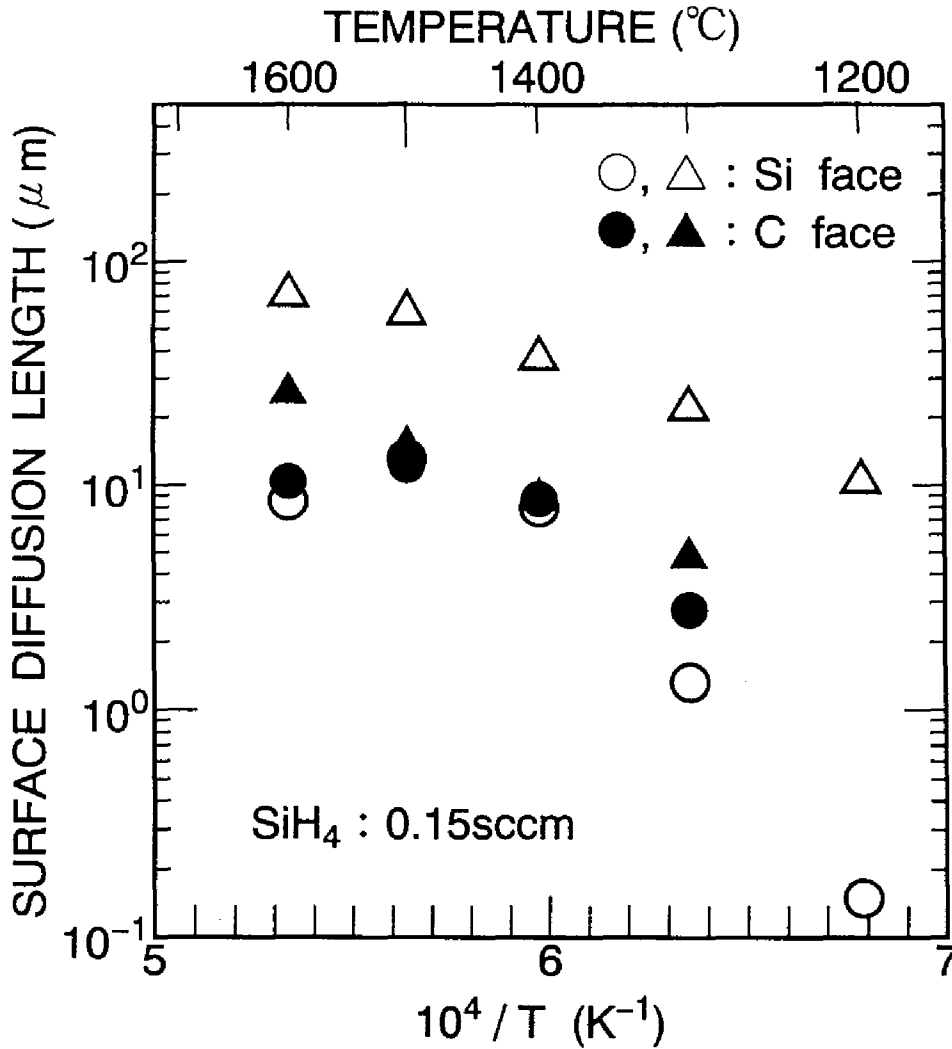


Fig.5.14 Temperature dependence of surface diffusion length (λ_s). The open and closed circles denote the results on (0001)Si and (000 $\bar{1}$)C faces, respectively. The open and closed triangles are the data (λ'_s) derived using eq.(5.13). The SiH_4 and C_3H_8 flow rates are 0.15 and 0.10sccm.

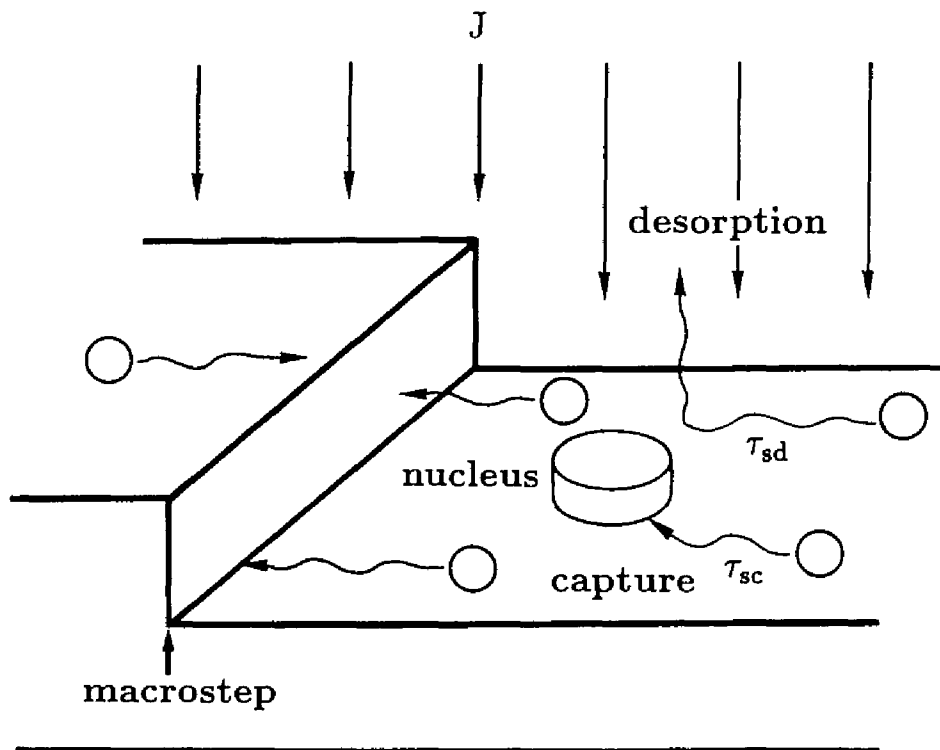


Fig.5.15 A schematic illustration of surface kinetics near a macrostep. The lifetime of migrating species is determined by desorption and capture processes.

Boltzmann constant and the absolute temperature. This equation suggests one of the reasons why the surface diffusion length shows serious decrease at reduced temperatures as shown in Fig.5.14.

The decrease in λ_s at low temperatures can be also attributed to the change of τ_{sc} . The nucleus density drastically increased for low-temperature growth, probably due to the increased supersaturation. The increased nucleus density (N_{nuc}) enhances the capture of migrating species at nuclei, which leads to the decrease in τ_{sc} , because τ_{sc} is inversely proportional to N_{nuc} . Thus, the reduction of surface diffusion length at low temperatures may be ascribed to the declines in both D_s and τ_{sc} . Although τ_{sd} is also dependent on temperature, it becomes longer with lowering temperature. This change of τ_{sd} has very little influence on the decrease in λ_s .

Nishizawa *et al.* reported pioneering works on surface kinetics in Si and GaAs growth through short-time growth experiments [7,17,20]. They proposed that the surface diffusion length (λ'_s) is approximately given by one-half of the average distance between growth nuclei [17];

$$\lambda'_s = \frac{1}{2\sqrt{N_{nuc}}}. \quad (5.13)$$

In Fig.5.14, the surface diffusion lengths estimated from the nucleus density (in Fig.5.2) using eq.(5.13) are shown by open and closed triangles. The open and closed triangles represent the data on (0001)Si and (000 $\bar{1}$)C faces, respectively. Although the surface diffusion length on the C face calculated using eq.(5.11) (λ_s) show relatively good agreement with that estimated from nucleus density (λ'_s), large difference is observed in the surface diffusion lengths on the Si face.

This contradiction can be explained by the difference of assumption employed in both the models. In eq.(5.13), all the migrating species are assumed to be captured by growth nuclei before desorption. Then, eq.(5.13) can be expressed by

$$\lambda'_s = \sqrt{D_s \tau_{sc}}. \quad (5.14)$$

This assumption may be valid when the surface diffusion length is very long or the nucleus density is high enough to satisfy $\tau_{sd} \gg \tau_{sc}$. In the present growth system, $\tau_{sd} \gg \tau_{sc}$ may be satisfied on the C face due to the much higher nucleus

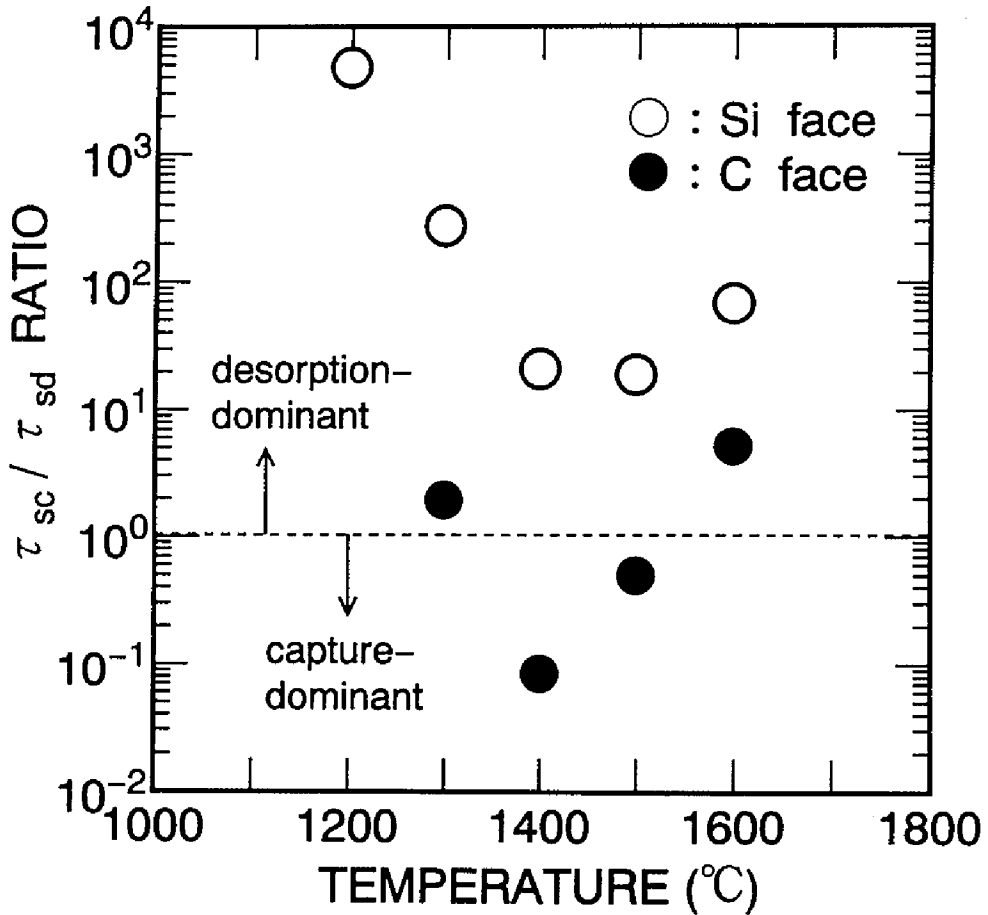


Fig.5.16 Temperature dependence of τ_{sc}/τ_{sd} ratio. The open and closed circles denote the results on (0001)Si and (000 $\bar{1}$)C faces, respectively.

density (Fig.5.2). On the Si face, however, the nucleus density is not so high as on the C face, and desorption of migrating species cannot be neglected. In this case, eq.(5.13) does not give true surface diffusion length.

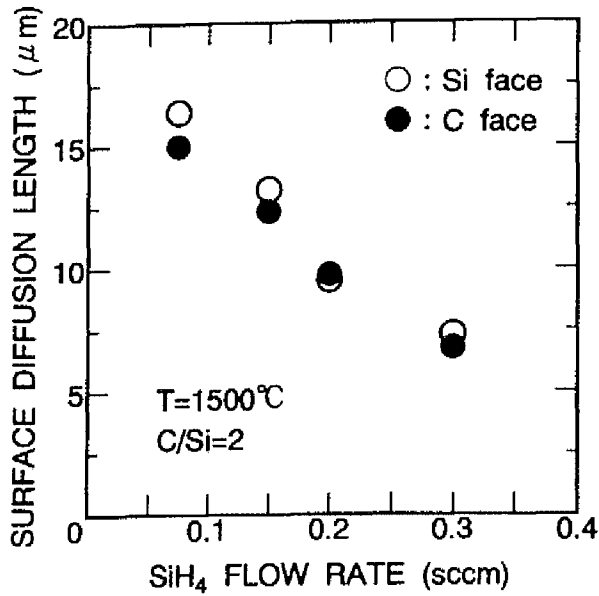
As is expected from eq.(5.12), the lifetime of migrating species is mainly determined by the shorter one between τ_{sd} and τ_{sc} . By combining eqs.(5.11) and (5.14), the following equation can be obtained.

$$\frac{\tau_{sc}}{\tau_{sd}} = \left(\frac{\lambda'_s}{\lambda_s}\right)^2 - 1. \quad (5.15)$$

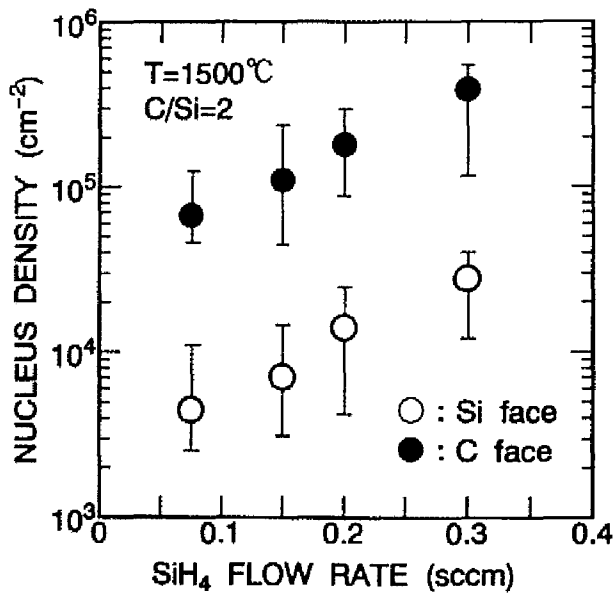
Thus, we can estimate the τ_{sc}/τ_{sd} ratio using the values of λ_s and λ'_s shown in Fig.5.14. The τ_{sc}/τ_{sd} ratio indicates which process is dominant to limit the lifetime of migrating species, desorption (for $\tau_{sc}/\tau_{sd} > 1$) or capture at growth nuclei (for $\tau_{sc}/\tau_{sd} < 1$).

Figure 5.16 shows the temperature dependence of τ_{sc}/τ_{sd} ratio derived from the data in Fig.5.14. The τ_{sc}/τ_{sd} ratios on the C face take smaller values, reflecting much higher nucleus density. Note that the τ_{sc}/τ_{sd} ratios on both the faces become the minima at 1400~1500°C. At low temperatures (1200~1300°C), τ_{sc}/τ_{sd} ratios decrease with temperature, probably owing to the activated surface diffusion which promotes the capture process. On the other hand, the τ_{sc}/τ_{sd} ratios increase in the high-temperature region (1500~1600°C), which may result from the enhanced desorption.

The dependence of surface diffusion length on source gas flow rates was investigated. Figure 5.17 shows the SiH_4 flow rate dependence of (a) surface diffusion length, and (b) nucleus density at 1500°C under a fixed flow rate ratio of SiH_4 and C_3H_8 ($\text{C}/\text{Si}=2.0$). Under these conditions, the vertical growth rate increases proportionally with the SiH_4 flow rate, as shown in Fig.3.10. The diffusion length decreased under high flow rate conditions. In this case, the surface diffusion coefficient (D_s) can be regarded as constant because of fixed growth temperature. On the other hand, the nucleus density increased monotonously with the flow rate owing to increased supersaturation, as shown in Fig.5.17(b). Then, only the decrease in τ_{sc} may be responsible for the reduction in surface diffusion length under high flow rate conditions. The SiH_4 flow rate dependence of τ_{sc}/τ_{sd} ratio is shown in Fig.5.18. The τ_{sc}/τ_{sd} ratios decrease gradually with increasing the SiH_4 flow rate, which can be again



(a)



(b)

Fig.5.17 SiH_4 flow rate dependence of (a) surface diffusion length, and (b) nucleus density at 1500°C under fixed flow rate ratio of SiH_4 and C_3H_8 . The open and closed circles denote the results on (0001)Si and (000 $\bar{1}$)C faces, respectively.

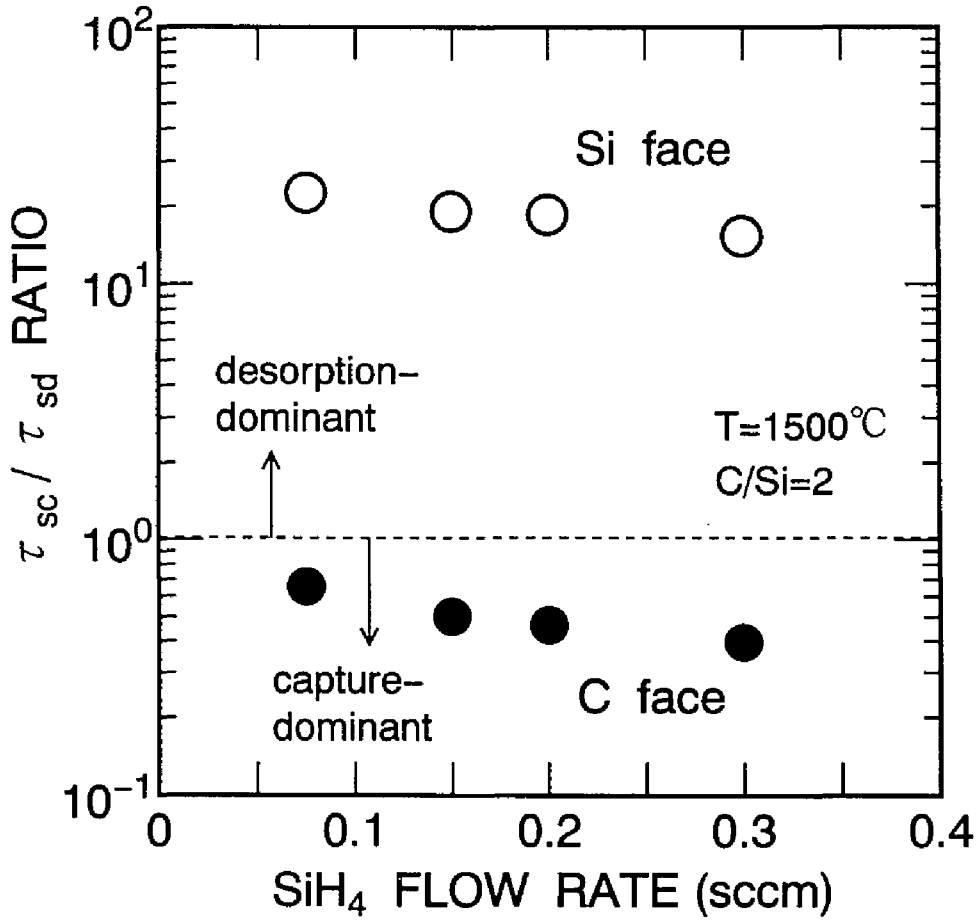
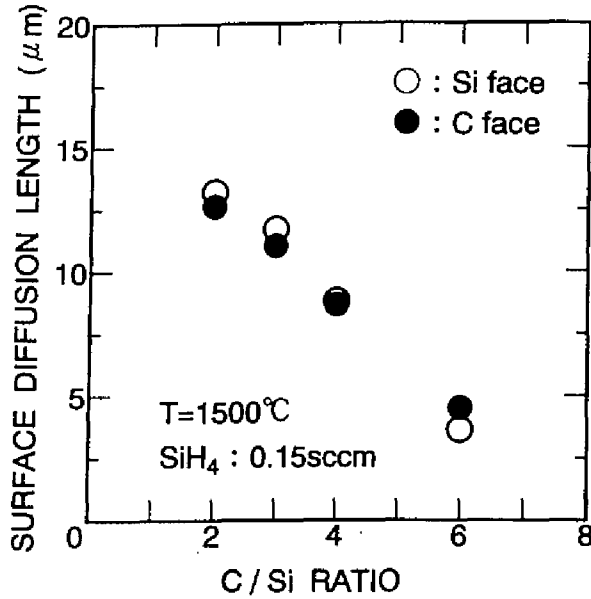
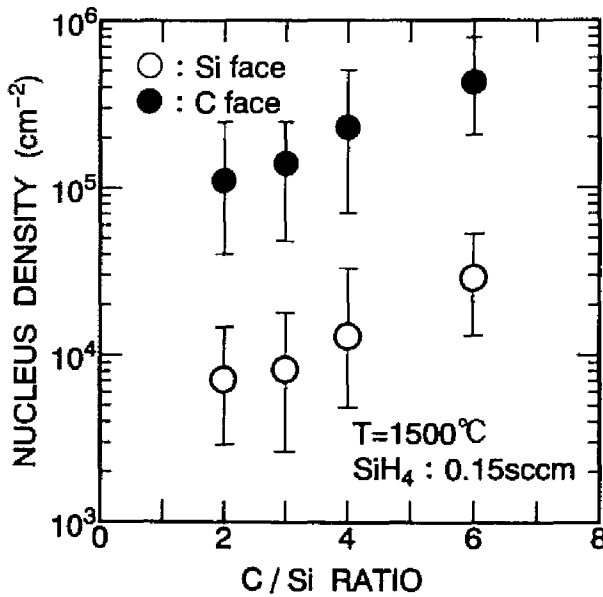


Fig.5.18 SiH_4 flow rate dependence of τ_{sc}/τ_{sd} ratio. The open and closed circles denote the results on $(0001)\text{Si}$ and $(000\bar{1})\text{C}$ faces, respectively.



(a)



(b)

Fig.5.19 C/Si ratio dependence of (a) surface diffusion length, and (b) nucleus density at 1500°C under fixed flow rate of SiH_4 (0.15 sccm). The open and closed circles denote the results on $(0001)\text{Si}$ and $(000\bar{1})\text{C}$ faces, respectively.

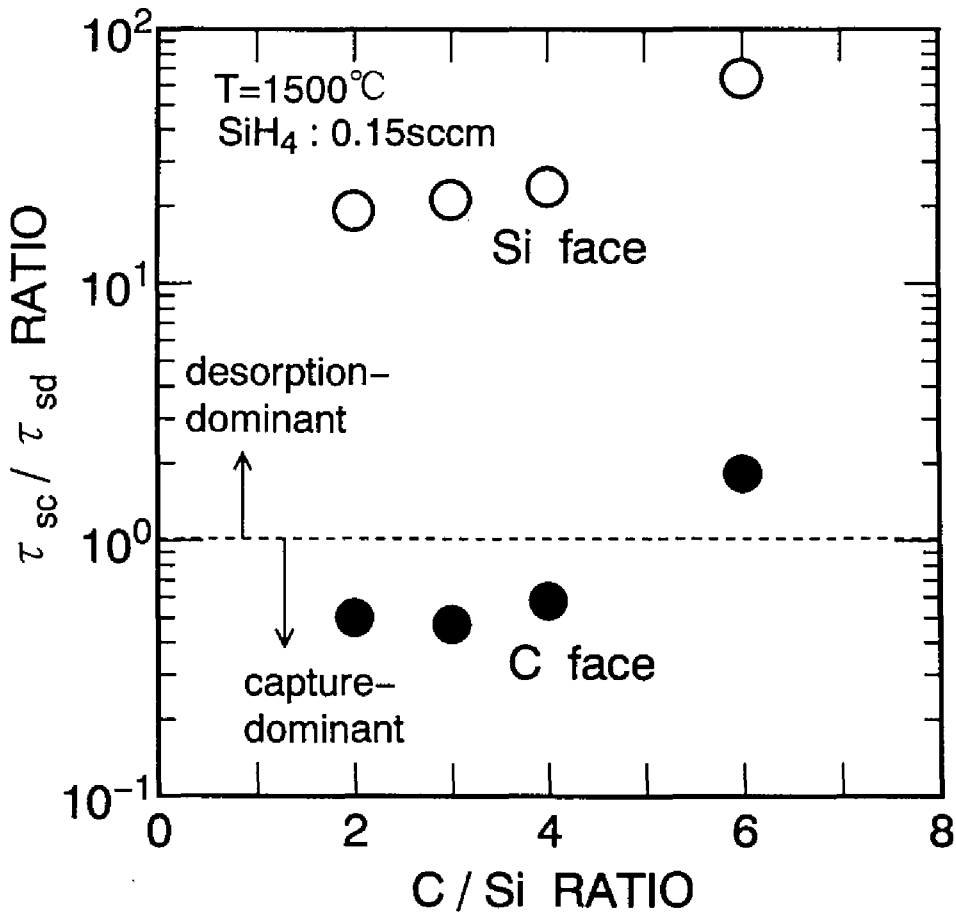


Fig.5.20 C/Si ratio dependence of τ_{sc}/τ_{sd} ratio. The open and closed circles denote the results on (0001)Si and (000 $\bar{1}$)C faces, respectively.

explained by the decrease in τ_{sc} .

Figure 5.19 shows the C/Si ratio (ratio of C and Si atoms in supplied source gases) dependence of (a) surface diffusion length, and (b) nucleus density at 1500°C under a fixed flow rate of SiH₄ (0.15sccm). Under these conditions, the vertical growth rate shows no significant change, indicating that the excess supply of C species does not contribute to SiC growth (cf. Fig.3.2). With the increase in C/Si ratio, the surface diffusion length decreased and the nucleus density increased. Although the shorter surface diffusion length under C-rich conditions can be attributed to the decrease in τ_{sc} caused by promoted nucleation, the real surface process may be more complicated. The corresponding change in τ_{sc}/τ_{sd} ratio is shown in Fig.5.20. The enhanced nucleation under C-rich conditions should shorten τ_{sc} , which leads to the decrease in τ_{sc}/τ_{sd} ratio as in the case of Fig.5.18. However, the τ_{sc}/τ_{sd} ratios increase with C/Si ratio, indicating the reduction of τ_{sd} . One possible explanation for this result is the change of migrating species by changing the source supply ratio, which may bring about different surface reactions and/or surface diffusion dynamics.

In crystal growth of compound semiconductors, it is generally difficult to identify migrating species. In GaAs growth, a model to explain the effects of V/III ratio on the lateral growth rates has been reported assuming that Ga adatoms as dominant migrating species [21]. However, dominant migrating species have not been revealed in CVD growth of SiC. Further study on surface kinetics including chemical reactions is required to clarify the effects of C/Si ratio on surface diffusion length.

5.3.3 Discussion

As for step-dynamics on 6H-SiC{0001} faces, the author estimated the surface diffusion lengths using a growth model on a vicinal surface and the critical growth conditions where the growth mode changes from step-flow to two-dimensional nucleation, which was presented in Chapter 4. The estimated surface diffusion lengths at 1500°C were about 0.3 and 3 μ m on Si and C faces, respectively. These values are much shorter than those derived in this study. This discrepancy may originate from an oversimplified model described in Chapter 4. For example, terraces uniformly distributed were assumed in the

model, which is not true in a real crystal surface, as the author already pointed out in 4.4.1. TEM and AFM observation revealed that relatively vast terraces exist on grown surfaces. On such a vast terrace, supersaturation becomes high, causing two-dimensional nucleation. Besides, the estimation of n_{s0}/τ_s and α_{crit} may contain an error due to the simplified assumptions.

On the other hand, the method proposed here employs only a few assumptions. One may think that the lateral advance of “giant macrosteps” with 120nm height is different from that of atomic or a few monolayer height steps. However, the relationship between the lateral advance and step height was checked as shown in Fig.5.13, supporting the validity of the present model. Another point one may ask is that $\{0001\}$ surfaces are not perfectly “step-free” terraces. This will be true: A small number of steps might exist on $\{0001\}$ surfaces. But such steps will bunch to disappear at the initial stage of growth, giving a minor influence on the calculation. Thus, the present model is a more direct method to estimate the surface diffusion length, and seems to give more reliable values, compared with the model in Chapter 4.

5.4 Summary

The surface kinetics of SiC growth on 6H-SiC $\{0001\}$ substrates by CVD at 1200~1600°C was studied. Through short-time growth experiments, the nucleation density and lateral growth rate of steps were investigated in detail.

On well-oriented 6H-SiC $\{0001\}$ faces, the nucleus density is much higher on (000 $\bar{1}$)C faces than on (0001)Si faces, which can be explained by the difference in surface energies between both the faces. At lower temperatures, the growth nuclei increase in number and become smaller in size, because of the reduced surface diffusion length and the increased supersaturation. Raman scattering measurements revealed that the nuclei have 3C-SiC component. The lateral growth rate is about three orders of magnitude higher than the vertical growth rate at temperatures higher than 1400°C. The lateral growth rate has anisotropy, higher in the $\langle 11\bar{2}0 \rangle$ direction and lower in the $\langle 1\bar{1}00 \rangle$ direction. With the decrease in growth temperature, the anisotropy is enhanced.

On the other hand, no nucleation is observed on off-oriented $\{0001\}$ faces

at 1500°C. This result can be attributed to quite low supersaturation caused by high-density of surface steps.

A simple diffusion model was proposed that the surface diffusion length can be estimated from the lateral growth rates of macrosteps. The surface diffusion length was about $13\mu\text{m}$ on (0001)Si and (000 $\bar{1}$)C faces under a typical growth condition at 1500°C. The diffusion length decreased for low-temperature growth. This decrease in diffusion length is attributed to the suppressed surface diffusion coefficient, and to the reduction in lifetime of migrating species caused by enhanced incorporation of migrating species into growth nuclei. The increased nucleus density under the high flow rate condition brought about the decrease in surface diffusion length. The reduced surface diffusion length under the C-rich condition was also observed. The method proposed in this study is useful for the estimation of surface diffusion length in epitaxial growth of any other materials.

References

- [1] S.Nilsson, E.van Gieson, D.J.Arent, H.P.Meier, W.Walter, and T.Forster, *Appl. Phys. Lett.*, **55**, 972(1989).
- [2] T.Shitara and T.Nishinaga, *Jpn. J. Appl. Phys.*, **28**, 1212(1989).
- [3] M.Hata, T.Isu, A.Watanabe, and Y.Katayama, *Appl. Phys. Lett.*, **56**, 2542(1990).
- [4] X.Q.Shen, D.Kishimoto, and T.Nishinaga, *Jpn. J. Appl. Phys.*, **33**, 11(1994).
- [5] J.P.Hirth and G.M.Pound, *Condensation and Evaporation, Nucleation and Growth Kinetics*, (Pergamon Press, Oxford, 1963).
- [6] B.A.Joyce, R.R.Bradley, and G.R.Booker, *Phil. Mag.*, **15**, 1167(1967).
- [7] J.Nishizawa, T.Terasaki, and M.Shimbo, *J. Crystal Growth*, **17**, 241(1972).
- [8] S.Yoshida, E.Sakuma, H.Okumura, S.Misawa, and K.Kondo, *J. Appl. Phys.*, **62**, 303(1987).
- [9] H.S.Kong, J.T.Glass and R.F.Davis, *J. Mat. Res.*, **4**, 204(1989).
- [10] H.Matsunami, T.Ueda and H.Nishino, *Mat. Res. Soc. Symp. Proc.*, **162**, 397(1990).
- [11] J.A.Powell, D.J.Larkin, L.G.Matus, W.J.Choyke, J.L.Bradshaw, L.Henderson, M.Yoganathan, J.W.Yang, and P.Pirouz, *Appl. Phys. Lett.*, **56**, 1353(1991).
- [12] E.Pearson, T.Takai, T.Halicioglu, and W.A.Tiller, *J. Crystal Growth*, **70**, 33(1984).
- [13] J.A.Powell, J.B.Petit, J.H.Edgar, I.G.Jenkins, L.G.Matus, J.W.Yang, P.Pirouz, W.J.Choyke, L.Clemen, and M.Yoganathan, *Appl. Phys. Lett.*, **56**, 333(1991).

- [14] D.W.Feldman, J.H.Parker, Jr., W.J.Choyke, and L.Patrick, *Phys. Rev.*, **170**, 698(1968).
- [15] S.Nakashima, H.Katahama, Y.Nakakura, and A.Mitsuishi, *Phys. Rev.*, **B33**, 5721(1986).
- [16] W.J.Choyke, Z.C.Feng, and J.A.Powell, *J. Appl. Phys.*, **64**, 3163(1988).
- [17] J.Nishizawa, Y.Kato, and M.Shimbo, *J. Crystal Growth*, **31**, 290(1975).
- [18] W.K.Burton, N.Cabrera, and F.C.Frank, *Philos. Trans. Roy. Soc. London*, **A243**, 299(1951).
- [19] F.C.Eversteyn, P.J.W.Severin, C.H.J.v.d.Brekel, and H.L.PEEK, *J. Electrochem. Soc.*, **117**, 925(1970).
- [20] J.Nishizawa and M.Kimura, *J. Crystal Growth*, **74**, 331(1986).
- [21] H.Asai, *J. Crystal Growth* **80**, 425(1987).

Chapter 6

Characterization of Epilayers and Impurity Doping

6.1 Introduction

Device performance is severely affected by defects and impurities in materials. In real semiconductor materials, many kinds of defects and impurities do exist, and different defects or impurities play quite different roles in optical and electrical properties of a material. Thus, characterization of semiconductor materials needs variety of measurement techniques which elucidate different aspects of crystal quality.

Nowadays, advanced α -SiC devices utilizing epilayers grown by step-controlled epitaxy have been successfully fabricated [1]. However, reports on characterization of SiC epilayers are very limited. High crystal quality is demonstrated by planar TEM observation [2,3] and infrared (IR) reflectivity [4]. Hall effect measurement revealed a low compensation ratio (~ 0.01) in undoped epilayers [4,5]. Low-temperature photoluminescence has been also used to check the quality and to estimate the impurity concentration [3,6]. However, these are not enough for full characterization of epilayers. For example, dislocations in epilayers and deep levels which control the carrier lifetime and electric conduction are of great importance.

In general, undoped SiC crystals show n-type conduction due to nitrogen

(N), an effective donor, contamination from a growth system. For device fabrication, precise control of n- and p-type conduction in a wide range is required. In Si or GaAs, three types of impurity doping techniques are employed, *in-situ* doping during epitaxial growth, diffusion, and ion implantation. In SiC, however, a diffusion process cannot be used due to the extremely low diffusion coefficients of impurities in SiC. Ion implantation should be a key technology especially for selective doping in SiC. Although there have been a few reports on *in-situ* doping [4,7,8] and ion implantation [9,10] into 6H-SiC epilayers, no systematic studies have been reported.

In this chapter, detailed characterization of SiC epilayers is presented. After examination of defects in crystals with etching and TEM observation, the optical and electrical properties are given together with deep level analyses. *In-situ* doping of impurities and ion implantation are also investigated. As dopants, N (donor), B and Al (acceptor) are employed.

6.2 Structural Characterization

The crystal quality of epilayers was characterized by Rutherford backscattering spectroscopy (RBS), double crystal X-ray diffraction, cross-sectional TEM, and chemical etching.

Figure 6.1 shows RBS spectra from a $5\mu\text{m}$ -thick 6H-SiC epilayer. The RBS measurement was performed using a 2.0MeV He^{2+} beam with a backscattering angle of 170° . The epilayers show a very small χ_{min} (the minimum yield in the aligned spectrum normalized by the random yield) at the Si edge of 1.7%, which almost coincides with the theoretical value (1.5%) for a perfect 6H-SiC crystal under this measurement condition [11]. Besides, the contamination of any heavy metals (Ti, Fe, Ni, *etc.*) was not detected, though the detection limit is rather high ($\sim 10^{18}\text{cm}^{-3}$).

A typical X-ray rocking curve from a $10\mu\text{m}$ -thick 6H-SiC epilayer is shown in Fig.6.2. The diffraction plane is $6\text{H-SiC}\{0006\}$ ($2\theta=35.60^\circ$). The curve is almost Gaussian with a full width of half maximum (FWHM) of 26arcsec. The FWHM for a perfect crystal (ΔW_0) depends on the measurement system, such as the diffraction plane of the first crystal, and can be approximately expressed

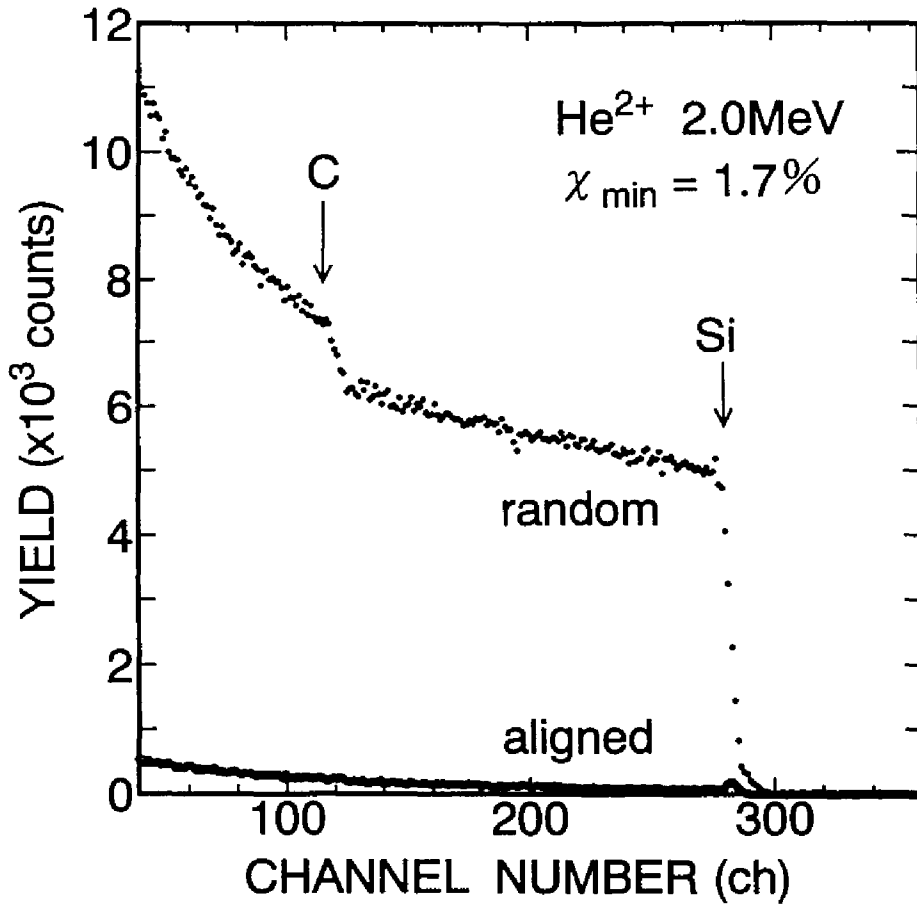


Fig.6.1 RBS spectra from a 5 μ m-thick 6H-SiC epilayer.

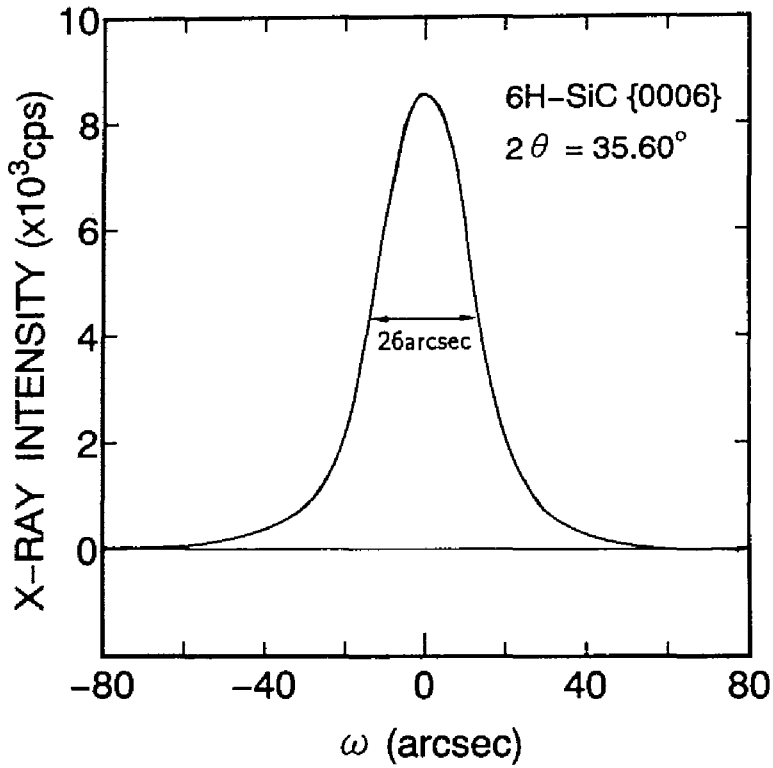


Fig.6.2 Typical X-ray rocking curve from a 10 μ m-thick 6H-SiC epilayer.

Table 6.1 Parameters in the present X-ray diffraction measurement system.

ΔW_1 (GaAs(400))	8.5 arcsec
ΔW_2 (6H-SiC(0006))	3.0 arcsec
δ	25.5 arcsec
FWHM	27.0 arcsec

by the following equation [12]

$$\Delta W_0 = \sqrt{(\Delta W_1)^2 + (\Delta W_2)^2 + \delta^2}, \quad (6.1)$$

where ΔW_1 and ΔW_2 are the FWHMs for the first and second (sample) crystals. δ comes from the difference in the diffraction angles between the first and second crystals, and is given by [12]

$$\delta = \frac{\Delta\lambda}{\lambda}(\tan\theta_1 - \tan\theta_2). \quad (6.2)$$

Here, λ is the X-ray wavelength (1.5406Å for Cu $K\alpha_1$), $\Delta\lambda$ the FWHM of the X-ray (5.8×10^{-4} Å). θ_1 and θ_2 are the diffraction angles for the first (GaAs(004)) and second (6H-SiC(0006)) crystals, respectively. These parameters in the measurement system are listed in Table 6.1. Using eq.(6.1), the FWHM is estimated to be 27arcsec for a perfect 6H-SiC{0001} crystal. Thus, the epilayer has excellent quality, keeping epitaxial relationship with the substrate. Glass *et al.* reported that 6H-SiC wafers prepared by a modified Lely method have a "domain structure" based on a high-resolution X-ray analysis [13]. For further study, a detailed analysis using an improved measurement system will be required. For example, 6H-SiC{0001} should be used as the first crystal.

Figure 6.3 shows typical cross-sectional TEM images of a 10 μ m-thick 6H-SiC epilayer. The sample was examined along the (1 $\bar{1}$ 00) zone axis. The author observed more than 80 images for 15 samples, and almost every time got TEM images as shown in Fig.6.3(a). This result indicates that it is hard to detect defects in epilayers with cross-sectional TEM, with which a small area is observed. However, a few TEM images exhibited the existence of stacking faults in the {0001} plane as shown in Fig.6.3(b). Dislocations are also observed near the stacking faults. From careful observation, all the stacking faults are turned out to come from substrates. The inheritance of stacking faults from substrates may be inevitable in step-controlled epitaxy.

For the epilayers grown under an optimum condition, very smooth surfaces can be obtained, and almost all the surface pits originate from so-called "micropipes" in the substrates. The micropipes are pin-holes with 0.1~5 μ m diameter, propagating along the c axis [14-16]. Figure 6.4 shows Nomarski microphotographs of 6H-SiC surfaces around a micropipe (a) before growth and

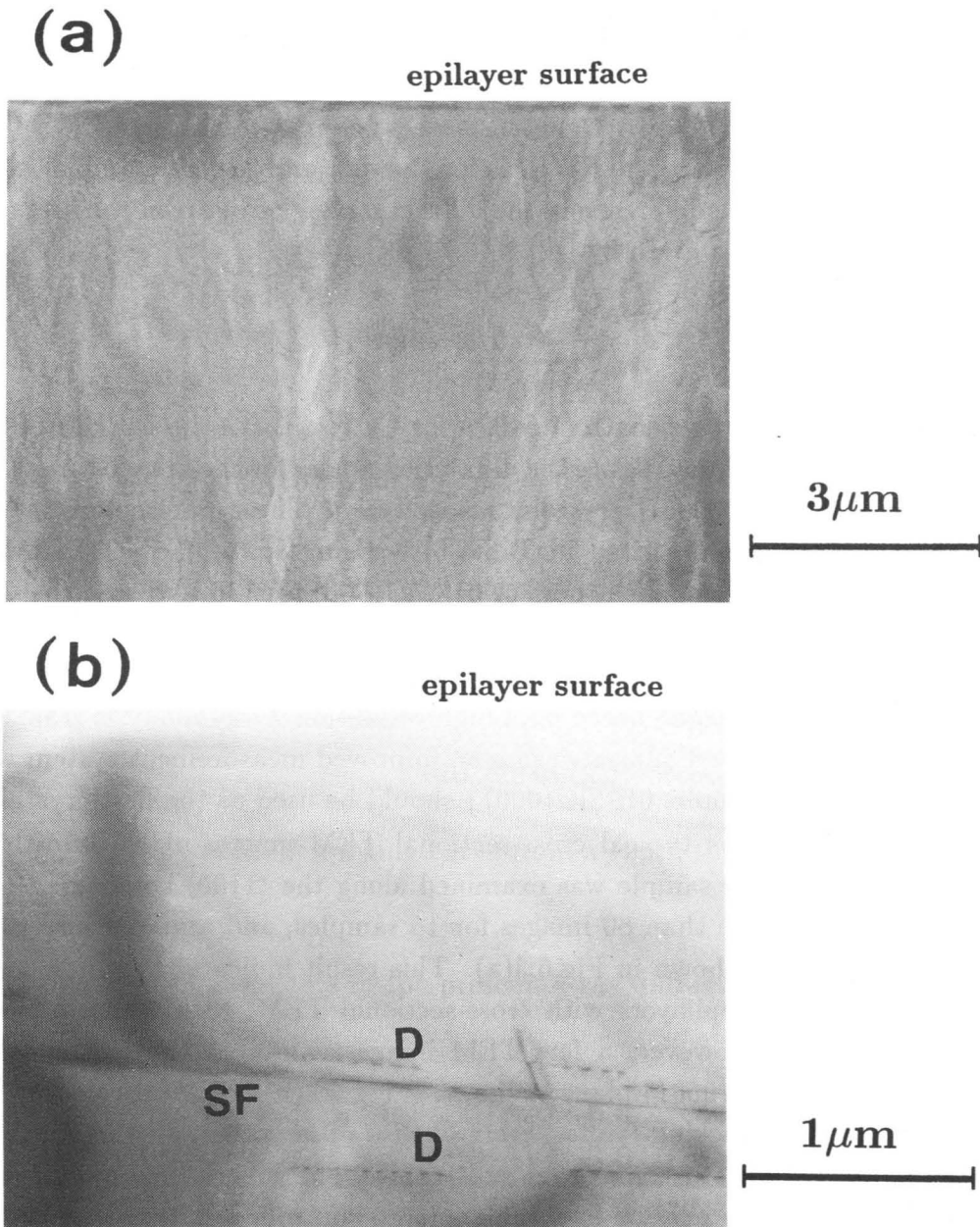


Fig.6.3 Cross-sectional TEM images of a 10 μm-thick 6H-SiC epilayer. (a) typical TEM image showing no defects, and (b) TEM image showing the existence of stacking faults and dislocations (SF:stacking faults, D:dislocation).

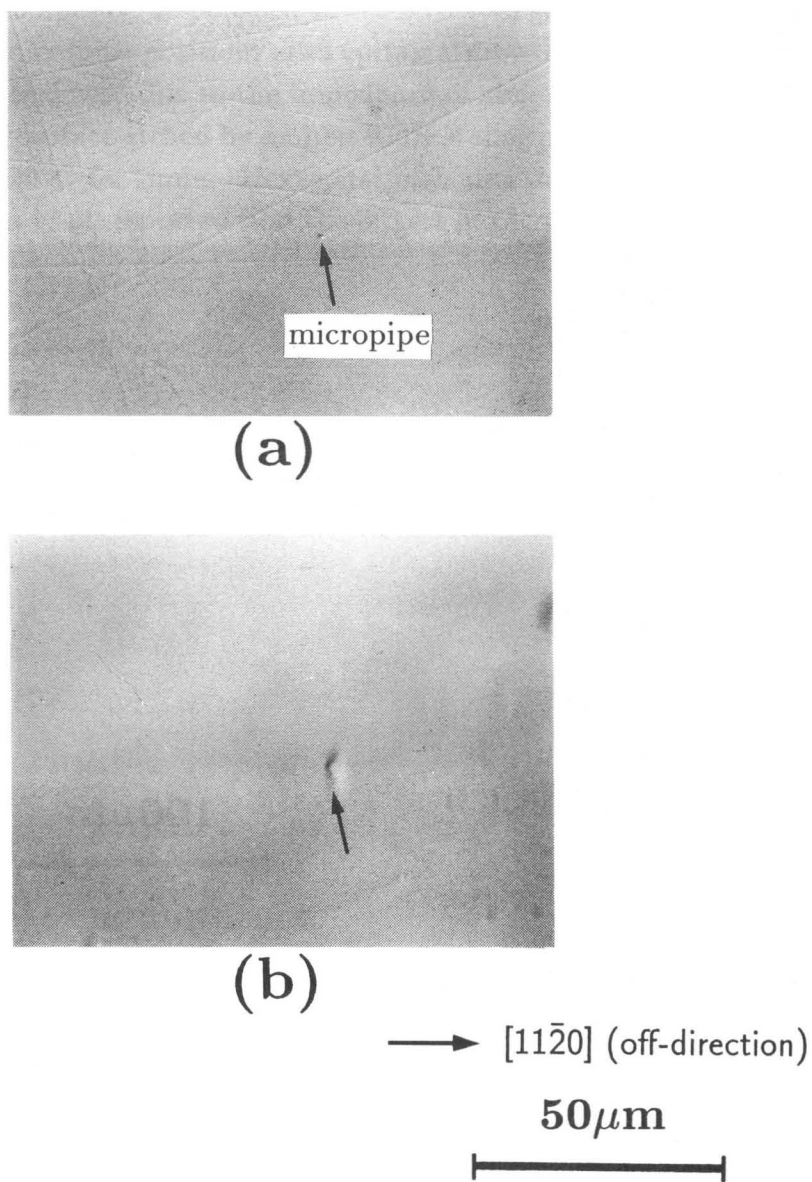


Fig.6.4 Nomarski microphotographs of 6H-SiC surface around a micropipe. (a) before growth and (b) after growth.

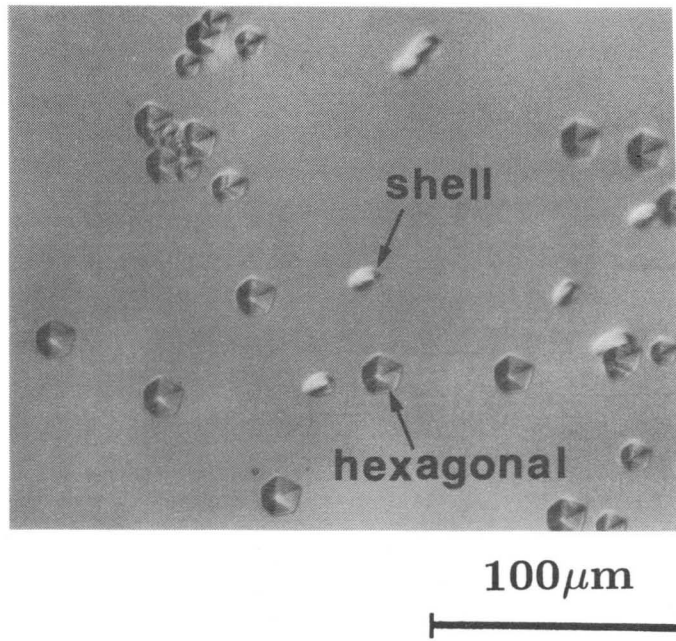


Fig.6.5 6H-SiC(0001) surface etched by molten KOH. Hexagonal and “shell” etch pits are observed.

(b) after growth (epilayer thickness= $10\mu\text{m}$). Although it is difficult to detect small micropipes on as-polished surfaces (before growth), rounded pits are formed at the micropipe positions after epitaxial growth. These pits are accompanied with "shadows" due to the impedance of step-advance (cf. Fig.2.15).

A typical surface etched by molten KOH is shown in Fig.6.5. The etching was done at 420°C for 5min. Hexagonal etch pits and "shell" etch pits are observed. Koga *et al.* reported that the largest hexagonal etch pits correspond to micropipes (not shown in Fig.6.5), and other hexagonal etch pits originate from dislocations with the Burgers vectors along the c axis [14]. Takahashi *et al.* revealed that the "shell" etch pits correspond to slip dislocations in the basal plane [17]. The etch pit density of epilayers depends on mainly substrates used for growth. The typical etch pit density was 10^4cm^{-2} for epilayers grown on commercial wafers, and $10^5\sim 10^6\text{cm}^{-2}$ for epilayers on home-made wafers or Acheson crystals. Wang *et al.* analyzed defects of 6H-SiC wafers and epilayers by X-ray topography, and reported that slip dislocations can be eliminated by epitaxial growth [18]. Successive etching of epilayers should be carried out to clarify the propagation and annihilation of dislocations.

6.3 Physical Properties of Undoped Epilayers

6.3.1 Photoluminescence

Photoluminescence (PL) measurement was performed to elucidate the quality and purity of epilayers. A suitably filtered He-Cd laser (325nm) was used as an excitation source. Samples were set in a cryostat with a heater. In low-temperature PL measurements, samples were immersed in pumped liquid helium at 2K.

Figure 6.6 shows the (a) wide range and (b) bandedge PL spectra at 2K from a $10\mu\text{m}$ -thick 6H-SiC epilayer. The epilayer was unintentionally doped n-type, produced with a C/Si ratio in source gases of 2.0. Estimated donor concentration is $1\times 10^{16}\text{cm}^{-3}$. Zero-phonon lines due to the recombination of an exciton bound to neutral nitrogen substituting at one hexagonal and two

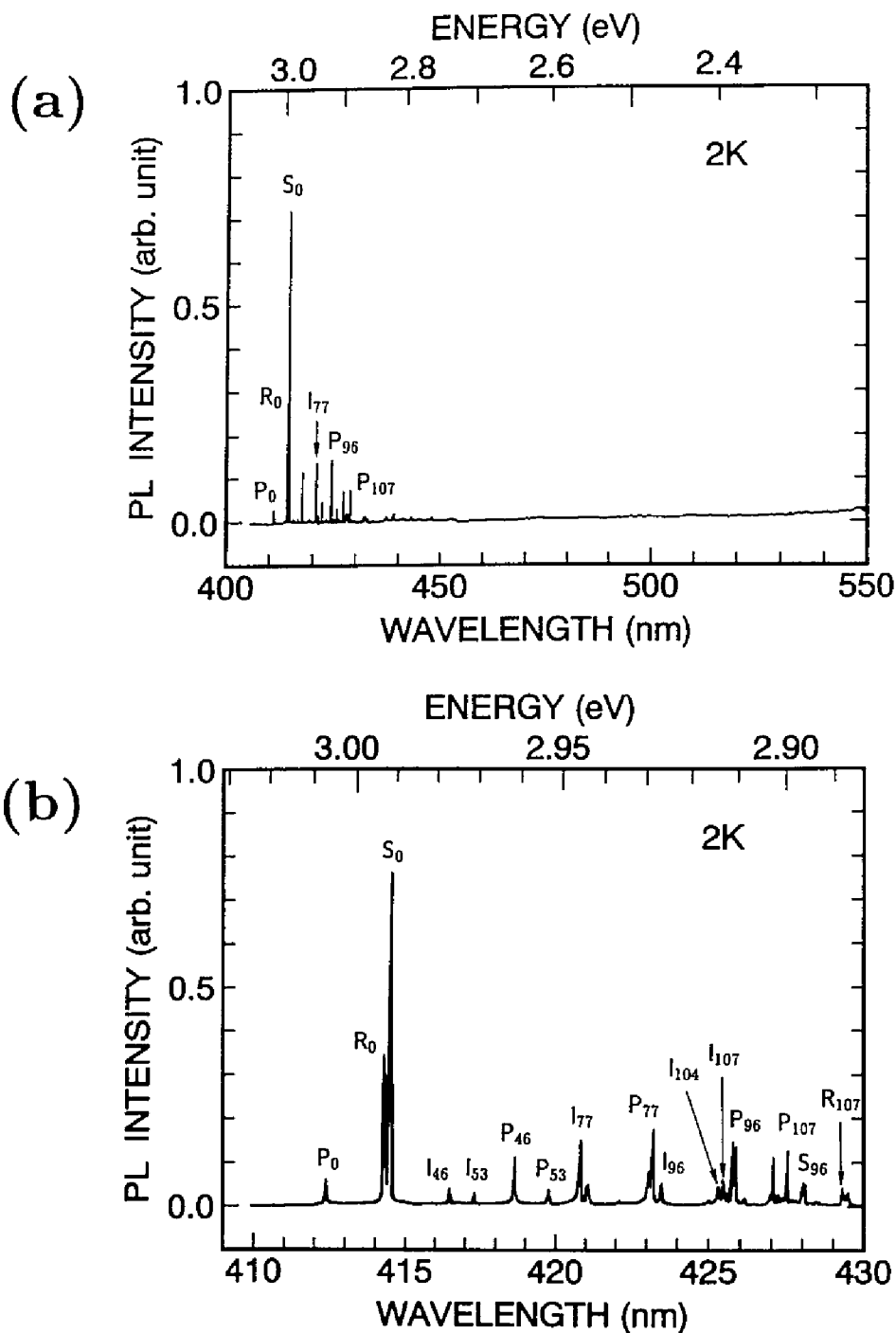


Fig.6.6 Photoluminescence spectra from a $10\mu\text{m}$ -thick 6H-SiC epilayer at 2K. (a) wide range spectrum and (b) bandedge spectrum.

cubic sites are labeled by P_0 (412.3nm), R_0 (414.3nm), and S_0 (414.5nm)¹ [19]. The subscript denotes phonon energies in meV involved in the recombination. The free exciton peaks are marked I with involved phonon energies. As shown in Fig.6.6(a), the bandedge luminescence is dominant, and the N donor - Al acceptor pair band (440~550nm) is negligibly small, whereas the donor - acceptor pair luminescence is dominant in substrates. Although Ti acts as an effective luminescent center in SiC [20,21], Ti-related peaks, of which zero-phonon peaks would appear at 433.5, 439.8, and 445.1nm, were not observed. Besides, no "L-lines" were seen, which appear at 472.3, 478.9, and 482.3nm and have been attributed to intrinsic defects (probably a divacancy) [22].

In Fig.6.6(b), sharp peaks are clearly distinguished. Note that phonon replicas are dominant for P-series luminescence, whereas the zero-phonon lines are the most intense in R- and S-series. This tendency may result from the difference in binding energies of the bound exciton. The binding energies of the exciton, which can be determined by the energy difference between the exciton bandgap (3.023eV) [23] and the luminescence peak, are 16meV, 31meV, and 32meV for P-, R-, and S-series, respectively. The higher binding energy at cubic-site N donors make the exciton more localized, increasing the recombination probability without momentum-conserving phonons. Although the free exciton peak intensities are relatively weak, definite free exciton peaks at 420.6nm (I_{77}), 423.5nm (I_{96}), and 425.2nm (I_{107}) were observed, suggesting the high quality and high purity of the epilayer. The lacking of zero-phonon line of free exciton peaks reflects the indirect band structure of SiC. It is known that the intensity of the free exciton peaks increases and that of N bound exciton peaks decreases with lowering background doping concentration [6,24]. More intense free exciton peaks can be expected by the reduction of doping level. The PL spectrum indicates very little contamination of Al acceptor, which would normally show the Al bound exciton peaks at 412.7~413.5nm [25]. In fact, secondary ion mass spectroscopy (SIMS) measurements of undoped layers revealed that the residual Al and B concentrations were below the detection limits ($< 10^{15} \text{cm}^{-3}$).

¹In α -SiC except for 2H-SiC, a substitutional impurity forms several energy levels, depending on the substituting sites (*e.g.* hexagonal/cubic sites). This phenomenon is called "site effect", and is briefly explained later in Fig.6.8.

6.3.2 Hall effect measurement

Hall effect measurement was carried out on undoped n-type 6H-SiC epilayers. The epilayers were electrically isolated from substrates by utilizing epitaxial pn junction. Ohmic contacts were Ni annealed at 1100°C in Ar.

Figure 6.7 shows the temperature dependence of carrier concentration of a 10 μ m thick 6H-SiC epilayer. The carrier concentration at room temperature is 2.5 $\times 10^{16}$ cm $^{-3}$. The author tried curve fitting with a two-donor model. In α -SiC, each dopant can substitute at two inequivalent sites, cubic site and hexagonal site, as mentioned in 6.3.1. The schematic illustration of 6H-SiC structure is shown in Fig.6.8, where two cubic and one hexagonal sites exist. The energy levels of impurities depends on the substituting sites (site effect).

The electrical neutrality condition is given by the following equation [26].

$$N_c \exp\left(-\frac{E_c - E_f}{kT}\right) + N_a = N_{d1} \left\{ 1 - \frac{1}{1 + \frac{1}{g} \exp\left(\frac{E_{d1} - E_f}{kT}\right)} \right\} + N_{d2} \left\{ 1 - \frac{1}{1 + \frac{1}{g} \exp\left(\frac{E_{d2} - E_f}{kT}\right)} \right\}. \quad (6.3)$$

Here, parameters are the donor concentrations N_{d1} , N_{d2} , the donor levels E_{d1} , E_{d2} , and the acceptor concentration N_a . E_c , E_f are the conduction band edge and the Fermi level. N_c and g are the effective density of states in the conduction band and the degeneracy factor (=2). In the calculation of N_c , the density-of-state effective mass for electrons (m_{de}^*) was assumed to be 0.56 m_0 (m_0 :electron rest mass), based on $m_{\parallel}^*=0.35m_0$ and $m_{\perp}^*=1.4m_0$ [27]. The number of the equivalent conduction band minima was assumed as 6 [28]. Since the fitting with these 5 parameters does not yield the unique solution, the author assumed the donor concentration at a cubic site (N_{d2}) is the double of that at a hexagonal site (N_{d1}) ($N_{d2}=2N_{d1}$), based on the crystal structure.

The best fit obtained by a least square method is shown by a solid curve in Fig.6.7. This fitting is given by parameters listed in Table 6.2. The donor levels are 97 and 141meV, which agree well with previous reports [29-31]. The acceptor concentration is as low as 8 $\times 10^{13}$ cm $^{-3}$, indicating very low compensation ratio ($N_a/(N_{d1}+N_{d2})=2\times 10^{-3}$).

Figure 6.9 shows the corresponding temperature dependence of electron mobility. The mobility is 351cm 2 /Vs at room temperature, and reaches up to

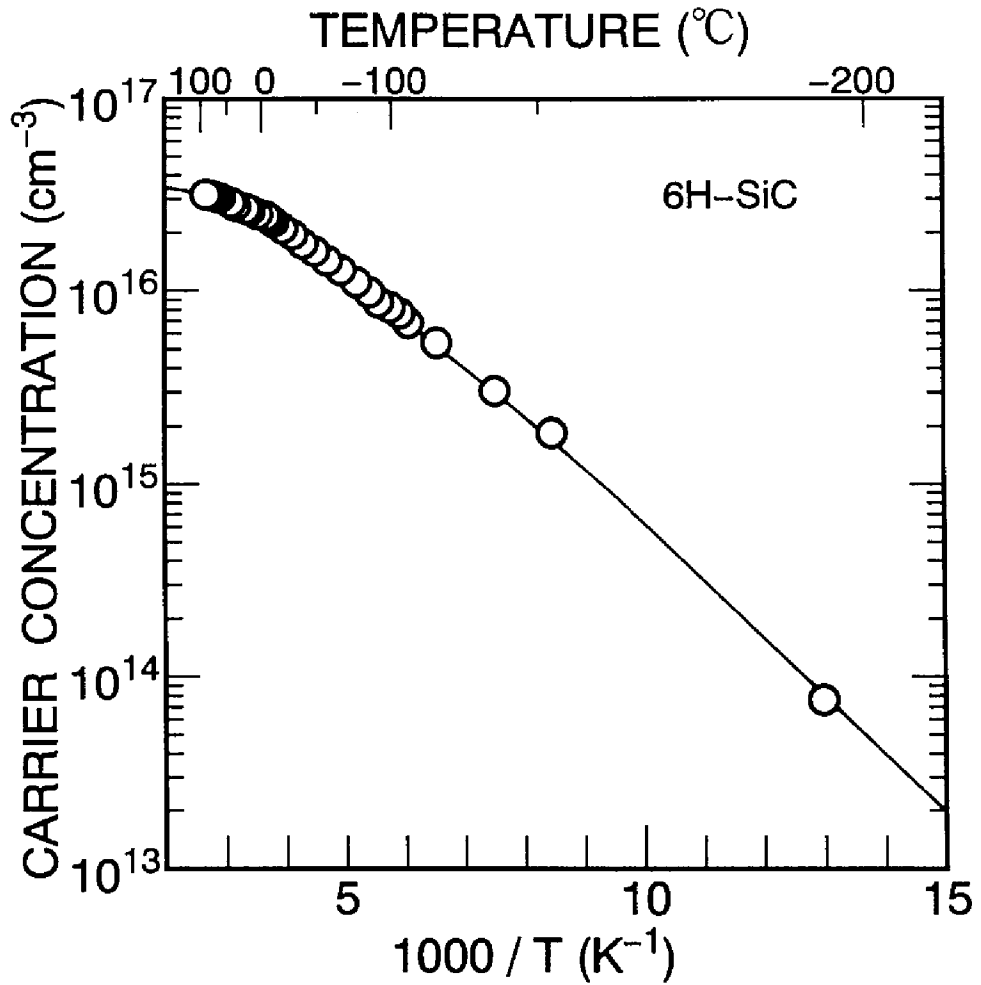


Fig.6.7 Temperature dependence of carrier concentration of a 6H-SiC epilayer.

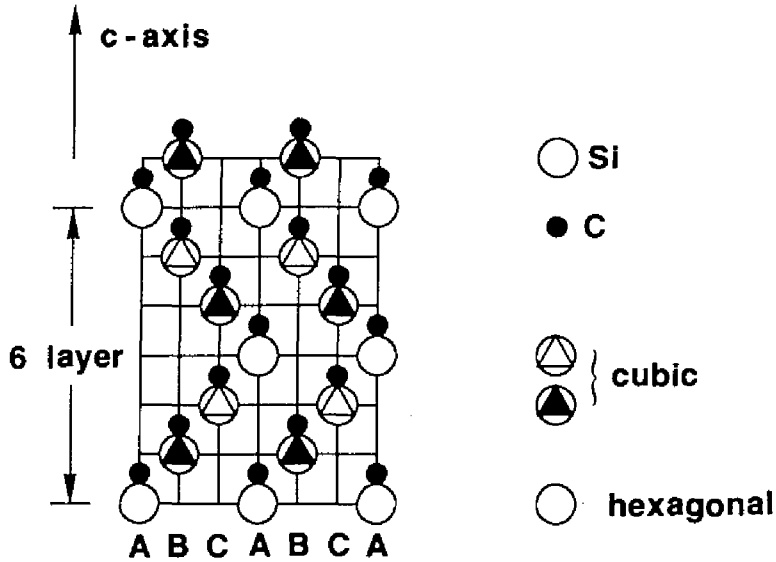


Fig.6.8 Schematic illustration of 6H-SiC structure. Two cubic and one hexagonal sites exist in 6H-SiC.

Table 6.2 Fitted result for the temperature dependence of an n-type 6H-SiC epilayer.

Parameter	6H-SiC epilayer
N_{d1}	$1.1 \times 10^{16} \text{cm}^{-3}$
N_{d2}	$2.2 \times 10^{16} \text{cm}^{-3}$
ΔE_{d1}	97meV
ΔE_{d2}	141meV
N_a	$7.7 \times 10^{13} \text{cm}^{-3}$
$N_a / (N_{d1} + N_{d2})$	2×10^{-3}

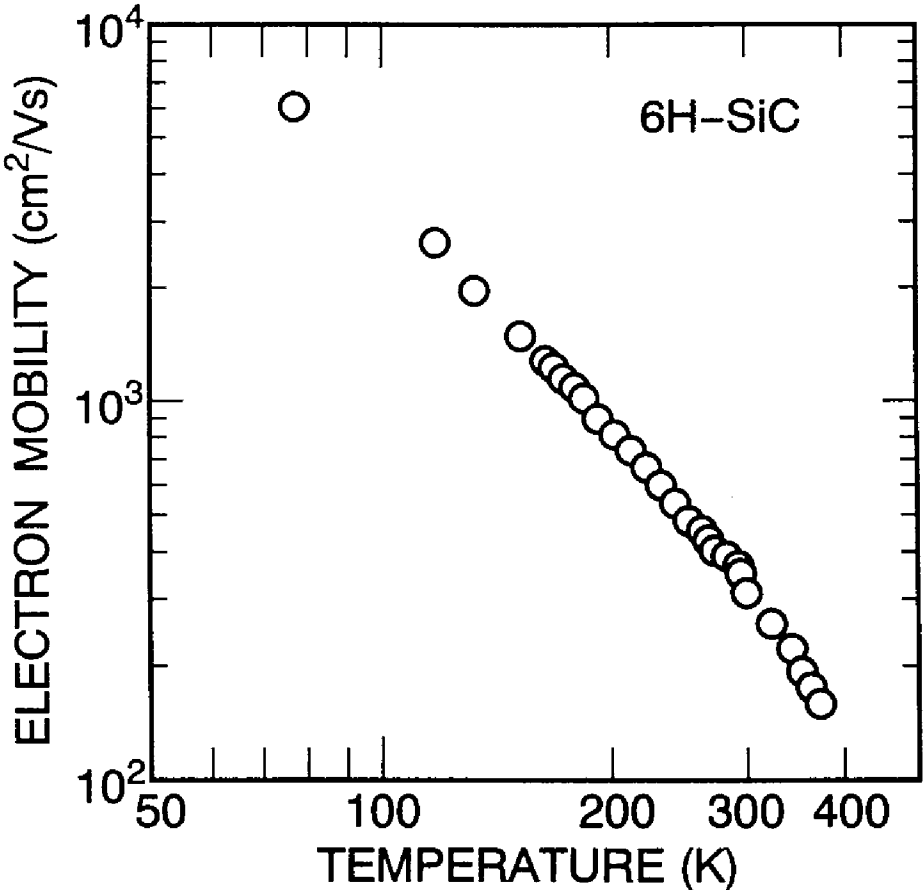


Fig.6.9 Temperature dependence of electron mobility of a 6H-SiC epilayer.

6050cm²/Vs at 77K. These values are comparable with a previous report on 6H-SiC [4]. For a low-doped 6H-SiC epilayers with a carrier concentration of $2 \times 10^{14} \text{cm}^{-3}$, which was produced with a C/Si ratio of 4.0, a high electron mobility of 431cm²/Vs was obtained at room temperature. This is the highest value ever reported in 6H-SiC. For device applications, 4H-SiC is much more attractive owing to higher electron mobility and smaller anisotropy in mobility [32]. The typical mobility of 4H-SiC epilayers is 724cm²/Vs at room temperature and 11000cm²/Vs at 77K [33].

The increasing mobility at low temperature reflects the low compensation of the epilayer. When the acoustic phonon scattering is the dominant scattering mechanism, the mobility should decrease with temperature according to $T^{-1.5}$ dependence [26]. However, the present result shows $T^{-(2.1 \sim 2.5)}$ dependence. This kind of rapid decrease in electron mobility at high temperatures has been also observed in Si, and is attributed to the influence of inter-valley scattering [34]. A similar mechanism may play a role in SiC, which has multi-valley structure in the conduction band. In order to reveal the scattering mechanism, detailed band structure and phonon dispersion must be known.

6.3.3 Deep level analysis

There have been only a few reports on trap centers in SiC [35-41]. Among them, in 6H-SiC, deep levels in pn junctions formed by Al ion implantation were observed by deep level transient spectroscopy (DLTS) measurements [38]. Another deep centers in B-doped 6H-SiC grown by liquid phase epitaxy (LPE) were investigated by DLTS, admittance spectroscopy and photoluminescence [39]. Recently, DLTS measurements of pn junction diodes formed by LPE revealed that an electron trap center with an activation energy of 0.71eV exists in n-type grown layers [41]. However, deep levels in 6H-SiC wafers grown by a modified Lely method and/or device-quality 6H-SiC epilayers grown by step-controlled epitaxy have not been investigated.

In this study, isothermal capacitance transient spectroscopy (ICTS) [42] and DLTS [43] measurements on Schottky structures have been carried out to investigate deep levels in 6H-SiC.

The samples used in this study were two kinds of undoped n-type 6H-SiC

single crystals. The one was 6H-SiC wafers grown by a modified Lely method. The growth temperature and growth rate were 2100°C and 0.6mm/h, respectively. The donor concentration of the wafers was determined to be in the range of $8.2 \times 10^{16} \sim 1.5 \times 10^{17} \text{ cm}^{-3}$ by capacitance-voltage (C-V) measurements. The other was epilayers grown by step-controlled epitaxy on 6H-SiC{0001} faces with $3 \sim 5^\circ$ off angles. The growth temperature and growth rate were 1500°C and $2.5 \mu\text{m/h}$, respectively. The thicknesses of grown layers were $2.5 \sim 5.0 \mu\text{m}$ and the donor concentrations were in the range of $1.3 \times 10^{15} \sim 3.2 \times 10^{16} \text{ cm}^{-3}$. For ICTS and DLTS measurements, Au Schottky contacts with a diameter of $500 \mu\text{m}$ were thermally evaporated on the surfaces and large-area ohmic contacts were formed using Ni on the back side of SiC samples.

The ICTS method is based on principles similar to the DLTS method. In the ICTS method, however, deep level signals can be spectroscopically obtained from a transient capacitance measured in the time domain under isothermal conditions. So this technique removes the difficulties arising from DLTS measurements that involve a temperature scanning process. The capacitance transient $C(t)$ of an abrupt junction diode is given by

$$C(t) = C_{\text{st}} \sqrt{1 + \frac{N_{\text{T}}}{N_{\text{B}}} \{1 - \exp(-\frac{t}{\tau_{\text{e}}})\}}. \quad (6.4)$$

Here, C_{st} is the capacitance of a steady-state under the reverse bias V_{R} , and given by

$$C_{\text{st}} = \sqrt{\frac{q\epsilon N_{\text{B}}}{2(V_{\text{D}} - V_{\text{R}})}} A, \quad (6.5)$$

where N_{B} is the concentration of a shallow level impurity, ϵ the dielectric constant, V_{D} the diffusion voltage, and A the junction area. N_{T} is the deep level concentration and τ_{e} the emission time constant. The ICTS signal $S(t)$ obtained from a capacitance transient $C(t)$ after the forward voltage pulse application is defined as [42]

$$S(t) = t \frac{dC^2(t)}{dt}. \quad (6.6)$$

The maximum peak intensity of $S(t)$ is obtained at $t = \tau_{\text{e}} \equiv \tau_{\text{em}}$, so the emission time constant τ_{em} is immediately determined from the peak position of $S(t)$.

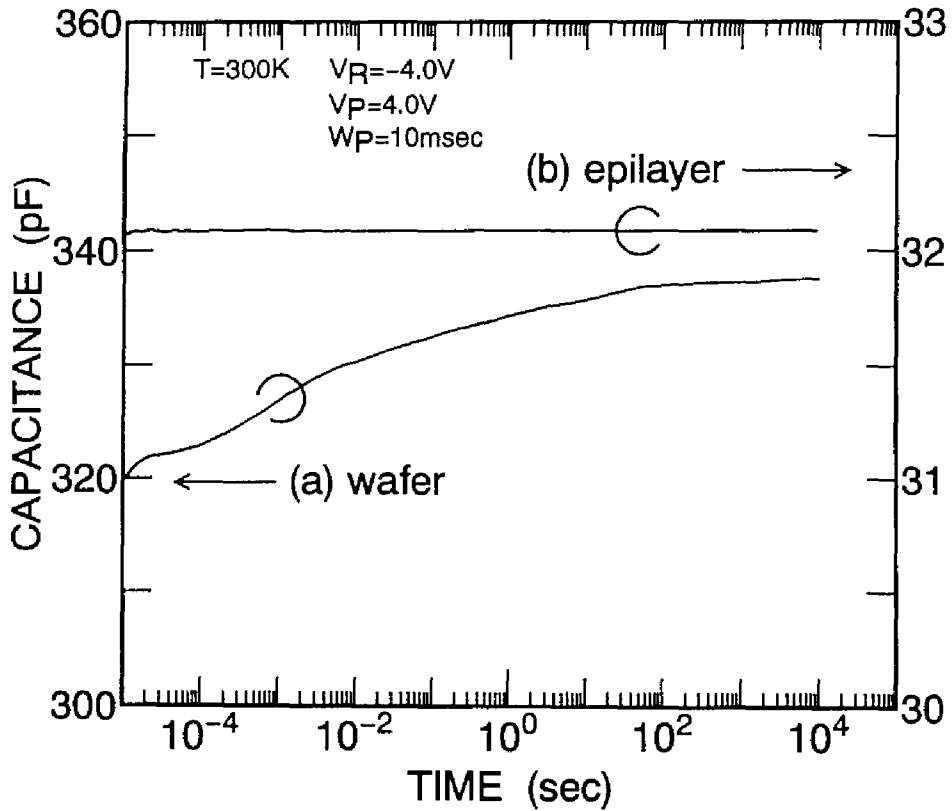
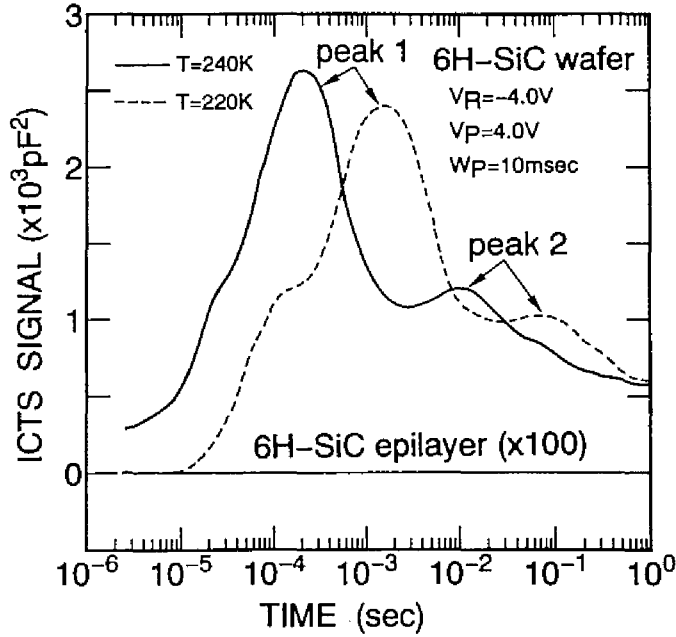
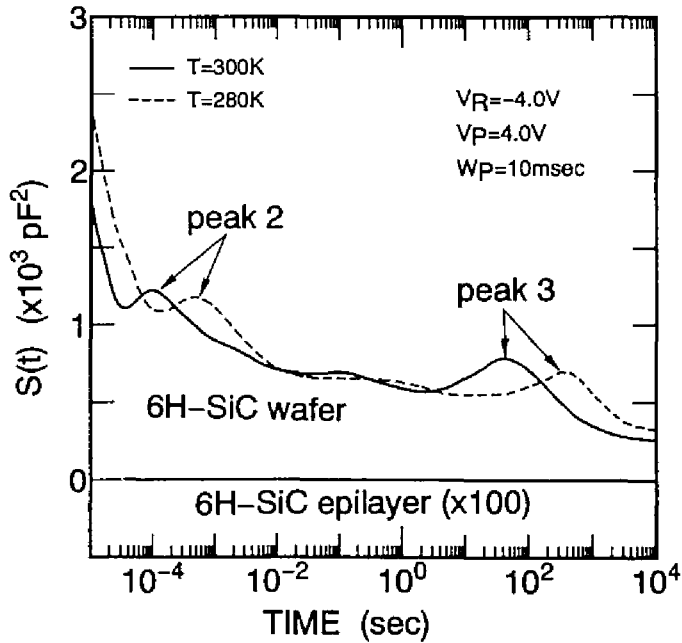


Fig.6.10 Capacitance transient obtained from samples of (a) a 6H-SiC wafer grown by a modified Lely method and (b) a 6H-SiC epilayer.



(a)



(b)

Fig.6.11 ICTS spectra from a 6H-SiC wafer and an epilayer. (a) in lower temperature range and (b) in higher temperature range.

The peak-position time τ_{em} gives the reciprocal of the thermal emission rate for the deep level:

$$\tau_{em} = \frac{1}{e_n + e_p} \simeq \frac{1}{e_n}, \quad (6.7)$$

where e_n and e_p are the thermal emission rates of electrons and holes, respectively. Here it is assumed that $e_n \gg e_p$ for electron trap levels, which is the present case of n-type Schottky structure. The peak of signal $S(t)$ is proportional to the density of the deep level N_T ;

$$S(\tau_{em}) = \frac{N_T}{N_B} C_{st} \exp(-1) \propto N_T. \quad (6.8)$$

All measurements were performed in a temperature-controlled system using liquid nitrogen and in a vacuum of 10^{-2} Torr. To obtain the saturated peak intensity of ICTS signal under isothermal conditions in the time range of $10^{-5} \sim 10^4$ sec, the values of the reverse-bias V_R , forward pulse-bias height V_P and width W_P were determined properly.

Figure 6.10 shows the spectra of capacitance transient $C(t)$ obtained from the 6H-SiC samples grown by (a) a modified Lely method, and (b) step-controlled epitaxy. As shown in the figure, the capacitance transients between the two kinds of samples are completely different. In the case of (a), the capacitance transient shows continuous increase after the forward voltage pulse application, indicating the existence of several deep traps. In the case of (b), however, the capacitance change is not observed at all in the wide time range. The capacitance change of epilayer samples was negligibly small in the wide temperature range from 130K to 400K.

Figure 6.11 shows the ICTS spectra obtained from a 6H-SiC wafer and an epilayer. The measurements were performed to detect both the levels with small time constant in the lower temperature range (Fig. 6.11(a)) and the levels with large time constant in the higher temperature range (Fig. 6.11(b)). For the ICTS spectra from the wafer, the broad peaks are observed in both cases, and the peaks seem to be composed of several overlapping signals. This result suggests that several deep electron traps with different activation energies and capture cross sections exist in the wafer. The author analyzed the three deep electron traps named peak 1, 2 and 3. The trap of peak 2 in the higher temperature range is the same as that of peak 2 in the lower temperature range. The

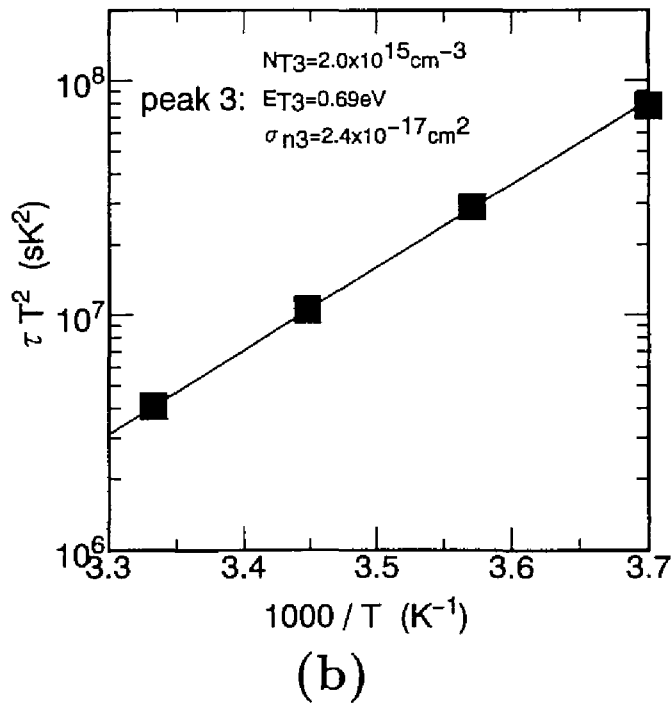
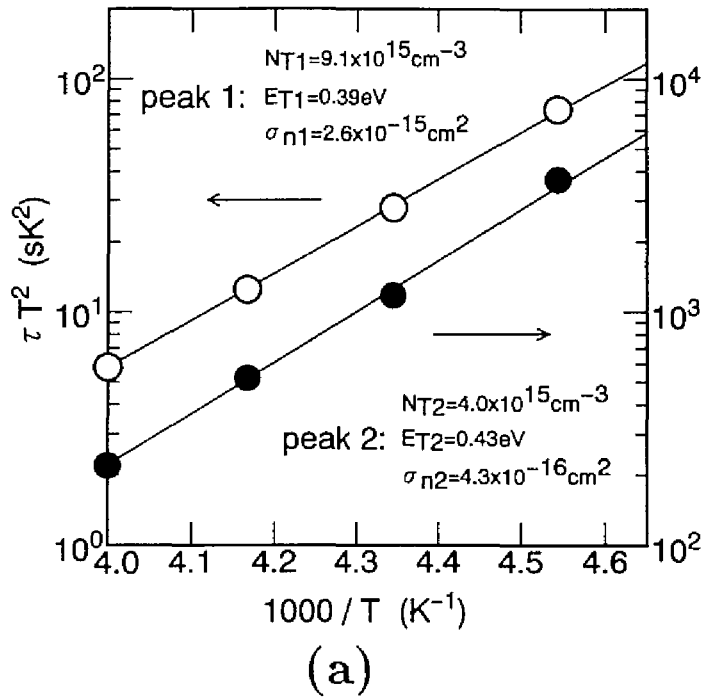


Fig.6.12 Arrhenius plots of τT^2 as a function of $1000/T$ obtained from three peaks. (a) in the lower temperature range and (b) in the higher temperature range.

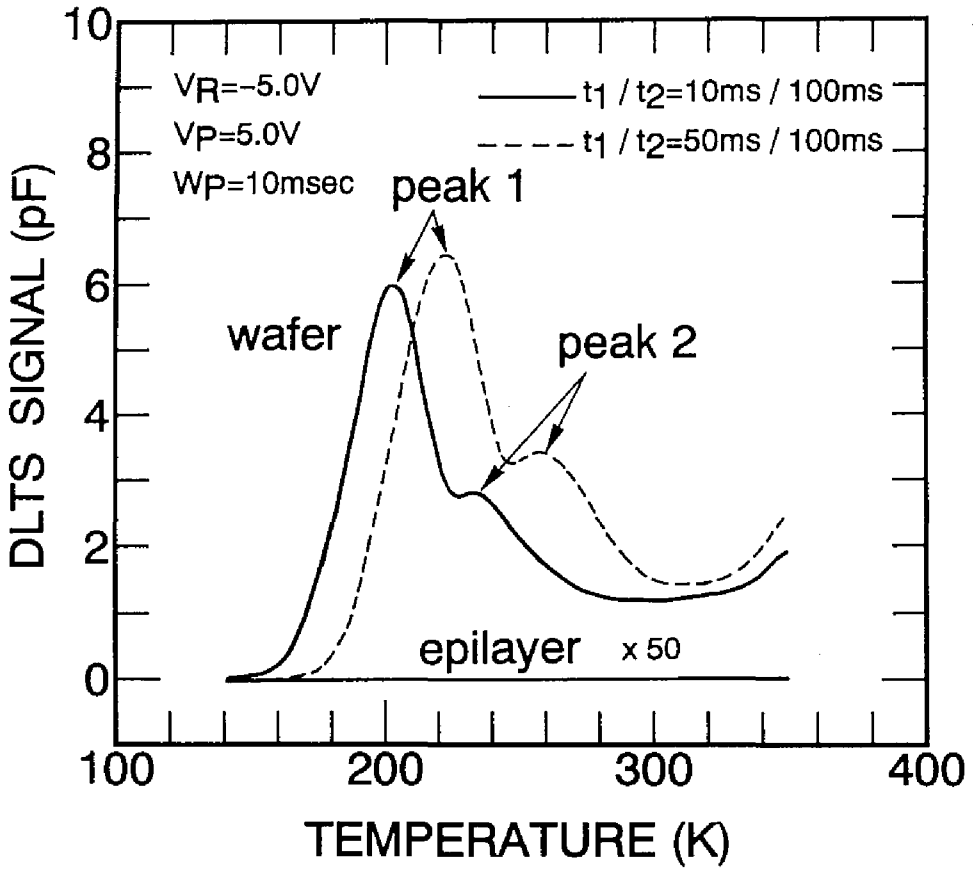


Fig.6.13 DLTS spectra from a 6H-SiC wafer and an epilayer.

concentrations of each trap are estimated to be $9.1 \times 10^{15} \text{cm}^{-3}$, $4.0 \times 10^{15} \text{cm}^{-3}$ and $2.0 \times 10^{15} \text{cm}^{-3}$ for peak 1, 2 and 3, respectively. Although the broad ICTS signal indicates that other peaks may exist, they could not be precisely analyzed because of the difficulty in peak separation. One reason for the broad ICTS peaks may be the site effect of substitutional impurities. The ICTS spectra of wafers varied from sample to sample, and some wafers showed very small signal of peak 2 and peak 3. However, the peak 1 trap with a concentration of $10^{15} \sim 10^{16} \text{cm}^{-3}$ was observed in all the wafers.

The peak positions of ICTS spectra shift towards smaller time constant as the temperature increases as shown in Fig.6.11. From the relationship between the time constant at the peak position and the reciprocal temperature, the activation energy E_T and the electron capture cross section σ_n can be obtained. The electron emission rate e_n is given by [43]

$$e_n = \frac{1}{\tau_{em}} = \frac{N_c v_{th} \sigma_n}{g} \exp\left(-\frac{E_T}{kT}\right) \propto T^2 \sigma_n \exp\left(-\frac{E_T}{kT}\right). \quad (6.9)$$

Here, N_c is the effective density of states in the conduction band, v_{th} the thermal velocity of electrons, and g the degeneracy factor of the trap level. Figure 6.12 shows the Arrhenius plots of τT^2 vs. $1000/T$. For the three deep levels, the activation energies are estimated to be 0.39eV, 0.43eV, and 0.69eV, respectively, from the slope of the Arrhenius plots. The intersecting points at the vertical axis of the plots yield the capture cross sections of $3 \times 10^{-15} \text{cm}^2$, $4 \times 10^{-16} \text{cm}^2$, and $2 \times 10^{-17} \text{cm}^2$, for peak 1, 2, and 3, respectively. In general, σ_n depends on the microscopic nature and the state of the defect, and also on temperature. However, the capture cross section σ_n was assumed to be independent of temperature in this study, due to the lack of detailed data.

DLTS measurements were also conducted in the temperature range from 130K to 300K on the same samples. Typical DLTS spectra are shown in Fig.6.13. The values of activation energies and the capture cross sections were similar to the results of ICTS measurements.

In order to reveal optical properties of the deep levels in 6H-SiC wafers, photoluminescence at 12~77K was investigated. However, broad peaks due to donor (N) - acceptor (Al) pair recombination disturbed the identification of peaks related with deep levels.

Uddin and Uemoto reported DLTS measurements of 6H-SiC pn junction diodes grown by LPE [41]. At the level 0.71eV below the conduction band edge in the n layer, they observed an electron trap with a concentration of $2 \times 10^{15} \text{cm}^{-3}$. The trap named peak 3 in this study may be the same as that they reported, from the close value in the level. The origins and characteristics of these deep levels, however, are unknown at present. A detailed analysis on impurities and defects in the crystals and/or ICTS measurements of intentionally doped samples are required.

On the other hand, epilayers showed very small ICTS signal at 130~400K in the time range of $10^{-5} \sim 10^4 \text{sec}$. Deep levels which are located above $E_c - 1.0\text{eV}$ (E_c : the conduction band edge) should bring about the capacitance transient under the measurement conditions. These results suggest that the concentrations of deep electron traps in epilayers are negligibly small ($< 10^{13} \text{cm}^{-3}$) compared with the shallow level concentrations. It is known that electron traps at energy levels of $E_c - 620\text{meV}$ and $E_c - 640\text{meV}$ (Z_1 and Z_2 traps) are formed in 6H-SiC epilayers prepared under particular growth conditions [40]. These electron traps are supposed to originate from intrinsic defects because they can be also created by the irradiation of any high-energy particles (H, He, electron, etc.) [40]. However, these traps could not be observed in the present epilayers. Thus, the epilayers have excellent quality, which is adequate for application to majority carrier devices. As for minority-carrier traps, further analyses on pn junction structures will be required.

6.4 In-situ Doping of Impurities

6.4.1 Nitrogen doping

In-situ n-type doping can be easily achieved by the introduction of N_2 during epitaxial growth. N doping gave very little influence on growth rate and surface morphology. Figure 6.14 shows the N donor concentration vs. the N_2 flow rate. The donor concentration was estimated from capacitance - voltage (C-V) characteristics of Au/6H-SiC Schottky structures. Note that this measurement provides not the electron concentration but the donor concentration,

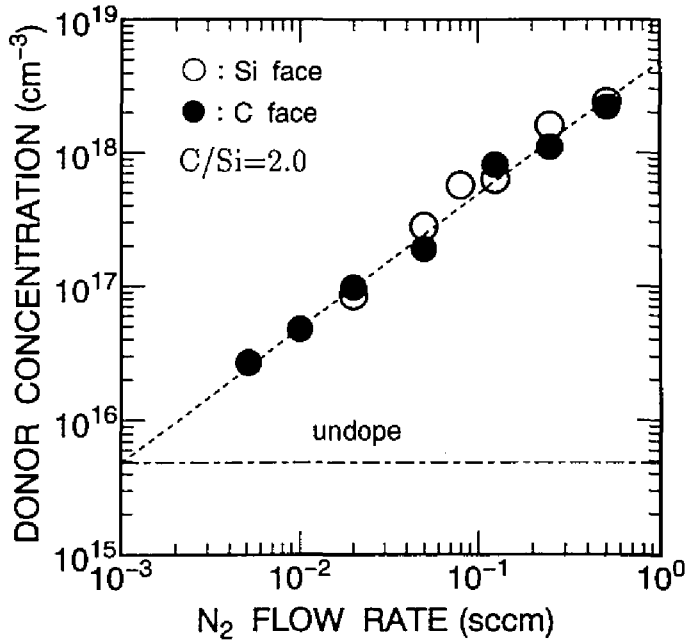


Fig.6.14 N donor concentration vs. N₂ flow rate in epitaxial growth of 6H-SiC.

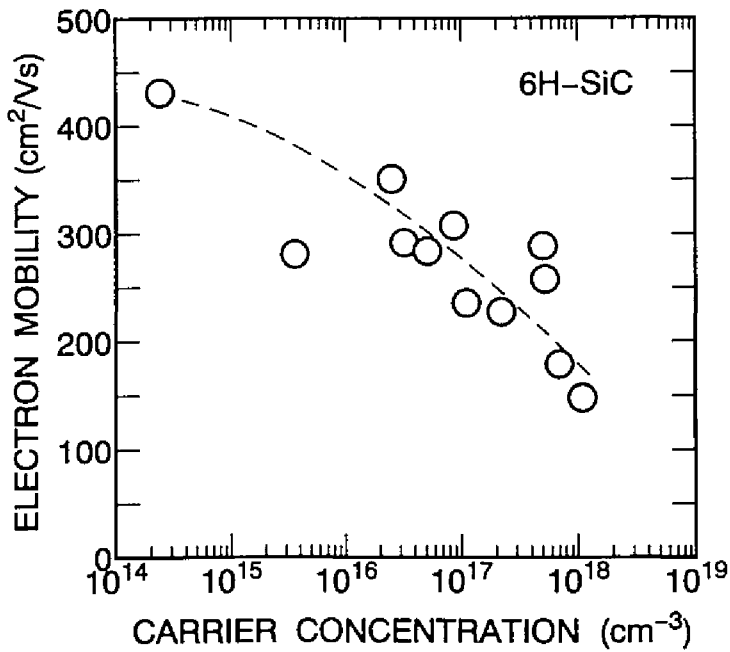


Fig.6.15 Electron mobility vs. carrier concentration of n-type 6H-SiC epilayers at room temperature.

because all the donors are ionized in the depletion region. The flow rates of SiH_4 and C_3H_8 were 0.15 and 0.10sccm, respectively ($\text{C/Si}=2.0$). The slope of the plot is unity, indicating the excellent doping controllability. This result is similar to the reports by Wang *et al.* [8] and Karmann *et al.* [4], though these previous studies employed only 6H-SiC(0001)Si substrates. The doping efficiency η_{doping} was defined by the following equation:

$$\eta_{\text{doping}} = \frac{N_{\text{dopant}}/F_{\text{dopant}}}{N_{\text{Si}}/F_{\text{SiH}_4}}, \quad (6.10)$$

where N_{dopant} and N_{Si} are the dopant and Si concentration in epilayers. F_{dopant} and F_{SiH_4} are the amount of dopant atoms and SiH_4 supplied per unit time². The calculated doping efficiency is 1.5×10^{-5} , independent of the substrate polarity. Recently, Larkin *et al.* have found that the doping efficiency of N strongly depends on the C/Si ratio during the growth on (0001)Si substrates: The higher C/Si ratio leads to the lower N concentration [44]. This phenomenon can be explained by that the higher C coverage on the growing surface prevents the incorporation of N atoms, which substitute at the C site, into the crystals. In order to clarify the doping mechanism, detailed study on the C/Si ratio dependence and surface coverage on both Si and C faces is required.

Relatively high ionization energies of N donors in SiC (80~144meV in 6H-SiC [30]) cause the incomplete activation at room temperature. The activation ratio n/N_d (n :electron concentration, N_d :donor concentration) was estimated to be 0.4~0.7 at room temperature.

Figure 6.15 shows the electron mobility in the basal plane vs. the carrier concentration of 6H-SiC epilayers. The mobility is $350\text{cm}^2/\text{Vs}$ at 10^{16}cm^{-3} , and $150\text{cm}^2/\text{Vs}$ at 10^{18}cm^{-3} at room temperature. This result is comparable to the data previously reported [4,32].

²N atoms substitute at the C site in SiC. However, the supply of Si species controls the growth rate as shown in Fig.3.2. Thus, the doping efficiency was normalized by the Si-related term.

6.4.2 Aluminum and boron doping

The addition of small amount of trimethylaluminum(TMA:Al(CH₃)) is effective for *in-situ* p-type doping [45]. Although most Al-doped epilayers showed very smooth surfaces, surface pits and hillocks were observed in heavily doped (Al concentration $\geq 10^{19}\text{cm}^{-3}$) samples grown on C faces. The supply of TMA causes the shift of growth conditions toward C-rich ambient due to the release of CH₃ species from TMA molecules. The surface migration is suppressed and the nucleation is promoted under C-rich growth conditions as described in 5.3. This may be the reason for the surface roughening of heavily doped epilayers grown on C faces.

The Al acceptor vs. TMA flow rate is shown in Fig.6.16. The flow rates of SiH₄ and C₃H₈ are 0.30 and 0.20sccm (C/Si ratio=2.0), respectively. The acceptor concentration estimated from C-V measurements agreed well with the Al concentration determined by SIMS measurements. Although the proportionality in the doping characteristics is quite good, remarkable difference in doping efficiency between Si and C faces is observed. The efficiency is much higher on Si faces (3.8×10^{-3}) than that on C faces (1.3×10^{-4}). The origin of this polarity dependence is not clear at present. Nishino observed the increasing Al doping efficiency under the C-rich conditions [46]. This result can be again explained by the site competition between Si and Al atoms on the growing surface which is controlled by surface C coverage. The polarity dependence of surface coverage and step structures should be studied in detail.

Because of high ionization energy of Al acceptors ($\sim 250\text{meV}$) [29], the activation ratio p/N_a (p :hole concentration, N_a :acceptor concentration) was as low as $10^{-2}\sim 10^{-1}$ at room temperature. However, a very high hole concentration of $4.2\times 10^{19}\text{cm}^{-3}$ could be achieved for heavily doped epilayers (Al concentration= $4\times 10^{20}\text{cm}^{-3}$). This result might arise from the decreased ionization energy due to the bandgap shrinkage in heavily doped samples, or to the formation of impurity band caused by the impurity-impurity interaction [47]. The average distance between the nearest Al atoms in heavily doped samples with an Al concentration of $4\times 10^{20}\text{cm}^{-3}$ is estimated to be 1.5nm, which is close to the effective Bohr radius in p-type 6H-SiC (0.51nm), assuming $m^*=m_0$.

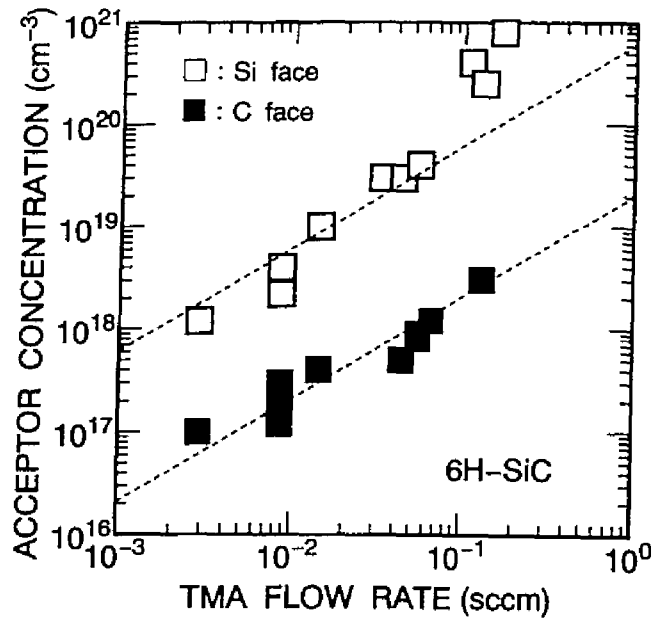


Fig.6.16 Al acceptor concentration vs. TMA flow rate in epitaxial growth of 6H-SiC.

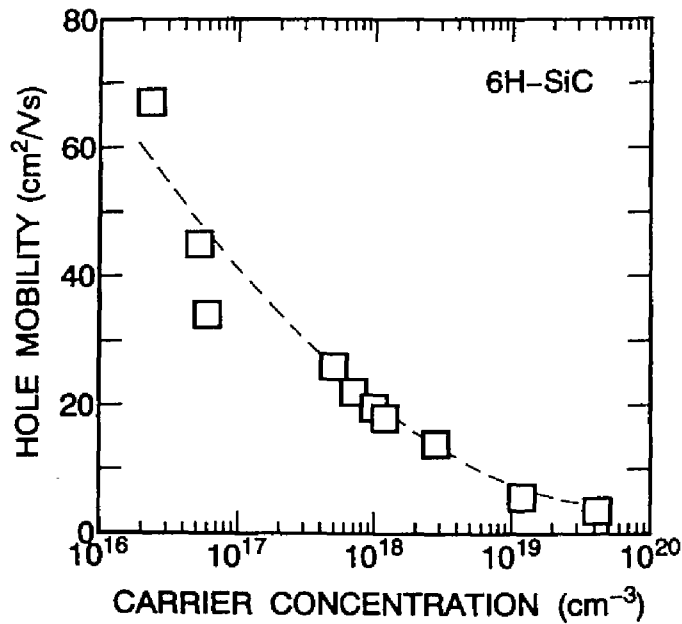


Fig.6.17 Hole mobility vs. carrier concentration of Al-doped 6H-SiC epilayers at room temperature.

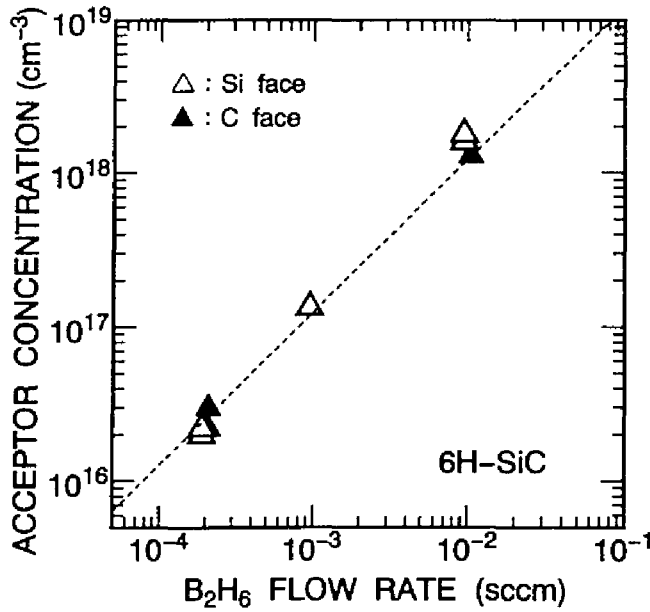


Fig.6.18 B acceptor concentration vs. B_2H_6 flow rate in epitaxial growth of 6H-SiC.

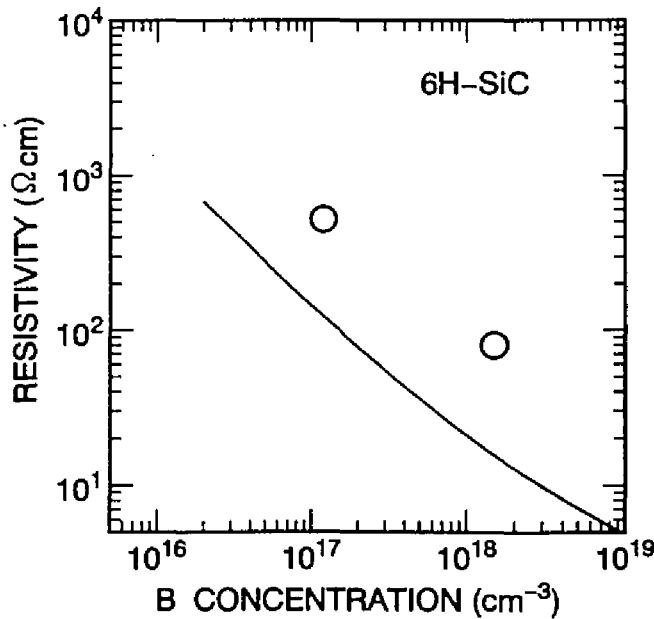


Fig.6.19 Resistivity vs. B concentration of 6H-SiC epilayers. The solid curve represents the calculated dependence, assuming $E_a - E_v = 350meV$ and $\mu = 50cm^2/Vs$.

Figure 6.17 shows the hole mobility vs. the carrier concentration of Al-doped 6H-SiC epilayers at room temperature. The hole mobility is $33\text{cm}^2/\text{Vs}$ at $6 \times 10^{16}\text{cm}^{-3}$, and $6\text{cm}^2/\text{Vs}$ at $1 \times 10^{19}\text{cm}^{-3}$. For heavily doped samples, a low resistivity of $0.04\Omega\text{cm}$ could be obtained, which is useful for contact layers with reduced ohmic contact resistances.

Another hopeful acceptor is B, which can be easily doped using a B_2H_6 gas. Although B doping did not affect surface morphology, the growth rate was reduced by 20~30% in epitaxial growth of B doping. Since B_2H_6 is a gas with high vapor pressure, the doping controllability and uniformity were excellent. Figure 6.18 shows the B acceptor concentration vs. the B_2H_6 flow rate. The flow rates of SiH_4 and C_3H_8 were 0.30 and 0.20sccm (C/Si ratio=2.0). The acceptor concentration estimated from C-V measurements coincided with the B concentration determined by SIMS within the experimental errors. The doping efficiency was 7.5×10^{-4} , independent of the substrate polarity.

B-doped samples exhibited high resistivity, and the formation of ohmic contacts was difficult. This may be ascribed to the high ionization energy of B acceptor (300~390meV) [39,48]. Figure 6.19 shows the B concentration dependence of resistivity at room temperature measured by the van der Pauw method. The dotted line represents the calculated dependence, assuming $E_a - E_v = 350\text{meV}$ and $\mu = 50\text{cm}^2/\text{Vs}$. This estimation is in good agreement with experimental results. At a B concentration of $1 \times 10^{17}\text{cm}^{-3}$, a high resistivity of $520\Omega\text{cm}$ could be obtained, which may be useful for isolation layers. Although higher resistivities are expected for lightly B-doped samples, such high resistivities prevented the accurate measurement.

6.5 Ion Implantation into Epilayers

6.5.1 Nitrogen ion implantation

Although ion implantation is widely used for Si and GaAs device fabrication, studies on ion implantation into SiC are very limited. Nitrogen ion (N^+) implantation into SiC has been reported by several groups [49-52]. But most studies have been performed using 6H-SiC bulk crystals grown by the

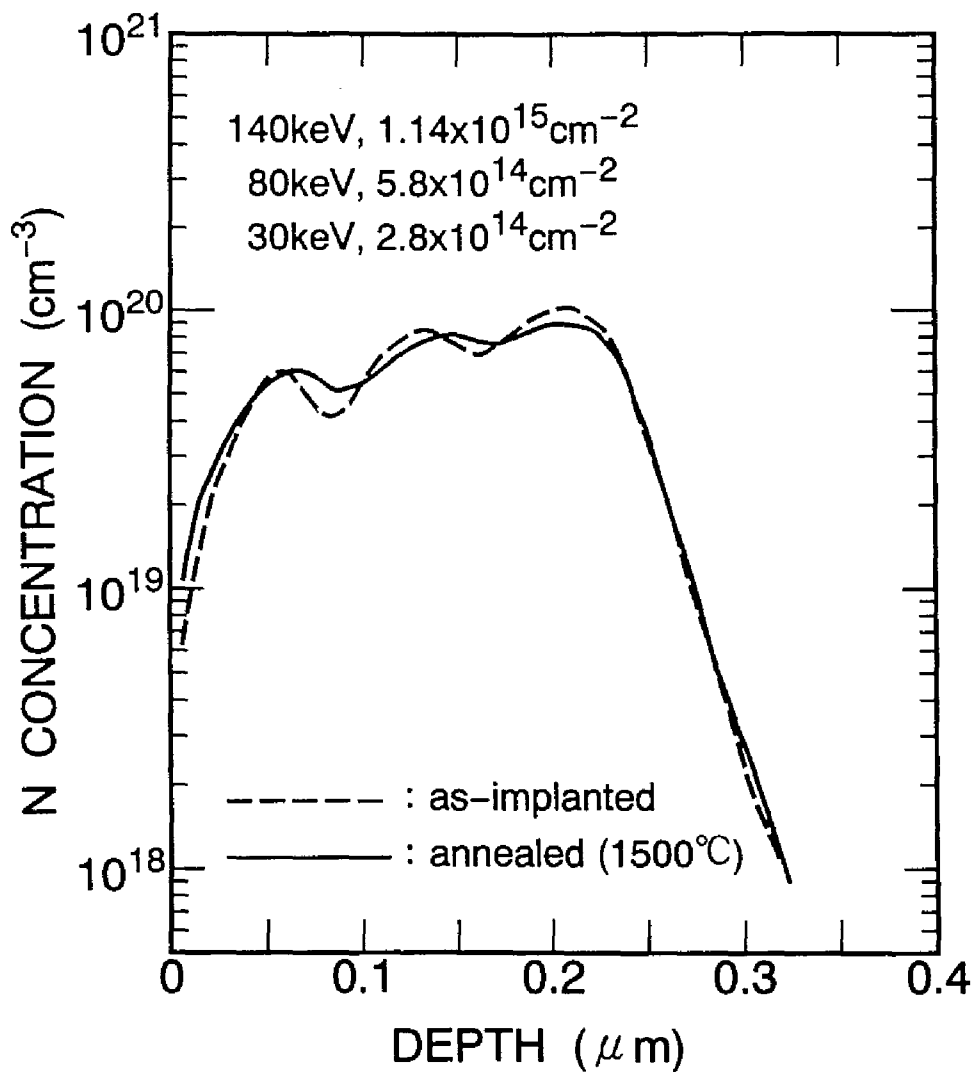


Fig.6.20 N depth profiles before and after annealing at 1500°C for 30min. Triple implantation was done with 140keV, $1.14 \times 10^{15} \text{cm}^{-2}$, 80keV, $5.8 \times 10^{14} \text{cm}^{-2}$, and 30keV, $2.8 \times 10^{14} \text{cm}^{-2}$ (total dose : $2.0 \times 10^{15} \text{cm}^{-2}$).

Lely method or 3C-SiC heteroepitaxially grown on Si substrates, and there have been only a few reports on ion implantation into 6H-SiC epilayers [9,10], which are recognized as device-quality materials. Although the implant dose significantly influences damages in implanted layers and the electrical activation of dopants, no systematic investigations have been reported on this subject.

In this subsection, the effects of N^+ dose on 6H-SiC epitaxial layers are described in detail. Lattice damage and its recovery by thermal annealing are investigated. Based on these results, the relationship between the implantation damage and the electrical activation of dopants is discussed.

P-type off-oriented 6H-SiC{0001} wafers grown by a modified Lely method were used as substrates. The surface polarity and off-angle of substrates were (000 $\bar{1}$)C face and 4° , respectively. Al-doped epilayers with a thickness of $4\mu\text{m}$ were grown by step-controlled epitaxy. The acceptor concentrations of epilayers and substrates were $2\times 10^{17}\text{cm}^{-3}$ and $2\times 10^{18}\text{cm}^{-3}$, respectively.

N^+ ions were implanted into the bare surface of samples at room temperature. The tilt angle between the ion beam direction and the c-axis (the (0001) direction) was 7° . The triple implantation was carried out at energies of 140, 80, and 30keV. In order to investigate the effects of implant dose, the dose was varied in the wide range of $3\times 10^{13}\sim 1\times 10^{16}\text{cm}^{-2}$ with a constant dose ratio for each implantation energy (N^+ dose=0.57:0.29:0.14 for 140keV, 80keV, 30keV). These total doses lead to the average nitrogen concentrations of about $9\times 10^{17}\sim 3\times 10^{20}\text{cm}^{-3}$ in the implanted layers. The typical ion current density during implantation was $1\sim 5\mu\text{A}/\text{cm}^2$. Post-implantation annealing was performed in a furnace heated by rf-induction with a gas flow of Ar. The annealing temperature and period were $1200\sim 1600^\circ\text{C}$ and 30min. During the annealing, samples were set on a SiC-coated graphite susceptor. It is known that the high-temperature annealing above 1300°C causes the damage of SiC surface. However, the formation of surface pits or roughening was not observed in this study. The lattice damage of implanted layers was monitored by RBS and TEM. The electrical properties were characterized by the van der Pauw method. Ni annealed at 1050°C was used as ohmic contacts.

Figure 6.20 shows the N depth profiles before and after annealing at 1500°C for 30min. The total dose of N^+ was $2.0\times 10^{15}\text{cm}^{-2}$. The profile before

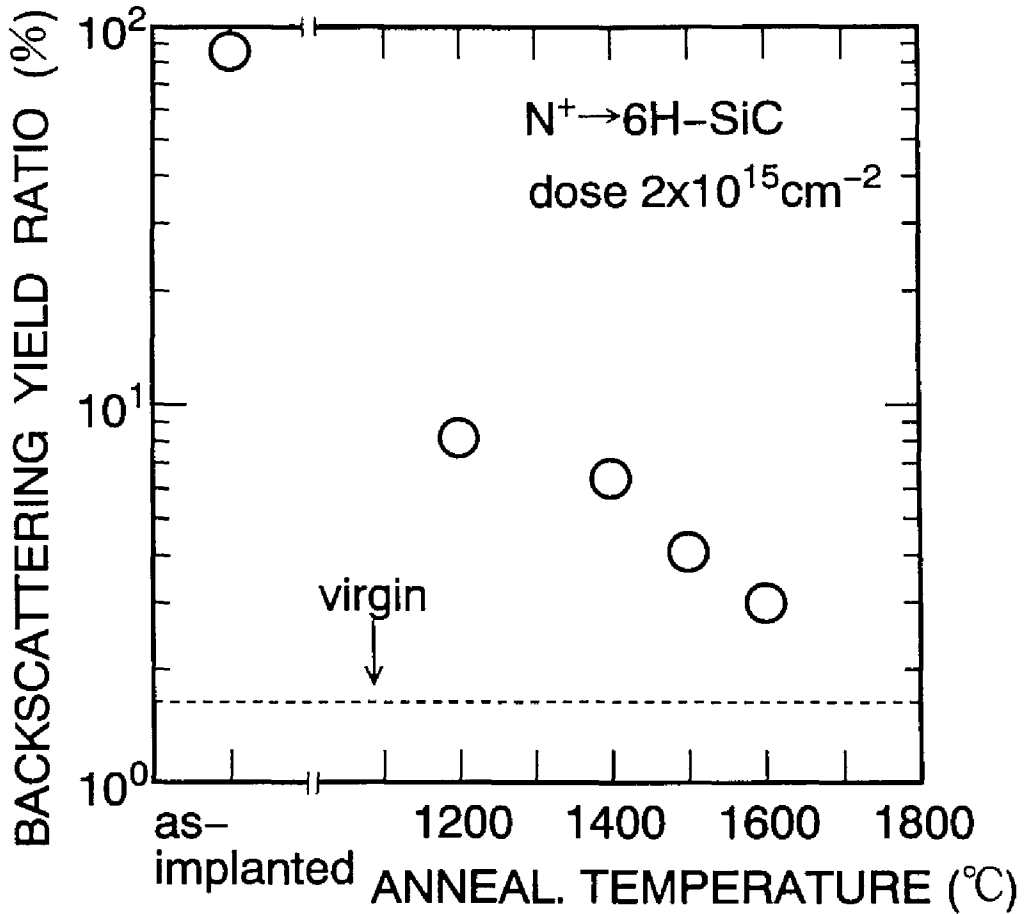


Fig.6.21 Annealing temperature dependence of backscattering yield at the Si edge in RBS spectra. Total dose is $2 \times 10^{15} \text{ cm}^{-2}$.

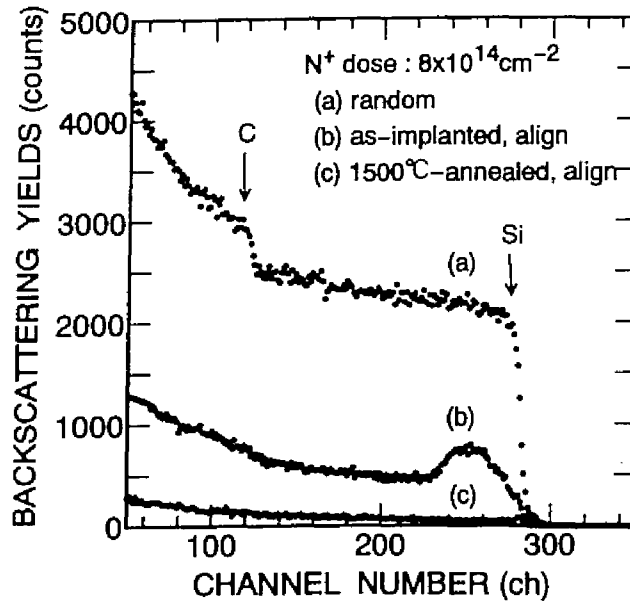


Fig.6.22 RBS spectra for as-implanted and 1500°C -annealed samples. Total N^+ dose is $8.0 \times 10^{14} \text{cm}^{-2}$.

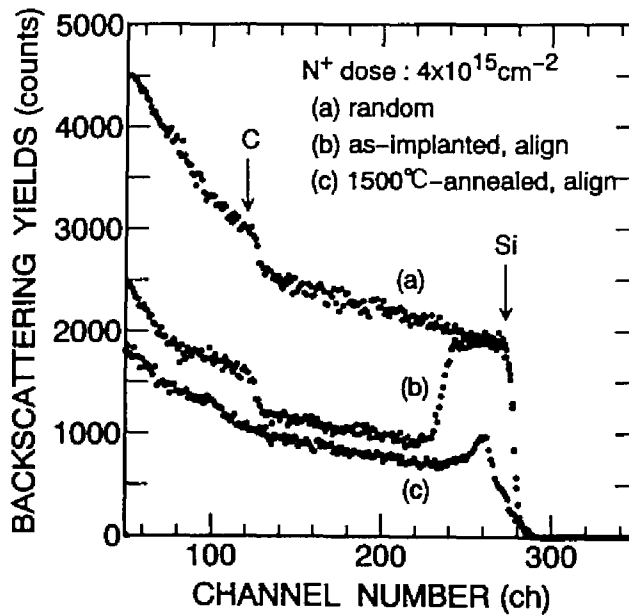


Fig.6.23 RBS spectra for as-implanted and 1500°C -annealed samples. Total N^+ dose is $4.0 \times 10^{15} \text{cm}^{-2}$.

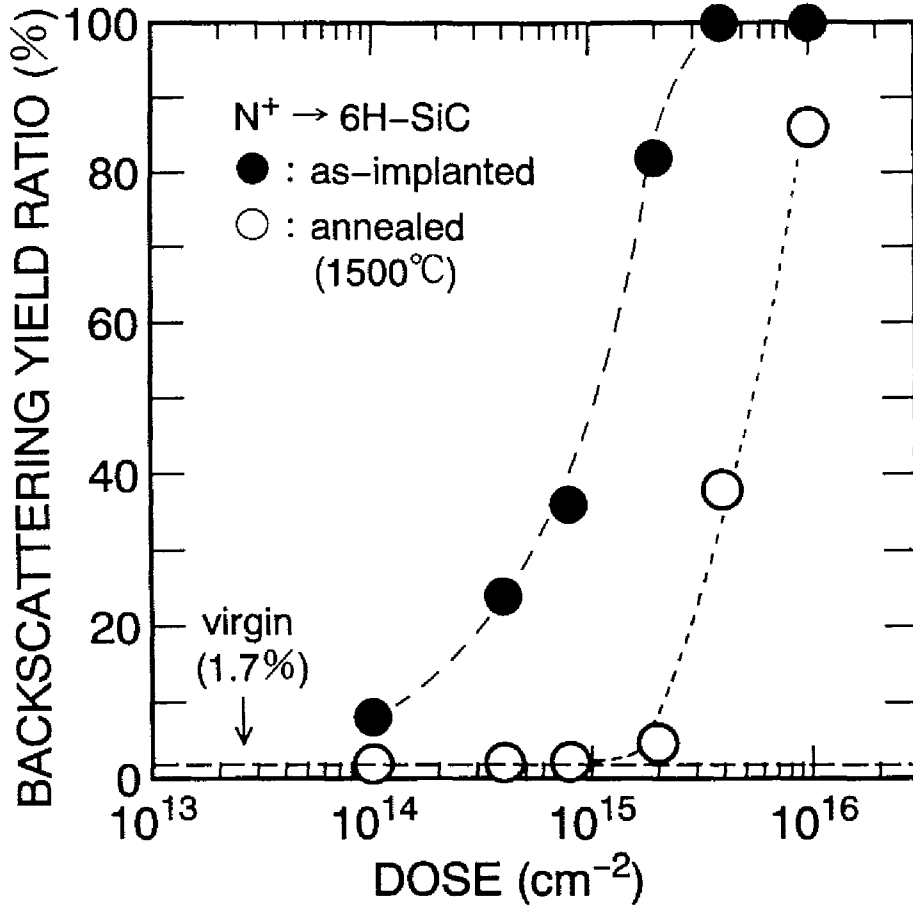


Fig.6.24 N^+ implant dose dependence of backscattering yield ratio in RBS spectra for as-implanted and 1500°C-annealed samples.

annealing can be well predicted by a Monte Carlo simulation [53]. The profiles show three peaks corresponding to the triple implantation at 30, 80, and 140keV. The implantation depth is estimated to be $0.35\mu\text{m}$. After the samples are subjected to high-temperature annealing at 1500°C , almost no redistribution of N is observed. This result reflects a very low diffusion coefficient of N in SiC. Based on the reported data [54], the diffusion coefficient of N in SiC is estimated to be less than $10^{-20}\text{cm}^2/\text{s}$ at 1500°C , which indicates that the diffusion of nitrogen in SiC is negligibly small, even if the diffusion coefficient might increase through the implantation-induced damage.

Figure 6.21 shows the annealing temperature dependence of the backscattering yield ratio at the Si edge in RBS spectra for layers implanted with $2\times 10^{15}\text{cm}^{-2}$ dose. Here, the backscattering yield ratio was defined as the maximum ratio between the aligned and random yields at the Si edge of implanted layers. The backscattering yield ratio decreases monotonously with the annealing temperature, and reaches about 3~4% when high-temperature annealing at $1500\sim 1600^\circ\text{C}$ is performed. In this study, an annealing temperature of 1500°C was mainly employed. Though annealing at a higher temperature (*e.g.* 1600°C) brings about slightly better results, such high-temperature annealing is not practical for device application due to the lack of stable masking materials.

Figures 6.22 and 6.23 show RBS spectra obtained from $8\times 10^{14}\text{cm}^{-2}$, and $4\times 10^{15}\text{cm}^{-2}$ implanted samples, respectively. In the figures, aligned spectra of as-implanted and 1500°C -annealed samples together with a random spectrum are shown. In the case of $8\times 10^{14}\text{cm}^{-2}$ implantation (Fig.6.22), the as-implanted layer has crystalline structure (Fig.6.22(b)), and the damage is almost completely removed by annealing at 1500°C (Fig.6.22(c)). In high-dose implantation of $4\times 10^{15}\text{cm}^{-2}$ (Fig.6.23), the randomized layer is formed at the surface (Fig.6.23(b)). The width of the randomized layer is $0.40\mu\text{m}$, which is a little deeper than the N profile. Through annealing, the epitaxial regrowth takes place mainly from the underlying undamaged layer, but a severely damaged layer does remain after annealing as shown in Fig.6.23(c).

Figure 6.24 shows the implant dose dependence of the backscattering yield ratio in RBS spectra for as-implanted and 1500°C -annealed samples. The ratios for as-implanted layers represent a steep increase with increasing

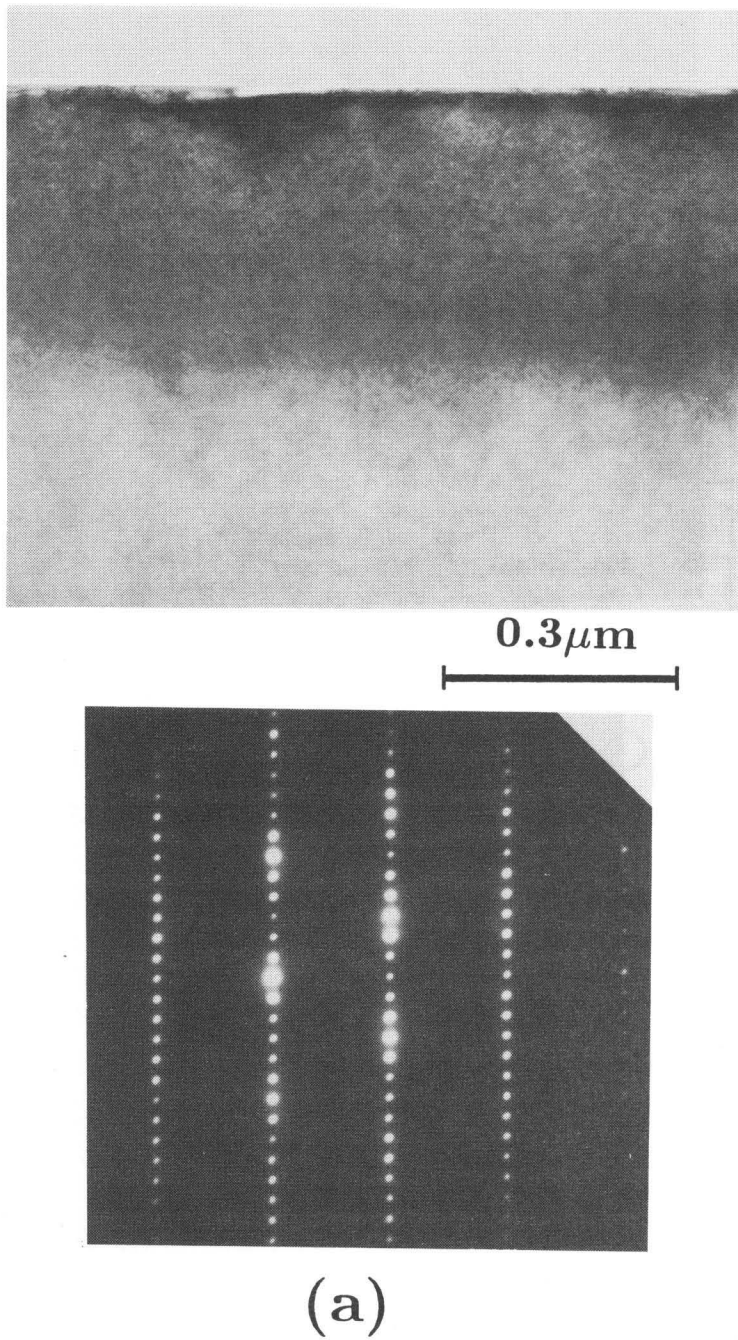
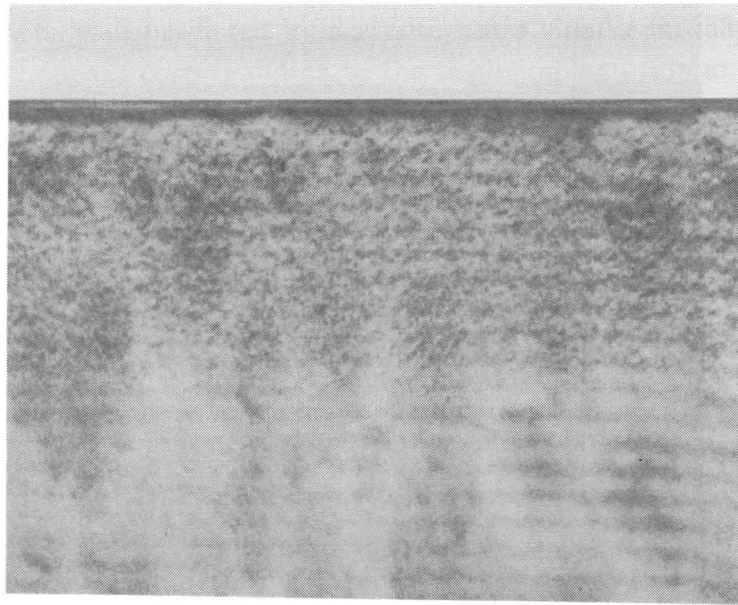
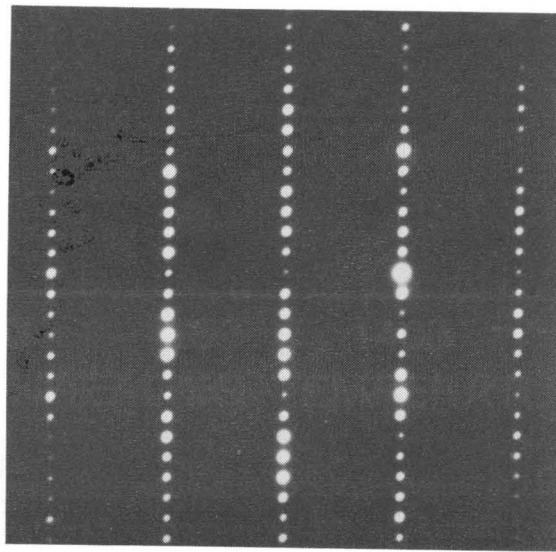


Fig.6.25 (a) Cross-sectional TEM image and diffraction pattern for an as-implanted sample (total dose= $2\times 10^{15}\text{cm}^{-2}$).



0.3 μm



(b)

Fig.6.25 (b) Cross-sectional TEM image and diffraction pattern for a 1500°C-annealed sample (total dose= $2 \times 10^{15} \text{cm}^{-2}$).

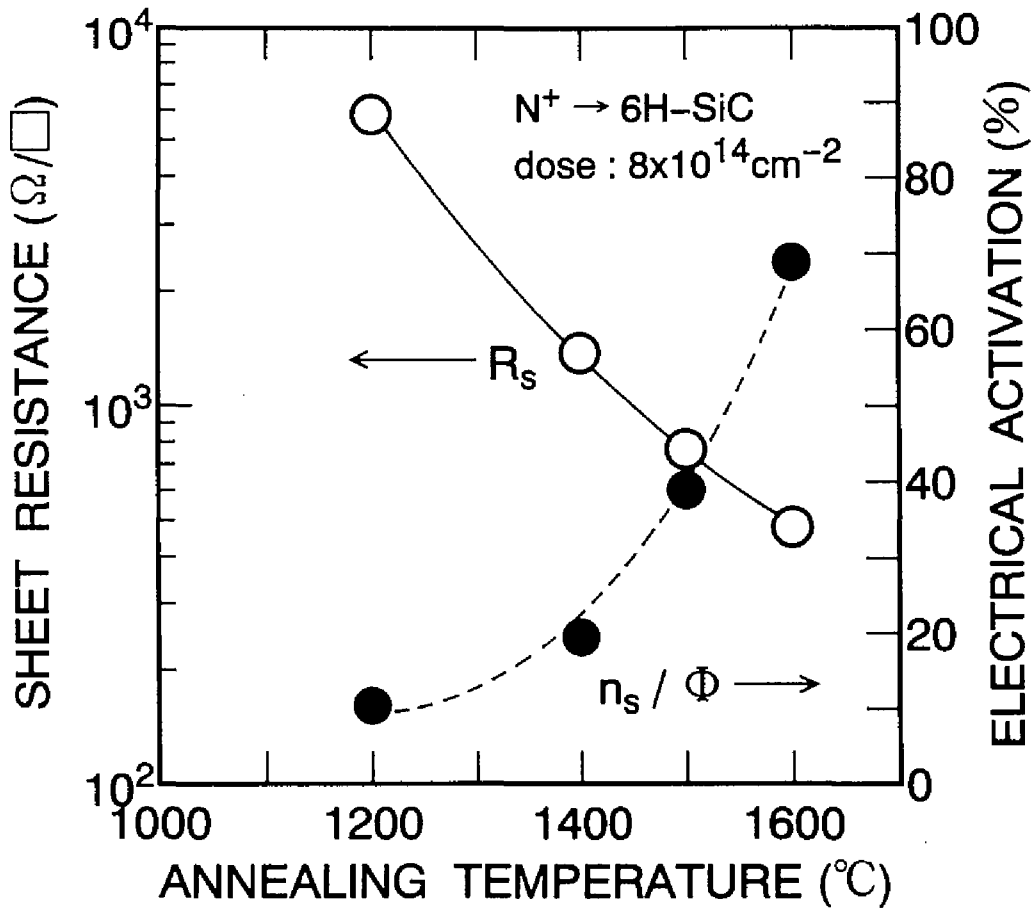


Fig.6.26 Annealing temperature dependence of sheet resistance and electrical activation for N^+ -implanted layers. The implant dose is $8.0 \times 10^{14} \text{ cm}^{-2}$.

dose, and reach up to 100% when the dose exceeds $4 \times 10^{15} \text{cm}^{-2}$, which is a threshold dose for amorphous formation. Figure 6.24 suggests that the damage cannot be removed by 1500°C -annealing, once amorphous layers are formed through implantation. Even in low-dose implantation ($1 \times 10^{14} \sim 8 \times 10^{14} \text{cm}^{-2}$), the ratios after 1500°C -annealing (1.9~2.3%) are slightly higher than that of a virgin sample (1.7%), indicating the difficulty of complete regrowth.

Figure 6.25 shows cross-sectional TEM images and diffraction patterns for (a) as-implanted and (b) 1500°C -annealed samples implanted with a dose of $2 \times 10^{15} \text{cm}^{-2}$. From the diffraction pattern, the as-implanted layer has crystalline structure (6H-SiC), which is consistent with the result of RBS measurement. Damaged (dark) region extends to $0.3 \mu\text{m}$ depth (Fig.6.25(a)). This dark region may originate from substantial strain and/or a number of point defects formed through implantation. The damage can be significantly removed by the annealing, though small dark spots remain, which might be ascribed to coalesced point defects or defect-complexes. However, the formation of dislocation loops and stacking faults was not observed.

The annealing temperature dependence of sheet resistance and electrical activation ratio is shown in Fig.6.26. Here, the electrical activation ratio was defined as the ratio of the sheet carrier concentration n_s ($n_s = nd$, n : the average carrier concentration, d : the junction depth) to the N^+ dose Φ . The annealing at 1200°C is not enough for the activation of implanted N, a very high sheet resistance of $5.8 \text{k}\Omega/\square$ and a low electrical activation of 11%. High-temperature annealing at 1500°C is required to obtain reasonable sheet resistances less than $1 \text{k}\Omega/\square$.

Figure 6.27 shows the dose dependence of the sheet resistance of implanted layers characterized by the van der Pauw method. The annealing was performed at 1500°C for 30min. In the low-dose region, the sheet resistance decreases with the dose. After showing minimum at a dose of $8 \times 10^{14} \text{cm}^{-2}$, however, the resistance increases with increasing dose. The minimum sheet resistance of $770 \Omega/\square$ obtained in this study is lower than the best value ($843 \Omega/\square$) ever reported in SiC, which has been obtained by hot-implantation at 1000°C and post-annealing at 1300°C [10].

In donor (phosphorus) ion implantation into Si, lower sheet resistances can be achieved through implantation with higher dose up to 10^{16}cm^{-2} [55],

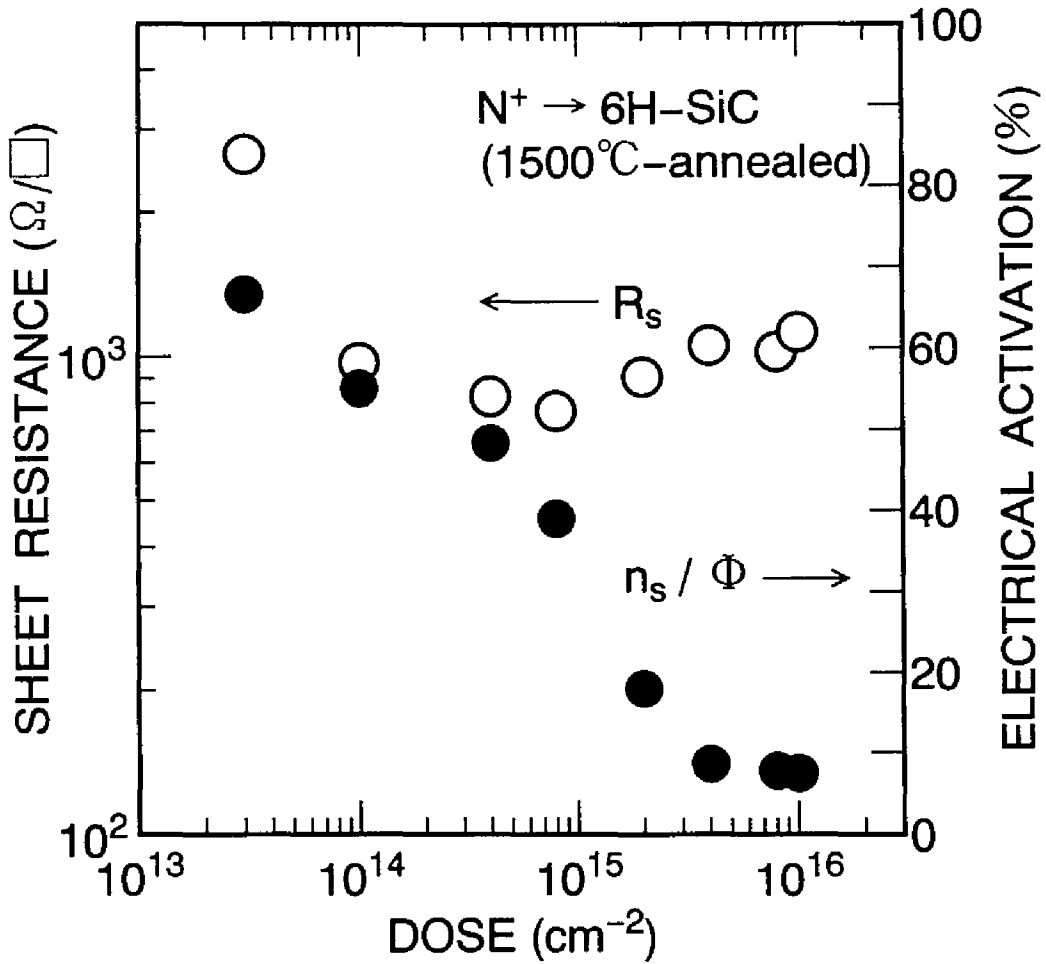


Fig.6.27 Implant dose dependence of sheet resistance and electrical activation ratio for N⁺ implanted layers annealed at 1500°C.

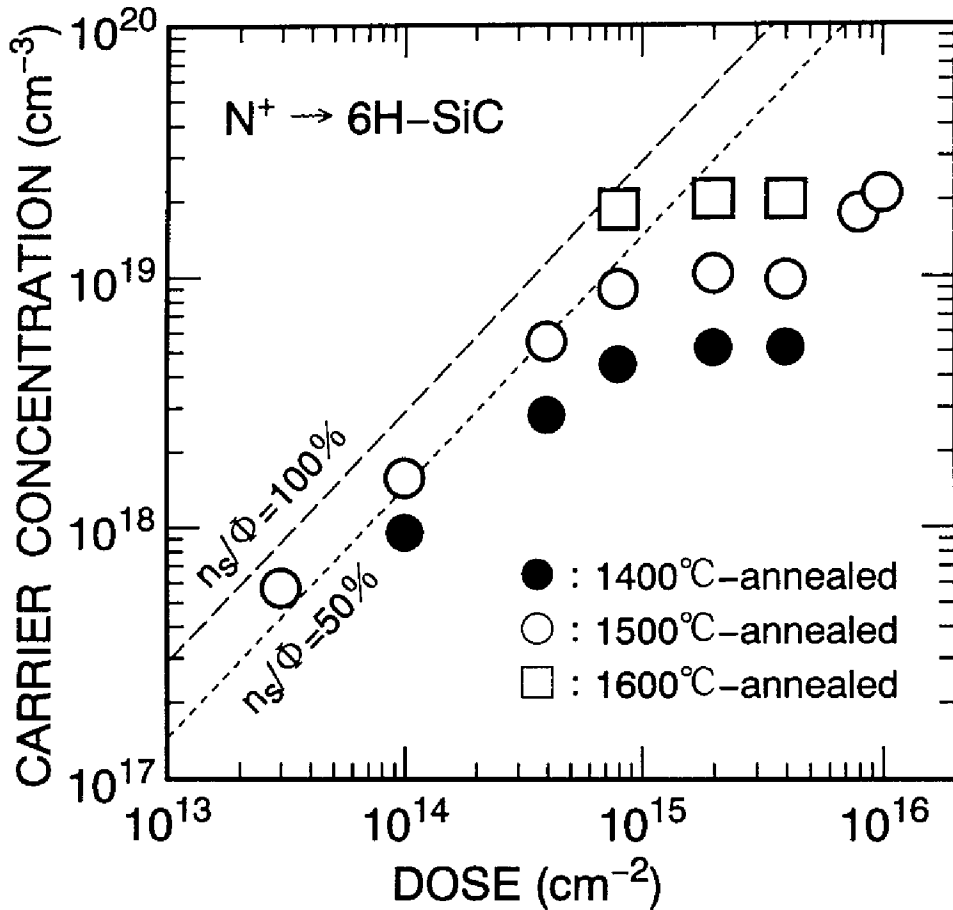


Fig.6.28 Implant dose dependence of average carrier concentration of N^+ -implanted layers. The closed circles, open circles, and open squares denote the results for implanted layers annealed at 1400, 1500, and 1600°C, respectively. The dotted lines represent 100% and 50% electrical activation.

owing to its very high solubility and complete recrystallization of implanted Si layers. However, the sheet resistance cannot be reduced by high-dose N^+ implantation into SiC. This different behavior of the sheet resistance in the high-dose region may result from the lower solubility of N in SiC or the low electrical activation due to the remaining lattice damage. Since the solubility of N in SiC is rather high ($\geq 10^{20} \text{cm}^{-3}$ at 1750°C) [56], the lattice damage seems to prevent the activation of implanted N atoms.

To clarify the electrical activation of implanted ions, the dose dependence of the average carrier concentration in implanted layers, which was obtained by Hall effect measurement, is shown in Fig.6.28. The results for samples annealed at 1400 , 1500 , and 1600°C are presented. In the figure, two dotted lines represent the dependences corresponding to electrical activation ratios of 100% and 50%. In the low-dose region, the carrier concentration increases almost proportionally to the implant dose, indicating the constant electrical activation ratio. The electrical activation ratios of 1500°C -annealed samples are about 50% in this region. Note that the N donor concentration should be a little higher than the carrier concentration because of the large ionization energies ($80\sim 144\text{meV}$) [30] of N donors. The analysis on the temperature dependence of carrier concentration will be required for the future study.

With the increase in dose, the carrier concentrations show saturation, which makes the electrical activation ratio decrease down to about 10% or less. Note that the saturated value of the carrier concentration depends on the annealing temperature: the annealing at higher temperature leads to the higher carrier concentration. This result suggests that the carrier concentration is limited by the remaining damage, and not by solubility. In fact, the damage cannot be removed when the dose exceeds 10^{15}cm^{-2} , which has been elucidated through RBS measurements. The difficulty of complete recrystallization of SiC may be attributed to its high activation energy for crystallization and/or microscopic deviation of stoichiometry caused by implantation. Therefore, the implantation-induced damage should be minimal during implantation into SiC. Hot-implantation may be promising especially for high-dose implantation [10,57].

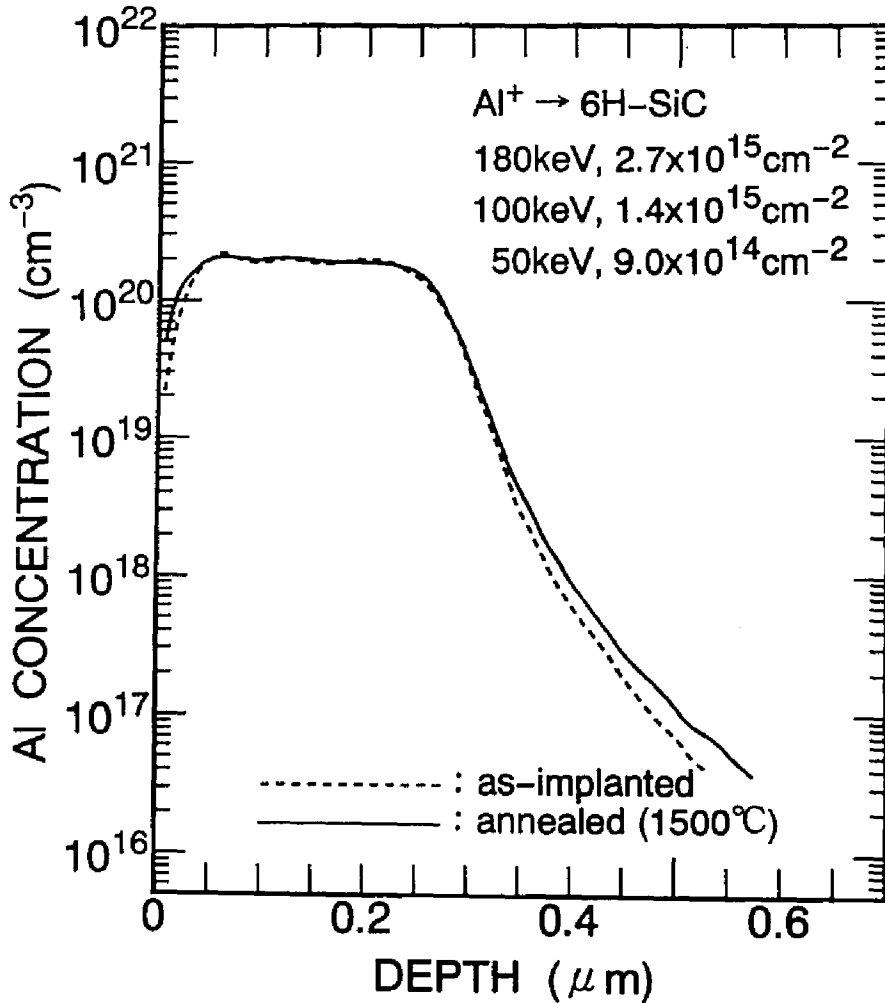


Fig.6.29 Al depth profiles before and after annealing at 1500°C for 30min. Triple implantation was done with 180keV, $2.7 \times 10^{15} \text{cm}^{-2}$, 100keV, $1.4 \times 10^{15} \text{cm}^{-2}$, and 50keV, $9.0 \times 10^{14} \text{cm}^{-2}$ (total dose: $5.0 \times 10^{15} \text{cm}^{-2}$).

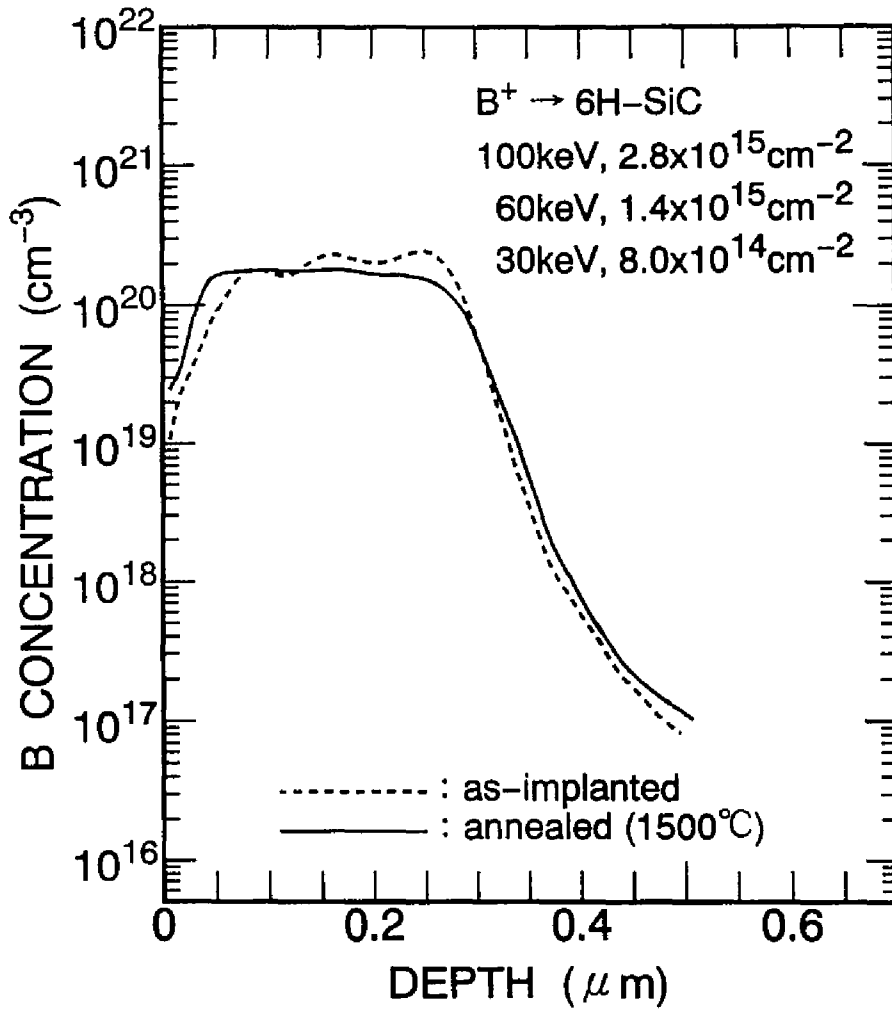


Fig.6.30 B depth profiles before and after annealing at 1500°C for 30min. Triple implantation was done with 100keV, $2.8 \times 10^{15} \text{cm}^{-2}$, 60keV, $1.4 \times 10^{15} \text{cm}^{-2}$, and 30keV, $8.0 \times 10^{14} \text{cm}^{-2}$ (total dose: $5.0 \times 10^{15} \text{cm}^{-2}$).

6.5.2 Aluminum and boron ion implantation

As for the Al ion implantation into SiC, there have been contradictions between the previous reports. Some groups succeeded in the formation of p-layer [58], whereas the formation of highly resistive layers by the implantation was reported by other groups [49]. Besides, only a few studies on B ion implantation into SiC have been published [39,59].

In this subsection, the author investigated Al and B ion implantations using device-quality 6H-SiC epilayers. The implantation-induced damage and electrical properties of implanted layers are characterized. In electrical measurements, Al/Ti annealed at 1000°C was used as ohmic contacts.

N-type 5 μ m-thick 6H-SiC epilayers grown on off-oriented 6H-SiC(000 $\bar{1}$)C faces were used. The donor concentrations of epilayers and substrates were $7 \times 10^{15} \sim 2 \times 10^{16} \text{cm}^{-3}$ and $2 \times 10^{18} \text{cm}^{-3}$, respectively. Al⁺ or B⁺ ions were implanted into the bare surface of samples at room temperature. The total implant dose was varied in the wide range of $1 \times 10^{14} \sim 2 \times 10^{16} \text{cm}^{-2}$ to investigate the dose effects. The implantation conditions except for the each implantation energy and dose are similar to those in the case of N⁺ implantation. For the electrical measurements, Al/Ti annealed at 1000°C was used as ohmic contacts. From SEM observation, the implantation depth was estimated to be 0.55~0.60 μ m for Al⁺- and B⁺-implanted samples.

Figure 6.29 shows Al profiles before and after annealing at 1500°C for 30min. The detailed implantation energy and dose are shown in the figure (total dose of Al⁺ was $5.0 \times 10^{15} \text{cm}^{-2}$). B atom profiles, implanted with the same total dose, before and after annealing at 1500°C for 30min are shown in Fig.6.30. Both the distributions exhibit box profiles of a peak concentration of $2 \times 10^{20} \text{cm}^{-3}$. By adjusting the implant energies, quite similar profiles could be obtained between Al⁺ and B⁺ implantations. Redistribution of Al and B is negligibly small after high-temperature annealing at 1500°C, though slight out-diffusion was observed in the B⁺-implanted sample. Addamiano *et al.* reported that annealing at 1400°C causes the serious out-diffusion of Al and B in implanted Lely crystals [60]. This disagreement may originate from the difference in quality of used crystals. The Lely crystals, which are grown at a very high temperature of 2400°C, may contain high density of vacancies and/or

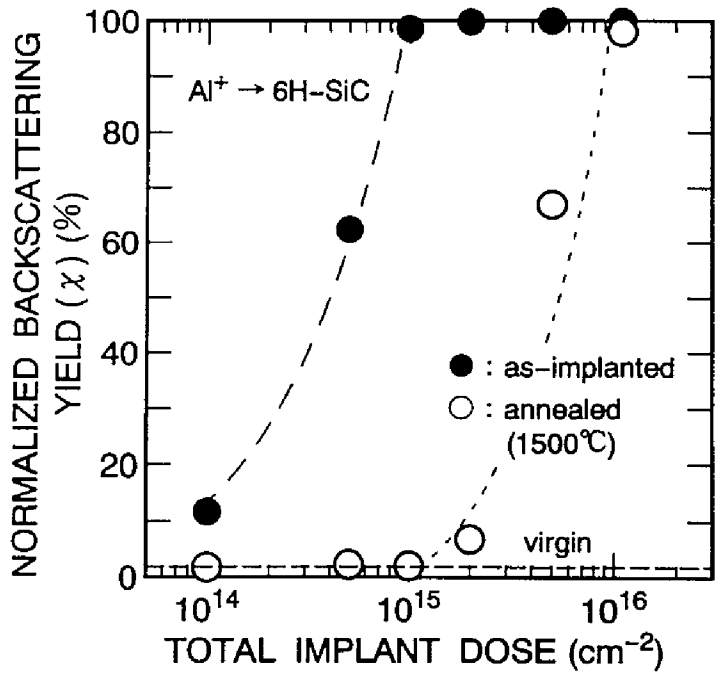


Fig.6.31 Al⁺ implant dose dependence of backscattering yield ratio in RBS spectra for as-implanted and 1500°C-annealed samples.

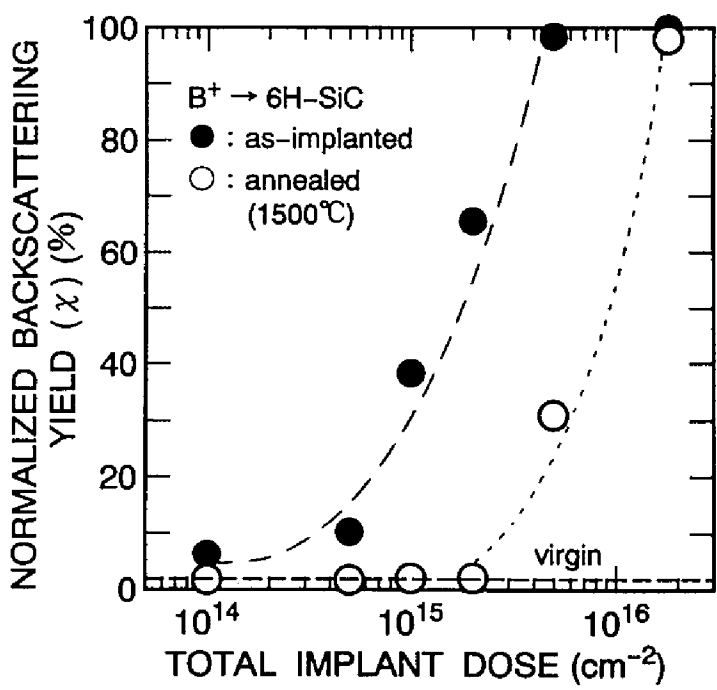


Fig.6.32 B⁺ implant dose dependence of backscattering yield ratio in RBS spectra for as-implanted and 1500°C-annealed samples.

interstitials, which enhance the diffusion of impurities during heat treatment.

The author briefly checked the annealing temperature dependence of the properties of Al⁺- and B⁺-implanted layers, and found that higher annealing temperatures are preferable to improve the quality of implanted layers. Thus, annealing at 1500°C was mainly employed. Figures 6.31 and 6.32 show the implant dose dependence of the backscattering yield ratio in RBS spectra for as-implanted and 1500°C-annealed samples in Al and B implantations. The normalized backscattering yield for as-implanted layers represent a steep increase at about $5 \times 10^{14} \text{cm}^{-2}$ dose in Al⁺ implantation (Fig.6.31), and $1 \times 10^{15} \text{cm}^{-2}$ dose in B⁺ implantation (Fig.6.32). The critical implant dose for complete amorphization can be estimated to be $1 \times 10^{15} \text{cm}^{-2}$ dose in Al⁺ implantation, and $5 \times 10^{15} \text{cm}^{-2}$ dose in B⁺ implantation. The lower critical implant dose in the former case indicates that the implantation-induced damages are more severe in Al⁺ implantation. This result reflects the difference in the mass of implanted ions: Al atoms are much heavier, which leads to dominant collisions of implanted ions with nuclei of a host material. In the present study, the author formed the almost same implantation profiles between Al⁺ and B⁺ implantations. The heavier mass of Al atoms requires higher-energy implantation to obtain a profile with the same junction depth, owing to its smaller projected ranges. This high-energy implantation is another reason why the lattice damages are more severe in Al⁺ implantation. After annealing at 1500°C, the damages are significantly removed when the as-implanted layers have crystalline structures. However, the severe damages remain even after 1500°C-annealing, once amorphous layers are formed through implantation, which is quite similar to the case of N⁺ implantation. For further investigation on lattice damages, cross-sectional transmission electron microscope (TEM) observation will be required.

After annealing at 1500°C, Al⁺-implanted layers showed p-type conduction. Figure 6.33 shows the dose dependence of the sheet resistance and electrical activation ratio of Al⁺-implanted layers characterized by the van der Pauw method. The sheet resistance gradually decreases with the increase of Al⁺ dose in the range of $1 \times 10^{14} \text{cm}^{-2} \sim 2 \times 10^{15} \text{cm}^{-2}$, and a sheet resistance of $22 \text{k}\Omega/\square$ was obtained with a corresponding electrical activation of 1.6%. For a sample implanted with $1.1 \times 10^{16} \text{cm}^{-2}$, the implanted layer was rather resistive,

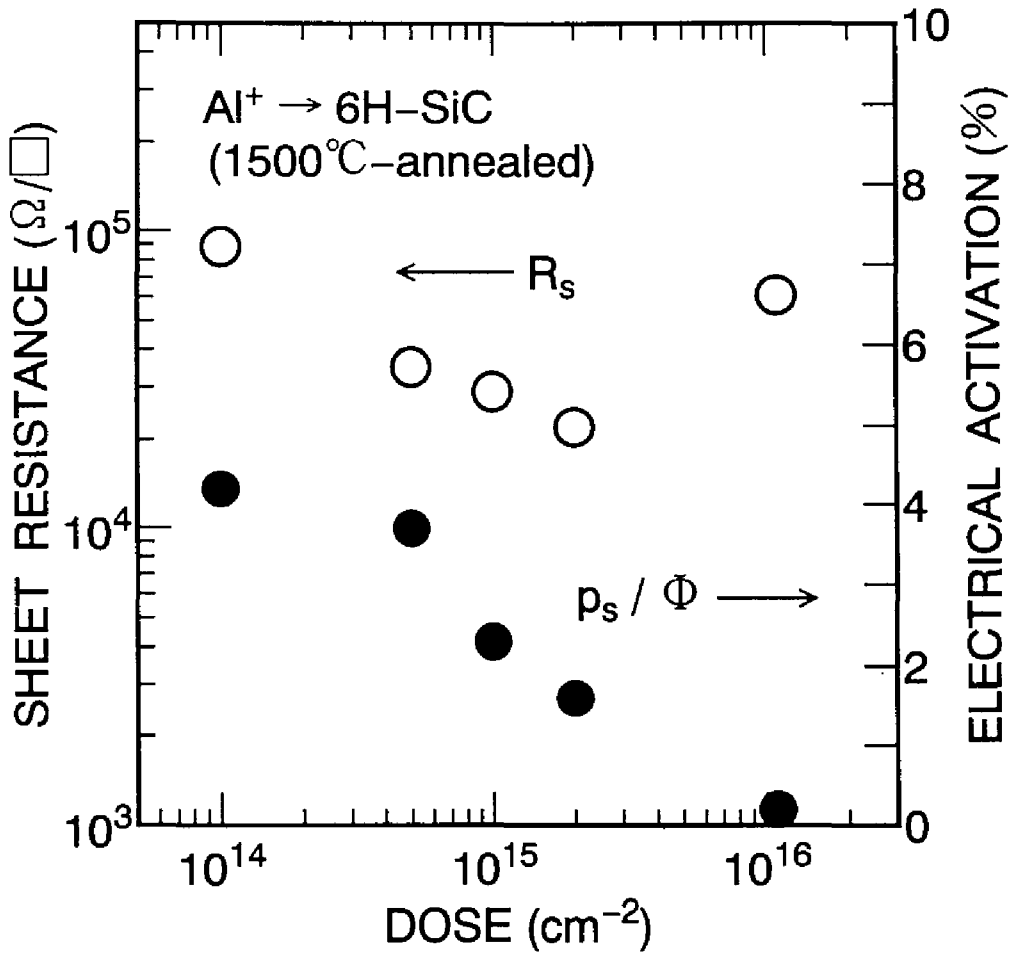


Fig.6.33 Implant dose dependence of sheet resistance and electrical activation ratio for Al⁺-implanted layers annealed at 1500°C.

which may be caused by the severe implantation damage as shown in Fig.6.31. The high sheet resistances of Al⁺-implanted layers come from the low electrical activation ratio caused by the deep Al acceptor level and the low hole mobility (about 1/5~1/10 of electron mobility). On the basis of rough estimation, the resistivities of implanted layers turned out to almost coincide with those of Al-doped epilayers with the similar Al concentrations. To reduce the sheet resistance, the Al⁺ dose should be increased, keeping the implantation-damages as small as possible. In this sense, hot-implantation may be promising.

Recently, Rao *et al.* reported a systematic study on Al⁺ and B⁺ implantations into 6H-SiC [61]. According to the report, Al⁺ implantation at room temperature resulted in the formation of n-type or resistive layers and p-type layers could be obtained only by hot implantation at 850°C followed by annealing at 1400°C. Although the origins of discrepancy between their and this results are not clear, one possible reason may be a difference in the annealing process. In sample annealing, Rao *et al.* used a conventional electric furnace, whereas we employed a rf-induction heated furnace, which allows very fast temperature rising ($\geq 40^\circ/\text{s}$). This rapid heating might prevent unfavorable annealing stages at low temperatures. Anyway, the present study is the first report that demonstrates clear p-type conduction of SiC layers implanted with Al⁺ at room temperature.

On the other hand, B⁺-implanted layers were highly resistive which prevented the identification of conduction type (p or n) as well as the accurate measurement of electrical activation. Figure 6.34 shows the implant dose dependence of resistivity for B⁺-implanted layers annealed at 1500°C³. The dotted line denotes the dependence calculated from the B acceptor ionization energy (350meV) [39,48] and a mobility (20cm²/Vs). The obtained resistivities (15~120Ωcm) agree with predicted values. The author confirmed the resistivities almost coincide with those of B-doped epilayers with the similar B concentration. Thus, the author believe that the high resistivities of B⁺-implanted layers are not due to remaining damages but inherent to B-doped SiC because of its deep acceptor level. B⁺ implantation may be effective to form highly resistive layers rather than to make p⁺ well. For example, the

³The resistivities of B⁺-implanted layers were so high that the plot of sheet resistance seems to make no sense.

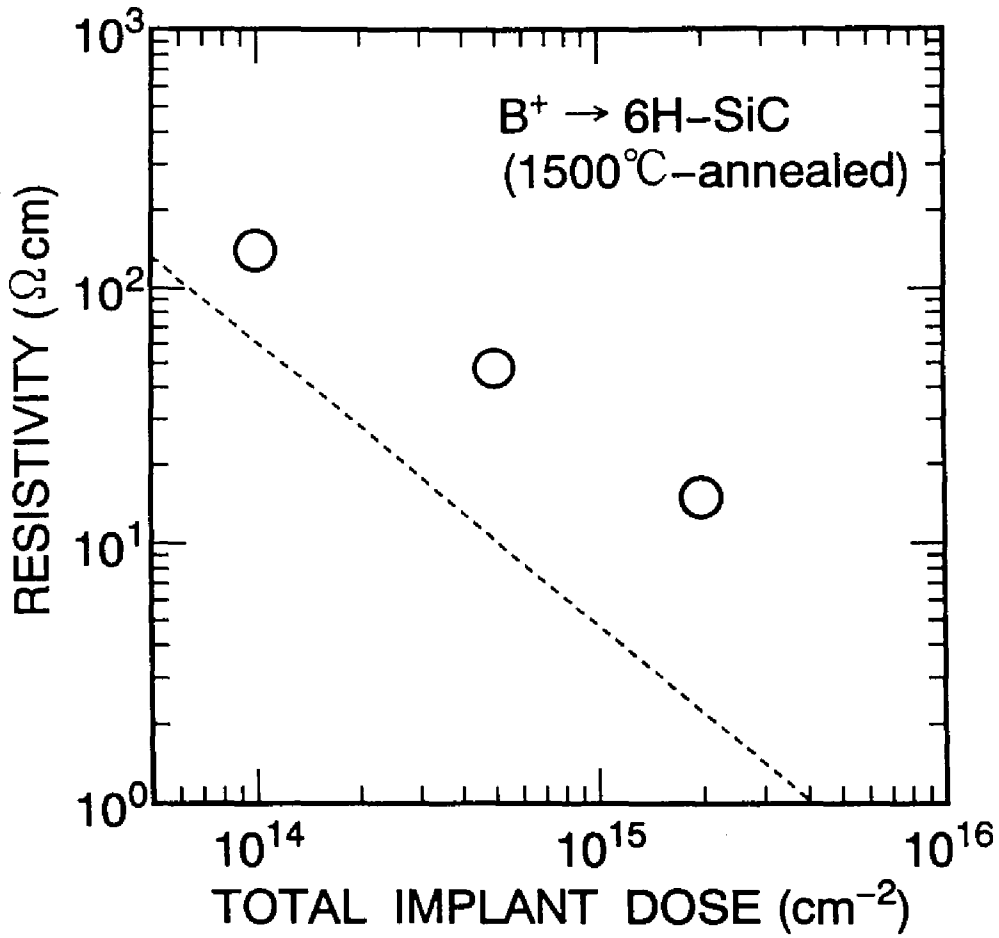


Fig.6.34 Implant dose dependence of resistivity for B⁺-implanted layers annealed at 1500°C. The dotted line denotes the dependence calculated from the B acceptor ionization energy (350meV) and a mobility of 20cm²/Vs.

edge termination of high-voltage Schottky rectifiers is a hopeful application of B^+ implantation [62].

6.6 Summary

In this chapter, detailed characterization of undoped n-type 6H-SiC epilayers was presented. *In-situ* doping and ion implantation of donor and acceptor impurities were systematically investigated.

RBS, X-ray diffraction, and cross-sectional TEM analyses demonstrated the high quality of epilayers. The typical etch pit density of epilayers was 10^4cm^{-2} . In low-temperature photoluminescence, the N bound exciton and free exciton peaks were dominant, and Al- and Ti-related luminescence was negligibly small, indicating high purity of epilayers. For low-doped epilayers with a carrier concentration of $2 \times 10^{14}\text{cm}^{-3}$, a high electron mobility of $431\text{cm}^2/\text{Vs}$ could be obtained, which is the highest ever reported in 6H-SiC. The temperature dependence of carrier concentration and mobility suggested the very low compensation. In ICTS and DLTS measurements, three deep electron traps with concentrations of $10^{15} \sim 10^{16}\text{cm}^{-3}$ were observed in 6H-SiC wafers. However, the epilayers have very few electron traps of which concentration is negligibly small ($< 10^{13}\text{cm}^{-3}$).

In-situ doping of N, Al, and B was achieved in the wide range of $10^{16} \sim 10^{19}\text{cm}^{-3}$ with excellent controllability, using N_2 , TMA, and B_2H_6 as source gases. Remarkable polarity dependence in Al doping efficiency was observed. The carrier concentration dependences of electron and hole mobilities were presented. Although the ionization energy of Al acceptors is high in SiC, a low resistivity of $0.04\Omega\text{cm}$ was obtained in heavily doped samples. B-doped layers showed high resistivities of $80 \sim 520\Omega\text{cm}$.

N^+ implantation into p-type 6H-SiC{0001} epilayers was investigated. The implantation-induced damages severely increased when the implant dose exceeds $1 \times 10^{15}\text{cm}^{-2}$. A low sheet resistance of $770\Omega/\square$ was obtained by 1500°C -annealing for a layer implanted with $8 \times 10^{14}\text{cm}^{-2}$. A relatively high electrical activation ratio ($\sim 50\%$) can be obtained in the case of low-dose implantation ($\leq 1 \times 10^{15}\text{cm}^{-2}$). In high-dose implantation ($\geq 1 \times 10^{15}\text{cm}^{-2}$), how-

ever, the electrical activation is limited by the residual damage in implanted layers. Al⁺ and B⁺ implantations into n-type 6H-SiC epilayers were also studied. The implantation-induced damages were severe in Al⁺ implantation due to the larger mass of implanted ions. P-type layers with a sheet resistance of 22k Ω /□ could be obtained by Al⁺ implantation followed by annealing at 1500°C. B⁺ implantation resulted in the formation of resistive layers with resistivities of 15~120 Ω cm, which may be attributed to the deep B acceptor level.

References

- [1] *Silicon Carbide and Related Materials*, M.G.Spencer, R.P.Devaty, J.A.Edmond, M.A.Khan, R.Kaplan, and M.M.Rahman, Eds. (Institute of Physics, Bristol, 1994).
- [2] H.S.Kong, J.T.Glass and R.F.Davis, *J. Appl. Phys.*, **64**, 2672(1988).
- [3] J.A.Powell, D.J.Larkin, L.G.Matus, W.J.Choyke, J.L.Bradshaw, L.Henderson, M.Yoganathan, J.Yang, and P.Pirouz, *Appl. Phys. Lett.*, **56**, 1442(1990).
- [4] S.Karmann, W.Suttrop, A.Schöner, M.Schadt, C.Haberstroh, F.Engelbrecht, R.Helbig, G.Pensl, R.A.Stein, and S.Leibenzeder, *J. Appl. Phys.*, **72**, 5437(1992).
- [5] T.Tachibana, H.S.Kong, Y.C.Wang, and R.F.Davis, *J. Appl. Phys.*, **67**, 10(1990).
- [6] A.Henry, O.Kordina, C.Hallin, C.Hemmingsson, and E.Janzén, *Appl. Phys. Lett.*, **65**, 2457(1994).
- [7] W. von Muench and I.Phaffeneder, *Thin Solid Films*, **31**, 39(1976).
- [8] Y.C.Wang, R.F.Davis, and J.A.Edmond, *J. Electron. Mat.*, **20**, 289(1991).
- [9] G.Pensl, R.Helbig, H.Zhang, G.Ziegler, and P.Lanig, *Mat. Res. Soc. Sympo. Proc.*, **97**, 195(1987).
- [10] M.Ghezzi, D.M.Brown, E.Downey, J.Kretchmer, W.Hennessy, D.L.Polla, and H.Bakhru, *IEEE Electron Device Lett.*, **12**, 639(1992).
- [11] A.Itoh, unpublished.
- [12] B.D.Cullity, *Elements of X-ray Diffraction* (Addison-Wesley, Massachusetts, 1956).
- [13] R.C.Glass, L.O.Kjellberg, V.F.Tsvetkov, J.E.Sundgren, and E.Janzén, *J. Crystal Growth*, **132**, 504(1993).
- [14] K.Koga, Y.Fujikawa, Y.Ueda, and T.Yamaguchi, *Amorphous and Crystalline Silicon Carbide IV, Springer Proc. in Physics 71* (Springer, Berlin, 1992), p.96.
- [15] R.A.Stein, *Physica B*, **185**, 211(1993).
- [16] H.M.Hobgood, D.L.Barrett, J.P.McHugh, R.C.Clark, S.Sriram, A.A.Burk,

- J.Greggi, C.D.Brandt, R.H.Hopkins, and W.J.Choyke, *J. Crystal Growth*, **137**, 181(1994).
- [17] J.Takahashi, M.Kanaya, and Y.Fujiwara, *J. Crystal Growth*, **135**, 61(1994).
- [18] S.Wang, M.Dudley, C.H.Carter, Jr., and H.S.Kong, *Mat. Res. Soc. Sympo. Proc.*, **339**, 735(1994).
- [19] W.Choyke and L.Patrick, *Phys. Rev.*, **127**, 1868(1962).
- [20] A.W.C. van Kemenade and S.H.Hagen, *Solid State Commun.*, **14**, 1331(1974).
- [21] K.M.Lee, L.S.Dang, G.D.Watkins, and W.J.Choyke, *Phys. Rev.*, **B32**, 2273(1985).
- [22] W.J.Choyke and L.Patrick, *Silicon Carbide 1973*, R.C.Marshall, J.W.Faust, Jr., and C.E.Ryan, Eds. (Univ. of South Carolina Press, Columbia, 1974), p.261.
- [23] W.J.Choyke, *Mat. Res. Bull.*, **4**, S141(1969).
- [24] L.L.Clemen, M.Yoganathan, W.J.Choyke, R.P.Devaty, H.S.Kong, J.A.Edmond, D.J.Larkin, J.A.Powell, and A.A.Burk, Jr., *Silicon Carbide and Related Materials*, M.G.Spencer, R.P.Devaty, J.A.Edmond, M.A.Khan, R.Kaplan, and M.M.Rahman, Eds. (Institute of Physics, Bristol, 1994). p.251.
- [25] L.L.Clemen, R.P.Devaty, M.F.MacMillan, M.Yoganathan, W.J.Choyke, D.J.Larkin, J.A.Powell, J.A.Edmond, and H.S.Kong, *Appl. Phys. Lett.*, **62**, 2953(1993).
- [26] S.M.Sze, *Physics of Semiconductor Devices* (John Wiley & Sons, New York, 1981).
- [27] H.Harima, S.Nakashima, and T.Uemura, to be published in *J. Appl. Phys.* (1995).
- [28] L.Patrick, *Phys. Rev.*, **B5**, 2198(1972).
- [29] M.Ikeda, H.Matsunami, and T.Tanaka, *Phys. Rev.*, **B22**, 2842(1980).
- [30] W.Suttrop, G.Pensl, W.J.Choyke, R.Stein, and S.Leibenzeder, *J. Appl. Phys.*, **72**, 3708(1992).
- [31] C.Raynaud, F.Ducroquet, G.Guillot, L.M.Porter, and R.F.Davis, *J. Appl. Phys.*, **76**, 1956(1994).
- [32] W.J.Schaffer, G.H.Negley, K.G.Irvine, and J.W.Palmour, *Mat. Res. Soc. Sympo. Proc.*, **339**, 595(1994).
- [33] A.Itoh, H.Akita, T.Kimoto, and H.Matsunami, *Appl. Phys. Lett.*, **65**, 1400(1994).
- [34] D.Long, *Phys. Rev.*, **120**, 2024(1960).
- [35] V.Nagesh, J.W.Farmer, R.F.Davis, and H.S.Kong, *Appl. Phys. Lett.*, **50**, 1138(1987).
- [36] P.Zhou, M.G.Spencer, G.L.Harris, and K.Fekade, *Appl. Phys. Lett.*, **50**, 1384(1987).
- [37] R.E.Avila, J.J.Kopanski, and C.D.Fung, *Appl. Phys. Lett.*, **49**, 334 (1986).
- [38] M.M.Anikin, A.A.Levdev, A.L.Syrkin, and A.V.Suvorov, *Sov. Phys.*

- Semicond., **19**, 69(1985).
- [39] W.Suttrop, G.Pensl and P.Lanig, Appl. Phys., **A51**, 231(1990).
- [40] G.Pensl and W.J.Choyke, Physica B, **185**, 264(1993).
- [41] A.Uddin and T.Uemoto, Jpn. J. Appl. Phys., **32**, L1670(1993).
- [42] H.Okushi and Y.Tokumaru, Jpn. J. Appl. Phys., **20**, Suppl. 20-1, 261(1980).
- [43] D.V.Lang, J. Appl. Phys., **45**, 3023(1974).
- [44] D.J.Larkin, P.G.Neudeck, J.A.Powell, and L.G.Matus, *Silicon Carbide and Related Materials*, M.G.Spencer, R.P.Devaty, J.A.Edmond, M.A.Khan, R.Kaplan, and M.M.Rahman, Eds. (Institute of Physics, Bristol, 1994). p.51.
- [45] S.Yoshida, E.Sakuma, S.Misawa, and S.Gonda, J. Appl. Phys., **55**, 169(1984).
- [46] H.Nishino, Master Thesis, Dept. of Electrical Eng., Kyoto Univ. (1990).
- [47] V.I.Fistul, *Heavily Doped Semiconductors* (Plenum, New York, 1969).
- [48] Yu.A.Vodakov, N.Zhumaev, B.P.Zverev, G.A.Lomakina, E.N.Mokhov, V.G.Oding, V.V.Semenov, and Yu.F.Simakhin, Sov. Phys. Semicond. **11**, 214(1977).
- [49] O.J.Marsh, *Silicon Carbide 1973*, R.C.Marshall, J.W.Faust, Jr., and C.E.Ryan, Eds. (Univ. of South Carolina Press, Columbia, 1974) p.471.
- [50] H.G.Bohn, J.M.Williams, C.J.McHargue, and G.M.Begun, J. Mat. Res., **2**, 107(1987).
- [51] J.A.Edmond, K.Das, and R.F.Davis, J. Appl. Phys., **63**, 922(1988).
- [52] K.Shibahara, T.Takeuchi, S.Nishino, and H.Matsunami, Jpn. J. Appl. Phys., **28**, 1341(1989).
- [53] S.Yaguchi, T.Kimoto, N.Ohyama, and H.Matsunami, Jpn. J. Appl. Phys., **34**, 3036(1995).
- [54] L.T.Kroko and A.G.Milnes, Solid State Electronics, **9**, 1129(1966).
- [55] H.Ryssel and I.Ruge, *Ion Implantation* (John Wiley & Sons, New York, 1986).
- [56] Yu.A.Vodakov and E.N.Mokhov, *Silicon Carbide 1973*, R.C.Marshall, J.W.Faust, Jr., and C.E.Ryan, Eds. (Univ. of South Carolina Press, Columbia, 1974) p.508.
- [57] N.Inoue, A.Itoh, T.Kimoto, H.Matsunami, T.Nakata, and M.Watanabe, presented at the *6th Int. Conf. Silicon Carbide and Related Materials - 1995* (Kyoto, 1995).
- [58] E.V.Kalinina, N.K.Prokof'eva, A.V.Suvorov, G.F.Kholuyanov, and V.E.Chelnokov, Sov. Phys. Semicond., **9**, 820(1976).
- [59] M.Ghezzeo, D.M.Brown, E.Downey, J.Kretchmer, and J.J.Kopanski, Appl. Phys. Lett., **63**, 1206(1993).
- [60] A.Addamiano, G.W.Anderson, J.Comas, H.L.Hughes, and W.Lucke, J. Electrochem. Soc., **119**, 1355(1972).
- [61] M.V.Rao, P.Griffiths, O.W.Holand, G.Kelner, J.A.Freitas, Jr., D.S.Simons, P.H.Chi, M.Ghezzeo, J. Appl. Phys., **77**, 2479(1995).

- [62] A.Itoh, T.Kimoto, and H.Matsunami, *Proc. 7th Int. Sympo. on Power Semiconductor Devices and IC's*(1995), p.101.

Chapter 7

Application to High-Power, High-Temperature Devices

7.1 Introduction

Step-controlled epitaxy has opened the way to obtain high-quality SiC epilayers with controlling polytypes, which allows the realization of advanced power devices and electronic devices operating at high temperatures.

As an application to power devices, it has been predicted that high-voltage Schottky rectifiers and metal-oxide-semiconductor FETs (MOSFETs) with extremely low specific on-resistances can be realized using SiC owing to its high breakdown field, and SiC devices can replace the present-day Si power devices on account of low power losses and the reduced chip sizes [1]. However, simulation cannot tell the whole story. The fabrication of real devices is the most important task.

Another prospective target of SiC is high-temperature devices. The large bandgap of SiC significantly suppresses the thermal excitation of electrons from the valence band to the conduction band, leading to the extremely low intrinsic carrier concentration ($\sim 10^{-6} \text{cm}^{-3}$ at room temperature for 6H-SiC). This property together with excellent thermal stability allows the realization of SiC devices operating at elevated temperatures with low leakage current.

Although several SiC power devices [2-5] and high-temperature devices

[6-8] have been fabricated, the detailed characteristics including the fabrication process have not been reported.

In this chapter, at first, the author theoretically investigates the performance of SiC power Schottky rectifiers and MOSFETs. Based on the simulation, the feasibility and technological problems of SiC power devices will be discussed. Preliminary results on high-voltage 6H-SiC Schottky rectifiers and pn junction diodes are presented. The current-voltage characteristics and their high-temperature operation are experimentally investigated. This chapter is constructed to offer the final characterization of epilayers with demonstrating the potential of SiC devices.

7.2 Prediction of SiC Power-Device Performance

Although Bhatnagar and Baliga have reported a principal guideline for numerical analyses on SiC power devices [1], more detailed simulation is required to predict real SiC device performance. For example, the anisotropy of electron mobility [9,10] should be taken account. Besides, the low drift-region resistances in SiC power devices should make the channel resistances of power MOSFETs much more important.

7.2.1 Specific on-resistance

A Schottky rectifier is the most simple and basic majority carrier device. The equivalent circuit of a Schottky rectifier is shown in Fig.7.1. The series resistance for unit area (specific on-resistance R_{on}) is given by the sum of epilayer (drift region) and substrate resistances. Here, the contact resistance was neglected due to the low value. The theoretical R_{on} 's are given by

$$R_{on} = R_{drift} + R_{sub} = \rho_{epi}W_{epi} + \rho_{sub}W_{sub}, \quad (7.1)$$

where R_{drift} and R_{sub} are the resistances for unit area of the epilayer and substrate, ρ_{epi} and ρ_{sub} the epilayer and substrate resistivities, W_{epi} and W_{sub} the thicknesses of the epilayer and substrate, respectively. To sustain the high

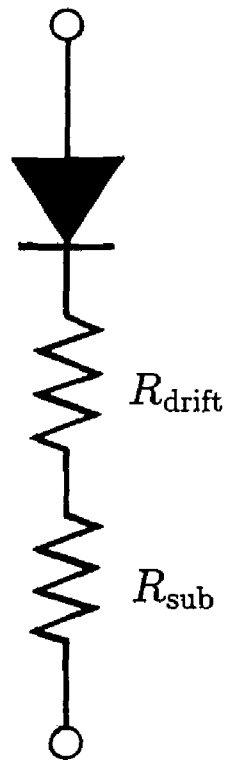


Fig.7.1 Equivalent circuit of a Schottky rectifier. The series resistance for unit area (specific on-resistance R_{on}) is given by the sum of epilayer (drift region) and substrate resistances.

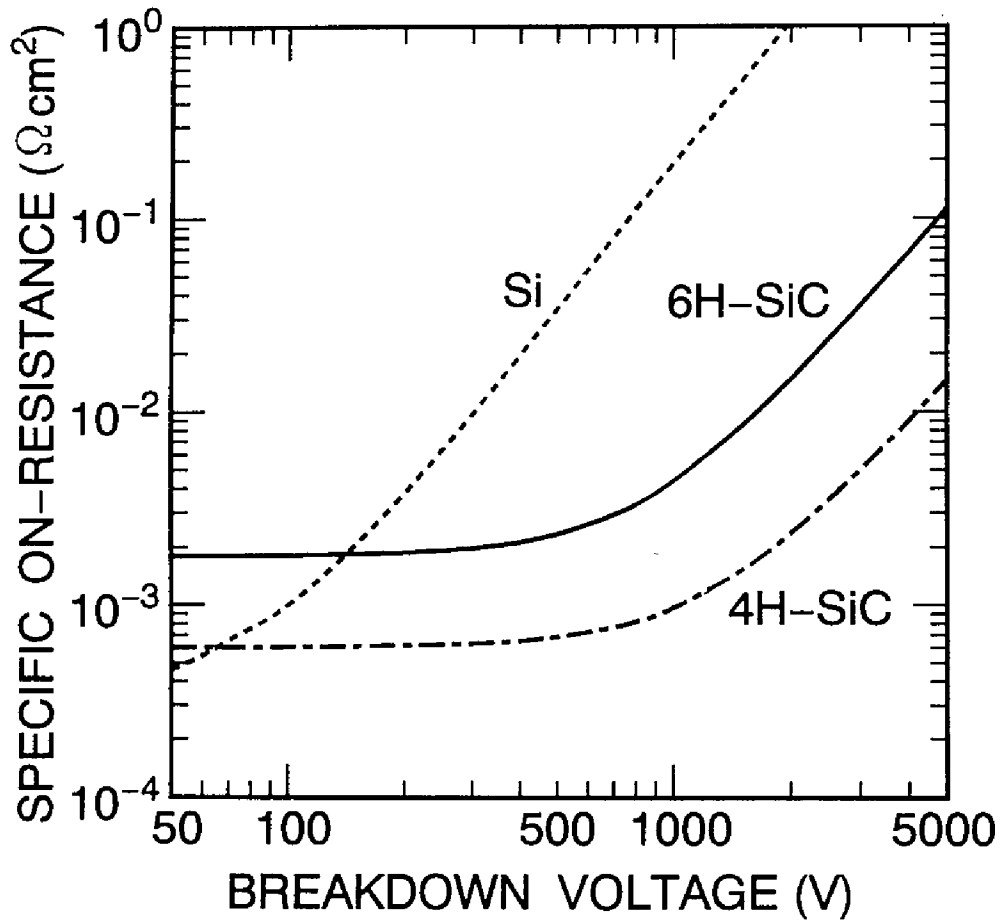


Fig.7.2 Specific on-resistance (R_{on}) as a function of breakdown voltage (V_B) for Si, 6H-, and 4H-SiC Schottky rectifiers.

blocking voltages, the reduced doping concentrations and the increased depletion widths are required, which lead to the increase in R_{drift} . Hence, R_{on} 's are determined mainly by R_{drift} for high-voltage devices. For calculation of R_{sub} , the author used a thickness of $300\mu\text{m}$ and resistivities of $0.01\Omega\text{cm}$, $0.06\Omega\text{cm}$, and $0.02\Omega\text{cm}$ for Si, 6H- and 4H-SiC, respectively, which are commercially available values. Using the breakdown field (E_{B}) and mobility (μ), R_{drift} for optimum structures can be calculated using the following equation [11]

$$R_{\text{drift}} = \eta \frac{4V_{\text{B}}^2}{\epsilon E_{\text{B}}^3 \mu}, \quad (7.2)$$

where ϵ is the permittivity ($\epsilon=11.9\epsilon_0$ for Si and $9.7\epsilon_0$ for SiC : ϵ_0 is the permittivity in vacuum). η is the activation ratio of dopants, and assumed as 1.0 for Si and 2.0 for SiC, taking account of the donor levels. R_{drift} 's were calculated using breakdown field and mobility data reported for Si [12] and SiC [10,13]. Here, the breakdown field of 4H-SiC was assumed to be the same as that of 6H-SiC [14].

It is known that α -SiC exhibits the anisotropy in electron mobility [9,10]. According to the previous reports, the mobility parallel to the c -axis (μ_{\parallel}) is only one-third to one-fifth of the mobility perpendicular to the c -axis (μ_{\perp}) in 6H-SiC. 4H-SiC, however, shows an opposite anisotropy, μ_{\parallel} is even higher than μ_{\perp} by 20%. In this simulation, μ_{\parallel} for 6H- and 4H-SiC was employed. Since μ_{\perp} of 4H-SiC is two times higher than that of 6H-SiC, about 10 times higher μ_{\parallel} can be expected in 4H-SiC. Thus, 4H-SiC is much more attractive for vertical power device applications.

Figure 7.2 shows the specific on-resistance (R_{on}) as a function of breakdown voltage (V_{B}). Although the theoretical R_{on} 's for low-voltage ($\leq 300\text{V}$) SiC rectifiers are saturated due to the relatively high substrate resistances, SiC devices show much lower R_{on} 's than Si in the high-voltage region. In particular, 4H-SiC is the most promising candidate owing to much higher mobility along the c -axis than 6H-SiC.

7.2.2 Effects of channel mobility

Power MOSFETs have inherent excellent properties such as high switching speed, high input impedance, and thermal stability. However, the on-

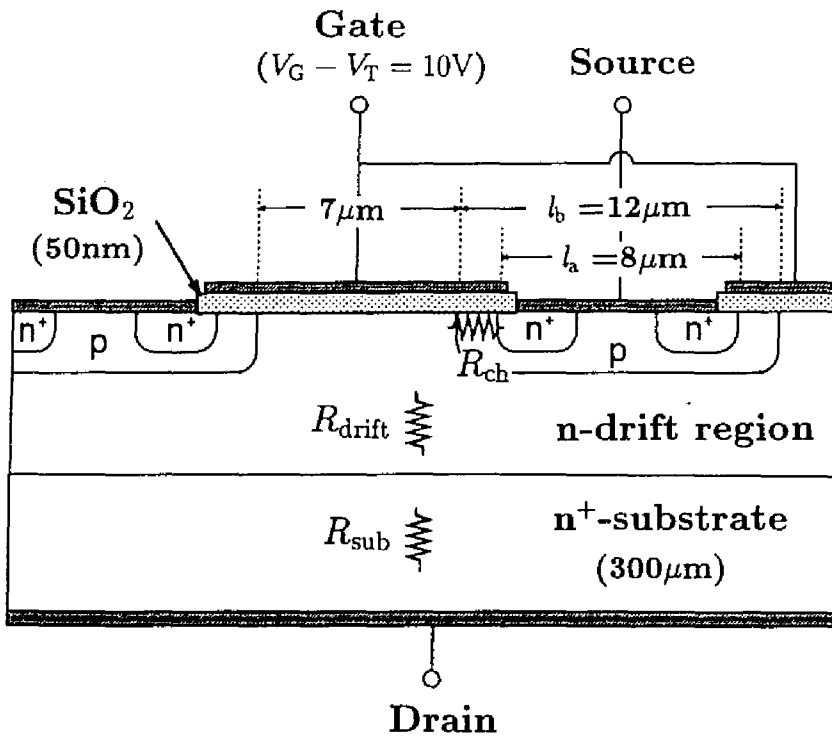


Fig.7.3 Structure of a D MOSFET assumed in the simulation. Gate length and gate width per unit area are $2 \mu\text{m}$ and $15 \text{m}/\text{cm}^2$, respectively.

resistances of power MOSFETs show very rapid increase with the increase in breakdown voltage [15]. Thus, the current handling capability is severely limited in high-voltage Si MOSFETs. In order to meet the needs for high-power and high-frequency applications, the development of SiC MOSFETs may be an ideal solution [1,16,17].

Figure 7.3 shows the structure of a double-diffused MOSFET (DMOSFET) assumed in the present simulation. This structure is employed in most of the present-day Si power MOSFETs. The gate length and gate width per unit area of the MOSFET are $2\mu\text{m}$ and $15\text{m}/\text{cm}^2$, which are typical in the present-day Si DMOSFETs [15]. The thickness of gate oxide and the acceptor concentration of p-well region are 50nm and $1 \times 10^{17}\text{cm}^{-3}$, respectively.

In this study, the total specific on-resistance R_{on} defined as the following equation was considered:

$$R_{\text{on}} = R_{\text{ch}} + R_{\text{drift}} + R_{\text{sub}}, \quad (7.3)$$

where R_{ch} , R_{drift} , and R_{sub} are the resistances for unit area of the channel (inversion layer), drift region, and substrate. Here, the contact resistance and the resistance of junction FET (JFET) region were neglected.

R_{drift} and R_{sub} were calculated in 7.2.1. Although the channel resistance R_{ch} cannot be expressed by a simple equation, it can be approximately calculated using the following equation [15].

$$R_{\text{ch}} \simeq \frac{\ln(l_b/l_a)}{2\pi\mu_c C_i (V_G - V_T)} \frac{1}{N_{\text{Tr}}}, \quad (7.4)$$

where μ_c , C_i , and V_G are the channel mobility, the gate capacitance, and the gate voltage. l_a and l_b are determined by the cell size as shown in Fig.7.3. N_{Tr} is the number of DMOSFETs per unit area ($4 \times 10^5\text{cm}^{-2}$), which can be calculated from the size of MOSFETs (Fig.7.3) and the gate width per unit area ($15\text{m}/\text{cm}^2$). V_T is the threshold voltage given by

$$V_T = 2\psi_B + \frac{\sqrt{4eq\psi_B N_a}}{C_i}, \quad (7.5)$$

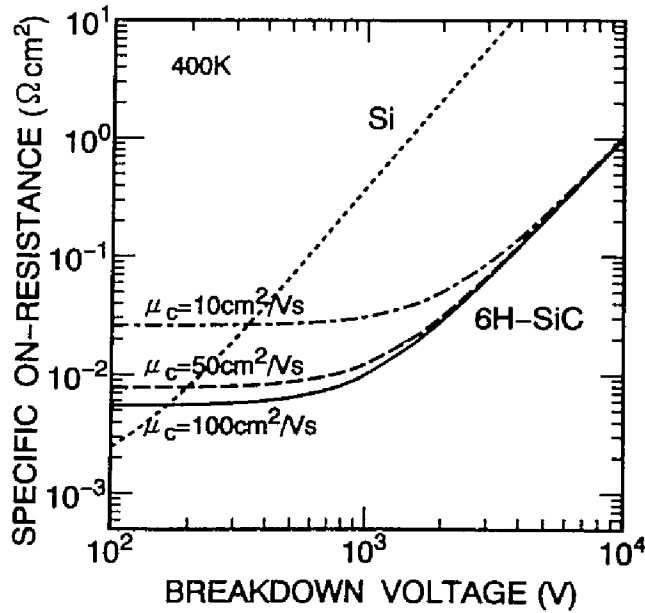
where N_a and ψ_B are the acceptor concentration and the potential difference between the intrinsic and Fermi levels in the p-well region. Here, the work

function difference between the gate and semiconductor, and the interface charge are neglected. $V_G - V_T$ of 10V was employed in this simulation. The channel mobility was assumed as $500\text{cm}^2/\text{Vs}$ for Si [15], and varied in the range of $10\sim 200\text{cm}^2/\text{Vs}$ for SiC because of the lack of reliable data.

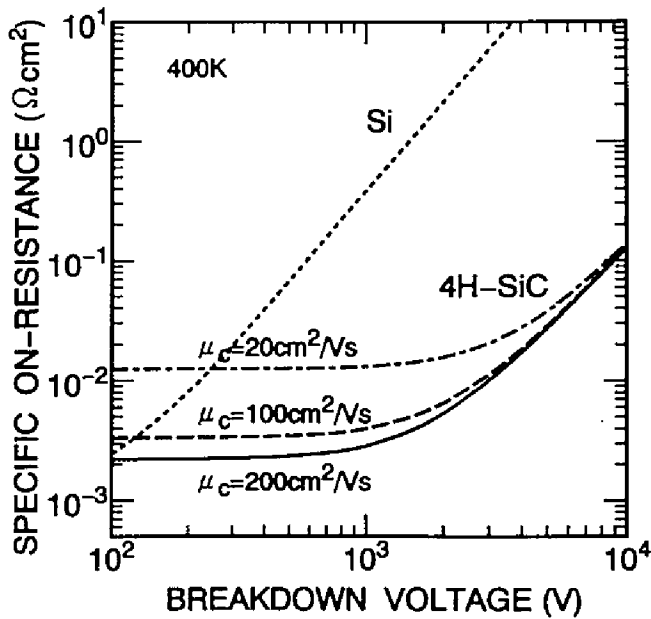
In general, power devices operate at elevated temperatures due to self-heating by power losses. Hence, the simulation was performed at a device temperature of 400K (127°C). The decreases in mobility and bandgap with the temperature increase were considered using their reported temperature dependences [18,19]. For the present DMOSFET structure, the threshold voltage at 400K can be estimated to be 2.8V for Si, 5.6V for 6H-SiC, and 6.4V for 4H-SiC using eq.(7.5). In order to clarify the relationship between the total on-resistance and the channel mobility, the on-resistances were calculated as a function of the breakdown voltage and channel mobility.

Figure 7.4 shows the breakdown voltage dependence of the specific on-resistances of (a) 6H-SiC and (b) 4H-SiC DMOSFETs at 400K, together with that of Si devices. Here, two times higher channel mobilities were assumed in 4H-SiC devices ($\mu_c(4\text{H})=2\mu_c(6\text{H})$), based on the difference in bulk mobilities. The effects of channel mobility in SiC MOSFETs are shown. In SiC MOSFET structures considered in this study, the substrate resistance R_{sub} is $1.8\times 10^{-3}\Omega\text{cm}^2$ for 6H and $6.0\times 10^{-4}\Omega\text{cm}^2$ for 4H-SiC devices, indicating that the contribution of the substrate resistance is small. For the 6H-SiC devices with breakdown voltages lower than 1000V, the total on-resistances are severely limited by the channel resistances, even if a high channel mobility of $100\text{cm}^2/\text{Vs}$ is assumed. Although the drift region resistances become gradually dominant in high-voltage SiC MOSFETs, the low channel mobilities lead to relatively high specific on-resistances. For example, in a 3000V 6H-SiC MOSFET, the channel resistances determined by the channel mobility of 100, 50, and $10\text{cm}^2/\text{Vs}$ account for 21%, 34%, and 72% of the total specific on-resistance. This tendency becomes more significant for 4H-SiC DMOSFETs, of which drift region resistances are very low. Recently, Bhatnagar *et al.* reported the effects of channel mobility on the performance of 6H-SiC power MOSFETs [20]. The present study basically agrees with their analysis.

Cross-over points of the theoretical curves for SiC and Si in Fig.7.4 give the lowest blocking voltages with which SiC MOSFETs can realize lower specific on-resistances than Si MOSFETs. The cross-over point shifts toward the



(a)



(b)

Fig.7.4 Breakdown voltage dependence of specific on-resistances of (a) 6H-SiC and (b) 4H-SiC DMOSEFTs at 400K together with Si DMOSEFTs. Effects of channel mobility of SiC FETs are shown.

higher voltage region with the decrease in channel mobility. In order to replace Si power MOSFETs with SiC MOSFETs, specific on-resistances much lower than Si devices will be required because of higher cost in SiC devices. If we assume a criterion for the replacement as the 1/10 on-resistances of Si MOSFETs, the lowest blocking voltages with which 6H-SiC MOSFETs should be developed are 420V, 620V, and 950V for the channel mobilities of 100, 50, and $10\text{cm}^2/\text{Vs}$, respectively. A channel mobility higher than $50\text{cm}^2/\text{Vs}$ may be required to realize a 500V (or higher) 6H-SiC MOSFET with excellent performance. Quite similar situation is expected in 4H-SiC DMOSFETs. In a 6H-SiC planar MOSFET, a channel mobility of $48\text{cm}^2/\text{Vs}$ has been obtained [21]. Although this value encourages us to develop a 6H-SiC MOSFET, the detailed characterization and improvement of channel mobility are necessary.

7.3 High-Voltage Schottky Rectifiers

In high-frequency power circuits, Schottky rectifiers are superior rectifiers because of its low turn-on voltage and fast reverse recovery characteristics. However, Si Schottky rectifiers with blocking voltages over 100V are not available due to the large reverse leakage current caused by the low barrier heights (typically 0.7eV) and to the high on-resistances. Although Si pin diodes have been used for high-voltage applications, they show slow switching characteristics [16]. In this study, the potential of high-power SiC Schottky rectifiers is investigated.

Single crystals of n-type 6H-SiC(000 $\bar{1}$)C faces were used as substrates. The off-orientation of substrates was 5° toward $\langle 11\bar{2}0 \rangle$. The typical substrate resistivity was $0.1\sim 0.2\Omega\text{cm}$. The n-type 6H-SiC layers were homoepitaxially grown by step-controlled epitaxy. The carrier concentration was controlled by *in-situ* doping with nitrogen using N_2 gas. The thickness of epilayers was $2.0\sim 9.6\mu\text{m}$.

For the fabrication of Schottky rectifiers, Ni was evaporated on the back of substrates, and annealed at 1100°C to form ohmic contacts. Au Schottky contacts were thermally evaporated on the epilayers. Before Au deposition, the as-grown surfaces were cleaned in organic solvents, heated K_2CO_3 [22],

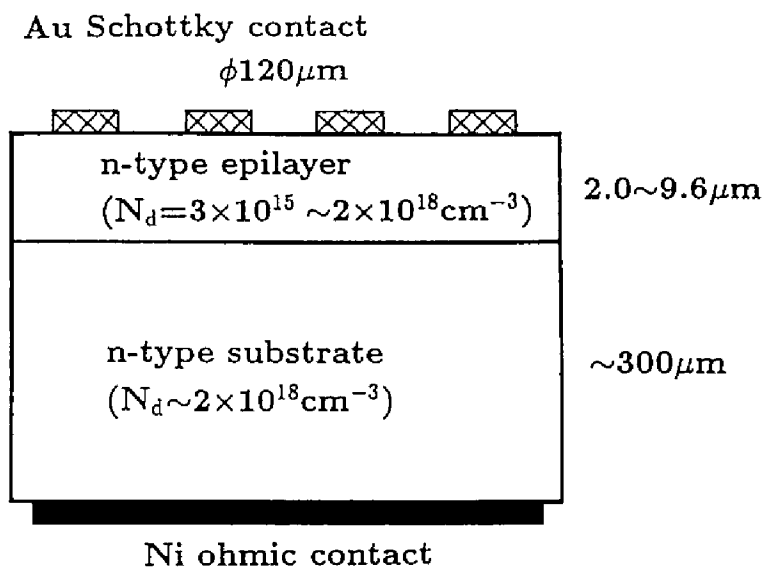


Fig.7.5 Structure of 6H-SiC Schottky rectifiers.

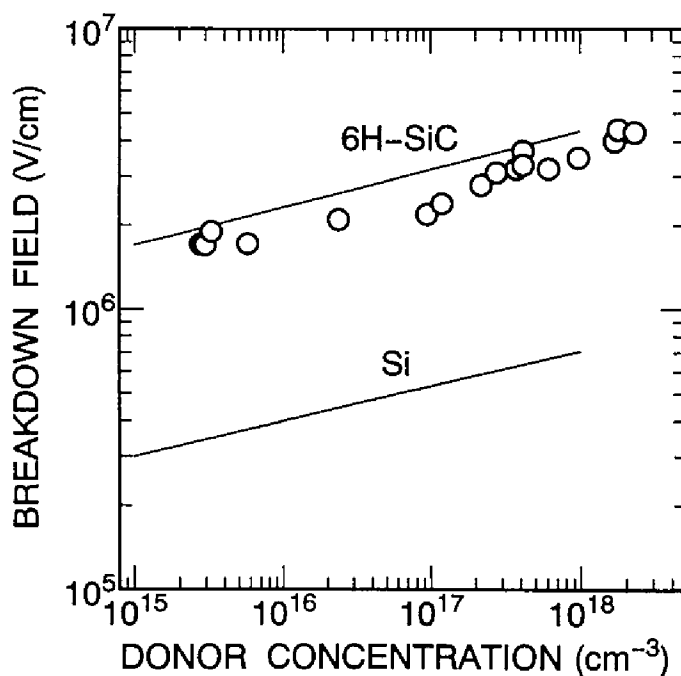


Fig.7.6 Dependence of breakdown field on doping concentration. Open circles indicate breakdown fields obtained in this study. Solid curve denotes the reported data [13].

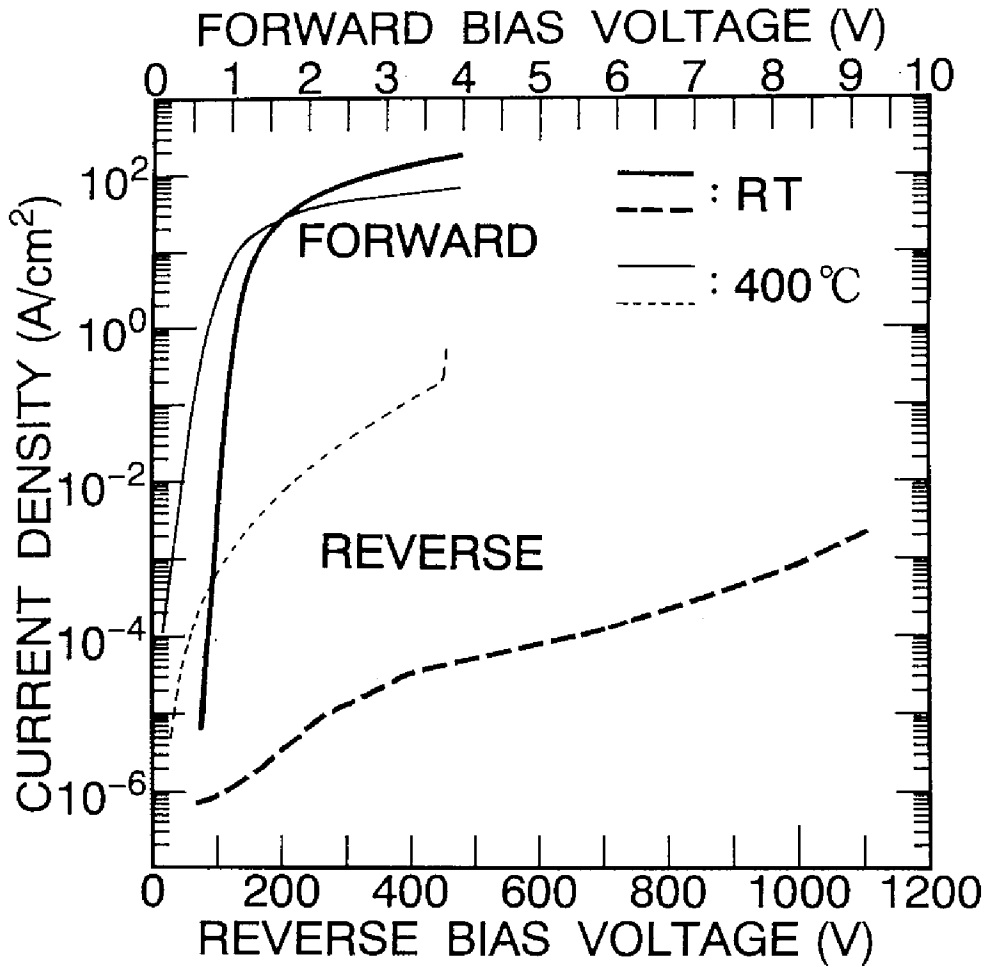


Fig.7.7 Current density - voltage characteristics of a 1100V 6H-SiC Schottky rectifiers at room temperature and 400°C .

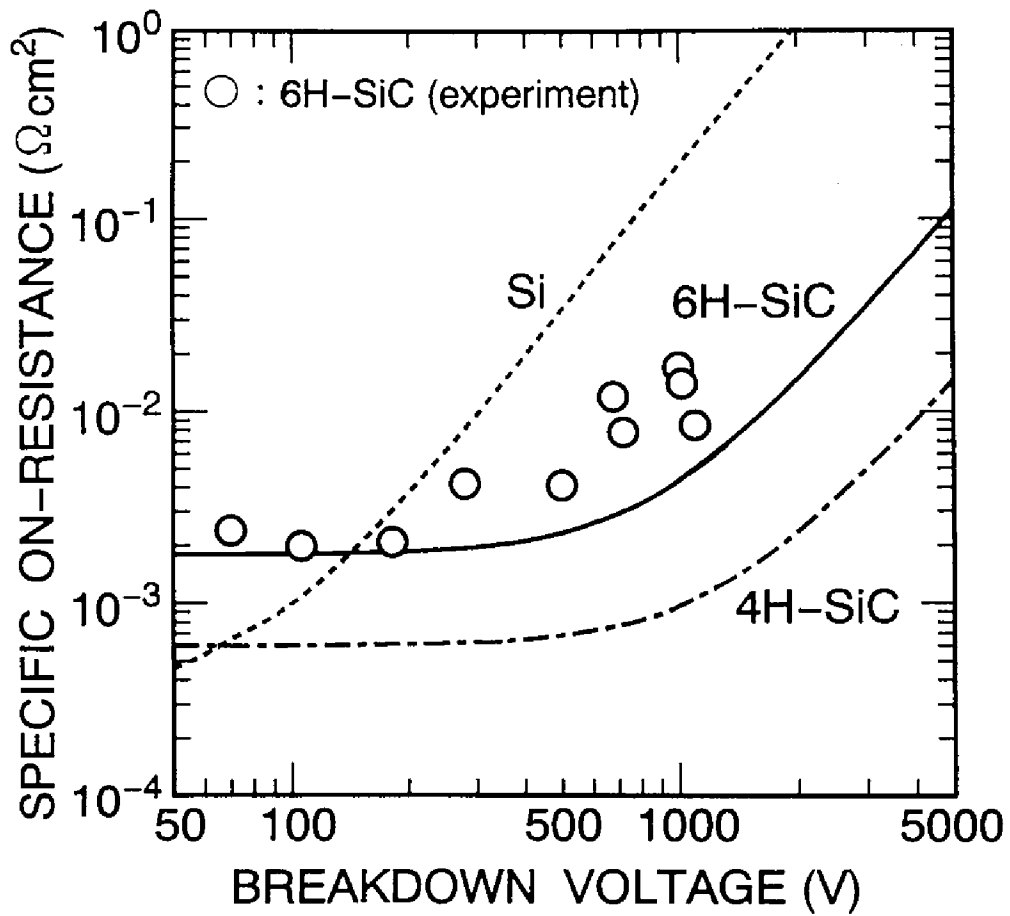


Fig.7.8 Breakdown voltage dependence of specific on-resistance for 6H-SiC and Si Schottky rectifiers.

aqua regia, and HF, and then rinsed in deionized water. The size of circular Au Schottky contacts was $120\mu\text{m}$ in diameter. The structure of Schottky rectifiers is shown in Fig.7.5. Current-voltage (I-V) and capacitance-voltage (C-V) measurements were conducted in air between room temperature and 400°C .

At first, the breakdown field was roughly estimated from the breakdown voltages of the rectifiers. Figure 7.6 shows the dependence of breakdown field on doping concentration. Open circles indicate breakdown fields obtained in this study. Estimated breakdown field of 6H-SiC was $1.9\times 10^6\text{V/cm}$ at $1\times 10^{16}\text{cm}^{-3}$, and $4.0\times 10^6\text{V/cm}$ at $1\times 10^{18}\text{cm}^{-3}$. Although about 10 times higher breakdown field than that of Si was obtained, these values are a little lower than those obtained from mesa pn junction diodes [13]. This is caused by the concentrated electric field at the contact periphery in our Schottky samples. The edge termination should be employed for the accurate estimation.

Figure 7.7 shows the current density – voltage characteristics of a typical 6H-SiC Schottky rectifier using an epilayer with a donor concentration of $5.8\times 10^{15}\text{cm}^{-3}$ at room temperature and 400°C . Under the forward bias condition, the characteristic follows the thermionic emission equation with an ideality factor (n) of $1.08\sim 1.15$ at current levels lower than 0.1A/cm^2 . From this characteristic, the barrier height of Au is estimated as 1.4eV . At high current levels ($\geq 10\text{A/cm}^2$), the series resistance comes into effect. At room temperature, a high current density of 100A/cm^2 was achieved at a small forward voltage of 2.64V . The diode showed a high breakdown voltage over 1100V , which is the highest value ever reported for Schottky rectifiers of any semiconductor materials. The leakage current density was quite low, $4.0\times 10^{-6}\text{A/cm}^2$ at -200V and $2.1\times 10^{-3}\text{A/cm}^2$ at -1100V , in spite of no surface passivation. These current densities are lower by orders of magnitude than those previously reported [2]. At 400°C , the reverse leakage current increased significantly, and the breakdown voltage decreased down to 460V . This result may be caused by surface breakdown due to no passivation structure. Note that the thickness of drift region sustaining a blocking voltage of 1100V is only $9.6\mu\text{m}$ for SiC, which is much thinner than that for Si pin diodes ($\geq 90\mu\text{m}$) with the same blocking voltage.

Figure 7.8 shows the breakdown voltage dependence of the specific on-

resistance (R_{on}) obtained in this study. The experimentally obtained specific on-resistances for 6H-SiC rectifiers with breakdown voltages of 500~1100V are lower than the theoretical limits of Si rectifiers by more than one order of magnitude. For example, R_{on} is only $8.5 \times 10^{-3} \Omega \text{cm}^2$ for 1100V 6H-SiC diodes. Recently, further reduction of R_{on} could be achieved by utilizing 4H-SiC [23]. Relatively high R_{on} 's were obtained for the low-voltage SiC rectifiers, which may be ascribed to the high substrate resistances used in this study (typically $3 \sim 6 \times 10^{-3} \Omega \text{cm}^2$). In the high-voltage devices, the experimental R_{on} 's are higher than theoretical values by a factor of 2~3, which may come from the non-optimized device structure. For example, an edge-termination technique is strongly required [14,24], because the breakdown voltages obtained in this study were only 40~70% of theoretical values.

Figure 7.9 shows the temperature dependence of R_{on} for a 1100V 6H-SiC Schottky barrier diode between room temperature and 400°C. Open circles represent the R_{on} 's for a SiC rectifier obtained in the present study. The solid curve shows the theoretical one for a Si Schottky rectifier with the same blocking voltage, calculated using mobility data [25]. The R_{on} of the SiC rectifier increases monotonously with temperature. The slopes of the plots for Si and 6H-SiC are 2.4 and 2.0, respectively. The increase in R_{on} for Si is caused by the decrease in electron mobility which follows $T^{-2.4}$ dependence [25]. Although SiC has the temperature dependence of electron mobility quite similar to Si [18,26], the carrier concentration increases with temperature, because N donors with ionization energies of 80~144meV [27] are not fully activated at room temperature. This may be the reason why the R_{on} for 6H-SiC is less sensitive to temperature. 6H-SiC Schottky rectifiers can operate with low R_{on} 's at temperatures up to the highest temperature tested, 400°C. This result shows that high-temperature tolerant power devices can be developed using SiC.

The temperature dependence of the forward voltage drop for different current density levels is shown in Fig.7.10. At a low current level of 10A/cm², the forward voltage drop decreases with temperature. This is attributed to the promoted thermionic emission across the Schottky barrier at higher temperatures. However, the raising temperature brings about the increase in on-resistance as shown in Fig.7.9. As a result, at high current levels ($\geq 50 \text{A/cm}^2$) where current is controlled by series resistances, higher forward voltages are

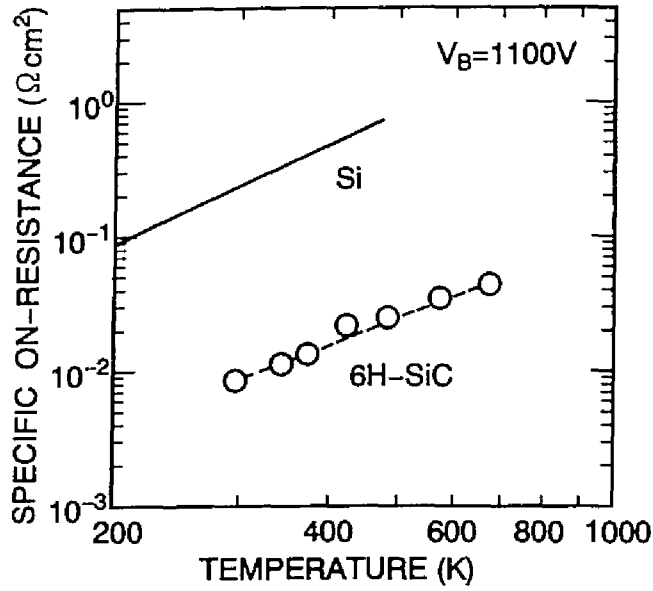


Fig.7.9 Temperature dependence of specific on-resistance for 6H-SiC (experiment) and Si (theory) Schottky rectifiers.

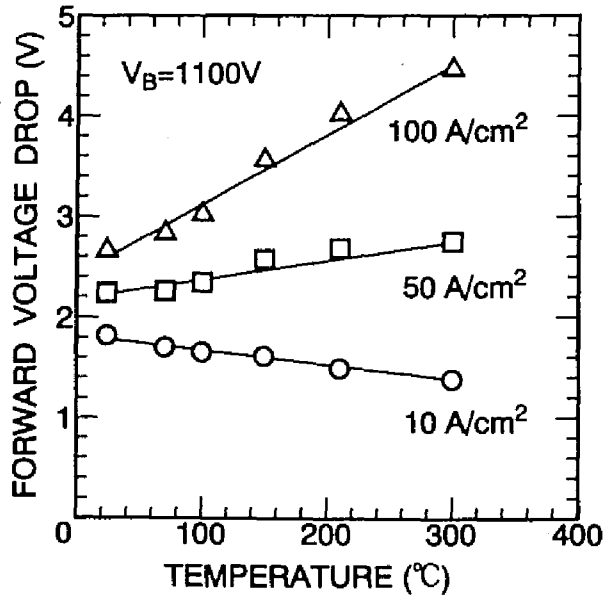


Fig.7.10 Temperature dependence of forward voltage drop for different current density levels.

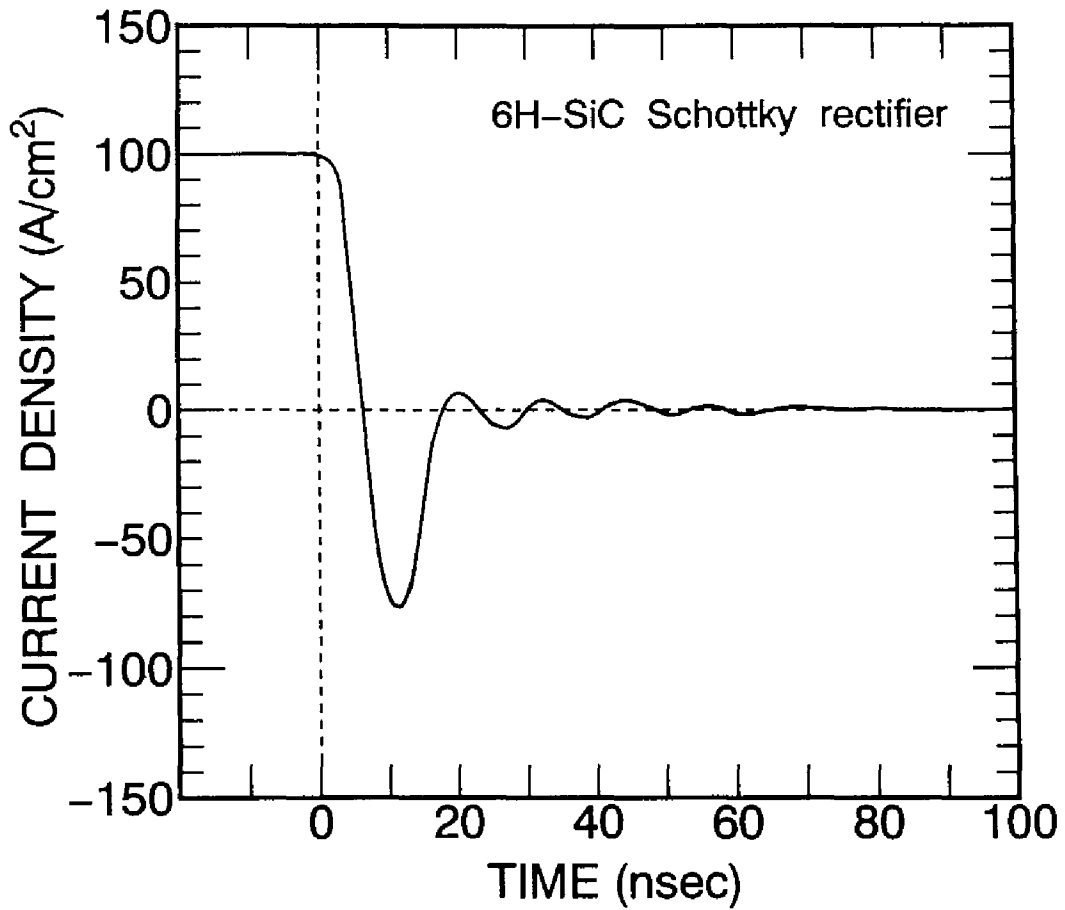


Fig.7.11 Switching characteristics of a high-voltage 6H-SiC Schottky rectifier.

needed for high-temperature operation. For example, the forward voltage drops which deliver $50\text{A}/\text{cm}^2$ are 2.24V and 2.75V at room temperature and 300°C , respectively. This result suggests that the diodes have a function to suppress thermal runaway and can be easily paralleled [2].

Figure 7.11 shows the switching characteristic of a typical high-voltage 6H-SiC rectifier. The bias was switched from 2.4V to -100V within 5nsec (turn-off). The diode exhibits very fast turn-off within 20nsec , since Schottky rectifiers are free from minority carrier injection. For high-voltage ($\geq 100\text{V}$) Si rectifiers, pin diodes are used at present. But pin diodes show very slow switching speed about μsec with huge reverse current overshoot, which brings about serious increase in power dissipation in high-frequency application [28]. This smart switching characteristic of SiC Schottky rectifiers is one of the most important advantages, compared with Si pin diodes.

The reverse current overshoot in Schottky rectifiers may come from discharging the diode capacitor during turn-off. Based on this model, the total charge per unit area ($Q_{\text{discharge}}$) which contributes to the current overshoot is given by

$$Q_{\text{discharge}} = C_{\text{on}}V_{\text{on}} - C_{\text{off}}V_{\text{off}}, \quad (7.6)$$

where C_{on} and C_{off} are the capacitance of the depletion layer per unit area in on- and off-states. V_{on} and V_{off} are the effective on- and off-state bias voltages which are applied at the Schottky barrier (not the total bias voltages). The effective on-state bias voltage V_{on} can be expressed by the following equation [16].

$$V_{\text{on}} = \frac{kT}{q} \ln\left(\frac{J_{\text{F}}}{A^*T^2}\right) + \phi_{\text{B}}. \quad (7.7)$$

Here, A^* is the effective Richardson constant, T the absolute temperature, k the Boltzmann constant, q the electron charge, and ϕ_{B} the barrier height. The estimated V_{on} is 1.2V for a J_{F} of $100\text{A}/\text{cm}^2$ in the present 6H-SiC rectifiers. Then, the total amount of discharge $Q_{\text{discharge}}$ can be calculated to be $3.3 \times 10^{-7}\text{C}/\text{cm}^2$, which is in good agreement with the experimental value ($4.4 \times 10^{-7}\text{C}/\text{cm}^2$).

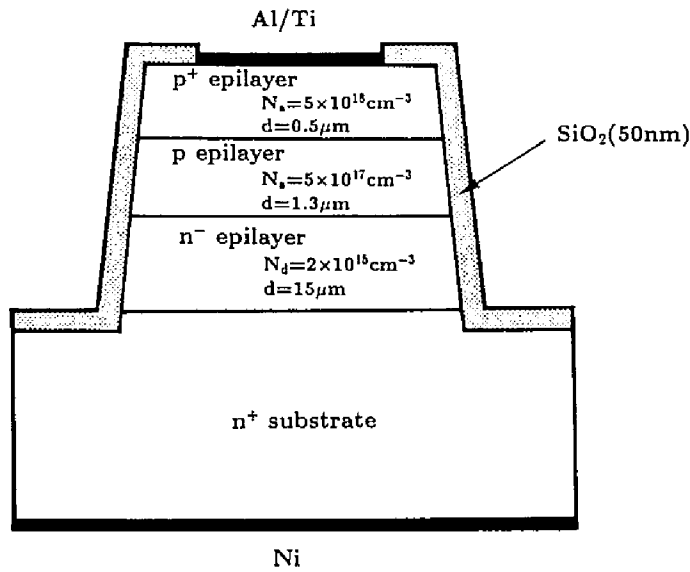


Fig.7.12 Structure of a 6H-SiC epitaxial pn diode with a low-doped base layer.

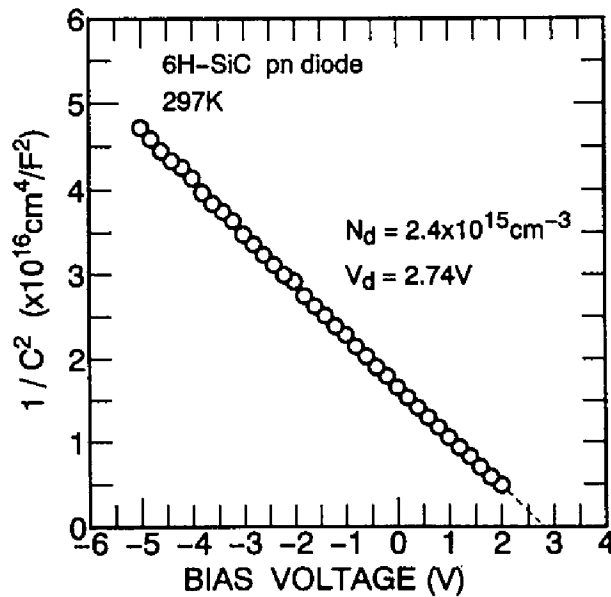


Fig.7.13 1/C²-V (C: capacitance, V: voltage) plot of a 6H-SiC epitaxial pn junction diode.

7.4 High-Voltage, High-Temperature pn Diodes

The characteristics of epitaxial pn junction give the most basic insight into the quality of epilayers which determines device performance. The author fabricated several kinds of 6H-SiC epitaxial pn junction diodes with different structures such as doping level and epilayer thickness. N-type off-oriented (0001)Si wafers grown by a modified Lely method were used as substrates. All the pn junction diodes were processed into a mesa structure by reactive ion etching using $\text{CF}_4 + \text{O}_2$ gases with an aluminum mask. The junctions were passivated with an oxide thermally grown at 1100°C in dry O_2 (oxide thickness=50nm). The structure of a pn diode with a low-doped base layer is shown in Fig.7.12. Al/Ti and Ni annealed at 1000°C were used as ohmic contacts on p- and n-type layers, respectively. The area of junctions was $7.85 \times 10^{-5} \sim 1.96 \times 10^{-3} \text{cm}^2$ ($100 \sim 500 \mu\text{m}\phi$). The reverse current-voltage characteristics were measured by immersing the diodes with FluorinertTM to avoid air sparking [4].

The breakdown field calculated from breakdown voltage and doping concentration was almost the same as the values Edmond *et al* reported [13], $1.5 \times 10^6 \text{V/cm}$ at $2 \times 10^{15} \text{cm}^{-3}$ and $3.2 \times 10^6 \text{V/cm}$ at $2 \times 10^{17} \text{cm}^{-3}$.

Figure 7.13 shows the $1/C^2$ -V (C: capacitance, V: voltage) plot of a pn junction diode. The good linearity of the plot indicates the abrupt junction, and the background doping concentration (n-type layer in this case) can be estimated to be $2.4 \times 10^{15} \text{cm}^{-3}$. The intercept on the voltage axis gives a diffusion voltage (V_d) of 2.74V. The theoretical diffusion voltage is determined by the difference of Fermi levels between p- and n-layers, and is given by [12]

$$V_d = \frac{kT}{q} \ln\left(\frac{p_{p0}n_{n0}}{n_i^2}\right). \quad (7.8)$$

Here, p_{p0} , n_{n0} , and n_i are the hole concentration in the p-layer, the electron concentration in the n-layer, and the intrinsic carrier concentration, respectively. k and T are the Boltzmann constant and absolute temperature. By using the intrinsic concentration of $1 \times 10^{-6} \text{cm}^{-3}$, the diffusion voltage can be calculated to be 2.54V for the structure shown in Fig.7.12. The slightly higher diffusion voltage obtained by the C -V measurement may be caused by the existence of a very thin i-layer at the interface.

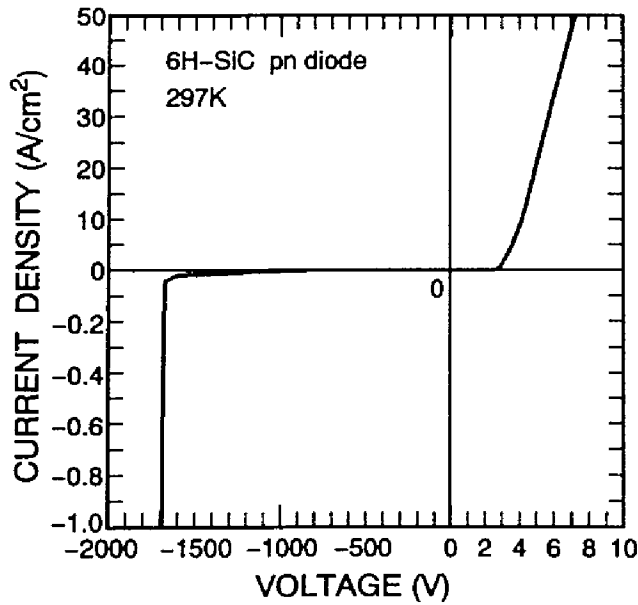


Fig.7.14 Linear plot of current density - voltage characteristics for a 6H-SiC epitaxial pn junction diode at room temperature.

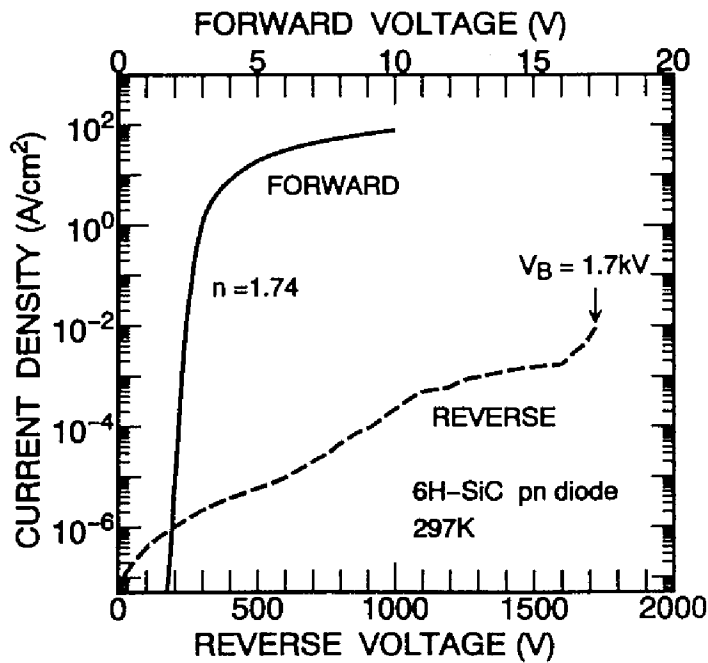


Fig.7.15 Semilogarithmic plot of current density-voltage characteristics of a 6H-SiC epitaxial pn junction diode.

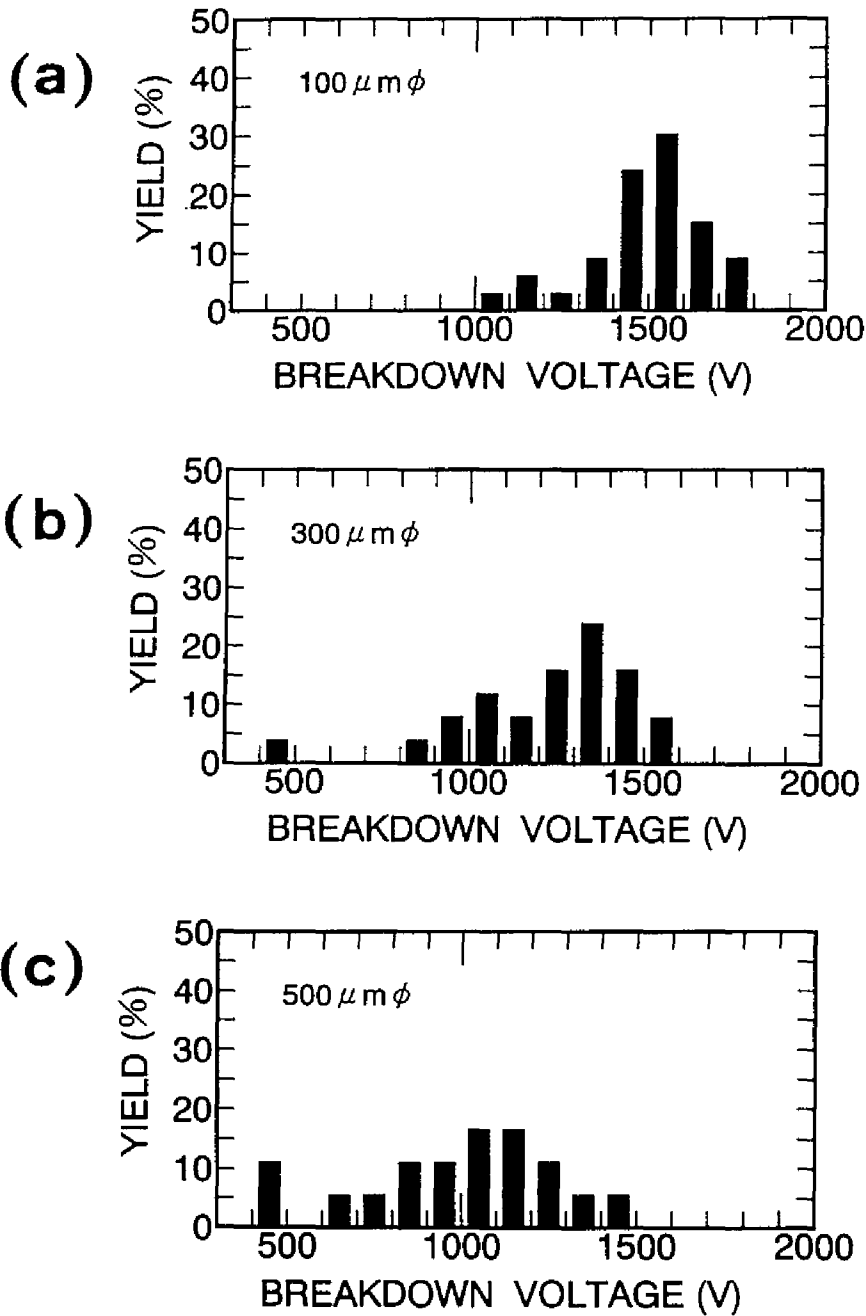


Fig.7.16 Histograms of breakdown voltage for (a) $100\mu\text{m}\phi$, (b) $300\mu\text{m}\phi$, and (c) $500\mu\text{m}\phi$ pn junction diodes.

Figures 7.14 and 7.15 show the linear and semi-logarithmic plots of the current density - voltage characteristics of the diode shown in Fig.7.12. The junction area is $7.85 \times 10^{-5} \text{cm}^2$ ($100\mu\text{m}\phi$). Excellent rectification characteristics were obtained with a very high breakdown voltage of 1720V. Under the reverse bias condition near breakdown, the punch-through takes place due to the low doping concentration and the relatively thin n-layer. Nevertheless, the breakdown field can be estimated as $1.5 \times 10^6 \text{V/cm}$. Neudeck *et al.* reported a 2.2kV 6H-SiC pn junction diode using a $24\mu\text{m}$ thick n-layer with a donor concentration of $2 \sim 5 \times 10^{15} \text{cm}^{-3}$ [4]. The breakdown voltage is a little lower in our experiments, probably due to the thinner n-layer thickness. The leakage current density is $3.4 \times 10^{-7} \text{A/cm}^2$ at -100V, and $2.1 \times 10^{-4} \text{A/cm}^2$ at -1000V, which are similar to the reported values [4]. However, the leakage current is higher than theoretical values by more than ten orders of magnitude. The leakage path and origin should be clarified.

Under the forward bias condition, the ideality factor is 1.74, which is indicative of current both diffusion and recombination processes: The characteristics may be explained by the Shockley-Noyce-Saah theory [13, 29]. In particular, the extremely low intrinsic carrier concentration of 6H-SiC at room temperature ($\sim 10^{-6} \text{cm}^{-3}$) makes the diffusion current very low under small bias-voltage condition, which leads to the relatively large contribution of recombination current. This is the main reason why the ideality factor is close to 2. The saturation current density is $2.4 \times 10^{-25} \text{A/cm}^2$. The on-resistance of the diode is rather high, $0.074 \Omega \text{cm}^2$, which may be attributed to the non-optimized ohmic contacts to the p-layer.

Figure 7.16 shows the histograms of breakdown voltage for (a) $100\mu\text{m}\phi$, (b) $300\mu\text{m}\phi$, and (c) $500\mu\text{m}\phi$ pn junction diodes. Diodes with the smaller size exhibited the higher breakdown voltage with the smaller distribution. The highest breakdown voltages for $100\mu\text{m}\phi$, $300\mu\text{m}\phi$, and $500\mu\text{m}\phi$ devices were 1720V, 1550V, and 1430V, respectively. Large-area diodes possess a high probability to meet dislocations at which the electric field is concentrated [30,31] (The dislocation density of epilayers is in the 10^4cm^{-2} range). This may be the reason why the breakdown voltage decreases with increasing the junction area. It should be also pointed out that the diodes which contain "micropipes" showed significantly reduced (30~40% lower) breakdown voltages and large

leakage current density as Neudeck *et al* reported [31].

Pn junction diodes were fabricated using N^+ implantation into p-type 6H-SiC epilayers. P-type off-oriented 6H-SiC(000 $\bar{1}$)C wafers grown by a modified Lely method were used as substrates. Al-doped epilayers with a thickness of $5\mu\text{m}$ were grown. The acceptor concentrations of epilayers and substrates were $4\times 10^{16}\text{cm}^{-3}$ and $5\times 10^{18}\text{cm}^{-3}$, respectively.

Nitrogen ions (N^+) were implanted through a 50nm screen oxide at room temperature. The implantation doses and energies were $5.0\times 10^{14}\text{cm}^{-2}$ at 100keV and $3.2\times 10^{14}\text{cm}^{-2}$ at 50keV. In the fabrication of pn junction diodes, a mesa structure was formed by reactive ion etching. The junction was passivated with an oxide thermally grown at 1000°C for 2h in dry O_2 (oxide thickness=50nm). Ni and AlSi annealed at 1000°C were used as ohmic contacts on n- and p-type SiC, respectively. The area of junctions was $7.1\times 10^{-4}\text{cm}^2$ ($300\mu\text{m}\phi$). The structure is shown in Fig.7.17. The diode characteristics were measured at temperatures between room temperature and 350°C .

Post-implantation annealing was done at $1400\sim 1600^\circ\text{C}$ for 15min. Since no significant differences were observed in the characteristics of the diodes annealed at different temperatures ($1400\sim 1600^\circ\text{C}$), typical characteristics of a 1400°C -annealed diode are shown here. The junction depth was $0.35\mu\text{m}$, which was estimated from the cross-sectional view of a cleaved sample by a scanning electron microscope. The background doping concentration was determined to be $4.0\times 10^{16}\text{cm}^{-3}$ from capacitance-voltage (C-V) measurements. The diffusion voltage obtained from C-V characteristics is 2.9V, which is a little higher than the value (2.6V) for an abrupt pn junction expected from the doping levels. This difference can be explained by that the junction has pin structure with a $20\sim 30\text{nm}$ thick i-layer, which was estimated from the capacitance at zero bias. The thickness of i-layer is thin enough, and this i-layer may give little influence on the current-voltage characteristics.

Figure 7.18 shows the current density - voltage characteristics of the diode at room temperature and 350°C (623K). The diode demonstrated good rectification up to the highest temperature tested, 350°C . The breakdown voltage is very high, 450V at room temperature and 410V at 350°C , which is the highest ever reported in SiC pn junction diodes fabricated by N^+ implantation. However, the calculated breakdown field at room temperature is $2.5\times 10^6\text{V/cm}$,

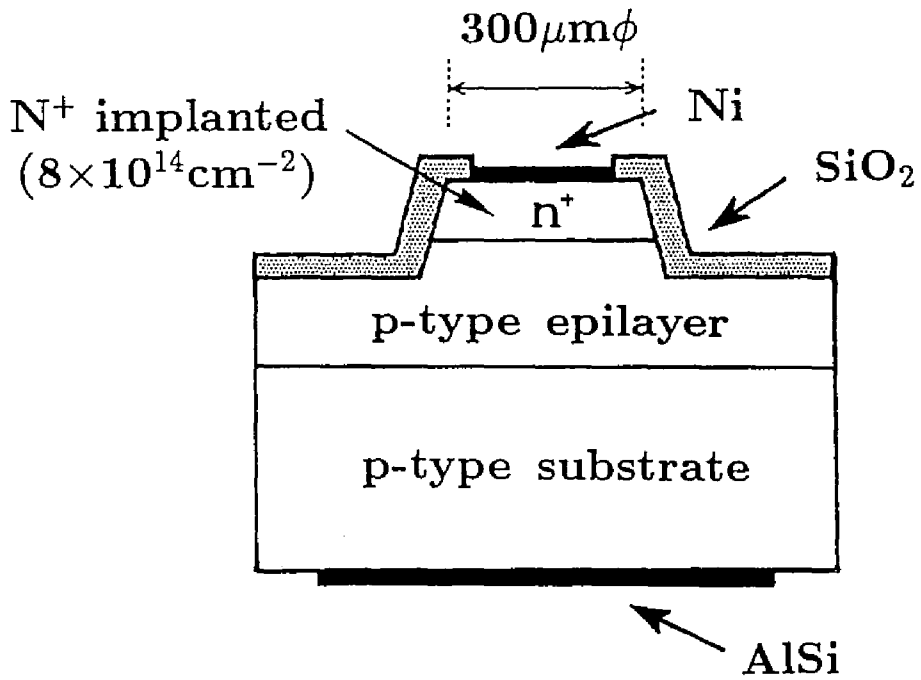


Fig.7.17 Structure of 6H-SiC pn junction diodes fabricated by N⁺ implantation.

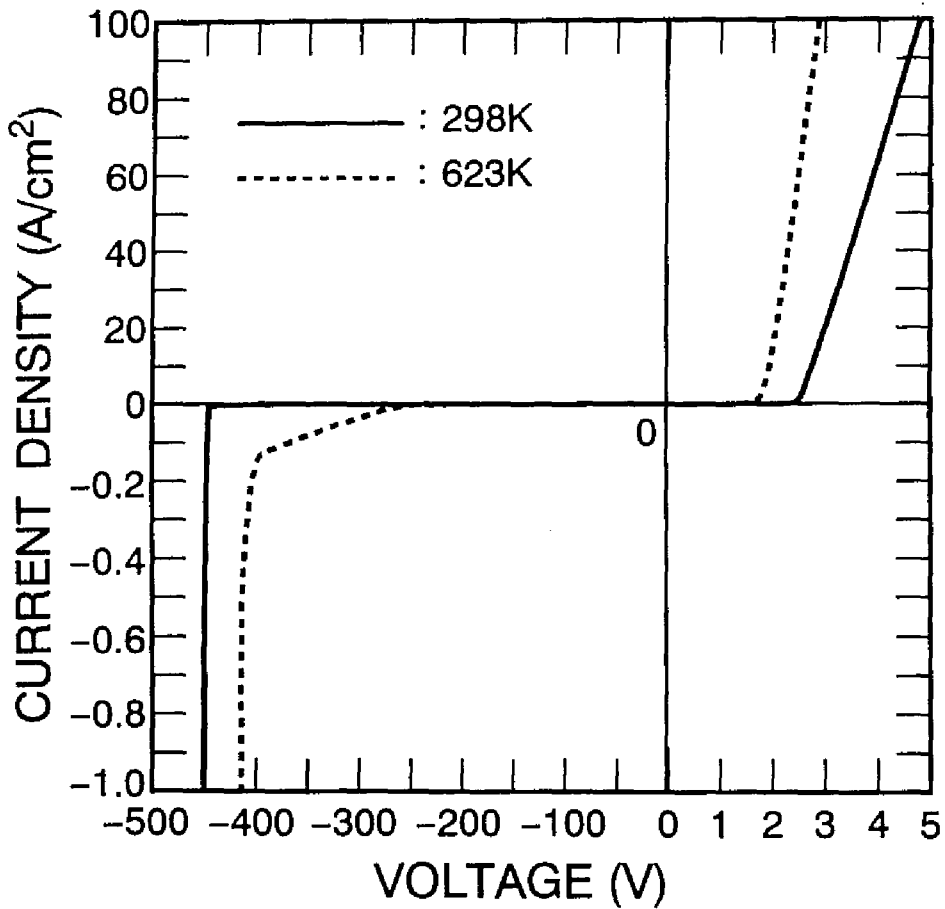


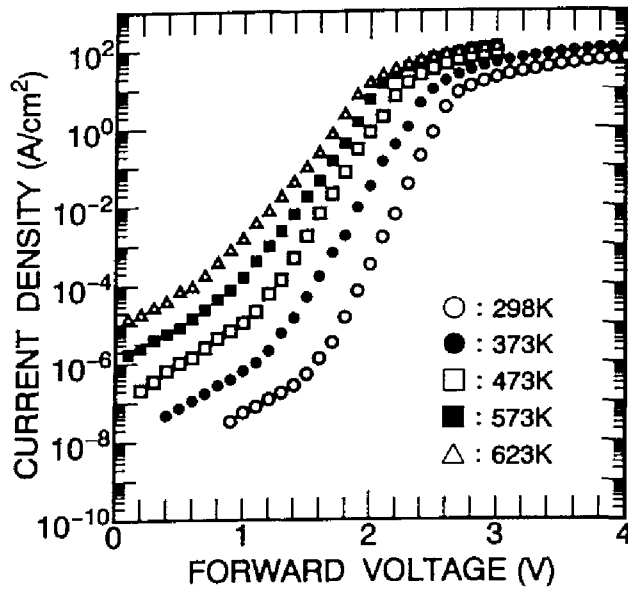
Fig.7.18 Linear plots of current density - voltage characteristics for a 6H-SiC pn junction diode at room temperature and 350°C (623K).

which is a little lower than that ($3.0 \times 10^6 \text{V/cm}$) obtained in a 6H-SiC epitaxial pn junction diode [13]. This result may be caused by defects remaining in the implanted layer.

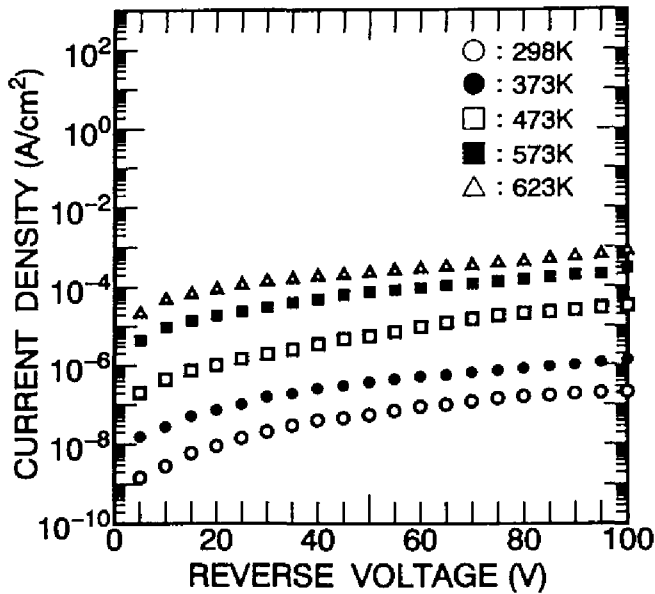
Figure 7.19(a) shows the semilogarithmic plots of typical forward current density (J_F) - voltage (V_F) characteristics at several temperatures. At all temperatures, the J_F - V_F curves consist of three regions. In the low current density region ($J_F \leq 10^{-6} \text{A/cm}^2$ at room temperature), the current increases according to roughly V_F^n with $n=1.0 \sim 1.5$. Edmond *et al.* have reported that the space-charge-limited current dominates in N^+ -implanted 3C-SiC pn junction diodes [32]. However, the J_F - V_F curves in this study cannot be explained by this theory. The conduction mechanism in this region is not clear at present, and further analyses are needed.

In the medium current density region ($J_F = 10^{-5} \sim 1 \text{A/cm}^2$ at room temperature), the current increases exponentially with an ideality factor of 2.1 at room temperature. This result suggests that recombination current is dominant in this region. The ideality factor gradually decreases with increasing temperature, and takes a value of 1.6 at 350°C . As for the forward current of pn junction diodes, diffusion current is proportional to n_i^2 , and recombination current proportional to n_i [12], where n_i is the intrinsic carrier concentration. Since the intrinsic carrier concentration in 6H-SiC is extremely low ($n_i \sim 10^{-6} \text{cm}^{-3}$) at room temperature, the forward conduction of pn junction diodes is supposed to be dominated by recombination current. At elevated temperatures, however, the component of diffusion current shows rapid increase, owing to the increased intrinsic carrier concentration ($n_i \sim 10^8 \text{cm}^{-3}$ at 350°C). Raising temperature also causes the enhanced emission of carriers trapped at deep levels. These factors may be the reasons for the decreased ideality factor at higher temperatures.

In the high current density region ($J_F \geq 10 \text{A/cm}^2$ at room temperature), the current is limited by the series resistance. The series resistance was $0.023 \Omega\text{cm}^2$ at room temperature, and $0.012 \Omega\text{cm}^2$ at 350°C . This includes the resistances from the ohmic contacts, epitaxial layer, and substrate. Through rough estimation of the series resistances, the main component seems to come from the p-type substrate. The reduction of series resistance at elevated temperatures may be attributed mainly to the promoted ionization of Al acceptors



(a)



(b)

Fig.7.19 Semilogarithmic plots of current density-voltage (V_F) characteristics of a 6H-SiC pn junction diode under (a) forward and (b) reverse bias conditions.

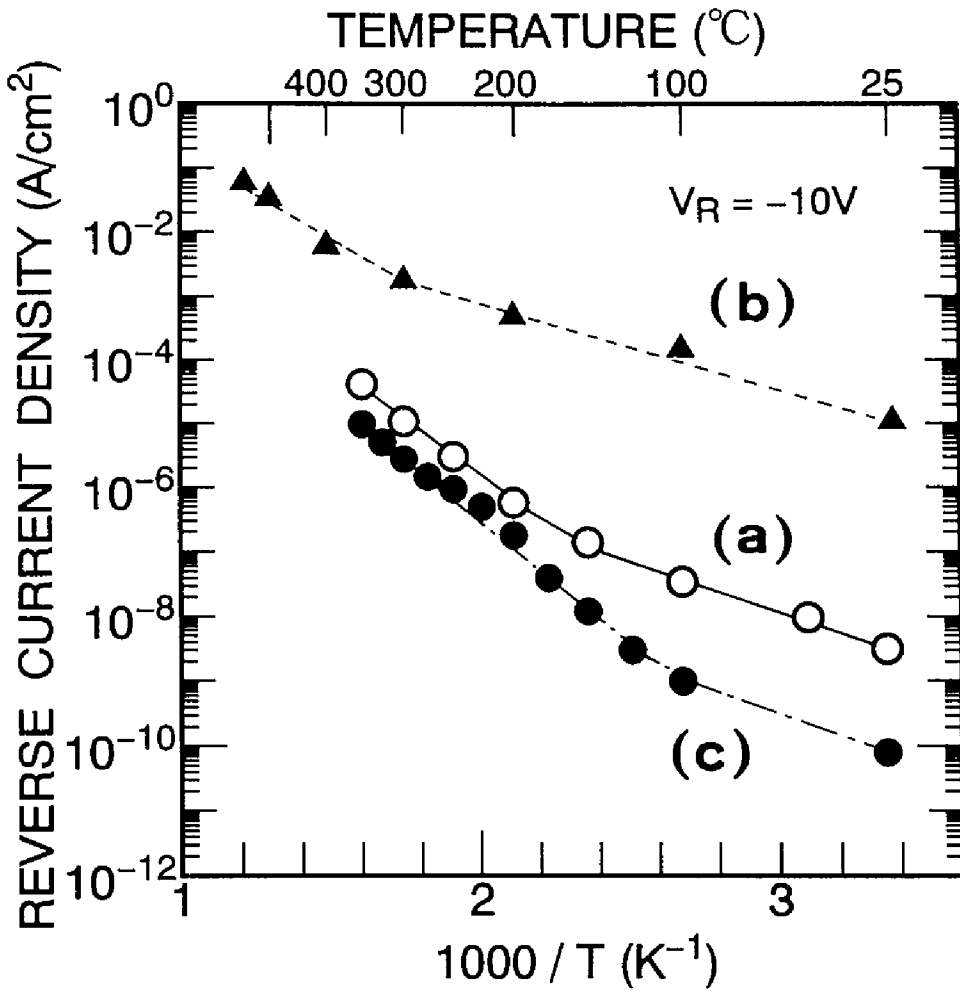


Fig.7.20 Arrhenius plot of the reverse current density at -10V of (a) the 6H-SiC pn junction diode fabricated in this study, (b) the data reported by Pensl *et al.* [34], and (c) those by Ghezzi *et al.* [35].

which have large ionization energies ($\sim 250\text{meV}$) [33].

Reverse bias characteristics of the diodes are shown in Fig.7.19(b). The leakage current density (J_R) is very low at room temperature, $3.2 \times 10^{-9}\text{A/cm}^2$ at -10V , and $2.1 \times 10^{-7}\text{A/cm}^2$ at -100V . The $\log J_R - \log V$ plot showed that the reverse current density increases according to V^n with $n=1\sim 2$ dependence. Since this dependence cannot be explained by the generation current in a depletion layer ($J_R \propto \sqrt{V}$), further analysis on the leakage mechanism is necessary.

Figure 7.20 shows the Arrhenius plot of the reverse current density at -10V , together with the data previously reported [34,35]. Although the leakage of the diodes increased at high temperatures, the leakage current density at 350°C is comparable to the best value of implanted 6H-SiC diodes reported by Ghezzi *et al* [35]. The estimated activation energy of the reverse current is 0.68eV . Although this activation energy might correlate with deep levels in the depletion layer, detailed characterization by DLTS measurement of the diodes will be required. The optimization of fabrication processes, including annealing and surface passivation, may bring about further improvement of the characteristics.

7.5 Summary

Numerical analyses on the performance of 6H- and 4H-SiC power Schottky rectifiers and MOSFETs have been carried out with consideration of the mobility anisotropy and channel resistances. The high breakdown field of SiC results in very low drift-region resistances compared with Si devices. This fact brings about the significant contribution of channel resistances to the total specific on-resistances. This effect becomes serious with the decrease in breakdown voltage. Even in high-voltage ($\sim 500\text{V}$) devices, a channel mobility higher than $50\text{cm}^2/\text{Vs}$ is required to maintain the advantage of SiC power MOSFETs.

High-voltage Au/6H-SiC Schottky rectifiers were successfully fabricated using step-controlled epitaxial layers. A breakdown voltage over 1100V could be achieved, which is the highest ever reported for any Schottky rectifiers. These high-voltage 6H-SiC rectifiers had specific on-resistances lower than the

theoretical limits of Si rectifiers by more than one order of magnitude: The on-resistance was $8.5\text{m}\Omega\text{cm}^2$ for a 1100V rectifier. The specific on-resistance increased with temperature according to $T^{2.0}$ dependence, which indicates good stability to avoid thermal runaway. The diodes were capable of operating at temperatures as high as 400°C . The present study demonstrates great potential of SiC power rectifiers.

6H-SiC epitaxial pn junction diodes with an abrupt junction doping profile were fabricated. The diode with a $15\mu\text{m}$ thick low-doped base layer with a donor concentration of $2\times 10^{15}\text{cm}^{-3}$ exhibited a very high breakdown voltage of 1720V. Under the forward bias condition, the ideality factor was 1.74, due to the contribution of recombination current.

The pn junction diodes formed by N^+ implantation showed a small reverse leakage current of $3.2\times 10^{-9}\text{A/cm}^2$ at a bias voltage of -10V, and high breakdown voltage of 450V at room temperature. The diodes operated with good rectification at temperature as high as 350°C .

References

- [1] M.Bhatnagar and B.J.Baliga, IEEE Trans. Electron Devices, **40**, 645(1993).
- [2] M.Bhatnagar, P.K.McLarty, and B.J.Baliga, IEEE Electron Device Lett., **13**, 501(1992).
- [3] J.W.Palmour, J.A.Edmond, H.S.Kong, and C.H.Carter, Jr., *Silicon Carbide and Related Materials*, M.G.Spencer, R.P.Devaty, J.A.Edmond, M.A.Khan, R.Kaplan, M.M.Rahman, Eds., (Inst. of Physics, Bristol, 1994), p.499.
- [4] P.G.Neudeck, D.J.Larkin, J.A.Powell, L.G.Matus, and C.S.Salupo, Appl. Phys. Lett., **64**, 1386(1994).
- [5] O.Kordina, J.P.Bergman, A.Henry, E.Janzén, S.Savage, J.André, L.P.Ramberg, U.Lindfelt, W.Hermansson, and K.Bergman, Appl. Phys. Lett., **67**, 1561(1995).
- [6] J.W.Palmour, J.A.Edmond, H.S.Kong and C.H.Carter, Jr., Physica B, **185**, 461(1993).
- [7] D.M.Brown, M.Ghezzi, J.W.Kretchmer, V.Krishnamarthy, G.Michon, and G.Gati, *Trans. 2nd High Temperature Electronics Conf.* (Charlotte, 1994). XI-17.
- [8] W.Xie, J.A.Cooper, Jr., and M.R.Melloch, IEEE Electron Device Lett., **15**, 455(1994).
- [9] G.A.Lomakina, *Silicon Carbide 1973*, R.C.Marshall, J.W.Faust, Jr., and

- C.E.Ryan, Eds., (Univ. of South Carolina Press, Columbia, 1974), p.520.
- [10] W.J.Shaffer, G.H.Negley, K.G.Irvine, and J.W.Palmour, *Mat. Res. Soc. Sympo. Proc.*, **339**, 595(1994).
- [11] B.J.Baliga, *IEEE Electron Device Lett.*, **10**, 455(1989).
- [12] S.M.Sze, *Physics of Semiconductor Devices*, 2nd ed., (Wiley-Interscience, New York, 1985).
- [13] J.A.Edmond, D.G.Waltz, S.Brueckner, H.S.Kong, J.W.Palmour, and C.H.Carter, Jr., *Trans. 1st Int. High Temperature Electronics Conf. (Albuquerque, 1991)*, p.207.
- [14] A.Itoh, T.Kimoto, H.Matsunami, *Proc. of 7th Int. Sympo. Power Semicond. Devices and ICs (ISPSD-95)*, p.101.
- [15] D.A.Grant and J.Gowar, *Power MOSFETs* (John Wiley & Sons, New York, 1989).
- [16] B.J.Baliga, *Modern Power Devices* (John Wiley & Sons, New York, 1987).
- [17] M.Ruff, H.Mitlehner, and R.Helbig, *IEEE Trans. Electron Devices*, **41**, 1040(1994).
- [18] S.Karmann, C.Haberstroh, F.Engelbrecht, W.Suttrop, A.Schöner, M.Schadt, R.Helbig, G.Pensl, R.A.Stein, and S.Leibenzeder, *Physica B*, **185**, 75(1993).
- [19] W.J.Choyke and L.Patrick, *Silicon Carbide – A High Temperature Semiconductor –*, J.R.O’Connor and J.Smiltens, Eds. (Pergamon Press, New York, 1960), p.306.
- [20] M.Bhatnagar, D.Alok, and B.J.Baliga, *Silicon Carbide and Related Materials*, M.G.Spencer, R.P.Devaty, J.A.Edmond, M.A.Khan, R.Kaplan, M.M.Rahman, Eds., (Inst. of Physics, Bristol, 1994), p.499.
- [21] J.W.Palmour, private communication.
- [22] S.Yoshida, K.Sasaki, E.Sakuma, S.Misawa, and S.Gonda, *Appl. Phys. Lett.*, **46**, 766(1985).
- [23] A.Itoh, T.Kimoto, and H.Matsunami, *IEEE Electron Device Lett.*, **16**, 280(1995).
- [24] D.Alok, B.J.Baliga, and P.K.McLarty, *IEEE Electron Device Lett.*, **15**, 394(1994).
- [25] C.Canali, C.Jacoboni, F.Nava, G.Ottaviani, and A.A.Quaranta, *Phys. Rev.*, **B12**, 2265(1975).
- [26] D.L.Barrett and R.B.Campbell, *J. Appl. Phys.*, **38**, 53(1967).
- [27] W.Suttrop, G.Pensl, W.Choyke, R.Stein, and S.Leibenzeder, *J. Appl. Phys.*, **72**, 3708(1992).
- [28] B.J.Baliga, *Proc. of the IEEE*, **82**, 1112(1994).
- [29] C.T.Sah, R.N.Noyce, and W.Shockley, *Proc. of the IRE*, **45**, 1228(1957).
- [30] H.J.Queisser and A.Goetzberger, *Solid State Electron.*, **5**, 1063(1963).
- [31] P.G.Neudeck and J.A.Powell, *IEEE Electron Device Lett.*, **15**, 63(1994).

- [32] J.A.Edmond, K.Das, and R.F.Davis, J. Appl. Phys., **63**, 922(1988).
- [33] M.Ikeda, H.Matsunami, and T.Tanaka, Phys. Rev., **B22**, 2842(1980).
- [34] G.Pensl, R.Helbig, H.Zhang, G.Ziegler, and P.Lanig, Mat. Res. Soc. Sympo. Proc., **97**, 195(1987).
- [35] M.Ghezzi, D.M.Brown, E.Downey, J.Kretchmer, W.Hennessy, D.L.Polla, and H.Bakhru, IEEE Electron Device Lett., **12**, 639(1992).

Chapter 8

Conclusions

8.1 Conclusions

In this thesis, chemical vapor deposition (CVD) of SiC on SiC{0001} substrates has been studied in detail. In epitaxial growth of SiC, which shows a polytypism phenomenon, the polytype control is crucial for device applications. Polytype-controlled growth of high-quality SiC epilayers could be achieved by utilizing off-oriented substrates, which provide a surface template forcing the epilayers to inherit the stacking order of substrates (step-controlled epitaxy). Main conclusions obtained in the present study can be summarized as follows.

- (1) From a viewpoint of growth mode, step-flow growth on off-oriented α -SiC{0001} substrates leads to homoepitaxy of α -SiC (step-controlled epitaxy), whereas two-dimensional nucleation leads to the growth of 3C-SiC with double positioning twin. This enables us to identify the growth mode through *ex-situ* observation of epilayers. This technique can be applied to any SiC polytypes, and may be to any materials showing a polytypism phenomenon.
- (2) Single crystalline 6H-SiC could be epitaxially grown at temperatures as low as 1200°C with a 1 μ m/h growth rate, utilizing step-flow growth. However, twinned crystalline 3C-SiC was grown at 1100°C.
- (3) SiC growth is limited by the supply of Si species. In step-controlled epitaxy, very little polarity dependence and a small activation energy of growth

rate (2.8kcal/mole) were observed. These results can be well explained by the fact that the growth is controlled by the diffusion of reactants in a stagnant layer.

(4) Clear step bunching on the surfaces of 6H- and 4H-SiC epilayers was observed. Epilayers grown on off-oriented (0001)Si faces showed hill-and-valley structures. 3 bilayer-height steps were the most dominant on 6H-SiC and 4 bilayer-height steps on 4H-SiC. On off-oriented (000 $\bar{1}$)C faces, however, the surfaces were flat with single bilayer-height steps.

(5) Chemical vapor deposition of SiC on off-oriented 6H-SiC{0001} substrates was quantitatively analyzed based on the BCF theory. Critical growth conditions where the growth mode changes from step-flow to two-dimensional nucleation were predicted as a function of growth temperature, growth rate and substrate's off-angle.

(6) Through short-time growth experiments, nucleation and step dynamics on 6H-SiC{0001} were investigated. On well-oriented {0001} faces, the nucleus density is much higher on (000 $\bar{1}$)C faces, which can be attributed to the lower surface energy on the faces. The lateral growth rate of steps is about three orders of magnitude higher than the vertical growth rate at temperatures higher than 1400°C. The lateral growth rate has anisotropy, higher in the $\langle 11\bar{2}0 \rangle$ direction and lower in the $\langle 1\bar{1}00 \rangle$ direction.

(7) A simple diffusion model was proposed that the surface diffusion length can be estimated from the lateral growth rates of macrosteps. The surface diffusion length was about 13 μm on (0001)Si and (000 $\bar{1}$)C faces under a typical growth condition at 1500°C. The diffusion length decreased at low temperatures, under the high SiH₄ flow rate condition, and under the C-rich growth condition.

(8) High quality of SiC epilayers was demonstrated through a cross-sectional TEM analysis, low-temperature photoluminescence, *etc.* For the low-doped epilayers with a carrier concentration of $2 \times 10^{14} \text{cm}^{-3}$, a high electron mobility of 431cm²/Vs could be obtained, which is the highest ever reported in 6H-SiC. Deep level analyses showed that undoped epilayers have very few electron traps of which concentration is negligibly small ($< 10^{13} \text{cm}^{-3}$).

(9) *In-situ* doping of N, Al, and B was investigated in the wide range of $10^{16}\sim 10^{19}\text{cm}^{-3}$ with excellent controllability, using N_2 , TMA, and B_2H_6 as source gases. Remarkable polarity dependence of Al doping efficiency was observed, whereas N and B doping exhibited no such dependence.

(10) N^+ , Al^+ , and B^+ implantations into 6H-SiC{0001} epilayers were investigated. Severe damages remained even after annealing at 1500°C , once amorphous layers were formed through implantation. The lowest sheet resistances of 1500°C -annealed samples were $770\Omega/\square$ (n-type) for N^+ implantation, and $22\text{k}\Omega/\square$ (p-type) for Al^+ implantation. B^+ implantation resulted in the formation of resistive layers ($\rho=15\sim 120\Omega\text{cm}$).

(11) Numerical analyses on the performance of 6H- and 4H-SiC power Schottky rectifiers and MOSFETs have been performed with consideration of the mobility anisotropy and channel resistances. The extremely low drift region resistances (about $1/50\sim 1/500$ of those of Si devices) can be expected, owing to its high breakdown field. This fact, however, makes the channel resistances very important in SiC power MOSFETs.

(12) Au/6H-SiC Schottky rectifiers were successfully fabricated with the record breakdown voltage of 1100V. These high-voltage 6H-SiC rectifiers had specific on-resistances lower than the theoretical limits of Si rectifiers by a factor of $10\sim 20$. 6H-SiC epitaxial pn junction diodes with $15\mu\text{m}$ thick low-doped layers exhibited a very high breakdown voltage of 1720V. The pn junction diodes formed by N^+ implantation showed high breakdown voltages of 450V. These diodes operated with good rectification at temperature as high as 350°C .

8.2 For the Future Work

As described in the introduction (1.3), this thesis has two aims:

- (i) to combine experimental and theoretical studies in order to provide complete understanding of crystal growth mechanism, and
- (ii) to demonstrate the feasibility of a new semiconductor material SiC for extending the frontiers of future electronics.

Although the author has spent more than 5 years to accomplish this thesis,

the obtained results are still far from the satisfactory levels. In this section, the author would like to list up several remaining problems together with suggestions for the future work.

As for the subject on revealing growth mechanism, the following issues should be clarified.

(1) In chemical vapor deposition, chemical reactions on the growing surface play an important role. In the present system, the decomposition process of SiH_4 and C_3H_8 , and the chemical reactions were assumed in a simplified manner. The amount and behavior of C species (CH_x , C_2H_x) will give significant influences on surface kinetics and surface coverage. A thermodynamic analysis might offer some information [1].

(2) In order to avoid the complicated consideration, surface migration and nucleation were treated with a Si-C pair as the unit which controls growth. In epitaxial growth of GaAs, Ga adatoms are supposed to be the dominant migrating species [2]. Although the author supposes that SiC growth is controlled by Si species, this speculation should be verified. *In-situ* coaxial impact collision ion scattering spectroscopy (CAICISS) [3] may be effective to clarify the species adsorbed at step edges. Fundamental investigation on MBE growth of SiC will also provide new aspects on surface kinetics.

(3) Mechanisms of step bunching and nucleation were not clear at present, though some primitive explanations were presented. In order to understand the mechanism, surface energies of arbitrary crystal planes, ledge energies, and step-step interactions should be known [4]. A study using molecular dynamics calculation may be hopeful as the first step.

(4) Although step-controlled epitaxy has realized the perfect *replication* of substrate's polytype in epilayers, this does not mean the perfect *control* of polytypes. An ultimate target will be to achieve layer by layer control in the stacking sequence. For example, 6H-SiC/4H-SiC superlattices with perfect lattice matching are attractive from a viewpoint of scientific interest. Since the origin of polytypism is an open question, concentrated experimental and theoretical studies are required. This subject is challenging, but of great interest.

Concerning the characterization and device applications of SiC, the following issues should be solved.

- (1) The growth temperature should be reduced down to 1200~1300°C. High-temperature growth causes the impurity contamination from a growth system and the shortening of susceptor life. Though homoepitaxy of 6H-SiC at 1200°C was achieved in this thesis, the quality of epilayers is poor. Epitaxial growth on (0 $\bar{1}$ 1 $\bar{4}$), (1 $\bar{1}$ 00) or (11 $\bar{2}$ 0) faces using a new feed-stock may be hopeful.
- (2) Further reduction of background doping concentration will be required to develop high-voltage (≥ 10 kV) SiC devices. To attain the excellent reproducibility, low-doped layers with a donor concentration of 10^{14} cm $^{-3}$ should be produced by intentional doping. For this purpose, the introduction of an air-locked growth system and the purification of a susceptor and source gases are necessary.
- (3) For practical device fabrication, the uniformity of epilayer thickness and the doping concentration should be improved. The employment of low-pressure CVD may be effective to obtain uniform epilayers with a large area. For low-doped epilayers, neutron transmutation doping, which is used to produce uniform low-doped drift regions in Si power devices [5], should be investigated.
- (4) Although low density of electron traps ($\leq 10^{13}$ cm $^{-3}$) was demonstrated, traps located at energy levels deeper than E_c-1 eV could not be characterized. Since very high temperature over 700°C is required in a conventional DLTS measurement to characterize such deep levels, a photo-assisted deep level analysis may be an effective technique. Besides, minority carrier traps and carrier lifetimes, which control the performance of bipolar devices, should be studied.
- (5) Microscopic defects in epilayers could not be analyzed at all. For example, there have been very few approaches on hydrogen and oxygen in SiC, which will exist in the crystals. The formation of point defects, defect-complexes, and the deviation from stoichiometry have become meaningful subjects.
- (6) The mechanism of doping efficiency - polarity dependence and C/Si ratio dependence - is not fully understood at present. The decomposition and adsorption processes of dopant gases should be studied. It would be suggestive to clarify the surface coverage and adsorbed species.
- (7) The sheet resistances of implanted layers should be reduced down to 100 Ω /□, especially in Al $^{+}$ implantation. Since the complete regrowth of SiC seems difficult, the employment of hot implantation may be promising

[6]. The post-implantation annealing process should be also improved through the development of high-temperature rapid thermal annealing (RTA) or laser-annealing processes.

(8) The author believes that high-voltage SiC Schottky rectifiers are the most attractive devices which will give innovational impacts on electronics in the nearest future. However, several problems should be solved before the production. The development of an edge-termination and a surface passivation techniques are important to achieve high reliability and to improve the production yield. The stabilization of Schottky contacts utilizing a silicidation reaction at the interface may be also effective. Preliminary trials on these subjects have been started [7].

(9) Although high breakdown voltages were obtained in Schottky rectifiers and pn junction diodes, the dominant pass of reverse leakage current, which is higher than theoretical values by orders of magnitude, is not clear. Besides, the negative temperature dependence of breakdown voltage in SiC devices has been a mystery. The reverse bias characteristics should be carefully investigated on the optimized structures which employ edge termination, surface passivation, and a guard ring. Detailed characterization of deep levels will be also helpful.

(10) To realize high-performance SiC power MOSFETs, the characteristics of MOS interfaces should be significantly improved, although this subject was not studied in this thesis. In SiC MOS devices, deep interface states act as "slow states" which cause charge trapping, bias stress instability, and abnormal temperature dependence of channel mobility [8,9]. This problem is serious in SiO₂/p-type SiC structures. One possible explanation is that the incorporation of Al (usual acceptors in SiC) into oxides severely degrades the oxide quality [10]. To improve the MOS interface, the employment of a different acceptor such as B may be effective [11].

(11) At last, the author cannot help touching the SiC wafer quality as the most important problem, though this topic is out of scope in this thesis. A major defect in SiC wafers is a "micropipe", as described in 6.2. Micropipes originating from SiC wafers cause pre-avalanche point failures in high-voltage junction devices [12]. To realize kV - kA SiC power devices, micropipes should

be eliminated.

Thus, there still remain a number of problems to be solved before SiC reaches its full potential. The author believes, however, that this material will exploit novel electronics in the near future. In particular, the development of high-performance SiC power devices can contribute to the energy saving, which has become one of the most serious and inevitable problems. However, the potential of SiC is so high that it can be used for advanced military applications. The author heartily wishes the peaceful use of this vital material.

References

- [1] M.D.Allendorf and R.J.Kee, *J. Electrochem. Soc.*, **138**, 841(1991).
- [2] T.Nishinaga and T.Suzuki, *J. Crystal Growth*, **115**, 398(1991).
- [3] T.Saitoh, A.Hashimoto, and M.Tamura, *J. Appl. Phys.*, **71**, 3802(1992).
- [4] E.D.Williams, R.J.Phaneuf, J.Wei, N.C.Bartelt, and T.L.Einstein, *Surf. Sci.*, **294**, 219(1993).
- [5] E.Meese, *Neutron Transmutation Doping in Semiconductors* (Plenum, New York, 1979).
- [6] N.Inoue, A.Itoh, T.Kimoto, H.Matsunami, T.Nakata, and M.Watanabe, presented at *the 6th Int. Conf. on Silicon Carbide and Related Materials - 1995*.
- [7] A.Itoh, T.Kimoto, and H.Matsunami, *Proc. of 7th Int. Sympo. on Power Semiconductor Devices and IC's* (1995), p.101.
- [8] T.Ouisse, N.Becourt, C.Jaussaud, F.Templier, *J. Appl. Phys.*, **75**, 604(1994).
- [9] P.G.Neudeck, S.Kang, J.Petit, M.Tabib-Azar, *J. Appl. Phys.*, **75**, 7949(1994).
- [10] P.Rai-Choudhury, Y.C.Kao, and G.G.Sweeney, *J. Electrochem. Soc.*, **121**, 1509(1974).
- [11] H.Akita, T.Kimoto, N.Inoue, and H.Matsunami, presented at *the 6th Int. Conf. on Silicon Carbide and Related Materials - 1995*.
- [12] P.G.Neudeck and J.A.Powell, *IEEE Electron Device Lett.*, **15**, 63(1994).

Appendix A.1 Critical Supersaturation Ratio α_{crit}

According to the classical nucleation theory, a critical nucleation rate J_{nuc}^* can be expressed by [1]

$$J_{\text{nuc}}^* = Z\omega^*n^*. \quad (1)$$

Here, n^* is the concentration of critical nuclei, ω^* the frequency with which a nucleus grows to become supercritical, and Z the Zeldovich non-equilibrium factor to account for depletion of the critical nuclei population due to their growth or decomposition. Using several equations, eq.(1) can be rearranged as [1],

$$J_{\text{nuc}}^* = \left[\left(\frac{E_{\text{nuc}}^*}{4\pi kT i^{*2}} \right)^{1/2} 2\pi r^* a\nu n_s n_0 \exp\left(-\frac{E_{\text{diff}}^*}{kT}\right) \right] \exp\left(-\frac{E_{\text{nuc}}^*}{kT}\right), \quad (2)$$

where E_{nuc}^* , r^* and i^* are the free energy for nucleus formation, the radius and the concentration of atoms for a critical nucleus, respectively. E_{diff} is the activation energy for surface diffusion, n_0 the density of adatom sites on a surface, ν the frequency of atomic vibration. Other symbols are listed on page 111 (Chapt.4). Since the term in brackets can be approximated as $\exp(65)$ [1], the above equation is reduced to

$$J_{\text{nuc}}^* = \exp(65) \exp\left(-\frac{E_{\text{nuc}}^*}{kT}\right). \quad (3)$$

In the case of a disk-shaped nucleus, the relationship between E_{nuc} and critical supersaturation ratio α_{crit} is expressed by [1]

$$E_{\text{nuc}}^* = \frac{\pi h_0 \sigma^2 \Omega}{kT \ln \alpha}, \quad (4)$$

where Ω and σ are the volume of an atom and the surface free energy, respectively. By substituting eq.(4) into eq.(3), the critical supersaturation ratio α_{crit} is given by

$$\alpha_{\text{crit}} = \exp\left\{\frac{\pi h_0 \sigma^2 \Omega}{(65 - \ln J_{\text{nuc}}^*) k^2 T^2}\right\}. \quad (5)$$

Thus, eq.(4.21) can be obtained for $J_{\text{nuc}}^* = 10^{12} \text{cm}^{-2} \text{s}^{-1}$.

Reference

- [1] J.P.Hirth and G.M.Pound, *Condensation and Evaporation, Nucleation and Growth Kinetics* (Pergamon Press, Oxford, 1963), Chapt.D.

List of Publications

A. Full length papers and letters

- (1) T.Kimoto, H.Nishino, T.Ueda, A.Yamashita, W.S.Yoo, and H.Matsunami, "Photoluminescence of Ti doped 6H-SiC grown by vapor phase epitaxy", Jpn. J. Appl. Phys., **30**, L289-L291(1991).
- (2) A.Yamashita, W.S.Yoo, T.Kimoto, and H.Matsunami, "Homoepitaxial chemical vapor deposition of 6H-SiC at low temperatures on $\{01\bar{1}4\}$ substrates", Jpn. J. Appl. Phys., **31**, 3655-3661(1992).
- (3) T.Kimoto, H.Nishino, W.S.Yoo, and H.Matsunami, "Growth mechanism of 6H-SiC in step-controlled epitaxy", J. Appl. Phys., **73**, 726-732(1993).
- (4) T.Kimoto, T.Urushidani, S.Kobayashi, and H.Matsunami, "High-voltage ($> 1\text{kV}$) SiC Schottky barrier diodes with low on-resistances", IEEE Electron Device Lett., **14**, 548-550(1993).
- (5) T.Kimoto, A.Yamashita, A.Itoh, and H.Matsunami, "Step-controlled epitaxial growth of 4H-SiC and doping of Ga as a blue luminescent center", Jpn. J. Appl. Phys., **32**, 1045-1050(1993).
- (6) T.Kimoto and H.Matsunami, "Surface kinetics of adatoms in vapor phase epitaxial growth of SiC on 6H-SiC $\{0001\}$ vicinal surfaces", J. Appl. Phys., **75**, 850-859(1994).

- (7) T.Kimoto and H.Matsunami,
"Nucleation and step-motion in chemical vapor deposition of SiC on 6H-SiC{0001} faces",
J. Appl. Phys., **76**, 7322-7327(1994).
- (8) S.Jang, T.Kimoto, and H.Matsunami,
"Deep levels in 6H-SiC wafers and step-controlled epitaxial layers",
Appl. Phys. Lett., **65**, 581-583(1994).
- (9) A.Itoh, H.Akita, T.Kimoto, and H.Matsunami,
"High-quality 4H-SiC homoepitaxial layers grown by step-controlled epitaxy",
Appl. Phys. Lett., **65**, 1400-1402(1994).
- (10) F.R.Chien, S.R.Nutt, W.S.Yoo, T.Kimoto, and H.Matsunami
"Interface structures of epitaxial beta-SiC on alpha-SiC substrates",
J. Crystal Growth, **137**, 175-180(1994).
- (11) F.R.Chien, S.R.Nutt, W.S.Yoo, T.Kimoto, and H.Matsunami
"Terrace growth and polytype development in epitaxial beta-SiC films on alpha-SiC (6H and 15R) substrates",
J. Mater. Res., **9**, 940-954(1994).
- (12) T.Kimoto, A.Itoh, H.Matsunami, T.Nakata, and M.Watanabe,
"The effects of N⁺ dose in implantation into 6H-SiC epilayers",
J. Electron. Mater., **24**, 235-240(1995).
- (13) T.Kimoto and H.Matsunami,
"Surface diffusion lengths of adatoms on 6H-SiC{0001} faces in chemical vapor deposition of SiC",
J. Appl. Phys., **78**, 3132-3137(1995).
- (14) S.Yaguchi, T.Kimoto, N.Ohyama, and H.Matsunami,
"Nitrogen ion implantation into 6H-SiC and application to high-temperature, radiation-hard diodes",
Jpn. J. Appl. Phys., **34**, 3036-3042(1995).
- (15) T.Kimoto, A.Itoh, and H.Matsunami,
"Step bunching in chemical vapor deposition of 6H- and 4H-SiC on vicinal SiC{0001} faces",
Appl. Phys. Lett., **66**, 3645-3647(1995).

- (16) A.Itoh, T.Kimoto, and H.Matsunami,
“High-performance of high-voltage 4H-SiC Schottky barrier diodes”,
IEEE Electron Device Lett., **16**, 280-282(1995).
- (17) T.Kimoto, A.Itoh, and H.Matsunami,
“Incorporation mechanism of N, Al, and B impurities in chemical
vapor deposition of SiC”,
Appl. Phys. Lett., **67**, 2385-2387(1995).
- (18) K.Nishino, T.Kimoto, and H.Matsunami,
“Photoluminescence of homoepitaxial 3C-SiC on sublimation-grown
3C-SiC substrates”,
Jpn. J. Appl. Phys. Lett., **34**, L1110-L1113(1995).
- (19) T.Kimoto, A.Itoh, H.Matsunami, S.Sridhara, L.L.Clemen, R.P.Devaty,
W.J.Choyke, T.Dalibor, C.Peppermüller, and G.Pensl,
“Nitrogen donors and deep levels in high-quality 4H-SiC epilayers grown
by chemical vapor deposition”,
Appl. Phys. Lett., **67**, vol.19, (1995), in press.
- (20) T.Kimoto, A.Itoh, H.Matsunami, T.Nakata, and M.Watanabe,
“Aluminum and boron ion implantations into 6H-SiC epilayers”,
J. Electron. Mater., **26**, (1996), in press.
- (21) T.Kimoto, A.Itoh, H.Matsunami, and T.Okano
“Step bunching mechanism in chemical vapor deposition of α -SiC{0001}”,
to be submitted to J. Appl. Phys.

B. Proceedings of international conferences

- (1) W.S.Yoo, A.Yamashita, T.Kimoto, and H.Matsunami,
“Bulk crystal growth of 6H-SiC on polytype-controlled substrates through
vapor phase and characterization”,
J. Crystal Growth, **115**, 733-739(1992).
(*Proc. of 7th Int. Conf. on Vapor Phase Epitaxy*, Nagoya, 1991)
- (2) T.Kimoto, H.Nishino, A.Yamashita, W.S.Yoo, and H.Matsunami,
“Low temperature homoepitaxial growth of 6H-SiC by VPE method”,
Amorphous and Crystalline Silicon Carbide IV (Springer-Verlag, Berlin,
1992), p.31-39.

- (*Proc. of 4th Int. Conf. Amorphous and Crystalline Silicon Carbide-1991*, Santa Clara, 1991).
- (3) W.S.Yoo, C.P.Beetz, F.R.Chien, S.R.Nutt, T.Kimoto, and H.Matsunami, "A model for double positioning twin formation in cubic SiC on noncubic SiC substrates", *Mat. Res. Soc. Sympo. Proc.*, **280**, 729-732(1993).
- (4) T.Urushidani, S.Kobayashi, T.Kimoto, and H.Matsunami, "SiC Schottky barrier diodes with high blocking voltage of 1kV", *Ext. Abstr. of 1993 Int. Conf. on Solid State Devices and Materials*, Chiba, 1993, p.814-816.
- (5) T.Kimoto and H.Matsunami, "Two-dimensional nucleation and step-dynamics in crystal growth of SiC", *Silicon Carbide and Related Materials 1993* (Inst. of Physics, Bristol, 1994), p.55-58.
(*Proc. of 5th Int. Conf. on Silicon Carbide and Related Materials-1993*, Washington DC, 1993)
- (6) T.Kimoto and H.Matsunami, "Growth model for step-controlled epitaxy of SiC", *Silicon Carbide and Related Materials 1993* (Inst. of Physics, Bristol, 1994), p.95-98.
(*Proc. of 5th Int. Conf. on Silicon Carbide and Related Materials-1993*, Washington DC, 1993)
- (7) K.Nishino, T.Kimoto and H.Matsunami, "Epitaxial growth of 3C-SiC on α -SiC substrates by chemical vapor deposition", *Silicon Carbide and Related Materials 1993* (Inst. of Physics, Bristol, 1994), p.33-36.
(*Proc. of 5th Int. Conf. on Silicon Carbide and Related Materials-1993*, Washington DC, 1993)
- (8) A.Itoh, H.Akita, T.Kimoto and H.Matsunami, "Step-controlled epitaxy of 4H-SiC and its physical properties", *Silicon Carbide and Related Materials 1993* (Inst. of Physics, Bristol, 1994), p.59-62.
(*Proc. of 5th Int. Conf. on Silicon Carbide and Related Materials-1993*,

Washington DC, 1993)

- (9) T.Urushidani, S.Kobayashi, T.Kimoto and H.Matsunami,
“High-voltage Au/6H-SiC Schottky barrier diodes”,
Silicon Carbide and Related Materials 1993 (Inst. of Physics, Bristol,
1994), p.471-474.
(*Proc. of 5th Int. Conf. on Silicon Carbide and Related Materials-1993*,
Washington DC, 1993)
- (10) H.Matsunami and T.Kimoto (invited),
“Nucleation and step dynamics in SiC epitaxial growth”,
Mat. Res. Soc. Sympo. Proc., **339**, 369-379(1994).
- (11) T.Kimoto, A.Itoh, H.Akita, T.Urushidani, S.Jang, and H.Matsunami,
“Step-controlled epitaxial growth of α -SiC and application to high-voltage
Schottky rectifiers”,
Compound Semiconductors - 1994 (Inst. of Physics, Bristol, 1995),
p.437-442.
(*Proc. of 21st Int. Sympo. on Compound Semiconductors*, San Diego,
1994)
- (12) A.Itoh, T.Kimoto, and H.Matsunami,
“Efficient power Schottky rectifiers of 4H-SiC”,
Proc. 7th Int. Sympo. on Power Semiconductor Devices and IC's,
Yokohama, 1995, p.101-106.
- (13) T.Kimoto, A.Itoh, N.Inoue, S.Yaguchi, and H.Matsunami,
“Ion-implantation into α -SiC epilayers and application to high-temperature,
high-voltage devices”,
to be published in *Compound Semiconductors - 1995* (Inst. of Physics,
Bristol, 1995), in press.
(*Proc. of 22st Int. Sympo. on Compound Semiconductors*, Cheju, 1995)
- (14) T.Kimoto, A.Itoh, and H.Matsunami,
“Step bunching in 6H- and 4H-SiC growth by step-controlled epitaxy”,
Silicon Carbide and Related Materials 1995 (Inst. of Physics, Bristol),
in press.
(*Proc. of 6th Int. Conf. on Silicon Carbide and Related Materials-1995*,
Kyoto, 1995)

- (15) H.Akita, T.Kimoto, N.Inoue, and H.Matsunami,
“Thermal oxidation of B-doped p-type 6H-SiC and fabrication of MOS diodes”,
Silicon Carbide and Related Materials 1995 (Inst. of Physics, Bristol),
in press.
(*Proc. of 6th Int. Conf. on Silicon Carbide and Related Materials-1995*,
Kyoto, 1995)
- (16) T.Kimoto, A.Itoh, H.Matsunami, S.Sridhara, R.P.Devaty, W.J.Choyke,
T.Dalibor, C.Peppermüller, and G.Pensl,
“Characterization of high-quality 4H-SiC epitaxial layers”,
Silicon Carbide and Related Materials 1995 (Inst. of Physics, Bristol),
in press.
(*Proc. of 6th Int. Conf. on Silicon Carbide and Related Materials-1995*,
Kyoto, 1995)
- (17) N.Inoue, A.Itoh, T.Kimoto, H.Matsunami, T.Nakata, and M.Watanabe,
“Hot implantation of N⁺ into α -SiC epilayers”,
Silicon Carbide and Related Materials 1995 (Inst. of Physics, Bristol),
in press.
(*Proc. of 6th Int. Conf. on Silicon Carbide and Related Materials-1995*,
Kyoto, 1995)
- (18) A.Itoh, T.Kimoto, and H.Matsunami,
“Low power-loss 4H-SiC Schottky rectifiers with high blocking voltage”,
Silicon Carbide and Related Materials 1995 (Inst. of Physics, Bristol),
in press.
(*Proc. of 6th Int. Conf. on Silicon Carbide and Related Materials-1995*,
Kyoto, 1995)

C. Review articles

- (1) T.Kimoto and H.Matsunami,
“Step-controlled epitaxy in semiconductor SiC polytypes”,
Oyo Buturi, **64**, 691-694(1995) (in Japanese).
- (2) T.Kimoto (invited),
“Step-controlled epitaxy of SiC polytypes and step dynamics”,
J. Jpn. Assoc. Crystal Growth, **22**, 105-108(1995) (in Japanese).
- (3) T.Kimoto and H.Matsunami,
“Crystal growth of high-quality silicon carbide by step-controlled epitaxy”,
Oyodenshibussei-bunkakai-shi, the Japan Society of Applied Physics,
1, No.3, 13-18(1995) (in Japanese).
- (4) T.Kimoto and H.Matsunami,
“Step-controlled epitaxial growth of SiC and step dynamics”,
J. Jpn. Assoc. Crystal Growth, **22**, (1995),
in press (in Japanese).

